THEORETICAL INVESTIGATION OF THE WATER SPLITTING MECHANISM ON TRANSITION METAL OXIDE CATALYSTS

by

AMENDRA FERNANDO HEWA DEWAGE

B.S., University of Colombo, 2010

AN ABSTRACT OF A DISSERTATION

submitted in partial fulfillment of the requirements for the degree

DOCTOR OF PHILOSOPHY

Department of Chemistry
College of Arts and Sciences

KANSAS STATE UNIVERSITY
Manhattan, Kansas

2016

Abstract

Water oxidation can be considered as the 'holy grail' of renewable energy research, where water is split into constituent molecular hydrogen and oxygen. Hydrogen is a very efficient energy source that is both clean and sustainable. The byproduct of hydrogen combustion is water, which in turn can be reused as the source for hydrogen generation. Natural water splitting is observed during photosynthesis in the oxygen-evolving complex of photosystem II, which consists of a $CaMn_4O_4$ cubane core. Herein, we report *in silico* approaches to understand bottom up catalytic design of model transition metal oxide complexes for water splitting. We have employed density functional theory to investigate model ligand-free architectures of cobalt and manganese oxide dimer ($Mn_2(\mu\text{-}OH)(\mu\text{-}O)(H_2O)_3(OH)_5$, $Mn_2(\mu\text{-}OH)_2(H_2O)_4(OH)_4$, $Mn_2(\mu\text{-}OH)_2(H_2O)_2(OH)_2(O(CH)_3O)_2$, $Co_2(\mu\text{-}OH)_2(H_2O)_4(OH)_4$) and cubane ($Co_4O_4(H_2O)_8(OH)_4$, $Mn_4O_4(H_2O)_x(OH)_y$ x = 4-8, y = 8-4) complexes.

The thermodynamically lowest energy pathway on the cobalt dimer catalyst proceeds through a nucleophilic attack of a solvent water molecule to a Co(V)-O radical moiety whereas the pathway on the cubane catalyst involves a geminal coupling of a Co(V)-O radical oxo group with bridging oxo sites. The lowest energy pathway for the fully saturated $Mn_2O_4\bullet 6H_2O$ ($Mn_2(\mu\text{-}OH)(\mu\text{-}O)(H_2O)_3(OH)_5$) and $Mn_2O_3\bullet 7H_2O$ ($Mn_2(\mu\text{-}OH)_2(H_2O)_4(OH)_4$) complexes occur through a nucleophilic attack of a solvent water molecule to Mn(IV½)O and Mn(V)O oxo moieties respectively. Out of all the oxidation state configurations studied for the manganese cubane, we observed that Mn_4(IV IV IV IV), Mn_4(III IV IV IV), and Mn_4(III III IV V) configurations are thermodynamically viable for water oxidation. All three of these reaction pathways proceed via nucleophilic attack of solvent water molecule to the manganese oxo species. The highest thermodynamic energy step in manganese dimer and cubane complexes corresponds to the

formation of the manganese oxo species, which is a significant feature that reoccurred in all these reaction pathways. We have also employed multireference and multiconfigurational calculations to investigate the $Mn_2(\mu\text{-}OH)_2(H_2O)_2(OH)_2(O(CH)_3O)_2$ system. The presence of $Mn(IV)O^{\bullet}$ radical moieties has been observed in this catalytic pathway. These simplest models of cobalt and manganese with water-derived ligands are essential to understand microscopic properties that can be used as descriptors in designing future catalysts.

THEORETICAL INVESTIGATION OF THE WATER SPLITTING MECHANISM ON TRANSITION METAL OXIDE CATALYSTS

by

AMENDRA FERNANDO HEWA DEWAGE

B.S., University of Colombo, 2010

A DISSERTATION

submitted in partial fulfillment of the requirements for the degree

DOCTOR OF PHILOSOPHY

Department of Chemistry
College of Arts and Sciences

KANSAS STATE UNIVERSITY
Manhattan, Kansas

2016

Approved by:

Major Professor
Christine M. Aikens

Copyright

Abstract

Water oxidation can be considered as the 'holy grail' of renewable energy research, where water is split into constituent molecular hydrogen and oxygen. Hydrogen is a very efficient energy source that is both clean and sustainable. The byproduct of hydrogen combustion is water, which in turn can be reused as the source for hydrogen generation. Natural water splitting is observed during photosynthesis in the oxygen-evolving complex of photosystem II, which consists of a $CaMn_4O_4$ cubane core. Herein, we report *in silico* approaches to understand bottom up catalytic design of model transition metal oxide complexes for water splitting. We have employed density functional theory to investigate model ligand-free architectures of cobalt and manganese oxide dimer ($Mn_2(\mu\text{-}OH)(\mu\text{-}O)(H_2O)_3(OH)_5$, $Mn_2(\mu\text{-}OH)_2(H_2O)_4(OH)_4$, $Mn_2(\mu\text{-}OH)_2(H_2O)_2(OH)_2(O(CH)_3O)_2$, $Co_2(\mu\text{-}OH)_2(H_2O)_4(OH)_4$) and cubane ($Co_4O_4(H_2O)_8(OH)_4$, $Mn_4O_4(H_2O)_x(OH)_y$ x = 4-8, y = 8-4) complexes.

The thermodynamically lowest energy pathway on the cobalt dimer catalyst proceeds through a nucleophilic attack of a solvent water molecule to a Co(V)-O radical moiety whereas the pathway on the cubane catalyst involves a geminal coupling of a Co(V)-O radical oxo group with bridging oxo sites. The lowest energy pathway for the fully saturated $Mn_2O_4\bullet 6H_2O$ ($Mn_2(\mu\text{-}OH)(\mu\text{-}O)(H_2O)_3(OH)_5$) and $Mn_2O_3\bullet 7H_2O$ ($Mn_2(\mu\text{-}OH)_2(H_2O)_4(OH)_4$) complexes occur through a nucleophilic attack of a solvent water molecule to Mn(IV½)O and Mn(V)O oxo moieties respectively. Out of all the oxidation state configurations studied for the manganese cubane, we observed that Mn_4(IV IV IV IV), Mn_4(III IV IV IV), and Mn_4(III III IV V) configurations are thermodynamically viable for water oxidation. All three of these reaction pathways proceed via nucleophilic attack of solvent water molecule to the manganese oxo species. The highest thermodynamic energy step in manganese dimer and cubane complexes corresponds to the

formation of the manganese oxo species, which is a significant feature that reoccurred in all these reaction pathways. We have also employed multireference and multiconfigurational calculations to investigate the $Mn_2(\mu\text{-}OH)_2(H_2O)_2(OH)_2(O(CH)_3O)_2$ system. The presence of $Mn(IV)O^{\bullet}$ radical moieties has been observed in this catalytic pathway. These simplest models of cobalt and manganese with water-derived ligands are essential to understand microscopic properties that can be used as descriptors in designing future catalysts.

Table of Contents

List of Figures xii
List of Tables xv
Acknowledgements xvi
Dedication xviii
Preface xix
Chapter 1 - Introduction 1
1.1 Manganese Oxides 4
1.1.1 Manganese Oxide Dimer Complexes 5
1.1.2 Manganese Oxide Cubane Complexes 8
1.2 Cobalt Oxide Complexes 10
1.2.1 Cobalt Oxide Dimer Complexes 11
1.2.2 Cobalt Oxide Cubane Complexes 12
1.3 Objective and Overview of the Thesis 14
1.4 References 17
Chapter 2 - Theory and computational methodology 21
2.1 Fundamentals of quantum mechanics 21
2.2 Approximation methods 22
2.2.1 The variational method 22
2.2.2 Perturbation theory 23
2.2.3 The Born-Oppenheimer approximation 23
2.3 Computational methods 26
2.3.1 Density functional methods 26
2.3.1.1 Density functional theory (DFT) 26
2.3.1.2 The Hohenberg-Kohn theorem 26
2.3.1.3 The Kohn-Sham method 28
2.3.1.4 Exchange-correlation functionals 31
Local density approximation (LDA) 31
Generalized gradient approximation (GGA) 32
Meta-GGA functionals 33

Hybrid functionals 33
2.3.2 Other correlation methods 34
2.3.2.1 Configuration Interactions (CI) method 34
2.3.2.2 Multiconfiguration self-consistent field method (MCSCF) 35
2.3.2.3 Multireference configuration interaction (MRCI) 37
2.3.2.4 Multireference Møller-Plesset perturbation theory (MRMP2) 37
2.4 Basis sets 38
2.5 References 40
Chapter 3 - Theoretical Investigation of Water Oxidation on Fully Saturated Mn_2O_3 and Mn_2O_4 Complexes 42
3.1 Abstract 42
3.2 Introduction 43
3.3 Computational Methodology 45
3.4 Results and Discussion 47
3.4.1 Water oxidation process with fully saturated Mn_2O_4 47
3.4.2 The saturation process of Mn_2O_3 56
3.4.3 The water oxidation process with the six water saturated Mn_2O_3 58
3.4.4 The water oxidation process with the fully saturated Mn_2O_3 60
3.5 General Discussion 66
3.6 Conclusions 68
3.7 Acknowledgements 69
3.8 References 69
Chapter 4 - Theoretical Investigation of Water Oxidation Catalysis by a Model Manganese Cubane Complex 73
4.1 Abstract 73
4.2 Introduction 73
4.3 Computational Methodology 77
4.4 Results and Discussion 79
4.4.1 Mn_4(IV IV IV IV) configuration with μ_3-oxo groups 80
4.4.2 Mn_4(IV IV IV IV) configuration with μ_3-hydroxo groups 84
4.4.3 Mn_4(III IV IV IV) configuration with μ_3-oxo groups 88

4.4.4 Mn_4(III IV IV IV) configuration with μ_3-hydroxo groups 91
4.4.5 Mn_4(III III IV IV) configuration with μ_3-oxo groups 94
4.4.6 Mn_4(III III IV IV) configuration with μ_3-hydoxo groups 95
4.4.7 Mn_4(III III III IV) configuration with μ_3-oxo groups 96
4.4.8 Mn_4(III III III IV) configuration with μ_3-hydroxo groups 97
4.4.9 Mn_4(III III III III) configuration with μ_3-oxo groups 98
4.4.10 Mn_4(III III III III) configuration with μ_3-hydroxo groups 99
4.5 General Discussion 99
4.6 Conclusions 101
4.7 Acknowledgements 103
4.8 References 103
Chapter 5 - Ab initio electronic structure study of a model water splitting dimer complex 108
5.1 Abstract 108
5.2 Introduction 108
5.3 Computational Methods 114
5.4 Results and discussion 116
5.4.1 Structure 1 118
5.4.2 Structure 2 122
5.4.3 Structure 3 125
5.4.4 Structure 4 127
5.4.5 Structure 5 129
5.4.6 Structure 6 130
5.4.7 Structure 7 131
5.5 Concluding Remarks 134
5.6 Acknowledgements 135
5.7 References 135
Chapter 6 - Reaction pathways for water oxidation to molecular oxygen mediated by model cobalt oxide dimer and cubane catalysts 140
6.1 Abstract 140
6.2 Introduction 140
6.3 Computational methodology 143

6.4 Results and Discussion 145
6.4.1 Cobalt Dimer Complex 145
6.4.1.1 Pathway 1 147
6.4.1.2 Pathway 2 150
6.4.1.3 Pathway 3 152
6.4.1.4 Comparison of Pathways 1-3 154
6.4.1.5 Pathways from Structure D10 154
6.4.1.6 Comparison between pathways from D1 and D10 156
6.4.2 Cobalt Cubane Complex 157
6.4.2.1 Pathway 4 158
6.4.2.2 Pathway 5 163
6.4.2.3 Pathway 6 165
6.4.2.4 Discussion of pathways 1-6 166
6.4.2.5 Pathway 7 from C7 isomer 167
6.4.2.6 Pathway 8 from C7 isomer 171
6.4.2.7 Cubane Pathways Discussion 173
6.5 Conclusions 174
6.6 Acknowledgements 175
6.7 References 175
Chapter 7 - Conclusions 178
Appendix A - Supporting information for “Theoretical Investigation of Water Oxidation on Fully Saturated Mn_2O_3 and Mn_2O_4 Complexes” 181
Appendix B - Supporting information for “Theoretical Investigation of Water Oxidation Catalysis by a Model Manganese Cubane Complex” 185
Appendix C - Supporting Information for “Ab initio electronic structure study of a model water splitting dimer complex” 188
Appendix D - Supporting Information for “Reaction pathways for water oxidation to molecular oxygen mediated by model cobalt oxide dimer and cubane catalysts” 191

List of Figures

Figure 1.1 Active complex of the OEC of PSII, a $CaMn_4O_4$ cubane complex with a dangling manganese atom. 2

Figure 3.1 Water oxidation process on the fully saturated $Mn_2O_4•6H_2O$ complex from Ref. 44. Relative energies are given in eV. Big white spheres, big red spheres, and small white spheres represent the manganese, oxygen, and hydrogen atoms, respectively. This color code is kept consistent through the article (Reprinted with permission from *J. Phys. Chem. A* 2014, *118*, 8204-8221. Copyright 2014 American Chemical Society). 48

Figure 3.2 Structures 76 and 77 of Figure 3.1 optimized with BP86/ATZP with different numerical cutoff values. The BP86/TZP values are also given for comparison. Bond lengths are given in Å (black dotted line or white/red line). 50

Figure 3.3 Fully saturated Mn_2O_4 complex optimized using different level of theories. The structures on the right are almost mirror images of the structures on the left; arrows indicate ligand orientations that differ from the left side images. 51

Figure 3.4 The lowest energy reaction pathway-1 calculated using the BP86/TZP level of theory for the fully saturated $Mn_2O_4•6H_2O$ structure 1. 52

Figure 3.5 The second lowest energy reaction pathway-2 on the fully saturated $Mn_2O_4•6H_2O$ structure 1 calculated using the BP86/TZP level of theory. 54

Figure 3.6 Isomers of Mn_2O_3 using the BP86/TZP level of theory. 56

Figure 3.7 Water adsorption and dissociation processes on the Mn_2O_3 complex. Relative energies are given in eV. 57

Figure 3.8 The lowest energy water oxidation pathway-3 on the fully saturated $Mn_2O_3•7H_2O$ structure 18. 60

Figure 3.9 The second lowest energy water oxidation pathway-4 on the fully saturated $Mn_2O_3•7H_2O$ structure 18. 64

Figure 4.1 Proposed lowest energy reaction pathway-1 from structure 1 with Mn_4(IV IV IV IV) configuration. ΔE values are shown in the figure; ΔG values are presented in Table 4.1. ... 80

Figure 4.2 Proposed lowest energy reaction pathway-2 from structure 8 with Mn_4(IV⅔ IV⅔ III⅔ III) configuration (8 is the lowest energy cluster of the structures with μ_3-hydroxo groups

that are related to 1). ΔE values are shown in the figure; ΔG values are presented in Table 4.2. 84
Figure 4.3 Proposed lowest energy reaction pathway-3 from structure 15 with Mn_4(III III IV V) configuration. ΔE values are shown in the figure; ΔG values are presented in Table 4.3. ... 88
Figure 4.4 Proposed lowest energy reaction pathway-4 from structure 22 with Mn_4(II⅔ IV⅔ III⅔ IV) configuration (22 is the lowest energy cluster of the structures with μ_3-hydroxo groups that are related to 15). ΔE values are shown in the figure; ΔG values are presented in Table 4.4. 92
Figure 4.5 First dehydrogenation reaction of pathway-5 from structure 26 with Mn_4(III III IV IV) configuration. 94
Figure 4.6 First two dehydrogenation reactions of pathway-6 from structure 27 with Mn_4(IV⅔ II⅔ III⅔ III) configuration (lowest energy structure containing μ_3-hydroxo groups related to 26). 95
Figure 4.7 First two dehydrogenation reactions of pathway-7 from structure 29 with Mn_4(II IV III IV) configuration. 96
Figure 4.8 First two dehydrogenation reactions of pathway-8 from structure 30 with Mn_4(II⅔ III⅓ III⅓ III⅔) configuration (lowest energy structure containing μ_3-hydroxo groups related to 29). 97
Figure 4.9 First two dehydrogenation reactions of pathway-9 from structure 32 with Mn_4(II III III IV) configuration. 98
Figure 4.10 First two dehydrogenation reactions of pathway-10 from structure 33 with the Mn_4(II⅓ III⅓ III⅓ V) configuration (lowest energy structure containing μ_3-hydroxo groups related to 32). 99
Figure 5.1 ROHF/TZVP optimized structures for the mechanism reported in Ref. 30. Red numbers indicate the electrochemical pathway and the black numbered structures are generated from purely chemical steps. Small white spheres represent hydrogen atoms and large grey spheres represent manganese atoms. Carbon and oxygen atoms are represented by black and red spheres. This color code is used in all figures. 116
Figure 5.2 Reaction energies (eV) of the high spin states of the catalyst cycle. 117
Figure 5.3 ROHF/TZVP SOMOs of structure 1. 119
Figure 5.4 ROHF/TZVP doubly occupied $R\pi_1$ and $R\pi_2$ orbitals of structure 1 120

Figure 5.5 CASSCF(8,10)/TZVP active space natural orbitals of structure 1 (natural orbital occupation numbers (NOONs) are given in parentheses). 120
Figure 5.6 CASSCF(7,10)/TZVP natural orbitals 86-96 in the sextet state of structure 2. Orbital 86 is a doubly occupied core orbital, and the other ten orbitals are included in the active space. 125
Figure 5.7 CASSCF(6,10)/TZVP active space natural orbitals of structure 3. 127
Figure 5.8 CASSCF(5,10)/TZVP active space natural orbitals of structure 4. 128
Figure 5.9 CASSCF(4,6)/TZVP active space natural orbitals of structure 5. 129
Figure 5.10 CASSCF(6,10)/TZVP natural orbitals 85-95 of structure 6. 131
Figure 5.11 Doubly occupied orbital 90 and CASSCF(6,10)/TZVP natural orbitals 91-100 of structure 7. 132
Figure 6.1 Selected isomers for the resting state of the model dimer catalyst. The relative isomer free energies are given in eV with respect to the lowest energy structure D1. The charge and multiplicity of the structures are given in parentheses. Small white spheres represent hydrogen atoms, red spheres represent oxygen atoms and gray spheres represent cobalt atoms. This color code is used in all the figures. 146
Figure 6.2 Proposed lowest energy reaction pathway 1 for the cobalt dimer catalyst D1. 148
Figure 6.3 Proposed second lowest energy reaction pathway 2 from the cobalt dimer catalyst D1. 150
Figure 6.4 Proposed third lowest energy reaction pathway 3 from the cobalt dimer catalyst D1. 152
Figure 6.5 Selected low energy isomers of the model cobalt cubane complex. 158
Figure 6.6 Proposed lowest energy reaction pathway 4 from the cobalt cubane complex C1. .. 159
Figure 6.7 Proposed second lowest energy reaction pathway 5 from the cobalt cubane complex C1. 163
Figure 6.8 Proposed third lowest energy pathway 6 from the cobalt cubane catalyst C1. 165
Figure 6.9 The lowest energy reaction pathway 7 from structure C7. 168
Figure 6.10 Direct coupling pathway 8 from structure C7. 171

List of Tables

Table 2.1 Jacob's ladder of functionals. 31
Table 3.1 Calculated reaction energies (eV) for the water oxidation process on the fully saturated Mn_2O_4 reaction pathway given in Figure 3.1 Energies are calculated at the BP86/ATZP level of theory with three different linear dependency cutoff values and at the BP86/TZP level of theory. 48
Table 3.2 Calculated reaction energies and free energies for pathway-1 of Figure 3.4. 54
Table 3.3 Calculated reaction energies and free energies for pathway-3 of Figure 3.8. 63
Table 3.4 Calculated reaction energies and free energies for pathway-4 of Figure 3.9. 66
Table 4.1 Calculated reaction energies and free energies for pathway-1 of..... 83
Table 4.2 Calculated reaction energies and free energies for pathway-2 of Figure 4.2. 87
Table 4.3 Calculated reaction energies and free energies for pathway-3 of Figure 4.3. 91
Table 4.4 Calculated reaction energies and free energies for pathway-4 of Figure 4.4. 94
Table 5.1 Relative CASSCF energies of electronic states for structure 1. 121
Table 5.2 Relative CASSCF and MRMP2 energies of different states for structure 2. 123
Table 5.3 Relative CASSCF energies of different states of structure 3..... 126
Table 5.4 Relative CASSCF energies of different states of structure 4..... 128
Table 5.5 Relative CASSCF energies of different states of structure 6..... 131
Table 5.6 Relative CASSCF energies of different states in structure 7..... 132

Acknowledgements

I would like to thank my advisor, Professor Christine Aikens, for her guidance, patience and unrelenting support for me over the past years. She is one of the smartest people I know. Thank you for showing me the path to being a better scientist and a researcher. Your advice, guidance and smile will serve me to the end of my journey of life.

I would also like to thank my advisory committee, Professor Paul Smith, Professor Stefan Bossmann, Professor Keith Hohn, and Professor Amy Betz for sharing their valuable time and knowledge.

A special gratitude is extended to Professor Bin Liu, Professor Viktor Chikan, Professor Ryszard Jankowiak, Professor Kenneth Klabunde and Professor Christopher Levy for helping me to widen my knowledge in Chemistry.

I want to acknowledge the Department of Chemistry, Kansas State University, and the National Science Foundation for funding throughout my Ph.D. program.

I was fortunate to work with wonderful people in Aikens group (both present and past members). The diversity in the group immensely helped me to build up a lovely experience in my Ph.D. life.

I would also like thank my undergraduate advisor Professor Dhammike Dissanayake and Professor Samantha Weerasinghe and other Professors in the Department of Chemistry, University of Colombo for laying the path and nurturing me with remarkable knowledge in Chemistry, Biochemistry, Computer Science and Zoology.

I am immensely thankful to all my teachers in Mahinda College, Galle for sharing their knowledge from grade 1 to 12 and all my Advanced Level teachers for their wonderful insights.

Finally, I would like to thank my father, mother and brother for their support, love and courage given to me in each steps of my life. I would also like to thank my other family members for their love and support. My gratitude is also extended all my friends here in United States and Sri Lanka.

Most importantly, I would like to thank my wife Dr. Tharanga Wijethunga for being my life partner, friend and love of my life. It is lovely to spend every second of my life with you.

Dedication

To my father, mother and brother

For helping me to pursue my dreams

To my wife

For being the greatest supporter and the best partner in life

And to all who explore science and technology

May your journey be a wonderful experience in your life!

Preface

Research carried out at the Kansas State University led to the following publications in scientific journals:

1. Fernando, A.; Aikens, C.M. "Reaction Pathways for Water Oxidation to Molecular Oxygen Mediated by Model Cobalt Oxide Dimer and Cubane Catalysts" *J. Phys. Chem. C* **2015**, *119*, 11072-11085.
2. Fernando, A.; Weerawardene, K.L.D.; Karimova, N.; Aikens, C.M. "Quantum Mechanical Studies of Large Metal, Metal Oxide and Metal Chalcogenide Nanoparticles and Clusters" *Chem. Rev.* **2015**, *15*, 6112-6216.
3. Fernando, A.; Aikens, C.M. "Ligand Exchange Mechanism on Thiolate Monolayer Protected $Au_{25}(SR)_{18}$ Nanoclusters" *J. Phys. Chem. C*. **2015**, *119*, 20179-20187.
4. Fernando, A.; Malalasekera, A.P.; Shrestha, T.B.; McLaurin, E.; Bossmann S.H.; Aikens, C.M. "Refined Insights in the Photochromic Spiro-Dihydroindolizine/Betaine System" *J. Phys. Chem. A*. **2015**, *119*, 9621-9629.
5. Fernando, A.; Aikens, C.M. "Ab initio electronic structure study of a model water splitting dimer complex" *Phys. Chem. Chem. Phys*. **2015**, *17*, 32443-32454.
6. Fernando, A.; Shrestha, T.B.; Liu, Y; Malalasekera, A.P.; Yu, J; McLaurin, E.; Turro, C; Bossmann S.H.; Aikens, C.M. "Insights from Theory and Experiment in the Photochromic Spiro-Dihydropyrrolo-Pyridine/Betaine system" *J. Phys. Chem. A*. **2016**, *120*, 875-883.

Chapter 1 - Introduction

Fossil fuels are the main source of energy in the present day and they are used in every aspect of our daily life including generation of electricity, industrial processes, transportation, cooking, etc. These natural resources are depleting exponentially due to excessive use. Burning of fossil fuels is also harmful to nature as the byproducts like carbon monoxide, carbon dioxide, sulfur dioxides, nitrous oxides, etc. can act as greenhouse gases, which in turn cause global warming. Burning of fossil fuels also causes other environmental problems like ozone depletion, acid rain, air pollution, climate change, oil spills, etc. Thus, it is essential to research alternative ways to generate energy that are renewable, sustainable and cleaner. Over the past few decades, investigation into finding the best alternative energy source has been many scientists' main goal.

Out of many proposed alternative energy sources, hydrogen is the most researched as it has the highest mass specific energy content (nearly 3 times that of gasoline),[1] and compared to the present carbon based fossil fuels it is environmentally friendly because the combustion products are free from carbon monoxide and carbon dioxide. Hydrogen can be stored directly in molecular form or by further reversible conversion into suitable carrier molecules. The stored molecular energy can then be used for combustion or more efficiently in hydrogen fuel cells. Efficient hydrogen generation and safe, accessible hydrogen storage are among the main problems associated with a hydrogen fuel source. Between these two problems, finding clean and efficient ways for hydrogen generation is a top priority. When there are complicated problems to solve, human beings often look at and learn from the nature.

Nature's solutions to complicated problems are impressively remarkable, uniquely selective, and efficient. Nature uses sunlight as the energy source to solve its energy requirement through photosynthesis. Photosynthesis converts carbon dioxide and water to carbohydrates

using sunlight. This process takes place on functional and structural units of protein complexes called photosystems, which are found in thylakoid membranes of green plants, algae, and cyanobacteria. In the oxygen-evolving complex (OEC) of photosystem II (PSII), water is oxidized into molecular oxygen, protons, and electrons. The active complex of OEC consists of a $CaMn_4O_4$ cubane (cubic shaped) core (Figure 1.1).

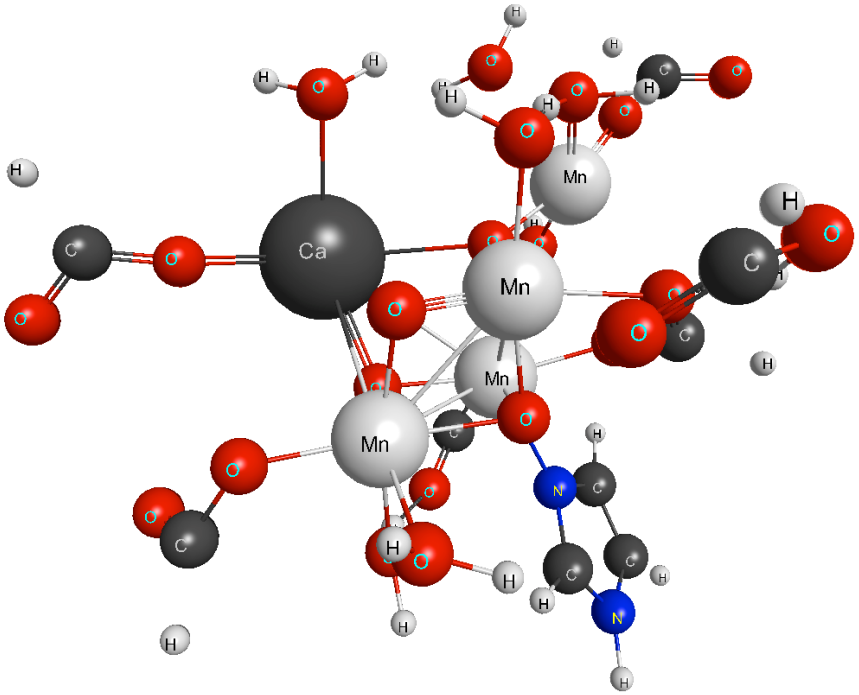

Figure 1.1 Active complex of the OEC of PSII, a $CaMn_4O_4$ cubane complex with a dangling manganese atom.

The artificial water splitting concept originated based on this natural water splitting blueprint. This blueprint has led researchers to investigate commercially viable biomimetic water splitting catalysts that can eventually split water and generate hydrogen. Artificial water splitting to generate hydrogen and reduction of carbon dioxide to form methanol are two widely discussed fuel-forming reactions. Converting energy to chemical energy via fuel-forming reactions are useful ways of storing energy. Since methanol also contains carbon, which generates carbon

dioxide after combustion, artificial water splitting to produce hydrogen is a very important albeit challenging process.

To deploy hydrogen generation on the large scale, electrolysis is the best candidate process. It is clean and efficient if the electricity necessary for the electrolysis is generated from solar, wind, waves, or other renewable sources. Photoelectrolysis is a good candidate process but industrial implementation is challenging, as we need to enhance ways to capture the sunlight. Current low temperature water electrolysis processes are only 50 - 70 % energy efficient. The cost analysis from United States Council for Automotive Research/Department of Energy (USCAR/DOE) suggests that overall system efficiency has to be higher than 74 % in order to meet the DOE cost goals.[2] The main source of energy inefficiency in this water electrolysis cell is the oxygen generating electrode where an excess electrode potential (overpotential) of > 450 mV is required for useful rates of water oxidation. For this reason, there have been many research efforts over the past few years in order to develop efficient electrocatalysts. Currently, industrial water oxidation is carried out with electrolysis using precious metals like Pt as electrodes. Other metal oxides like Ru[3-6] and Ir[7, 8] oxides are reported as efficient electrocatalysts but commercial applications of these catalysts are limited due to their higher costs. Thus, earth abundant inexpensive transition metals are desirable as electrocatalysts.

For optimum efficiency, electrocatalysts should be active, durable, and minimize the required overpotential. A commercial catalyst should contain a minimum of or no rare or noble metals. Finally, electrocatalysts should possess a high surface to bulk ratio to minimize the current densities and the amount of metal deployed. It must exhibit sufficient electronic conductivity to minimize ohmic losses.

In this thesis, we investigate two of the most commonly used transition metal oxides: cobalt and manganese oxides. Specific systems studied include dimer complexes with two manganese or cobalt atoms ($Mn_2(\mu\text{-}OH)_2(H_2O)_4(OH)_4$,[9] $Mn_2(\mu\text{-}OH)(\mu\text{-}O)(H_2O)_3(OH)_5$,[9] $Mn_2(\mu\text{-}OH)_2(H_2O)_2(OH)_2(O(CH)_3O)_2$,[10] $Co_2(\mu\text{-}OH)_2(H_2O)_4(OH)_4$)[11] and cubane complexes ($Co_4O_4(H_2O)_8(OH)_4$,[11] $Mn_4O_4(H_2O)_x(OH)_y$ x = 4-8, y = 8-4) to explore the electronic structure, properties, and mechanism of water oxidation. A brief literature review of both cobalt and manganese oxides are discussed below.

1.1 Manganese Oxides

Manganese oxide complexes with μ-oxo and μ-hydroxo groups are among the most theoretically and experimentally investigated transition metal oxide catalysts. This is primarily due to the presence of manganese oxides in the OEC as well as the abundance (Mn is the 10th most abundant element in the earth crust) and efficiency of these systems. Mn also has a low toxicity compared to Co and Ni. Understanding the electronic structure, properties, and mechanism of the water oxidation process in the active core of the OEC and related systems is an essential part of designing and developing a commercially viable water splitting catalyst as this artificial water splitting is a clean and sustainable way to produce hydrogen. Consequently, a very large number of experimental and theoretical studies have been devoted to achieve this for the OEC, models of the OEC, other biomimetic complexes, etc. However, other than some of the ruthenium catalysts the catalysts developed so far are a couple of orders of magnitude slower than the natural system.[6] The activity of the manganese cubane complex and how it achieves such efficiency and stability is still not fully understood. The presence of this remarkable cubane core geometry is found in other water splitting catalysts as well (i.e. Nocera's catalyst,[12] and other cobalt catalysts reported by McAlpin *et al*.,[13] McCool *et al*.,[14] and Evangelisti *et al*.[15]) Most

of the manganese catalysts reported are stabilized with organic ligands, and there are only few experimental or theoretical studies reported with ligand-free or with water-derived ligand architectures of manganese complexes.

1.1.1 Manganese Oxide Dimer Complexes

Manganese dimer complexes with μ-oxo and μ-hydroxo ligands have been investigated as water oxidation catalysts since the 1980s. Herein, we report a few selected turning points associated with these manganese dimer catalysts. Some of these manganese complexes for water oxidation have been reviewed thoroughly by Mullins,[16] Liu,[5] Yagi,[17] Mukhopadhyay,[18] and Wu *et al*.[19]

Ashmawy and coworkers[20] reported water oxidation by a manganese dimer complex in 1985. They synthesized a $[\{Mn(salpd)(H_2O)\}_2][ClO_4]_2$ [salpd = propane-l,3-diylbis(salicylideneiminate)] complex that evolves oxygen when irradiated in the presence of a *p*-benzoquinone. The oxygen evolution is dependent on the concentration of these Mn(III) complexes and the pH of the reaction and is independent of the solvent. In 1994, Watkinson *et al*.[21] reported a manganese dimer complex that also splits water upon irradiation with visible light in the presence of *p*-benzoquinone. This complex was considered to be not as active as the complex reported by Ashmawy *et al*. Limburg *et al*.[22] reported a functional model of a μ-oxo bridged manganese dimer ($[H_2O(terpy)Mn(O)_2Mn(terpy)OH_2](NO_3)_3$) complex. This complex catalyzes the conversion of sodium hypochlorite to molecular oxygen. ^{18}O isotopic experiments revealed that the source of the oxygen atoms in the generated molecular oxygen is water. Collomb and coworkers[23] also reported this complex independently at the same time. In one of the early studies, a four electron water oxidation reaction catalyst ($[Mn_2(mcbpen)_2(H_2O)_2](ClO_4)_2$) (mcbpen = *N*-methyl-*N'*-carboxymethyl-*N,N'*-bis(2-

pyridylmethyl)ethane-1,2-diamine) synthesized by Poulsen *et al*.[24] has been reported to generate oxygen in the presence of a tert-butylhydrogenperoxide as an oxidant. Formation of a Mn(V)=O species during O-O bridging was first reported by Naruta *et al*.[25] with a porphyrin type Mn(III) dimer. The Mn(V)=O species can also be described as a Mn(IV)-O radical group. The terminology of this oxo group has been a topic of debate even to date.[10, 26-28]

Zhao and coworkers[29] reported an early detailed theoretical study of the electronic structure, charge distribution, and spin coupling of manganese μ-oxo compounds surrounded by triazacyclonoane and acetate ligands. Their calculated charge distribution showed strong metal-ligand covalency. Bloomberg and coworkers[30] reported a theoretical study of different manganese monomer and dimer complexes. These authors employed hybrid density functional theory calculations and investigated the hydrogen abstraction process from these water coordinated manganese complexes via a tyrosyl radical. The coordination of a water molecule to the manganese ion is found to lower the energy required for hydrogen abstraction of either one or two hydrogen atoms from the water molecule.

The structural and electronic properties of reduction and oxidation of an O-O bond in Mn dimer ($Mn_2(\mu\text{-}O)_2(\mu\text{-}O_2)(NH_3)_6^{2+}$) complex was reported by McGrady *et al*.[31] The authors reported that the σ bond of O-O can be broken by transfer of two electrons of opposite spin between the metal and ligand whereas the formation of the O-O π bond requires transfer of two electrons of the same spin. The μ-oxo bridged manganese dimer ($[H_2O(terpy)Mn(O)_2Mn(terpy)OH_2](NO_3)_3$) complex was studied by Lundberg and coworkers[27] to investigate the requirements for O-O bond formation. It was reported that the Mn(IV) oxyl radical state is a requirement (rather than the Mn(V)O state) for this complex as well as some models of OEC.

Zhou and coworkers[32] employed density functional theory calculations on a biomimetic manganese dimer complex, $[H_2O(terpy)Mn^{III}(\mu\text{-}O)_2Mn^{IV}(terpy)OH_2]^{3+}$ (terpy = 2,2':6'2"-terpyridine) as a structural model for the OEC. These authors investigated asymmetry features in the geometric and electronic structures of this complex and their influence on the chemical functions of the two-manganese center in the presence of water solvent. They reported that the water environment has an almost symmetric influence on Mn(III) and Mn(IV) centers. The chemical behavior of this complex is largely determined by its geometric and electronic features. The authors noted that the Mn(IV) center is slightly more electrophilic than the Mn(III) center, which imposes a larger steric repulsion for coordination of a molecule or ligand.

A few authors have also studied manganese oxide compounds without organic ligands. Lang and coworkers[33] reported an experimental and theoretical investigation of the water splitting mechanism on free manganese oxide clusters $Mn_2O_2^+$ and $Mn_4O_4^+$. They used gas phase ion trap measurements in combination with Born-Oppenheimer spin density functional molecular dynamics calculations. This will be further discussed under the manganese cubane complex section 1.1.2 in the introduction. In 2014, Lee and Aikens[34] reported a theoretical investigation of water oxidation on fully saturated Mn_2O_4 and $Mn_xTi_{2-x}O_4$ (x = 0-2) complexes using the BP86/ATZVP level of theory in their calculations.

There are only very few studies on manganese complexes reported using levels of theory higher than DFT. Several ab initio calculations with complete active space self consistent field theory (CASSCF) were reported on Mn(salen) complexes. These complexes are popular systems due to their high-yield catalytic activity towards enantioselective epoxidation of unfunctionalized olefins. The stability of the singlet, triplet, and quintet states of these complexes has been a question of interest. The electronic structure of these complexes were researched extensively by

Sears *et al*.[35] and Ivanic *et al*.[36] using a model oxoMn(salen). Ivanic *et al*.[36] first studied the system with 12 electrons in 11 active space orbitals (CASSCF(12/11)); later, Sears and coworkers[35] used CASSCF(8/7) to study this system. These authors chose the smaller active space after examining the unrestricted Hartree-Fock (UHF) natural orbital occupation numbers. The closed shell singlet state was found to be the ground state; the triplet states are around 3 kcal mol^{-1} higher in energy whereas a quintet state lies at a little more than 40 kcal mol^{-1}. There is a relative energy difference of 0.5 kcal mol^{-1} for the singlet and triplet states with the different active spaces employed. This difference is more significant for the quintet state with a difference of 1.4 kcal mol^{-1}. It is noteworthy that the UHF solutions to the calculations were highly spin-contaminated. In 2014, Wouters and coworkers used the density matrix renormalization group (DMRG) method with 28 electrons in 22 orbitals to investigate this system.[37] This method can be used to include a considerably large number of orbitals into the active space. In comparison with previous results, they found that the triplet is 5 kcal mol^{-1} more stable than the singlet state whereas the quintet lies 12-14 kcal mol^{-1} higher than the singlet state.

1.1.2 Manganese Oxide Cubane Complexes

As described in the beginning of the introduction section, a considerable amount of theoretical work in the last two decades has been undertaken to investigate and understand the OEC of photosystem II. Significant knowledge has been gained, which has aided in designing many other biomimetic water splitting catalysts. Reporting a summary of the large quantity of experimental and theoretical studies of OEC is not possible in this thesis, although the theoretical studies have been briefly summarized in in our recent review.[38] Instead, we will concentrate on the studies that examined a related Mn_4O_4 cubane core.

Hybrid DFT calculations using UB3LYP and UBHandHLYP functionals were employed by Yamaguchi and coworkers[39] to investigate mixed valance $CaMn(III)_2Mn(IV)_2O_4OH(H_2O)_4$ (X = OH or O) and $CaMn(III)_2Mn(IV)_2O_4(OH)_2(H_2O)_3$ clusters. The degree of symmetry breaking of the Mn-O-Mn (180^0 bond between the dangling manganese atom and O-Mn bond in cubane) is found to be not significant under their level of theory; however, it is seen to be larger with hybrid DFT methods. These authors also reported a computational study of a mixed valance $Mn(III)_{4-x}Mn(IV)_xO_4$ cluster to investigate the Jahn-Teller (JT) effects of Mn(III) ions.[40] The optimized geometries of the cubane demonstrated an acute triangle for $Mn(III)_2Mn(X)$ (X = III, IV) indicating JT effects. It was found that JT effects are not significant for $Mn(IV)_2Mn(III)$ cores showing an obtuse triangle geometry. JT effects are further diminished for the $Mn(IV)_3$ core, which forms an equilateral triangle. It was found that Ca doping suppresses the JT effects even for the $Mn(III)_2Mn(X)$ (X = III, IV) case.

Li and Siegbahn[41] recently demonstrated the significance of using simplified models to investigate the OEC. The model was simplified by replacing some ligands by water-derived ligands. These authors investigated mainly the O-O bond formation step. A remarkable similarity was seen in the energetics of this model with some of the larger cluster models previously used for PSII. Krewald and coworkers[42] investigated the magnetic and spectroscopic properties of the core structure of the OEC of PSII and two other synthetic cubane clusters. It was previously established that all synthetic and model $Mn(IV)_3CaO_4$ cubane complex systems have a high-spin state of S = 9/2 for the ground state. These authors' theoretical study was in agreement with this previously established spin state. An energetic comparison of protonated models showed that a tris-μ-oxo bridge protonated version (containing three μ-hydroxo bridges) connecting only Mn ions in the cubane rather than Ca has the lowest proton affinity.

There are only few studies reported with ligand-free or with water-derived architectures of pure manganese cubane complexes. Recently in 2013, Lang *et al*.[33] described the water splitting process on singly charged $Mn_2O_2^+$ and $Mn_4O_4^+$ species. Gas phase ion trap measurements were used together with Born-Oppenheimer spin density functional molecular dynamic calculations. The two-dimensional ring-like ground state structure of the $Mn_4O_4^+$ complex changed to a cuboidal octahydroxo complex when it was hydrated. This $Mn_4O_4^+$ system was further investigated with $D_2{}^{16}O$ and $H_2{}^{18}O$ in a gas phase ion trap experiment where the exchange of the oxygen atoms of the cluster with water oxygen atoms was observed. The authors suggested a reaction mechanism that dissociates water via hydroxylation of the oxo-bridges. Lang *et al*.[43] also demonstrated the interaction of water with the $Mn_4O_4^+$ complex using IR spectroscopy in conjunction with spin density functional calculations. It was found that hydroxylation of μ-oxo bridges is an essential part of the dissociation of the O-H bond of water. This hydroxylation continues until all the μ-oxo bridges are hydroxylated. Additional water molecules then bound molecularly with a favored preference for the hydrogen-bridge-bound H_3O_2 units involving hydroxylated bridges. It was found that an open cuboidal structure emerges when $n \geq 3$ for $Mn_4O_4^+(H_2O)_n$, and for $n > 6$ the $Mn_4O_4^+$ cluster transforms into a closed cuboidal structure.

1.2 Cobalt Oxide Complexes

Compared to manganese oxide complexes, cobalt oxides are underexplored as water splitting catalysts. Early studies of cobalt oxides date back to the 1960s but their development slowed when it was found that the catalyst precipitated from the solution as cobalt oxides or hydroxides.[44] Recently, cobalt oxide gained wide popularity for its remarkable catalytic activity towards water splitting after its reinvention by Nocera and coworkers.[12] With this reinvention,

cobalt oxides have been brought to the attention of both theoreticians and experimentalists; thus, over the last few years we have seen many cobalt and related complexes emerging as water oxidation catalysts. The Nocera cobalt oxide catalyst is a black thin film deposited on an indium tin oxide surface.[12] It is a heterogeneous catalyst that is very stable, easy to synthesize from readily available precursors, self-healing through a series of linked equilibria, and shows high activity under neutral pH. There are no crystal structure details solved, as this is a highly amorphous catalyst. Recent extended X-ray absorption spectroscopy (EXAFS) studies[45, 46] reported that this catalyst has similar structural features to a manganese cubane complex. In the next sections, we briefly discuss some experimental and theoretical studies of cobalt dimer and cubane complexes that act as water splitting catalysts.

1.2.1 Cobalt Oxide Dimer Complexes

There are only a few reports related to cobalt oxide dimers investigated as water splitting catalysts. Cobalt dimer complexes ligated with bispyridylpyrazolate ligands that can serve as molecular electrocatalysts for water oxidation under acidic conditions were reported by Rigsby and coworkers.[47] These were Co(III)Co(III) bridging peroxo complexes with a structural similarity to previously reported ruthenium water oxidation catalysts. In 2014, Smith and coworkers[48] investigated dimer, trimer, and tetramer cobalt oxide catalysts with two sets of ligands for water oxidation activity. In contrast to previous reports by Rigsby *et al*., both dimer and trimer clusters were found to be catalytically inactive. This shows that catalytic activity and the mechanism may depend on the ligand environment for cobalt oxide complexes with smaller nuclearity.

1.2.2 Cobalt Oxide Cubane Complexes

The Nocera cobalt oxide catalyst is thought to contain Co_4O_4 units in the form of $Co(III)O_6$ octahedra. Over the last few years, multiple edge sharing and corner sharing structural models have been proposed based on experimental and theoretical evidence.[45, 46, 49, 50] Theoretical investigations of the mechanism for water oxidation on cobalt oxide and related catalysts have been reported in the last few years by Wang *et al.*,[49] Mattioli *et al.*,[50] Li *et al*.,[51] and Kwapien *et al*.[52]

Wang *et al*.[49] employed quantum mechanics and hybrid quantum mechanics/molecular mechanics (QM/MM) methods on a model cubane complex with water-derived ligands and reported that O-O bond formation takes place by direct coupling between the Co(IV)O oxo groups. Later, Li and Siegbahn[51] reported a study of several cobalt oxide complexes including a model complex similar to that of Wang *et al.*[49] but with μ-OH groups (the model of Wang *et al*.[49] has μ-O ligands, not μ-OH groups). These authors also discussed a comparison between manganese complexes and cobalt complexes for water splitting. It was reported that a state with an oxygen radical coupled to a Co(IV) state, i.e. a formal Co(V) state, is required for reactivity. They also noted that the probable mechanism is a water attack on the oxygen radical.

Mattioli and coworkers[50] investigated two different cobalt oxide systems: saturated $Co_7O_{24}H_{24}$ and $Co_6O_{23}H_{28}$ complexes. Ab initio molecular dynamics simulations were carried out with static geometry optimizations both based on Hubbard U corrected DFT (DFT+U). They reported that a Co(IV) oxyl radical species is the driving ingredient for the catalytic mechanism. The thermodynamically favorable pathway is a geminal coupling with oxygen atoms coordinated by the same Co. A nucleophilic attack by a solvent water molecule is found not to be favorable due to high activation barriers. Kwapien *et al*.[52] reported a benchmark study with model cobalt

oxide complexes. They employed coupled (CC) cluster calculations to benchmark the accuracy of commonly used exchange and correlation functionals. It was found that hybrid B3LYP and PBE0 lead to fair agreement with the CC energies while there were important discrepancies with standard gradient-corrected functionals. It was also reported that DFT+U improves the calculated electronic structure and properties but no value of the U parameters reproduced the CC results.

A cobalt cubane complex with a Co_4O_4 unit, i.e. $[Co_4O_4(C_5H_5N)_4(CH_3CO_2)_4]^+$, with the ability to catalyze the water oxidation reaction was proposed recently by McAlpin *et al*.[13] McCool and coworkers[14] also reported a neutral version of this catalyst, $[Co_4O_4(C_5H_5N)_4(CH_3CO_2)_4]$, which catalyzes water oxidation activity efficiently with the presence of standard photochemical or electrochemical oxidation sources. The first Co(II)-based cubane water oxidation catalyst with a Co_4O_4 core was reported by Evangelisti and coworkers.[15] This $[Co^{II}_4(hmp)_4(\mu\text{-}OAc)_2(\mu_2\text{-}OAc)_2(H_2O)_2]$, (OAc = acetate, hmp = 2-(hydroxymethyl)pyridine) catalyst is a distorted cubane catalyst that increases its catalytic activity upon photoirradiation with increasing pH through aqua ligand deprotonation.

Our theoretical work on both dimer and cubane complexes indicated the formation of a Co(V)O oxo species that acts as a reaction mediating species.[11] We also demonstrated that nucleophilic attack of a solvent water molecule to the Co(V)O species is the lowest energy pathway in the cobalt dimer complex. A geminal coupling of this Co(V)O with a bridging oxo group is found to be the lowest pathway in the cubane complex.[11] However, there are other competitive pathways for the oxygen evolution reaction (OER) on these cobalt oxide catalysts. We have demonstrated that a combination of these reaction pathways can collectively contribute to the oxygen evolution process on these complexes. This will be discussed further in Chapter 6.

After our extensive investigation of the cobalt dimer and cubane complexes, Li *et al*.[53] reported an experimental study using molecular complexes including Co-cubane ($[Co_4(\mu_3\text{-}O)_4(\mu\text{-}OAc)_4py_4]$), Co-trimer ($[Co_3(\mu_3\text{-}O)(\mu\text{-}OAc)_6py_3]PF_6$), and Co-dimer ($[Co_2(\mu\text{-}OH)_2(\mu\text{-}OAc)(OAc)_2py_4]PF_6$) (py = pyridine, OAc = acetate). These authors investigated electrochemical, photochemical, and photoelectrochemical water oxidation methodologies in phosphate electrolyte. It was found that the cubane showed no activity in electrochemical and photochemical water oxidation reaction (WOR) but was active in the photoelectrochemical WOR. The cobalt dimer also showed no activity in the electrochemical WOR but behaved as a precursor to catalytically active species in both photochemical and photoelectrochemical reactions. The cobalt trimer behaved as a precursor to catalytically active species in all three WOR methods.

Nguyen and coworkers[54] investigated the [Co(III)$_4$] cubane $[Co_4O_4(C_5H_5N)_4\,(CH_3CO_2)_4]$ complex. Oxygen isotopic labeling demonstrated that the cubane core remains intact during the OER and terminal ligands were responsible for the generation of O_2. These authors suggested formation of Co(V)O like species during the catalytic cycle and emphasized that catalytic frameworks should be designed to stabilize these higher oxidation states.

The cobalt cubium complex, $[Co_4O_4(C_5H_5N)_4(CH_3CO_2)_4]^+$ was investigated recently in 2015 by Smith *et al*.[55] It was reported that this complex converts to the neutral species during the oxygen evolution. The authors also showed that the cubium reacts with hydroxide but not with water molecules to produce oxygen.

1.3 Objective and Overview of the Thesis

The behavior and the reactivity of the $CaMn_4O_4$ active manganese cubane complex in the OEC of photosystem II are uniquely remarkable. Its unprecedented efficiency and stability, that

is so far unmatchable by any synthetic mimetic complexes, is still not fully understood. The presence of this remarkable cubane core structure is found in other water splitting catalysts like cobalt oxides. The purpose of this thesis is to employ theoretical tools to model manganese and cobalt oxide complexes consisting of two and four manganese and cobalt atoms surrounded by water-derived ligands to investigate the water oxidation reaction process. We believe detailed understanding of these simplest model complexes may provide essential details for future bottom up commercial catalytic design. Also, it should be noted that both these manganese and cobalt dimer and cubane complexes could be used as minimal units of bulk surfaces. So, fundamental behavior and properties of bulk oxide surfaces can also be understood by these studies.

The objectives of the studies of manganese dimer $Mn_2(\mu\text{-}OH)_2(H_2O)_4(OH)_4$ and $Mn_2(\mu\text{-}OH)(\mu\text{-}O)(H_2O)_3(OH)_5$ complexes and manganese cubane $Mn_4O_4(H_2O)_x(OH)_y$ x = 4-8, y = 8-4 complexes in Chapters 3 and 4 are to investigate the electronic and geometric structure and properties with a goal towards understanding the reaction mechanism of water oxidation on manganese complexes. These complexes are primarily designed by incorporating water-derived ligands to account for their respective oxidation states. A fully saturated pure Mn_2O_4 complex (six water molecules adsorbed), with an average oxidation state of Mn(IV), as well as fully saturated Mn_2O_3 complex (seven water molecules adsorbed) with an average oxidation state of Mn(III) are used to investigate the water splitting process.[9] Then, we use this knowledge to further investigate manganese cubane complexes with oxidation state configurations ranging from all Mn(IV) to all Mn(III) to investigate the water splitting mechanisms.

We also employed both multiconfigurational and multireference methods to investigate the electronic structure and energetics of a model manganese dimer complex, $Mn_2(\mu\text{-}OH)_2(H_2O)_2(OH)_2(O(CH)_3O)_2$, that may undergo a direct coupling of two adjacent manganese

oxo groups to generate an O-O bond (Chapter 5).[10] Our primary focus for using these higher levels of theories is to identify underlying electronic states that contribute to the water oxidation catalytic cycle. This can also help to identify orbital configurations that contribute to different states of this direct-coupling pathway.

The main goal of our cobalt oxide study in Chapter 6 is to model the water oxidation process and to identify which process/processes are contributing to the oxygen evolution reaction.[11] We have investigated a $Co_2(\mu\text{-}OH)_2(H_2O)_4(OH)_4$ cobalt dimer complex and a $Co_4O_4(H_2O)_8(OH)_4$ cobalt cubane complex with resting state oxidation states of Co(III). We extensively investigated the electronic structure and properties of the intermediate states involved in the lowest energy pathways to predict common characteristic features in cobalt oxide water splitting catalysts.

In general, understanding the electronic properties, structure, and the mechanism of water oxidation on these simple model catalytic systems is essential to further develop and enhance water splitting catalysts based on transition metal oxides. Herein, with all these studies we have reported significant microscopic properties that can be used as essential descriptors for designing efficient electrocatalysts. It is also important to note that comprehensive knowledge of the reaction mechanism for water oxidation on manganese and cobalt oxide species can help us to find commonalities and differences between these systems, and thus enhance and develop a next generation of future catalysts. Combining advantageous features and eliminating disadvantageous factors in a new design principle can produce optimum, efficient, and stable water oxidation catalysts.

1.4 References

1. Wengenmayr, R.; Bührke, T., *Renewable Energy: Sustainable Energy Concepts for the Energy Change*. John Wiley & Sons: 2013.

2. Partnership, F. F. Hydrogen Delivery Technology Roadmap. https://www1.eere.energy.gov/vehiclesandfuels/pdfs/program/delivery_tech_team_roadmap.pdf.

3. Dau, H.; Limberg, C.; Reier, T.; Risch, M.; Roggan, S.; Strasser, P. The Mechanism of Water Oxidation: From Electrolysis via Homogeneous to Biological Catalysis. *ChemCatChem* **2010,** *2*, 724-761.

4. Duan, L.; Bozoglian, F.; Mandal, S.; Stewart, B.; Privalov, T.; Llobet, A.; Sun, L. A Molecular Ruthenium Catalyst with Water-Oxidation Activity Comparable to that of Photosystem II. *Nat Chem* **2012,** *4*, 418-423.

5. Liu, X.; Wang, F. Transition Metal Complexes that Catalyze Oxygen Formation from Water: 1979–2010. *Coord. Chem. Rev.* **2012,** *256*, 1115-1136.

6. Matheu, R.; Ertem, M. Z.; Benet-Buchholz, J.; Coronado, E.; Batista, V. S.; Sala, X.; Llobet, A. Intramolecular Proton Transfer Boosts Water Oxidation Catalyzed by a Ru Complex. *J. Am. Chem. Soc.* **2015,** *137*, 10786-10795.

7. Tilley, S. D.; Cornuz, M.; Sivula, K.; Grätzel, M. Light-Induced Water Splitting with Hematite: Improved Nanostructure and Iridium Oxide Catalysis. *Angew. Chem. Int. Ed.* **2010,** *49*, 6405-6408.

8. Youngblood, W. J.; Lee, S.-H. A.; Kobayashi, Y.; Hernandez-Pagan, E. A.; Hoertz, P. G.; Moore, T. A.; Moore, A. L.; Gust, D.; Mallouk, T. E. Photoassisted Overall Water Splitting in a Visible Light-Absorbing Dye-Sensitized Photoelectrochemical Cell. *J. Am. Chem. Soc.* **2009,** *131*, 926-927.

9. Fernando, A.; Haddock, T.; Aikens, C. M. Theoretical Investigation of Water Oxidation on Fully Saturated Mn_2O_3 and Mn_2O_4 Complexes. *J. Phys. Chem. A*, Submitted.

10. Fernando, A.; Aikens, C. M. Ab Initio Electronic Structure Study of a Model Water Splitting Dimer Complex. *Phys. Chem. Chem. Phys.* **2015,** *17*, 32443-32454.

11. Fernando, A.; Aikens, C. M. Reaction Pathways for Water Oxidation to Molecular Oxygen Mediated by Model Cobalt Oxide Dimer and Cubane Catalysts. *J. Phys. Chem. C* **2015,** *119*, 11072-11085.

12. Kanan, M. W.; Nocera, D. G. In Situ Formation of an Oxygen-Evolving Catalyst in Neutral Water Containing Phosphate and Co^{2+}. *Science* **2008,** *321*, 1072-1075.

13. McAlpin, J. G.; Stich, T. A.; Ohlin, C. A.; Surendranath, Y.; Nocera, D. G.; Casey, W. H.; Britt, R. D. Electronic Structure Description of a $Co(III)_3Co(IV)O_4$ Cluster: A Model for the Paramagnetic Intermediate in Cobalt-Catalyzed Water Oxidation. *J. Am. Chem. Soc.* **2011,** *133*, 15444-15452.

14. McCool, N. S.; Robinson, D. M.; Sheats, J. E.; Dismukes, G. C. A Co_4O_4 "Cubane" Water Oxidation Catalyst Inspired by Photosynthesis. *J. Am. Chem. Soc.* **2011,** *133*, 11446-11449.

15. Evangelisti, F.; Güttinger, R.; Moré, R.; Luber, S.; Patzke, G. R. Closer to Photosystem II: A Co_4O_4 Cubane Catalyst with Flexible Ligand Architecture. *J. Am. Chem. Soc.* **2013,** *135*, 18734-18737.

16. Mullins, C. S.; Pecoraro, V. L. Reflections on small molecule manganese models that seek to mimic photosynthetic water oxidation chemistry. *Coord. Chem. Rev.* **2008,** *252*, 416-443.

17. Yagi, M.; Syouji, A.; Yamada, S.; Komi, M.; Yamazaki, H.; Tajima, S. Molecular catalysts for water oxidation toward artificial photosynthesis. *Photochem. Photobiol. Sci.* **2009,** *8*, 139-147.

18. Mukhopadhyay, S.; Mandal, S. K.; Bhaduri, S.; Armstrong, W. H. Manganese Clusters with Relevance to Photosystem II. *Chem. Rev.* **2004,** *104*, 3981-4026.

19. Wu, A. J.; Penner-Hahn, J. E.; Pecoraro, V. L. Structural, Spectroscopic, and Reactivity Models for the Manganese Catalases. *Chem. Rev.* **2004,** *104*, 903-938.

20. Ashmawy, F. M.; McAuliffe, C. A.; Parish, R. V.; Tames, J. Water Photolysis. Part 1. The Photolysis of Co-ordinated Water in $[\{MnL(H_2O)\}_2][ClO_4]_2$(L = Dianion of Tetradentate O_2N_2-Donor Schiff Bases). A Model for the Manganese Site in Photosystem II of Green Plant Photosynthesis. *J. Chem. Soc., Dalton Trans.* **1985**, 1391-1397.

21. Watkinson, M.; Whiting, A.; McAuliffe, C. A. Synthesis of a bis-manganese water splitting complex. *J. Chem. Soc., Chem. Commun.* **1994**, 2141-2142.

22. Limburg, J.; Vrettos, J. S.; Liable-Sands, L. M.; Rheingold, A. L.; Crabtree, R. H.; Brudvig, G. W. A Functional Model for O-O Bond Formation by the O_2-Evolving Complex in Photosystem II. *Science* **1999,** *283*, 1524-1527.

23. Collomb, M.-N.; Deronzier, A.; Richardot, A.; Pecaut, J. Synthesis and Characterization of a New Kind of $Mn_2^{III,IV}$ μ-oxo Complex: $[Mn_2O_2(terpy)_2(H_2O)_2](NO_3)_3.6\ H_2O$, terpy=2,2':6',2"-terpyridine. *New J. Chem.* **1999,** *23*, 351-354.

24. Poulsen, A. K.; Rompel, A.; McKenzie, C. J. Water Oxidation Catalyzed by a Dinuclear Mn Complex: A Functional Model for the Oxygen-Evolving Center of Photosystem II. *Angew. Chem. Int. Ed.* **2005,** *44*, 6916-6920.

25. Naruta, Y.; Sasayama, M.-a.; Sasaki, T. Oxygen Evolution by Oxidation of Water with Manganese Porphyrin Dimers. *Angew. Chem. Int. Ed. Engl.* **1994,** *33*, 1839-1841.

26. Britt, R. D.; Suess, D. L. M.; Stich, T. A. An Mn(V)–oxo role in splitting water? *Proc. Natl. Acad. Sci. U. S. A.* **2015,** *112*, 5265-5266.

27. Lundberg, M.; Blomberg, M. R. A.; Siegbahn, P. E. M. Oxyl Radical Required for O−O Bond Formation in Synthetic Mn-Catalyst. *Inorg. Chem.* **2003,** *43*, 264-274.

28. Neu, H. M.; Baglia, R. A.; Goldberg, D. P. A Balancing Act: Stability versus Reactivity of Mn(O) Complexes. *Acc. Chem. Res.* **2015,** *48*, 2754-2764.

29. Zhao, X. G.; Richardson, W. H.; Chen, J. L.; Li, J.; Noodleman, L.; Tsai, H. L.; Hendrickson, D. N. Density Functional Calculations of Electronic Structure, Charge Distribution, and Spin Coupling in Manganese−Oxo Dimer Complexes. *Inorg. Chem.* **1997,** *36*, 1198-1217.

30. Blomberg, M. R. A.; Siegbahn, P. E. M.; Styring, S.; Babcock, G. T.; Åkermark, B.; Korall, P. A Quantum Chemical Study of Hydrogen Abstraction from Manganese-Coordinated Water by a Tyrosyl Radical: A Model for Water Oxidation in Photosystem II. *J. Am. Chem. Soc.* **1997,** *119*, 8285-8292.

31. McGrady, J. E.; Stranger, R. Redox-Induced Formation and Cleavage of O−O σ and π Bonds in a Peroxo-Bridged Manganese Dimer: A Density Functional Study. *Inorg. Chem.* **1999,** *38*, 550-558.

32. Zhou, T.; Lin, X.; Zheng, X. First-Principles Study on Structural and Chemical Asymmetry of a Biomimetic Water-Splitting Dimanganese Complex. *J. Chem. Theory Comput.* **2013,** *9*, 1073-1080.

33. Lang, S. M.; Fleischer, I.; Bernhardt, T. M.; Barnett, R. N.; Landman, U. Dimensionality Dependent Water Splitting Mechanisms on Free Manganese Oxide Clusters. *Nano Lett.* **2013,** *13*, 5549-5555.

34. Lee, C.; Aikens, C. M. Theoretical Investigation of Water Oxidation Processes on Small $MnxTi_{2-x}O_4$ (x = 0–2) Complexes. *J. Phys. Chem. A* **2014,** *118*, 8204-8221.

35. Sears, J. S.; Sherrill, C. D. The Electronic Structure of Oxo-Mn(salen): Single-Reference and Multireference Approaches. *J. Chem. Phys.* **2006,** *124*, 144314.

36. Ivanic, J.; Collins, J. R.; Burt, S. K. Theoretical Study of the Low Lying Electronic States of oxoX(salen) (X = Mn, Mn^-, Fe, and Cr^-) Complexes. *J. Phys. Chem. A* **2004,** *108*, 2314-2323.

37. Wouters, S.; Bogaerts, T.; Van Der Voort, P.; Van Speybroeck, V.; Van Neck, D. Communication: DMRG-SCF study of the singlet, triplet, and quintet states of oxo-Mn(Salen). *J. Chem. Phys.* **2014,** *140*, 241103.

38. Fernando, A.; Weerawardene, K. L. D. M.; Karimova, N. V.; Aikens, C. M. Quantum Mechanical Studies of Large Metal, Metal Oxide, and Metal Chalcogenide Nanoparticles and Clusters. *Chem. Rev.* **2015,** *115*, 6112-6216.

39. Yamaguchi, K.; Isobe, H.; Yamanaka, S.; Saito, T.; Kanda, K.; Shoji, M.; Umena, Y.; Kawakami, K.; Shen, J. R.; Kamiya, N.; Okumura, M. Full Geometry Optimizations of the Mixed-Valence $CaMn_4O_4X(H_2O)_4$ (X=OH or O) Cluster in OEC of PS II: Degree of Symmetry Breaking of the Labile Mn-X-Mn Bond Revealed by Several Hybrid DFT Calculations. *Int. J. Quantum Chem.* **2013,** *113*, 525-541.

40. Yamaguchi, K.; Yamanaka, S.; Isobe, H.; Saito, T.; Kanda, K.; Umena, Y.; Kawakami, K.; Shen, J. R.; Kamiya, N.; Okumura, M.; Nakamura, H.; Shoji, M.; Yoshioka, Y. The Nature of Chemical Bonds of the $CaMn_4O_5$ Cluster in Oxygen Evolving Complex of Photosystem II: Jahn-Teller Distortion and its Suppression by Ca Doping in Cubane Structures. *Int. J. Quantum Chem.* **2013,** *113*, 453-473.

41. Li, X.; Siegbahn, P. E. M. Water Oxidation for Simplified Models of the Oxygen-Evolving Complex in Photosystem II. *Chem. Eur. J.* **2015,** *21*, 18821-18827.

42. Krewald, V.; Neese, F.; Pantazis, D. A. On the Magnetic and Spectroscopic Properties of High-Valent Mn_3CaO_4 Cubanes as Structural Units of Natural and Artificial Water-Oxidizing Catalysts. *J. Am. Chem. Soc.* **2013,** *135*, 5726-5739.

43. Lang, S. M.; Bernhardt, T. M.; Kiawi, D. M.; Bakker, J. M.; Barnett, R. N.; Landman, U. The Interaction of Water with Free $Mn_4O_4^+$ Clusters: Deprotonation and Adsorption-Induced Structural Transformations. *Angew. Chem. Int. Ed.* **2015,** *54*, 15113-15117.

44. Du, P.; Eisenberg, R. Catalysts Made of Earth-Abundant Elements (Co, Ni, Fe) for Water Splitting: Recent Progress and Future Challenges. *Energy Environ. Sci.* **2012,** *5*, 6012-6021.

45. Kanan, M. W.; Yano, J.; Surendranath, Y.; Dincă, M.; Yachandra, V. K.; Nocera, D. G. Structure and Valency of a Cobalt−Phosphate Water Oxidation Catalyst Determined by in Situ X-ray Spectroscopy. *J. Am. Chem. Soc.* **2010,** *132*, 13692-13701.

46. Risch, M.; Khare, V.; Zaharieva, I.; Gerencser, L.; Chernev, P.; Dau, H. Cobalt−Oxo Core of a Water-Oxidizing Catalyst Film. *J. Am. Chem. Soc.* **2009,** *131*, 6936-6937.

47. Rigsby, M. L.; Mandal, S.; Nam, W.; Spencer, L. C.; Llobet, A.; Stahl, S. S. Cobalt Analogs of Ru-Based Water Oxidation Catalysts: Overcoming Thermodynamic Instability and Kinetic Lability to Achieve Electrocatalytic O_2 Evolution. *Chemical Science* **2012,** *3*, 3058-3062.

48. Smith, P. F.; Kaplan, C.; Sheats, J. E.; Robinson, D. M.; McCool, N. S.; Mezle, N.; Dismukes, G. C. What Determines Catalyst Functionality in Molecular Water Oxidation? Dependence on Ligands and Metal Nuclearity in Cobalt Clusters. *Inorg. Chem.* **2014,** *53*, 2113-2121.

49. Wang, L.-P.; Van Voorhis, T. Direct-Coupling O_2 Bond Forming a Pathway in Cobalt Oxide Water Oxidation Catalysts. *J. Phys. Chem. Lett.* **2011,** *2*, 2200-2204.

50. Mattioli, G.; Giannozzi, P.; Amore Bonapasta, A.; Guidoni, L. Reaction Pathways for Oxygen Evolution Promoted by Cobalt Catalyst. *J. Am. Chem. Soc.* **2013,** *135*, 15353-15363.

51. Li, X.; Siegbahn, P. E. M. Water Oxidation Mechanism for Synthetic Co–Oxides with Small Nuclearity. *J. Am. Chem. Soc.* **2013,** *135*, 13804-13813.

52. Kwapien, K.; Piccinin, S.; Fabris, S. Energetics of Water Oxidation Catalyzed by Cobalt Oxide Nanoparticles: Assessing the Accuracy of DFT and DFT+U Approaches against Coupled Cluster Methods. *J. Phys. Chem. Lett.* **2013,** *4*, 4223-4230.

53. Li, X.; Clatworthy, E. B.; Masters, A. F.; Maschmeyer, T. Molecular Cobalt Clusters as Precursors of Distinct Active Species in Electrochemical, Photochemical, and Photoelectrochemical Water Oxidation Reactions in Phosphate Electrolytes. *Chem. Eur. J.* **2015,** *21*, 16578-16584.

54. Nguyen, A. I.; Ziegler, M. S.; Oña-Burgos, P.; Sturzbecher-Hohne, M.; Kim, W.; Bellone, D. E.; Tilley, T. D. Mechanistic Investigations of Water Oxidation by a Molecular Cobalt Oxide Analogue: Evidence for a Highly Oxidized Intermediate and Exclusive Terminal Oxo Participation. *J. Am. Chem. Soc.* **2015,** *137*, 12865-12872.

55. Smith, P. F.; Hunt, L.; Laursen, A. B.; Sagar, V.; Kaushik, S.; Calvinho, K. U. D.; Marotta, G.; Mosconi, E.; De Angelis, F.; Dismukes, G. C. Water Oxidation by the $[Co_4O_4(OAc)_4(py)_4]^+$ Cubium is Initiated by OH– Addition. *J. Am. Chem. Soc.* **2015**.

Chapter 2 - Theory and computational methodology

2.1 Fundamentals of quantum mechanics

The theories of classical mechanics are inadequate to describe microscopic systems such as electrons, protons, atoms and molecules. In small particles, wave-like properties predominate and quantum mechanics can be used to account for the properties and behavior of this remarkable world. In quantum mechanics there is a mathematical operator for each experimentally measurable physical quantity. The eigenvalues of these operators describe the corresponding physically observable property. The eigenfunctions of a quantum mechanical operator depend on the coordinates upon which the operator acts. In quantum mechanics, these eigenfunctions are the wavefunctions (Ψ). The state of a system is described by these wavefunctions; it is a function of the coordinates ($\mathbf{x}$) and of time (t). The probability density ρ of finding a particle at coordinates $\mathbf{x}$ at time t is represented by:

$$\rho(\mathbf{x}, t) = |\Psi(\mathbf{x}, t)|^2 \, d\mathrm{x} \tag{2.1}$$

The equation that describes the energy levels of a quantum system is known as the Schrödinger equation. This equation is an eigenvalue equation for the Hamiltonian operator ($\widehat{H}$), which is the energy operator. It has two variants; if the Hamiltonian operator contains time as a variable, we use the time-dependent Schrödinger equation:

$$\widehat{H}(\mathbf{x}, t)\Psi(\mathbf{x}, t) = i\hbar \frac{\partial \Psi(\mathbf{x}, t)}{\partial t} \tag{2.2}$$

where $i = \sqrt{-1}$, ħ is defined as $h/2\pi$ and $\widehat{H}$ is given as:

$$\widehat{H}(\mathbf{x}, t) = -\sum_{i=1}^{N} \frac{1}{2m} \nabla_i^2 + \sum_{i=1}^{N} V(\mathbf{x}_i, t) + \sum_{i>j}^{N} \frac{q_i \, q_j}{r_{ij}} \tag{2.3}$$

The Hamiltonian operator between two electrons, i and j, contains three parts: the first term defines the kinetic energy of the electrons, the second term represents the potential energy, and the third term gives the Coulomb interactions between the particles. The mass and the charge of the electrons are given as m_e and q, respectively. N is the total number of electrons in the system. The distance between i and j electrons is given as r_{ij}. The Laplacian operator (∇_i^2) is the second derivative of the position of the particle in three dimensions.

In scenarios where the Hamiltonian operator does not contain terms that are explicitly time dependent, we use the time-independent Schrödinger equation:

$$\hat{H}\Psi(\mathbf{x}) = E\Psi(\mathbf{x}) \tag{2.4}$$

Here, the wavefunction only depends on the position of the particle. These systems are in stationary states where time does not affect the probability density. We cannot get an exact solution to the Schrödinger equation for most systems. However, we use multiple approximation methods to solve the Schrödinger equation that can predict the behavior and properties of large systems with reasonable accuracy.

2.2 Approximation methods

Approximation methods are used when the exact solution to the Schrödinger equation cannot be found. There is no analytical solution to this equation for systems with three or more particles, so we use mathematical methods to provide us with approximate solutions to such eigenvalue equations. There are two methods widely used in computational chemistry: the variational method and the perturbation theory.

2.2.1 The variational method

This theory is a way of assessing and improving guesses about the wavefunctions in complicated systems. The first step is to guess the form of a trial function (ϕ) and then optimize

it. In a system whose Hamiltonian operator $\widehat{H}$ is time independent, the lowest eigenvalue of this Hamiltonian is E_0, and if ϕ is any normalized, well-behaved trial function, then the variational theorem states that:[1]

$$\int \emptyset^* \, \widehat{H} \, \emptyset \, d\tau \geq E_0 \tag{2.5}$$

If the trial function is identical to the true ground state function then the equal sign holds. In order to get the lowest value for the $\int \emptyset \, \widehat{H} \, \emptyset \, d\tau$ integral, we can vary any parameter that defines the trial wavefunction; however it should have the proper spin and space symmetry as the Hermitian eigenfunctions.

2.2.2 Perturbation theory

When the mathematical solution is known for a given system, we can write Hamiltonians for related systems by adding an additional term representing a weak "perturbation" into the Hamiltonian. If the differences are not significant, perturbation theory allows calculation of the shifts and splitting of energy levels and changes in the wavefunction as "corrections" to the system. If $\widehat{H}^0$ is the Hamiltonian for the unperturbed system and $\widehat{H}$ is the Hamiltonian for the perturbed system, then the difference between the two Hamiltonians describes the external field or the perturbation, $\widehat{H}'$ can be written as:

$$\widehat{H}' = \widehat{H} - \widehat{H}^0 \tag{2.6}$$

In order to apply perturbation theory, the unperturbed states should be known because the energy and wavefunction corrections are expressed in terms of integrals over the unperturbed energies.

2.2.3 The Born-Oppenheimer approximation

The approximation of separating electronic motion from nuclear motion is called the Born-Oppenheimer approximation. In essence, the Born-Oppenheimer approximation corresponds to assuming that the nuclei are infinitely heavier than the electrons; thus the

coupling between the nuclear and the electronic motion is neglected. This allows electronic wavefunctions to be solved for a given set of stationary nuclei.

Consider a system that consists of a and b nuclei with *M* representing the total number of nuclei. The mass of the nucleus is given as m_a and the charge is given as q_a. r_{ia} is the distance between the electron i and nucleus *a* and r_{ab} corresponds to the distance between a and b nuclei. In order to properly describe the motions and energy of these particles we need to consider the full Hamiltonian. We can write the full Hamiltonian for a non-relativistic molecule as:

$$\widehat{H} = -\frac{\hbar^2}{2m_e}\sum_{i=1}^{N}\nabla_i^2 - \frac{\hbar^2}{2}\sum_{a=1}^{M}\frac{1}{m_a}\nabla_a^2 - \sum_{a=1}^{M}\sum_{i=1}^{N}\frac{q_a}{r_{ia}} + \sum_{j=1}^{N}\sum_{i>j}^{N}\frac{q_e^2}{r_{ij}} + \sum_{b=1}^{M}\sum_{b>a}^{M}\frac{q_a q_b}{r_{ab}} \tag{2.7}$$

The first and the second terms in the equation denote the kinetic energy of the electrons and nuclei respectively. The Columbic attraction force between the electrons and nuclei is given in the third term, and the fourth and fifth terms correspond to the repulsion forces between the electrons and nuclei respectively.

Solving the full Hamiltonian is a challenge for molecules as it contains terms that are difficult to compute. Acceptable approximations like the Born-Oppenheimer approximation are necessary to solve the equation efficiently. We can write the modified Hamiltonian as:

$$\widehat{H} = \widehat{H}_{elec} + V_{NN} \tag{2.8}$$

where $\widehat{H}_{elec}$ defines the electronic Hamiltonian:

$$\widehat{H}_{elec} = -\frac{\hbar^2}{2m_e}\sum_{i=1}^{N}\nabla_i^2 - \sum_{a=1}^{M}\sum_{i=1}^{N}\frac{q_a}{r_{ia}} + \sum_{j=1}^{N}\sum_{i>j}^{N}\frac{q_e^2}{r_{ij}} \tag{2.9}$$

Comparing the masses of the nuclei with the electron mass, nuclei are much heavier and move more slowly, and thus can be considered as stationary with respect to the motion of the electrons. This makes the second term related to the kinetic energy of the nuclei zero and since the nuclei

are not changing coordinates the fifth term is a constant. As r_{ab} is fixed, the V_{NN} term representing repulsion between nuclei becomes constant:

$$V_{NN} = \sum_{b=1}^{M} \sum_{b>a}^{M} \frac{q_a q_b}{r_{ab}} \tag{2.10}$$

Since V_{NN} is a constant for any given set of nuclear coordinates, it can thus be omitted from the Schrodinger equation, which gives:

$$\hat{H}_{elec} \Psi_{elec} = E_{elec} \Psi_{elec} \tag{2.11}$$

Here the term E_{elec} corresponds to the purely electronic energy. Thus we can calculate the total electronic energy U with nuclear-nuclear repulsion:

$$U = E_{elec} + V_{NN} \tag{2.12}$$

We can solve the nuclear motion from the same principle we used above. As we described above, the electrons move really fast compared to nuclear motion. So if the nuclei move slightly, the electrons adjust immediately, which changes the wavefunction of the system. So, the electronic energy changes as a function of the parameters defining the nuclear configuration. The nuclear Hamiltonian can be written as:

$$\hat{H}_{nuc} = -\frac{\hbar^2}{2} \sum_{a=1}^{M} \frac{1}{m_a} \nabla_a^2 + U(x_a) \tag{2.13}$$

Here, the first term represents the kinetic energy of the nuclei and the second term is the potential energy for the nuclear motion. We can write the Schrödinger equation for the nuclear motion:

$$\hat{H}_{nuc} \Psi_{nuc} = E_{nuc} \Psi_{nuc} \tag{2.14}$$

The nuclear energy, E_{nuc}, is a combination of the approximate sum of electronic, vibrational, rotational and translational energies. In a more elaborate fashion the Schrödinger equation that describes the interparticle potential energies of the nuclei and electrons of the atoms or molecule

can be divided into two parts. In one part we find the solution to the electronic Schrödinger equation for the wavefunctions and energies of electrons and both of these depend on the nuclear geometry. In the other part we solve the vibrational, rotational and translational Schrödinger equation for the motion of nuclei on the electronic energy surface. This separation is actually an important basis of spectroscopy and molecular modeling and optimization in computational chemistry, where we first calculate the electronic energy levels in a grid with different nuclear coordinates and solve the motion of the nuclei using this grid of data.[2]

2.3 Computational methods

2.3.1 Density functional methods

2.3.1.1 Density functional theory (DFT)

Present day computational chemistry, solid-state chemistry and nuclear physics widely applies computational methods such as density functional theory (DFT). Density functional theory provides a computationally efficient, powerful tool for calculating the quantum state of atoms, molecules and solids. The DFT method is based on the ground state electron density; the ground state energy and other properties are calculated as a function of electron density rather than the wavefunction. The wavefunction of an N electron system depends on $3N$ spatial and N spin coordinates and consists of more information than needed to calculate energy and other properties, thus making it very difficult to compute. To understand the fundamentals of density functional theory, we need to understand the landmark paper by Hohenberg and Kohn.

2.3.1.2 The Hohenberg-Kohn theorem

If we consider the purely electronic wavefunction (Equation 2.9) in terms of atomic units, we can write it as:

$$\widehat{H}_{elec} = -\frac{1}{2}\sum_{i=1}^{N}\nabla_i^2 + \sum_{i=1}^{N} v(r_i) + \sum_{j=1}^{N}\sum_{i>j}^{N}\frac{1}{r_{ij}} \tag{2.15}$$

As explained above the second term in this equation describes the interaction energy between the nuclei and the electron i. This directly depends on the coordinates of the electron i and on the nuclear coordinates. The Hohenberg-Kohn theorem states that ground state electron density describing a system with N electrons determines the potential $v(r_i)$ in the Hamiltonian.[3] Since we are considering fixed nuclei, the nuclear coordinates are not variables for this electronic Hamiltonian. Thus the $v(r_i)$ only depends on the coordinates of the electrons. We can express $v(r_i)$ as:

$$v(r_i) = \sum_{a=1}^{M}\frac{q_a}{r_{ia}} \tag{2.16}$$

Hohenberg and Kohn proved that for a system with a non-degenerate ground state, the external potential $v(r_i)$ is determined by the ground-state electron probability density $\rho_0\,(r)$. Hence, the $\widehat{H}$ defines the ground state energy and the wavefunction of the system; the ground state density $\rho_0\,(r)$ determines the ground state behavior of the system. The proof of the theorem can be explained as follows.[2-4]

The $\rho_0\,(r)$ determines the number of electrons:

$$\int \rho_0\,(r) d^3r = N \tag{2.17}$$

Assuming that there are two different external potentials $v(r_i)$ and $v'(r_i)$, the electronic Hamiltonians corresponding to these potentials are $\widehat{H}$ and $\widehat{H}'$. Let Ψ and Ψ' and E_0 and $E_0{}'$ be the normalized wavefunctions and energies respectively. In order to solve for two ground states (represented by E_0,Ψ and $E_0{}'$, Ψ') that have the same one-electron density:

$$\int |\Psi|^2 \, dr_2, dr_3 \ldots dr_N = \rho_0(r) = \int |\Psi'|^2 \, dr_2, dr_3 \ldots dr_N \tag{2.18}$$

If we think of Ψ' as trial variational wavefunction for Hamiltonian $\widehat{H}$, we know that:

$$E_0 < \int \Psi' H \Psi' \, dr = \int \Psi' \, H' \, \Psi' \, dr + \int \rho(\boldsymbol{r}) \, [v(r_i) - v'(r_i)] \, d^3r \tag{2.19}$$

$$= E_0{}' + \int \rho(\boldsymbol{r}) \, [v(r_i) - v'(r_i)] \, d^3r$$

We can write a similar equation taking Ψ as a trial function for the H' Hamiltonian:

$$E_0{}' < E_0 + \int \rho(\boldsymbol{r}) \, [v'(r_i) - v(r_i)] \, d^3r \tag{2.20}$$

One finds that adding equations 2.19 and 2.20 gives $E_0 + E_0{}' < E_0 + E_0{}'$. This is clearly not valid; thus, it is not possible to have two different potentials for the same ground state density. So, the ground state electron density determines the electronic Hamiltonian and the ground state wavefunction, and thus the ground state energy and other properties.

The ground state electronic energy E_0 can be written as a functional of function $\rho_0(r)$:

$$E_0 = E_v[\rho_0] \tag{2.21}$$

where v demonstrates the dependence of the ground state energy E_0 on the external potential $v(r_i)$. The electronic Hamiltonian is the sum of average kinetic energy, electron-nuclear attractions and electron-nuclear repulsion energies. We can prove that $\int \rho(\boldsymbol{r}) v(r_i) \, d^3r = \bar{V}_{Ne}$, where $\bar{V}_{Ne}$ represents the electron-nuclear interactions in terms of the ground state electron density but the kinetic energy and the electron-electron interaction energies are not known from the Hohenberg-Kohn theorem.[2]

2.3.1.3 The Kohn-Sham method

Modern progress of density functional theory started with the introduction of orbitals suggested by Kohn and Sham. Even though the Hohenberg-Kohn theory states that it is possible to calculate all the ground state properties from the ground state electron density without writing

the wavefunction, it does not provide a means of calculating the total ground state energy from the electron density (i.e. the kinetic energy and the electron-electron repulsion energy terms). Kohn-Sham theory[5] reintroduces the orbitals, thus increasing the computation complexity from 3 to $3N$ variables and causing the electronic correlation to appear as a separate term.

If we consider a hypothetical system with non-interacting electrons with external potential $v_s(r_i)$ where the ground state electron probability density $\rho_s(r)$ of this hypothetical system is equal to the exact ground state electron density of $\rho_0(r)$, we can write the electronic Hamiltonian as:

$$\hat{H} = \hat{h}^{ks} = -\sum_{i=1}^{N}\left(\frac{1}{2}\nabla_i^2 + v_s(r_i)\right) = \sum_{i}^{N}\hat{h}_i^{ks} \tag{2.22}$$

where $\hat{h}_i^{ks} = -\frac{1}{2}\nabla_i^2 + v_s(r_i)$ represents the Kohn-Sham Hamiltonian for electron i. We can write the Hamiltonian of this hypothetical system related to an actual system as:

$$\hat{H}_\lambda = \hat{T} + \sum\nolimits_i v(r_i)(\lambda) + \lambda\hat{V}_{ee} \tag{2.23}$$

Here, $\hat{T}$ is the kinetic energy term, $v(r_i)$ is the external energy operator, and V_{ee} is the electronic-electronic repulsion operator. The external potential $v(r_i)$ is equal to V_{Ne} for $\lambda = 1$ (real system with interacting electrons) and for $\lambda = 0$ (non-interacting electrons), the exact solution to the Schrödinger equation is given as a Slater determinant composed of molecular orbitals, $\Psi_{s,0}$.

The kinetic energy of this hypothetical system can be written as:

$$\bar{T}_s[\rho_0] = -\frac{1}{2}\langle\Psi_{s,0}\left|\sum_{i=1}^{N}\nabla_i^2\right|\Psi_{s,0}\rangle + \Delta\bar{T}[\rho_0] \tag{2.24}$$

The first term represents the kinetic energy of the ground state of the non-interacting system and the second term is the kinetic energy difference between the real and the non-interacting system. For the electron-electron repulsion energy, we can write:

$$\bar{V}_{ee}[\rho_0] = \frac{1}{2}\iint \frac{\rho(r_1)\rho(r_2)}{r_{12}} dr_1 dr_2 + \Delta\bar{V}_{ee}[\rho_0] \tag{2.25}$$

Here, the first part represents the classical expression of the electrostatic interelectronic repulsion energy. The second term represents the difference of the repulsion energy between the real system and the imaginary system.

Although the Kohn-Sham theory defines the kinetic energy and the electron-electron repulsion energies, it assumes a hypothetical non-interacting electron system. This is similar to the Hartree-Fock (HF) method, and in most cases this provides ~99% of the correct solution mainly because the difference of the kinetic energy and the repulsion energy between the actual and reference system is very small. However, in reality there are electron-electron interactions, which cannot be neglected.[2, 4, 6]

The terms $\Delta\bar{V}_{ee}[\rho_0]$ and $\Delta\bar{T}[\rho_0]$ are combined into a new term called the exchange and correlation functional, E_{xc}:

$$E_{xc}[\rho_0] = \Delta\bar{T}[\rho_0] + \Delta\bar{V}_{ee}[\rho_0] \tag{2.26}$$

Now, the total ground state energy of the non-interacting system can be written in terms of:

$$E_0 = E_v[\rho_0] = \int \rho(r)v(r)dr + \bar{T}_s[\rho_0] + \frac{1}{2}\iint \frac{\rho(r_1)\rho(r_2)}{r_{12}} dr_1 dr_2 + E_{xc}[\rho_0] \tag{2.27}$$

where the first term is the nuclear-electron attraction energy term $\bar{V}_{Ne}$ and the second term is the kinetic energy of the electrons. The electron-electron repulsion energy term $\bar{V}_{ee}[\rho_0]$ is represented by the third term and the exchange and correlation energy term $E_{xc}[\rho_0]$ is represented by the fourth term.

2.3.1.4 Exchange-correlation functionals

In order to accurately predict the properties one need to have a good approximation to the exchange and correlation functional term. To date there is no one functional that can describe all the system properties but we have many different exchange and correlational functionals that can be used based on the properties we are investigating. The general types of approximations are summarized in Table 2.1 and this is known as the Jacob's ladder.[7]

When you step up the ladder, accuracy is expected to improve. The first step in this ladder is called the local-density approximation (LDA), which is based on the local electron density ρ. The second step is the generalized gradient approximation (GGA) that depends on the local density ρ and the gradient of the density $\nabla\rho$. The third step includes the first two steps and the second derivative of the gradient $\nabla^2\rho$ and/or the kinetic energy density τ, and the fourth step is the hybrid functionals that includes the first three steps and exact HF exchange.

Table 2.1 Jacob's ladder of functionals.

Functional	Variables	Examples
LDA	ρ	VWN[8]
GGA	$\rho, \nabla\rho$	PBE,[9] BP86,[10, 11] PW91[12]
Meta-GGA	$\rho, \nabla\rho, \nabla^2\rho$ or τ	TPSS[13]
Hybrid	$\rho, \nabla\rho, \nabla^2\rho$ or τ and HF	B3LYP[10, 14]

Local density approximation (LDA)

In the first step of the Jacob's ladder we find the LDA functionals. In essence LDA assumes that the electron density is single valued at every position and is reasonably treated as a uniform electron gas (jellium). The LDA for the exchange and correlation energy functional is given as:

$$E_{xc}^{LDA}[\rho] = \int \rho(r) \in_{xc} (\rho) dr \tag{2.28}$$

where $\in_{xc}$ is the exchange and correlation energy per electron in a uniform gas with $\rho(r)$ electron density. When the spin density due to the α spin electrons, $\rho^{\alpha}(r)$, and the spin density due to the β spin electrons, $\rho^{\beta}(r)$, are not equal, we replace the LDA functionals with local spin density approximation (LSDA). Generally, this is given as the sum of individual densities raised to the 4/3 power.

Generalized gradient approximation (GGA)

In order to avoid the limitation of the hypothetical uniform electron gas model, we can allow the exchange and correlation energies to depend not only on the electron density but also on derivatives of the density. If we consider the gradients of the α and β spin densities to be $\nabla\rho^{\alpha}(r)$ and $\nabla\rho^{\beta}(r)$, we can write the exchange and correlation energy in terms of:

$$E_{xc}^{GGA}\left[\rho^{\alpha}, \rho^{\beta}\right] = \int f\left(\rho^{\alpha}(r), \rho^{\beta}(r), \nabla\rho^{\alpha}(r), \nabla\rho^{\beta}(r)\right) dr \tag{2.29}$$

where f is some function of the spin densities and their gradients. In the GGA method, the exchange part and the correlation part are usually divided into two sections and modeled separately. Commonly used exchange functionals include Becke's 1988 functional denoted as B88,[10] Perdew and Wang's 1986 and 1991 exchange functionals denoted as PWx86 and PWx91,[11, 12] etc. The B88 functional is given as:

$$\in_x^{B88} = \in_x^{LDA} + \Delta\in_x^{B88} \tag{2.30}$$

$$\Delta\in_x^{B88} = -\beta\rho^{1/3}\frac{x^2}{1 + 6\beta x sinh^{-1}x} \tag{2.31}$$

$$x = \frac{|\nabla\rho|}{\rho^{4/3}}$$

Here, β is determined by fitting data of the rare gas atoms using the dimensionless variable x. Commonly used correlation functionals include the Lee-Yang-Parr (LYP) functional,[14] Perdew 1986 correlation functional (P86),[11] etc. Another commonly used GGA functional, Perdew-Burke-Ernzerhof (PBE),[9] contains both the exchange and the correlation energy. A GGA functional is often named by combining the exchange and correlation functionals: BP86, BLYP, etc. In our calculations we employed the exchange correlation functional of BP86.

Meta-GGA functionals

The next development to the GGA functionals can be achieved if the second derivative of the electron density ($\nabla^2\rho$) and/or kinetic energy density functionals (τ) are incorporated. Such functionals have the form:

$$E_{xc}^{MGGA}[\rho^{\alpha},\rho^{\beta}] = \int f(\rho^{\alpha},\rho^{\beta},\nabla\rho^{\alpha},\nabla\rho^{\beta},\nabla^2\rho^{\alpha},\nabla^2\rho^{\beta},\tau)\,dr \tag{2.32}$$

The kinetic energy density functional (τ) is given by:

$$\tau = \frac{1}{2}\sum_{i}\left|\nabla\theta_{i\alpha}^{KS}\right|^2 \tag{2.33}$$

where $\theta_{i\alpha}^{KS}$ is the Kohn-Sham orbitals for the α spin electrons.

Hybrid functionals

Hybrid functionals consist of a combination of different exchange and correlation functionals. The commonly used B3LYP functional is defined by:

$$E_{xc}^{B3LYP} = (1-a_0-a_x)E_x^{LSDA} + a_0E_x^{exact} + a_xE_x^{B88} + (1-a_c)E_c^{VWN} + a_cE_c^{LYP} \tag{2.34}$$

2.3.2 Other correlation methods

2.3.2.1 Configuration Interactions (CI) method

CI is a method to treat electron correlation at a high-level for the ground state as well as excited states. The CI wavefunction is given by:

$$\Psi = \sum_{i=1}^{N} a_i \phi_i \tag{2.35}$$

where the ϕ_i are the configuration state functions (CSF) (electronic configurations can have spatial and spin adapted determinantal wavefunctions; such functions are called configuration state functions) and a_i are the expansion coefficients which are to be determined in the variational calculation. A set of orthonormal molecular orbitals is obtained from a self-consistent field (SCF) calculation. The linear combinations of atomic orbitals-molecular orbitals (LCAO-MO) coefficients are not considered as variational parameters during the CI procedure. These molecular orbitals (MOs) are then used to construct CSFs. These CSFs are generated from single, double, triple, etc. excitations relative to the reference CSFs. These configuration functions in a CI are restricted to include different level of excitations and denoted as S (singly excited), D (doubly excited), T (triply excited), etc.

The electronic Hamiltonian H_{IJ} in a CI calculation is solved in terms of one- and two-electron integrals over the molecular orbitals using the Slater determinants. A CI wavefunction can be interpreted as a linear combination of Slater determinants. If we include all the possible CSFs with proper symmetry, the solution to the CI gives the exact energy of the wavefunction and it is called full CI. In reality this can be achieved for small molecules with rather small basis sets but beyond that it is highly impractical due to the computational cost.[4, 15]

2.3.2.2 Multiconfiguration self-consistent field method (MCSCF)

The MCSCF method can be considered as a CI method where we write the molecular wavefunction as a linear combination of CSFs and the variational principle is used to optimize not only the coefficients in front of the determinants but also the MO coefficients used for constructing the determinants.

This parallel optimization of the LCAO-MO and CI coefficients within an MCSCF calculation is a complex process. An MCSCF wavefunction can be written in the CI form as:

$$\Psi_{MCSCF} = \sum_{I}^{CI} C_I \, \phi_I \tag{2.36}$$

where ϕ_I are individual slater determinants or CSFs.

From the CI expression, we can write the energy as:

$$E = \sum_{IJ}^{CI} C_I^* C_J H_{IJ} \tag{2.37}$$

where H_{IJ} denotes the matrix element of the electronic Hamiltonian between determinants ϕ_I and ϕ_J.

$$H_{IJ} = \langle \phi_I | H | \phi_J \rangle \tag{2.38}$$

These matrix elements can all be written in terms of one and two electron integrals according to the Slater rules. The energy can be expressed from the form of unitary group generators:

$$\hat{E}_{pq} = a_{p\alpha}^{\dagger} a_{q\alpha} + a_{p\beta}^{\dagger} a_{q\beta} \tag{2.39}$$

where $a_{p\alpha}^{\dagger}$ is a creation operator for an electron in orbital p with α spin, $a_{q\alpha}$ is an annihilation operator for an electron in orbital q with α spin, etc. The electronic Hamiltonian can be written in terms of these operators:

$$\hat{H} = \sum_{pq}^{K} (p|h|q)\hat{E}_{pq} + \frac{1}{2}\sum_{pqrs}^{K} (pq|rs)\left(\hat{E}_{pq}\hat{E}_{rs} - \delta_{qr}\hat{E}_{ps}\right) \tag{2.40}$$

Adding the matrix element H_{IJ}:

$$H_{IJ} = \sum_{pq} \gamma_{pq}^{IJ} h_{pq} + \frac{1}{2}\sum_{pqrs} \Gamma_{pqrs}^{IJ} (pq|rs) \tag{2.41}$$

The terms in front of the one- and two-electron integrals for this matrix element, γ_{pq}^{IJ} and Γ_{pqrs}^{IJ}, are the coupling coefficients respectively:

$$\gamma_{pq}^{IJ} = \langle \phi_I | \hat{E}_{pq} | \phi_J \rangle \tag{2.42}$$

$$\Gamma_{pqrs}^{IJ} = \langle \phi_I | \hat{E}_{pq}\hat{E}_{rs} - \delta_{qr}\hat{E}_{ps} | \phi_J \rangle \tag{2.43}$$

The coupling coefficients have the following properties due to the anticommutation relations of creation and annihilation operators:

$$\gamma_{pq}^{IJ} = (\gamma_{pq}^{IJ})^* \tag{2.44}$$

$$\Gamma_{pqrs}^{IJ} = \Gamma_{rspq}^{IJ} = (\Gamma_{srqp}^{IJ})^* = (\Gamma_{qpsr}^{IJ})^* \tag{2.45}$$

We can write the MCSCF energy term as:

$$E = \sum_{IJ}^{CI} C_I^* C_J \left[\sum_{pq} \gamma_{pq}^{IJ} h_{pq} + \frac{1}{2}\sum_{pqrs} \Gamma_{pqrs}^{IJ} (pq|rs) \right] \tag{2.46}$$

MCSCF wavefunctions are much harder to converge compared to SCF where most of the time it converges to a minimum without problems. This is basically because the minimization of energy with several non-linear parameters suffers from poor convergence and can often locate local minima rather than the global minima. MCSCF wavefunction calculations are usually

carried out by expanding the energy to second order variational parameters and using Newton-Raphson Methods for acquiring convergence to a minimum.[16, 17]

Because of this reason, the number of CSFs is usually kept to a moderate number chosen to describe important correlations. One of the well-known approaches is the complete active space self-consistent field (CASSCF) method. Configurations are selected by splitting the molecular orbitals into active and inactive spaces. The active MOs are taken from a restricted Hartree-Fock (RHF) calculation and include some of the highest occupied and lowest unoccupied MOs. The inactive space is usually unoccupied or doubly occupied with 0 or 2 electrons. Full CI is performed within the active space with all proper symmetry adapted configurations in the MCSCF optimization. The decision of how many orbitals should be included into the active space has to be considered with the problem in hand.

2.3.2.3 Multireference configuration interaction (MRCI)

This method combines the MCSCF and the standard CI methods. In a general CI method, we consider CSFs generated by exciting electrons from a single determinant. In other words, a HF type wavefunction is chosen as the reference. However, in some cases that is not enough to account for the chemical phenomenon observed, so configuration interaction methods involving single and double excitations (CISD functions) are used as the reference. The final MRCI wavefunction includes some triple and quadruple excitations.

2.3.2.4 Multireference Møller-Plesset perturbation theory (MRMP2)

We can start the zeroth order wavefunction from MCSCF wavefunction and apply the Møller-Plesset (MP) perturbation theory to produce multireference-perturbation theory (MR-PT), whereas in a general MP calculation we apply perturbation theory to a single Slater determinant. The MRMP2 method enables the calculation of low-lying potential energy surfaces for each state

in the system. In this method the reference function is created by diagonalizing the Hamiltonian in the reference space first and then perturbing it. This MRMP2 approach can recover dynamic correlation energy for the MCSCF wavefunction. Compared to the MRCI results, MRMP2 results are significantly faster but may not be as accurate as MRCI.

2.4 Basis sets

In a simple definition, a basis set is a set of mathematical functions from which the wavefunction is constructed. This is a type of approximation that is used in all ab initio calculations. In a full HF wavefunction the optimal description of the wavefunction can be achieved by a complete basis set. A complete basis set means combination of an infinite number of functions, which is impossible to calculate.

There are several types of basis functions that can be used in electronic structure calculations including Slater type orbitals (STO) and Gaussian type orbitals (GTO). For STOs we can write:

$$\chi_{\zeta,n,l,m}(r,\theta,\varphi) = NY_{l,m}(\theta,\varphi)r^{n-1}e^{-\zeta r} \tag{2.47}$$

where $Y_{l,m}$ are spherical harmonic functions and the N is the normalization constant. Gaussian type orbitals can be written in spherical coordinates as:

$$\chi_{\zeta,n,l,m}(r,\theta,\varphi) = NY_{l,m}(\theta,\varphi)r^{2n-2-l}e^{-\zeta r^2} \tag{2.48}$$

or in Cartesian coordinates as:

$$\chi_{\zeta,l_x l_y l_z}(x,y,z) = Nx^{l_x}y^{l_y}z^{l_z}e^{-\zeta r^2} \tag{2.49}$$

The sum of l_x, l_y, l_z determines the type of orbital; when the sum is zero the GTO has spherical symmetry and it is called a *s*-type GTO. If the sum is one, then it is a p-type GTO. The r^2 part of the GTO function makes it problematic compared to the STO functions. For *s*-type

functions, close to the nucleus the GTO has a zero slope whereas in a real s function it has a cusp as in STO functions.

The tail part of the GTO is also poorly represented; in reality AOs have a radial exponential decay with respect to r but with GTOs this is r^2, suggesting a rapid fall off far from nucleus compared to the STO functions. It should also be noted that a linear combination of multiple GTOs can be created for a close approximation to a STO. Such a basis function built up with a linear combination of Gaussians is referred to as a contracted Gaussian function (assuming that contraction coefficients are not optimized), and the individual functions are called primitive Gaussians.

Improvement of the basis sets can also be achieved by doubling and tripling the number of functions used, which produces double zeta and triple zeta basis sets respectively. In most of the calculations used in this work, we employed triple zeta (TZ) basis functions. These functions contain three times the number of basis functions with respect to the minimal basis. A common variation of this basis set type involves tripling only the valence orbitals, which generates a split valance basis usually called triple zeta valence (TZV). Additional improvement to the basis functions can be achieved by introducing polarization and diffuse functions. With polarization functions, additional accuracy can be achieved by adding extra functions that are one quantum number higher than the valence orbitals. For example, in the first row elements, d functions are added for this extra flexibility and for hydrogen p functions are generally added to increase the accuracy of the properties predicted. This adds an extra 'polarization' (P) term to TZV or TZ and thus the basis sets are denoted TZVP or TZP. Diffuse functions are added in some scenarios like in anions and higher excited electronic states, where molecular orbitals tend to be more spatially spread than in usual MOs. We can add the extra flexibility to these functions by allowing

electron density to be spread out, which is termed as diffuse functions (diffuse functions have a small ζ exponent, meaning that the electron is held far away from the nucleus). We did not employ diffuse functions in our calculations, as such scenarios are not present with the systems we studied.

2.5 References

1. Jensen, F., *Introduction to Computational Chemistry*. second ed.; John Wiley & Sons: 2007.

2. Simons, J.; Nichols, J., *Qunatum Mechanics in Chemistry*. Oxford University Press: 1997.

3. Hohenberg, P.; Kohn, W. Inhomogeneous Electron Gas. *Physical Review* **1964,** *136*, B864-B871.

4. Levine, I. N., *Quantum Chemsitry*. Sixth ed.; Pearson Prentice Hall: Upper Saddle River: 2009.

5. Kohn, W.; Sham, L. J. Self-Consistent Equations Including Exchange and Correlation Effects. *Physical Review* **1965,** *140*, A1133-A1138.

6. Cramer, C. J., *Essentials of Computational Chemisrty Theories and Models*. second ed.; John Wiley & Sons: 2004.

7. Perdew, J. P.; Schmidt, K. Jacob's ladder of density functional approximations for the exchange-correlation energy. *AIP Conf. Proc.* **2001,** *577*, 1-20.

8. Vosko, S. H.; Wilk, L.; Nusair, M. Accurate spin-dependent electron liquid correlation energies for local spin density calculations: a critical analysis. *Can. J. Phys.* **1980,** *58*, 1200-1211.

9. Perdew, J. P.; Burke, K.; Ernzerhof, M. Generalized Gradient Approximation Made Simple. *Phys. Rev. Lett.* **1996,** *77*, 3865-3868.

10. Becke, A. D. Density-Functional Exchange-Energy Approximation with Correct Asymptotic Behavior. *Phys. Rev. A* **1988,** *38*, 3098-3100.

11. Perdew, J. P. Density-Functional Approximation for the Correlation Energy of the Inhomogeneous Electron Gas. *Phys. Rev. B* **1986,** *33*, 8822-8824.

12. Perdew, J. P.; Wang, Y. Accurate and simple analytic representation of the electron-gas correlation energy. *Phys. Rev. B* **1992,** *45*, 13244-13249.

13. Tao, J.; Perdew, J. P.; Staroverov, V. N.; Scuseria, G. E. Climbing the Density Functional Ladder: Nonempirical Meta-Generalized Gradient Approximation Designed for Molecules and Solids. *Phys. Rev. Lett.* **2003,** *91*, 146401.

14. Lee, C.; Yang, W.; Parr, R. G. Development of the Colle-Salvetti Correlation-Energy Formula into a Functional of the Electron Density. *Phys. Rev. B* **1988,** *37*, 785-789.

15. Sherrill, C. D.; Schaefer III, H. F., The Configuration Interaction Method: Advances in Highly Correlated Approaches. In *Adv. Quantum Chem.*, Per-Olov Löwdin, J. R. S. M. C. Z.; Erkki, B., Eds. Academic Press: 1999; Vol. Volume 34, pp 143-269.

16. Wilson, A. K. ; Peterson, K. A., *Electron Correlation Methodology*. American Chemical Society: 2007; Vol. 958, p 232.

17. Schmidt, M. W.; Gordon, M. S. The Construction and Interpretation of MCSCF Wavefunciton. *Annu. Rev. Phys. Chem.* **1998,** *49*, 233-266.

Chapter 3 - Theoretical Investigation of Water Oxidation on Fully Saturated Mn_2O_3 and Mn_2O_4 Complexes

Amendra Fernando, Tyler Haddock, and Christine M. Aikens

3.1 Abstract

Understanding the factors that affect efficiency of manganese oxides as water oxidation catalysts is an essential step towards developing commercially viable electrocatalysts. It is important to understand the performance of the smallest versions of these catalysts, which will in return be advantageous with bottom up catalytic design. Density functional theory calculations have been employed to investigate water oxidation processes on $Mn_2(\mu\text{-}OH)(\mu\text{-}O)(H_2O)_3(OH)_5$ ($Mn_2O_4\bullet 6H_2O$), $Mn_2(\mu\text{-}OH)_2(H_2O)_3(OH)_4$ ($Mn_2O_3\bullet 6H_2O$), and $Mn_2(\mu\text{-}OH)_2(H_2O)_4(OH)_4$ ($Mn_2O_3\bullet 7H_2O$) complexes. The effect of different oxidation states of manganese is considered in this study. Thermodynamically, the lowest energy pathway for the fully saturated $Mn_2O_4\bullet 6H_2O$ complex occurs through a nucleophilic attack of a solvent water molecule to a Mn(IV½)O oxo moiety. The lowest energy pathway on the $Mn_2O_3\bullet 6H_2O$ complex proceeds with an attack of Mn(VI)O group to the surface hydroxo group on the same manganese atom; this pathway is related to the third lowest energy pathway on the $Mn_2O_4\bullet 6H_2O$ complex. The water oxidation process on the fully saturated $Mn_2O_3\bullet 7H_2O$ complex also involves a nucleophilic attack from a solvent water molecule to a Mn(V)O moiety**.** The formation of these manganese oxo groups can be used as a descriptor for selecting a manganese-based water splitting catalyst due to the high electrochemical potentials required for their generation.

3.2 Introduction

Water oxidation catalysis using earth abundant transition metal oxides has been a widely researched topic over the past few decades. The water oxidation process is a cornerstone of a future based on hydrogen. It is a clean and sustainable way to produce hydrogen, as the byproducts are free from toxic substances. The blueprint for this water splitting into hydrogen and oxygen has its roots in nature. In green plants, solar energy is converted to chemical energy via water splitting into molecular oxygen, protons, and electrons by the oxygen evolution complex (OEC) of photosystem II (PSII). The reaction center of the OEC consists of a metal oxide framework with a cubane core: $CaMn_4O_4$.[1] Extensive theoretical and experimental investigations have been reported in order to understand the reaction mechanism of water oxidation process on this cubane core.[2-14] There have been many theoretical suggestions on the reaction mechanism and role of the calcium in the active center, but many unknowns still exist.[15]

Learning from these studies, there have been many reports of biomimetic catalytic systems.[16-25] Nevertheless, to date there is no commercially viable efficient catalyst available for this process. Among the reported catalytic systems, transition metal oxide based photocatalysts and electrocatalysts have gained wide popularity. Electrocatalytic water oxidation is particularly interesting due to its potential for large-scale distribution. Currently, industrial water oxidation is carried out with electrolysis using precious metals like Pt as electrodes. Other metal based oxides like Ru[22, 26, 27] and Ir[28, 29] oxides are reported as efficient electrocatalysts but commercial applications of all these catalysts are limited due to their higher costs. Water oxidation catalysts using the earth abundant and inexpensive Co,[19, 22-24] Ni,[17, 19, 30] Fe,[19, 22] and Mn[16, 23, 25, 31] oxides have also been examined previously.

Manganese oxide complexes with μ-oxo and μ-hydroxo groups are among the most theoretically and experimentally investigated transition metal oxide catalysts.[15, 32-38] This is due mainly to the presence of manganese oxides in the OEC as well as the abundance and efficiency of these systems. Manganese possesses a large number of stable oxidation states and has orbital near degeneracies and nondynamical correlation that result in a challenge for the theoretical treatment of these systems.[39, 40] There are only a few theoretical studies related to water oxidation on ligand-free manganese oxides. Blomberg *et al*.[41] reported an early theoretical study of ligand-free manganese monomer and dimer compounds mimicking the hydrogen abstraction process. They employed the B3LYP/6-311+G(d,p) level of theory and suggested that coordination of a water molecule to the manganese ion lowers the energy required to abstract hydrogen atoms from the water molecule. McGrady and coworkers[42] also reported a density functional study of redox-induced formation and cleavage of the O-O bond in an inorganic manganese dimer. It was found that in order to break the O-O σ bond, a transfer of two electrons of opposite spin between the metal and ligand is necessary whereas the formation of the O-O π bond requires transfer of two electrons of the same spin.[42] The antiferromagnetic or ferromagnetic coupling of the metal centers affect the stability of the intermediate species where the redox process is metal based and thus affects the kinetic barrier to bond formation or cleavage. Lang *et al*.[43] investigated the water splitting mechanism on free manganese oxide clusters $Mn_2O_2^+$ and $Mn_4O_4^+$. They used gas phase ion trap measurements in combination with Born-Oppenheimer spin density functional molecular dynamics calculations. These calculations were done with norm conserving soft pseudopotentials using GGA for the exchange correlation functional. Recently, Lee and Aikens[44] reported a theoretical investigation of water oxidation on ligand-free fully saturated Mn_2O_4 and $Mn_xTi_{2-x}O_4$ (x = 0-2) complexes. They employed the

BP86/ATZVP level of theory in their calculations. In this work, we revisit the water oxidation reaction processes on fully saturated pure Mn_2O_4 complexes, with an average oxidation state of Mn(IV), and adsorption of six waters. This knowledge is used to investigate water oxidation reactions on six and seven water adsorbed (fully saturated) Mn_2O_3 complexes with an average oxidation state of Mn(III). These ligand-free model compounds can be used to investigate and gain a molecular level understanding of catalytic water oxidation processes and the effect of oxidation states. Thus, insights from this study may promote the future design of efficient, water splitting catalysts.

3.3 Computational Methodology

All the geometry optimizations are performed with the Amsterdam Density Functional (ADF) software package.[45] We employed the BP86[46, 47] exchange and correlation functional with an augmented polarized triple-zeta (ATZP) basis set to revisit the water oxidation process on fully saturated Mn_2O_4 previously reported by Lee and Aikens.[44] The Mn_2O_4 water oxidation process and Mn_2O_3 water adsorption and water oxidation processes have also been investigated with BP86 and a triple-zeta polarized (TZP) basis set. Because the ATZP basis set includes many diffuse functions, linear dependence of the basis functions is a potential issue. We have examined numerical cutoffs of $1x10^{-3}$, $1x10^{-4}$ (default in ADF when used), and $5x10^{-5}$ for removing orbitals from the valence space.

Processes investigated in the water splitting process include four dehydrogenation steps, addition of two water molecules, and removal of one oxygen molecule. The water molecule adsorption and dissociation energies on the Mn_2O_3 complex are marked as ΔE_{Ads} and ΔE_{Diss}, respectively and the total energy of both the adsorption and dissociation is given as $\Delta E_{Wx.}$ The charge and the multiplicity of the structures are given in parentheses in the figures. The areas of

the complex where changes are occurring, such as chemically relevant stages between the calculated intermediate states of each structure, are highlighted in green circles. When addressing the aqua and hydroxo ligands attached to manganese atoms above, below, and in the plane of the central $Mn_2(\mu\text{-}OH)_2$ unit, the terms "surface", "bottom", and "geminal", respectively are used in the text with respect to the orientation of the structures given in each figure. All oxidation states described in this study refer to formal oxidation states.

The reference system is chosen as $2H^{\bullet} \rightarrow H_2$. This reference system has previously been useful for investigating water splitting processes on cobalt dimer and cubane complexes.[48] The use of the standard hydrogen electrode reaction ($2H^+ + 2e^- \rightarrow H_2$) as a reference system is problematic as it depends on the solvation of proton, which is challenging to accurately calculate with theory. The choice of the $2H^{\bullet} \rightarrow H_2$ reference system also benefits from removing the strong pH and solvent dependence known for the former reaction. Nonetheless, choice of the reference system is arbitrary for the electrochemical steps (i.e. dehydrogenation reactions) in the process because it does not change the qualitative predictions; it affects all hydrogen abstractions equally.

We have included the zero point energy (ZPE), enthalpy and entropy correction terms for a temperature of 298.15 K. The total internal energy (U) of an intermediate structure is calculated by adding the nuclear internal energy term to the electronic energy of the structure. The nuclear internal energy of the structure is the sum of ZPE, 3 kT and a small correction term that account for the vibration partition function. The 3 kT term describe the 3/2 kT for rotation and 3/2 kT for the translation motion. The Gibbs free energy is calculated with the standard formula G = H-TS, where enthalpy H is calculated by H = U + pV. The pV term is obtained from the ideal gas equation pV/n = RT. The energy differences are calculated according to

$\Delta E = \sum_{i}^{\text{products}} \nu_i E_i - \sum_{i}^{\text{reactants}} \nu_i E_i$ and $\Delta G = \sum_{i}^{\text{products}} \nu_i G_i - \sum_{i}^{\text{reactants}} \nu_i G_i$, where ΔE and ΔG represent reaction energy and reaction free energy. The term ν_i is the stoichiometric coefficient, E_i is the electronic energy and G_i is the Gibbs free energy value. The energy values given in the paper are reported as reaction energies unless otherwise noted and both values are given in the tables.

In this study we target the thermochemistry of intermediate reactions. Kinetics also plays an important role but is not considered because multiple transition states are possible for these dynamic reactions and the transition states are very sensitive to the hydrogen atom orientation. All possible isomers of the intermediate states have been considered when predicting the lowest energy step.

3.4 Results and Discussion

3.4.1 Water oxidation process with fully saturated Mn_2O_4

In the first stage of this work, we revisited the water oxidation process on the fully saturated $Mn_2(\mu\text{-}OH)(\mu\text{-}O)(H_2O)_3(OH)_5$ ($Mn_2O_4 \bullet 6H_2O$) complex. We used the same BP86/ATZP level of theory previously employed by Lee and Aikens,[44] but we took an extra step to achieve tighter energy convergence. The geometric structures from Ref. 44 (Figure 3.1) were optimized with three numerical cutoff values: $1x10^{-3}$, $1x10^{-4}$, and $5x10^{-5}$.

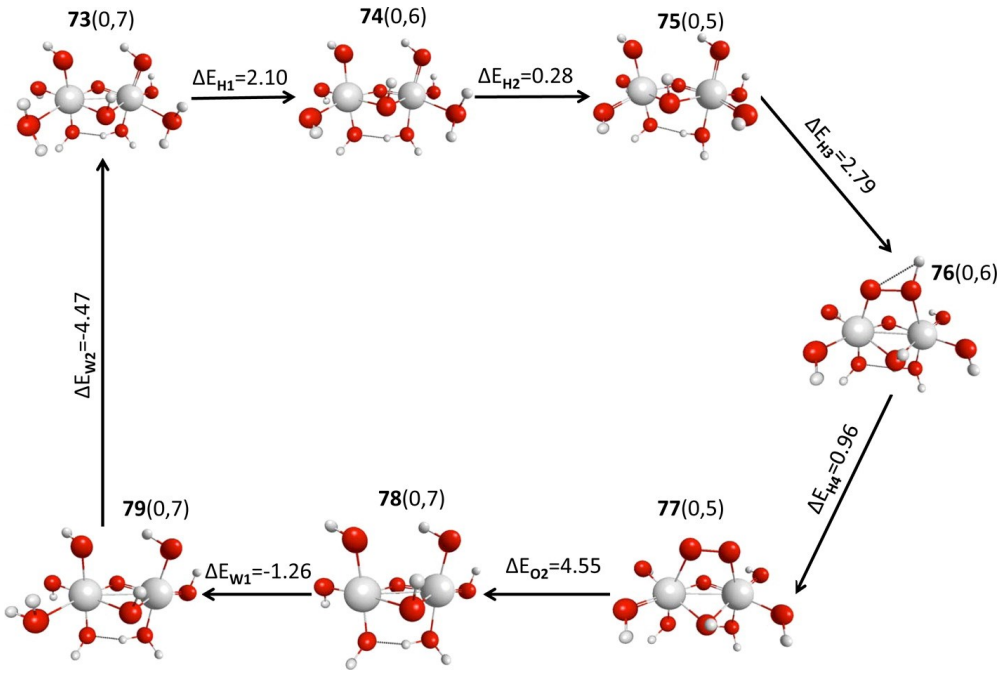

Figure 3.1 Water oxidation process on the fully saturated Mn_2O_4•$6H_2O$ complex from Ref. 44. Relative energies are given in eV. Big white spheres, big red spheres, and small white spheres represent the manganese, oxygen, and hydrogen atoms, respectively. This color code is kept consistent through the article (Reprinted with permission from *J. Phys. Chem. A* **2014**, *118*, 8204-8221. Copyright 2014 American Chemical Society).

Table 3.1 Calculated reaction energies (eV) for the water oxidation process on the fully saturated Mn_2O_4 reaction pathway given in Figure 3.1 Energies are calculated at the BP86/ATZP level of theory with three different linear dependency cutoff values and at the BP86/TZP level of theory.

Reaction Processes	BP86/ATZP ($1x10^{-3}$)	BP86/ATZP ($1x10^{-4}$)	BP86/ATZP ($5x10^{-5}$)	BP86/TZP	BP86/ATZP from Ref. 44
ΔE_{H1}	1.66	1.63	1.67	1.78	2.10
ΔE_{H2}	1.89	1.92	1.90	1.92	0.28
ΔE_{H3}	2.07	2.07	2.09	1.83	2.79
ΔE_{H4}	0.96	0.94	0.26	0.49	0.96
ΔE_{O2}	-0.63	-0.59	-0.05	-0.13	4.55
ΔE_{W1}	-0.55	-0.55	-0.48	-0.57	-1.26
ΔE_{W2}	-0.44	-0.46	-0.43	-0.34	-4.47

Except for the fourth dehydrogenation and the oxygen removal process, the reaction energies (Table 3.1) are essentially the same for all three linear dependency cutoff values. With the cutoff value of $5x10^{-5}$, the fourth dehydrogenation is calculated to be around 0.7 eV lower and oxygen removal is around 0.6 eV higher than with the other two cutoff energies. Because the $5x10^{-5}$ cutoff eliminates the fewest orbitals, this value is expected to provide the most accurate results. Upon lowering the cutoff value, the bridged -O-O- is found to detach from one manganese atom in the fourth dehydrogenated product (structure **77** in Figure 3.1 and Figure 3.2). All geometries are also optimized with the BP86/TZP level of theory; no linear dependency cutoff is needed for this level of theory. Again, noticeable differences in reaction energies are observed for the fourth dehydrogenation and for the oxygen removal process. These reaction energy values are moderately close to the BP86/ATZP values calculated with the $5x10^{-5}$ cutoff value, with four of the seven reaction energies differing by less than 0.1 eV.

Notable geometric changes are seen for the intermediate states with bridged -O-OH- and -O-O- groups that correspond to the fourth dehydrogenation and the oxygen removal products (structures **76** and **77** in Figure 3.2) depending on the level of theory employed. These groups bond to only one manganese atom and no longer appear as bridging groups with BP86/ATZP with tightened numerical cutoff values. For the $1x10^{-3}$ cutoff value, the other Mn-O distance is 2.11 Å and for the $1x10^{-4}$ and $5x10^{-5}$ values the Mn-O distance lengthens to 2.31 Å and 3.72 Å, respectively. The distance between the other Mn atom and the oxygen atom is further increased with the BP86/TZP level of theory to 3.81 Å.

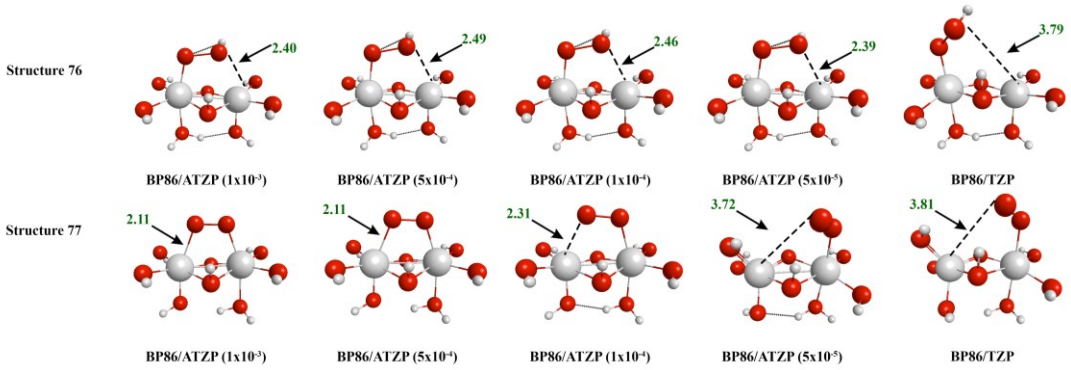

Figure 3.2 Structures **76** and **77** of Figure 3.1 optimized with BP86/ATZP with different numerical cutoff values. The BP86/TZP values are also given for comparison. Bond lengths are given in Å (black dotted line or white/red line).

The relative energy values obtained with a tighter energy convergence are significantly different from those reported in Ref. 44. The highest energy endothermic oxygen release (originally 4.55 eV) is now predicted to be exothermic with an energy of -0.05 eV and the highest energy exothermic second water addition (originally -4.47 eV) is now predicted to be exothermic with an energy of -0.43 eV with the BP86/ATZP level of theory. The relative energy values and the geometries obtained with BP86/ATZP using the smallest linear dependence cutoff value are generally similar to those calculated with the BP86/TZP level of theory. Because of this good agreement and due to the computational efficiency of BP86/TZP, we use this level of theory to investigate the additional reaction pathways described in this study. We also investigate other reaction pathways (pathway-4 and pathway-A1) with the PBE/TZP level of theory and the relative energies are given in Table A1 of the Appendix A. There are no noticeable energy differences between these exchange and correlation functionals for the reaction pathways we compared.

Starting with a slightly different, lower energy isomer (structure **1** in Figure 3.3) as the resting state of the catalyst, we reinvestigate the water oxidation reaction on the fully saturated Mn_2O_4 complex (pathway-1 given in Figure 3.4). Compared to structure **73**, structure **1** is -0.12

eV lower in energy calculated with BP86/ATZP with a $5x10^{-5}$ cutoff value and it is also -0.12 eV lower in energy with the BP86/TZP level of theory.

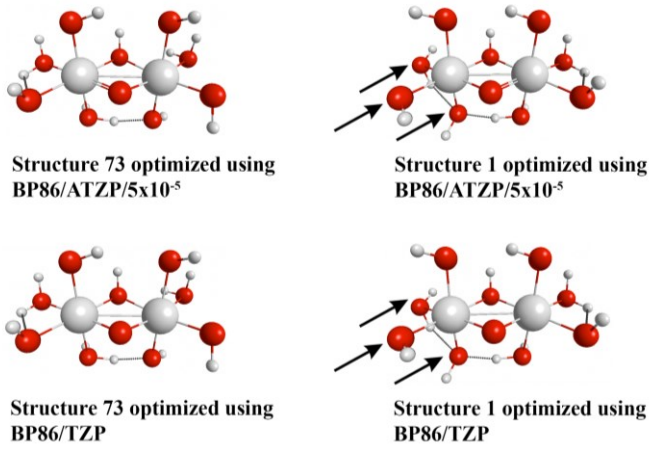

Figure 3.3 Fully saturated Mn_2O_4 complex optimized using different level of theories. The structures on the right are almost mirror images of the structures on the left; arrows indicate ligand orientations that differ from the left side images.

The lowest energy fully saturated $Mn_2O_4•6H_2O$ complex **1** has different hydrogen atom orientations compared to structure **73** with both the BP86/ATZP/$5x10^{-5}$ cutoff value and BP86/TZP levels of theory. Structures **73** and **1** are almost mirror images except for a few rotations of aqua and hydroxo groups which are marked with arrows in Figure 3.3. In general, the formal oxidation states of the two manganese atoms in the $Mn_2O_4•6H_2O$ complex are III½ and IV½ for both structures.

The first step in the new reaction pathway is a geminal dehydrogenation from a hydroxo ligand in structure **1**. This step has a reaction energy of 1.77 eV. It is noteworthy that the removal of hydrogen from the bridging hydroxo group on structure **1** results in structural distortions where aqua ligands attached to manganese detach and bond to the cluster via hydrogen bonding to hydroxo ligands. In some cases, these distortions lower the energies of the structures quite

remarkably. Because these water molecules are not attached to the manganese atoms, we do not consider these structures further. All ligands interact with the manganese atoms in structure **2**.

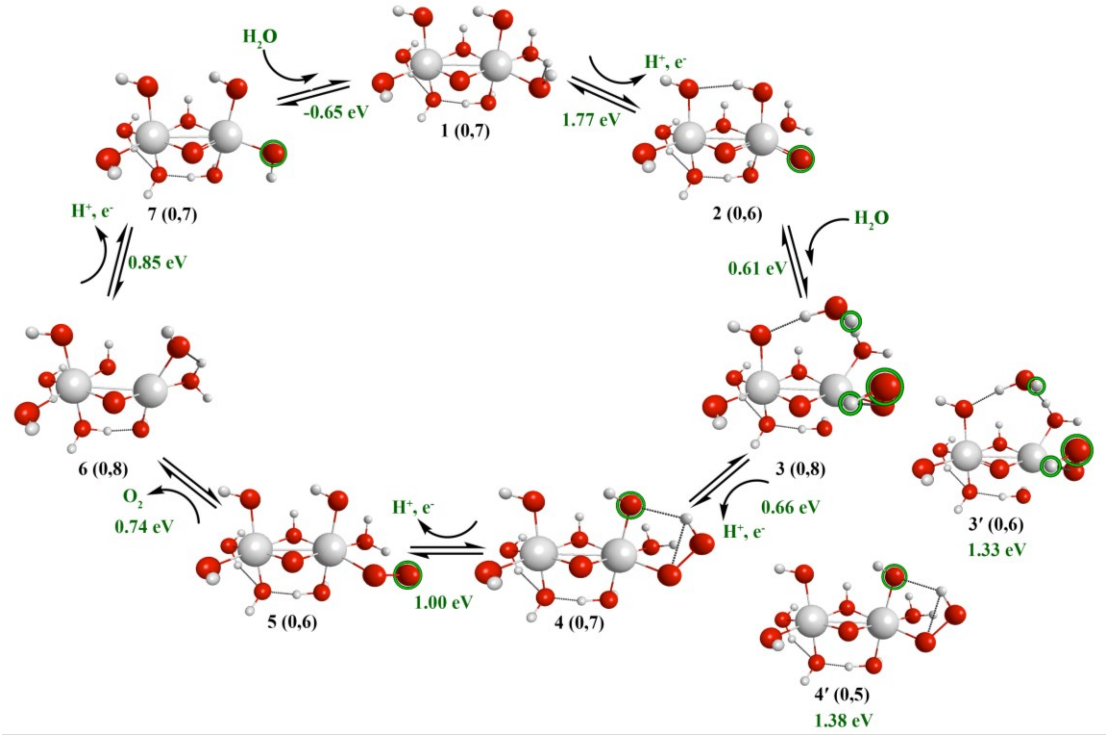

Figure 3.4 The lowest energy reaction pathway-1 calculated using the BP86/TZP level of theory for the fully saturated Mn_2O_4•$6H_2O$ structure **1**.

The spin multiplicity changes from a septet in structure **1** to a sextet in structure **2**. The resulting structure **2** has a terminal oxo species. This Mn(IV½)O is an active species that can undergo nucleophilic attack from nearby solvent water molecules. This process is endothermic by 0.61 eV and generates structure **3** with an octet spin state. The sextet spin state of the structure **3** (denoted **3'**) has the same geometry but is thermodynamically higher in energy to generate (it lies 0.72 eV higher in energy than the octet state). Structure **3** has two water molecules with elongated bonds with their lone pair electrons pointing towards the manganese atom. The lowest energy second dehydrogenation process takes place from one of the water molecules on the top (surface) site with an elongated bond to manganese. This dehydrogenation from the system is

endothermic by 0.66 eV and produces structure **4**. A consecutive third dehydrogenation occurs at the HO-O- group and requires 1.00 eV of energy. This generates sextet structure **5** with an -O-O group. Oxygen is then removed endothermically to generate structure **6** with an octet spin state. The oxygen removal process costs 0.74 eV of energy. Hydrogen is removed from a geminal aqua ligand on structure **6** to form structure **7**, requiring 0.85 eV of energy. A solvent water molecule coordinates to the vacant site on structure **7** left by oxygen removal, exothermically (-0.65 eV) regenerating the resting state of the catalyst. The highest positive energy step in this reaction pathway is the first dehydrogenation step forming the Mn(IV½)O species. All the intermediate steps except for the catalyst regeneration process (from **7** to **1**) possess endothermic reaction energies. The O-O bond is seen to form at an early stage on one manganese atom. The calculated free energy values for pathway-1 are given in Table 3.2. There were no significant differences between ΔE and ΔG energy values. However, we noticed a decrease in magnitudes of the ΔG values for the reactions compared to the ΔE values except for $\Delta E_{(3\text{-}2)}$ and $\Delta E_{(3'\text{-}2)}$.

Due to some of the highly endothermic chemical reaction steps present in pathway-1, we investigate additional reaction pathways on the $Mn_2O_4 \bullet 6H_2O$ complex. In a favorable reaction pathway we would expect the chemical steps in the reactions to be nearly thermoneutral. In addition, if the chemical steps are too exothermic then this extra energy must be balanced by more highly endothermic dehydrogenations. The second lowest reaction pathway-2 for the water oxidation process is given in Figure 3.5.

Table 3.2 Calculated reaction energies and free energies for pathway-1 of Figure 3.4.

Reaction Processes (Pathway-1, Figure 3.4)	ΔE (eV)	ΔG (eV)
$\Delta E_{(2\text{-}1)}$	1.77	1.65
$\Delta E_{(3\text{-}2)}$	0.61	0.69
$\Delta E_{(3'\text{-}2)}$	1.33	1.37
$\Delta E_{(4\text{-}3)}$	0.66	0.52
$\Delta E_{(4'\text{-}3)}$	1.38	1.23
$\Delta E_{(5\text{-}4)}$	1.00	0.85
$\Delta E_{(6\text{-}5)}$	0.74	0.67
$\Delta E_{(7\text{-}6)}$	0.85	0.72
$\Delta E_{(1\text{-}7)}$	-0.65	-0.55

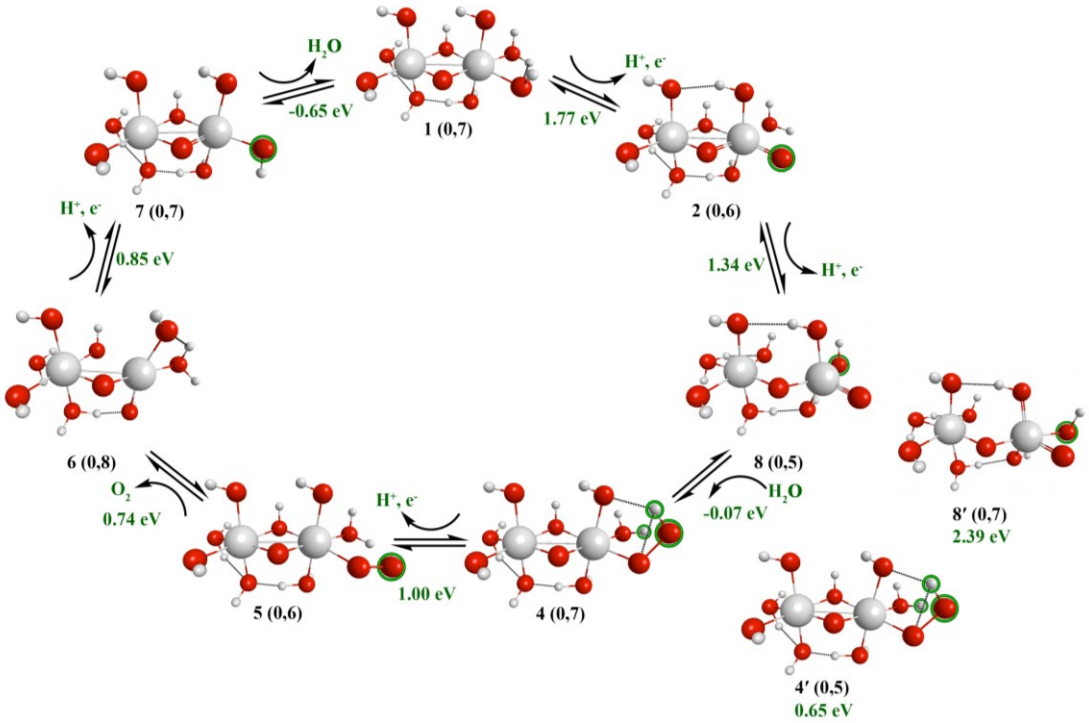

Figure 3.5 The second lowest energy reaction pathway-2 on the fully saturated Mn_2O_4•$6H_2O$ structure **1** calculated using the BP86/TZP level of theory.

After the first dehydrogenation, we again see it forms structure **2** with a terminal oxo group. Consequently, the second dehydrogenation takes place at an aqua ligand adjacent to the oxo group with an endothermic reaction energy of 1.34 eV (ΔG = 1.20 eV). Dehydrogenation reactions on the surface hydroxo groups are around 0.2 eV higher in energy than the aqua ligand dehydrogenation reaction. Dehydrogenation of the hydrogen on the bridging hydroxo group again results in structural distortions similar to dehydrogenation of the bridging hydroxo on structure **1**. The generated structure **8** with quintet spin multiplicity has a Mn(VI)=O oxo group. The septet state of structure **8** (given as **8'** in Figure 3.5**)** is calculated to be 1.05 eV (1.03 eV of free energy difference) higher in energy than the quintet state. This dehydrogenation occurs with an intramolecular hydrogen atom transfer from the bottom aqua ligand to the bottom hydroxo ligand. The higher oxidation state in this manganese atom leads to opening of the μ-hydroxo bond on structures **8** and **8'**. We also calculated an alternative reaction involving oxo attack to the surface hydroxo group on structure **2**. This attack is 0.47 eV higher in energy than the dehydrogenation of the aqua ligand geminal to the oxo group. The attack to the surface hydroxo group on structure **8** has an endothermic energy of 0.57 eV. A reaction pathway that follows through this intermediate is given in the Appendix A (Figure A1).

In the next step, structure **8** undergoes a nucleophilic attack from a solvent water molecule to the oxo group to generate structure **4** (which is the same structure in pathway-1). This reaction is exothermic with an energy of -0.07 eV (ΔG = 0.01 eV). The geminal hydroxo group abstracts one hydrogen atom of the water molecule. The spin multiplicity would need to change from quintet in structure **8** to a septet state in structure **4**. A spin allowed quintet to quintet transition is calculated to require 0.65 eV (ΔG = 0.72 eV). The quintet state of structure **4** is given as **4'** in Figure 3.4. After the formation of structure **4**, reaction pathway-2 reconnects

back to pathway-1, where it goes through intermediate states **5**, **6**, and **7** and regenerates structure **1**. In this reaction pathway-2, both water addition reactions have exothermic reaction energies. However, oxygen evolution is endothermic by 0.74 eV in both pathways. In comparison to pathway-1, pathway-2 is more likely to occur because its water addition steps are exothermic. Also comparing pathway-1 and pathway-2, we can see that the formation of the radical moiety in structure **2** is a significant step in the reaction mechanism. Generation of the radical moiety represents the highest endothermic energy of both of these reaction pathways, which ultimately determines the oxidation potential and feasibility of the catalyst for the water oxidation process.

3.4.2 The saturation process of Mn_2O_3

The two manganese atoms in the lowest energy isomer of Mn_2O_3 (structure **9**, shown in Figure 3.6) are joined by two μ-oxo groups. This structure has formal oxidation states of Mn(IV)-Mn(II). Structure **9′**, which is a Mn_2O_3 isomer with formal oxidation states of Mn(III)-Mn(III), contains three μ-oxo groups. However, structure **9′** is calculated to be 0.93 eV (ΔG = 0.92 eV) higher in energy than the lowest energy Mn(IV)-Mn(II) isomer **9**.

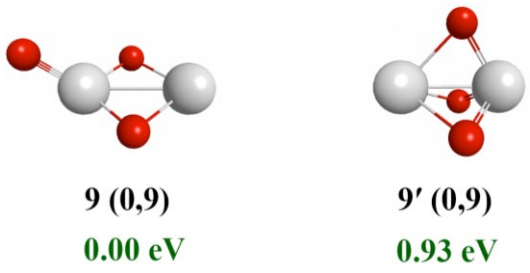

Figure 3.6 Isomers of Mn_2O_3 using the BP86/TZP level of theory.

We investigated water adsorption and dissociation processes on the Mn_2O_3 cluster **9** (Figure 3.7). The nonet spin multiplicity of this cluster is kept constant throughout the saturation process. This cluster can adsorb up to seven water molecules to generate a fully saturated

Mn_2O_3•$7H_2O$ complex. The first water molecule adsorption on the Mn_2O_3 system is exothermic with an energy of -0.86 eV (ΔG = 0.80 eV). This water molecule coordinates with a vacant site on the Mn(II) atom in the plane of the manganese atoms and μ-oxo bridges (structure **10**). One hydrogen atom of water is abstracted by the μ-oxo group and forms a μ-hydroxo bridge (structure **11**). The reaction energy of this dissociation is -0.67 eV (ΔG = -0.70 eV). The total process of adsorption and dissociation of the first water (ΔE_{W1}) is exothermic with an energy of -1.53 eV (ΔG_{W1} = 1.50 eV).

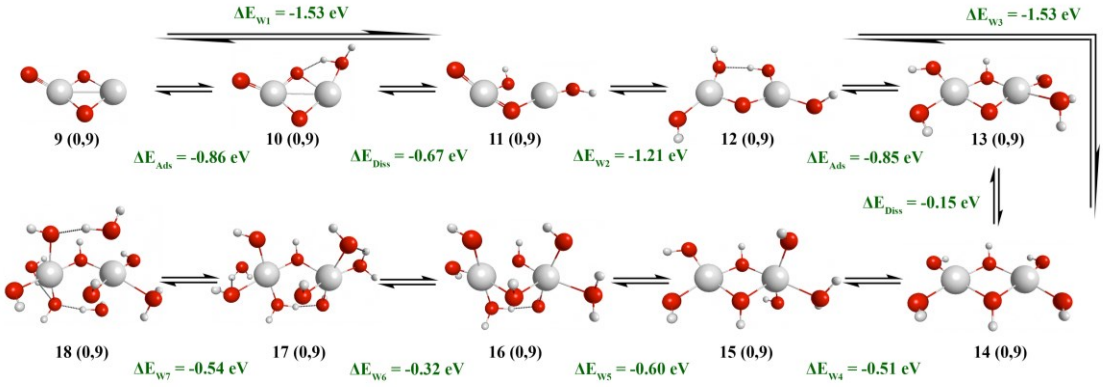

Figure 3.7 Water adsorption and dissociation processes on the Mn_2O_3 complex. Relative energies are given in eV.

The second water molecule coordinates with a vacant site on the Mn(IV) atom. The oxo group on this manganese readily abstracts hydrogen from the incoming water molecule while the μ-hydroxo group transfers to the other manganese atom and forms structure **12**. The two manganese atoms are now bound together by one μ-oxo group and have formal oxidation states of Mn(III). This W2 process is less exothermic than the W1 process, with an overall reaction energy of -1.21 eV (ΔG = 1.18 eV). The adsorption of a third water molecule to structure **12** reforms the μ-hydroxo bridge in structure **13**. The third water molecule dissociates, forming structure **14** with four hydroxo groups and two μ-hydroxo groups. Structure **14** has a C_2 axis

along the manganese atoms. The fourth water addition W4 process is higher in energy than the W3 process. This may be due to the loss of symmetry compared to structure **14** and the incomplete octahedral environment that results instead of the square planar environments in **14**. The addition of the fourth water molecule leads to a rotation of two of the planar hydroxo ligands by 90^0 in structure **15** to accommodate an equatorial coordination. Hydrogen atoms of the bridging hydroxo groups in structure **15**, in which one hydrogen atom is above the plane and the other is below the plane, orient in the same direction (above the plane) in structure **16** with the adsorption of the fifth water molecule (W5). Adsorption of a sixth water molecule forms structure **17**, which was a structure observed during the third lowest energy pathway (pathway-A1 in Figure A1 of Appendix A) for water oxidation from $Mn_2O_4{\cdot}6H_2O$ complex. This structure still has formal oxidation numbers of Mn(III)-Mn(III). A seventh and final water addition forms the fully saturated Mn_2O_3 structure **18**. Both of the manganese atoms in this structure have a distorted octahedral geometry. The fourth, fifth, sixth and seventh water addition reaction have exothermic reaction energy values of -0.51 eV, -0.60 eV, -0.32 eV and -0.54 eV respectively. Their respective free energy values are exoergic by -0.44 eV, -0.51 eV, -0.25 eV and -0.46 eV. The formal oxidation states change to Mn(IV)-Mn(II). In this work, we employ structures **17** and **18** with six and seven water molecules adsorbed, respectively, to investigate the water oxidation process.

3.4.3 The water oxidation process with the six water saturated Mn_2O_3

There are two possible reaction pathways for the oxygen evolution from structure **17** (Mn(III)-Mn(III)). The importance of investigating the water oxidation process from the not quite fully saturated $Mn_2(\mu\text{-}OH)_2(H_2O)_3(OH)_4$ ($Mn_2O_3{\bullet}6H_2O$) complex is that the lowest energy water oxidation pathway for this complex is present in the third lowest water oxidation pathway-

S1 for the Mn_2O_4•$6H_2O$ complex (Figure A1). In this case, the resting state of the catalyst is structure **17**. Starting with structure **17**, two dehydrogenations and one water addition occur to generate structure **1** with a fully saturated Mn_2O_4 complex. From structure **1**, the two remaining dehydrogenation reactions occur consecutively. After two chemical steps followed by the second water addition, oxygen is removed to regenerate the resting state of the catalyst (structure **17**). The water oxidation process with Mn_2O_3•$6H_2O$ initiates with dehydrogenation of a geminal aqua ligand followed by a consecutive dehydrogenation of bridging hydroxo group. In comparison, we have discussed above that the Mn_2O_4•$6H_2O$ water oxidation process initiates with dehydrogenation of a geminal hydroxo group followed by a consecutive dehydrogenation of a geminal aqua ligand.

The second lowest energy pathway on the Mn_2O_3•$6H_2O$ complex is given in Figure A2 of the Appendix A. The reactions leading from structure **17** to structure **2** are the same as in the lowest energy pathway. We have observed various fates of the oxo group of structure **2**: in pathway-1 it undergoes direct nucleophilic attack from the solvent water molecule and in pathway-2 it undergoes dehydrogenation of the aqua ligand geminal to the oxo group which then experiences a nucleophilic attack from the solvent water molecule to this same oxo group in structure **8**. The other probable fate of the oxo group in structure **8** is to attack the surface hydroxo group which then proceeds to react via an intramolecular hydrogen atom transfer from the hydrogen of the generated -OOH group to the bridged oxo group as seen in pathway-A1. In pathway-A2, we investigated the direct attack of the oxo group of structure **8** to the bottom hydroxo group which proceeds after an intramolecular hydrogen atom transfer from the bottom aqua ligand on manganese with the oxo group to the adjacent bottom hydroxo group. We

included both of these reaction pathways (pathway-A1 and -A2) in the Appendix A (Figure A1 and A2).

3.4.4 The water oxidation process with the fully saturated Mn_2O_3

The water oxidation reaction pathway-3 (Figure 3.8) from the fully saturated $Mn_2(\mu\text{-}OH)_2(H_2O)_4(OH)_4$ structure **18** ($Mn_2O_3 \bullet 7H_2O$) with seven waters adsorbed with formal oxidation states of Mn(IV)-Mn(II) has interesting characteristics compared to the fully saturated Mn_2O_4 compound. Similar to the lowest energy reaction pathway on the fully saturated Mn_2O_4 complex, the fully saturated Mn_2O_3 complex also involves a nucleophilic attack from a solvent water molecule.

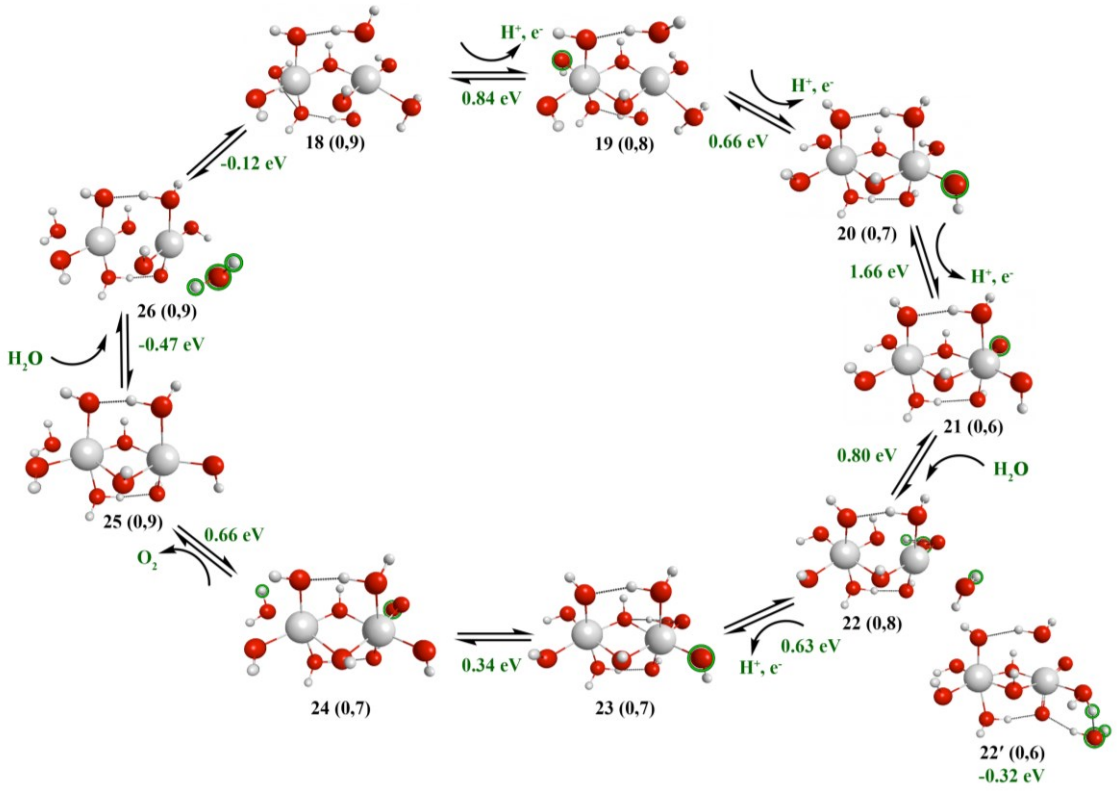

Figure 3.8 The lowest energy water oxidation pathway-3 on the fully saturated $Mn_2O_3 \bullet 7H_2O$ structure **18**.

The first dehydrogenation from the resting state of the catalyst proceeds with a dehydrogenation of a geminal aqua ligand of structure **18**, which is a process similar to that of

pathway-2 but from a different aqua ligand. This has reaction energy of 0.84 eV and leads to structure **19** with an octet multiplicity. The second dehydrogenation takes place on the aqua ligand of the other manganese atom, which leads to septet structure **20**. The second dehydrogenation has a reaction energy of 0.66 eV. Similar to pathway-1 and pathway-2, we observe that early dehydrogenations from any of the bridging hydroxo groups resulted in structural distortions to structure **18**. However, the initial steps are somewhat different for these systems. The water oxidation process with Mn_2O_3•$6H_2O$ initiates with a dehydrogenation from a geminal aqua ligand followed by a second dehydrogenation from a bridging hydroxo group, whereas the water oxidation process from the Mn_2O_4•$6H_2O$ complex initiates with a dehydrogenation of a geminal hydroxo group followed by a nucleophilic attack of solvent water molecule.

In pathway-3, the Mn(V)O moiety is formed on structure **21** after the third dehydrogenation process. This dehydrogenation step is the highest energy step, requiring 1.66 eV, in pathway-3. In the lowest energy reaction pathway-3, this oxo group undergoes a nucleophilic attack from a solvent water molecule requiring 0.80 eV of reaction energy to form structure **22** with an octet spin state. The sextet state of structure **22** (structure **22′** in Figure 3.8) is lower in energy but has water molecules that are bonded to the cluster via hydrogen bonds rather than through a donation of lone pair electrons to a manganese atom; this cluster will not be considered further. In comparison, the attack of the oxo group to the geminal hydroxo group is calculated to have a large chemical reaction step energy of 1.62 eV, whereas a fourth dehydrogenation process requires 1.53 eV (the second lowest energy pathway-4 proceeds via the fourth dehydrogenation process which will be discussed below). During the nucleophilic attack,

the oxo group forms a bond with the oxygen of the water molecule and one hydrogen atom of the water molecule dissociates to bond with the geminal hydroxo group on structure **21**.

The next step would involve a dehydrogenation that occurs at a geminal aqua ligand on the manganese atom with the -O-OH moiety, which occurs with a reaction energy of 0.63 eV to form structure **23**. In the lowest energy nucleophilic attack pathway-1 on the Mn_2O_4•$6H_2O$ complex, we observe that the third dehydrogenation occurs at the -O-OH group, which creates a -O-O group that can be removed as an oxygen molecule in the next step. In contrast, in pathway-3 at this stage, four hydrogen atoms have been removed from the system, yet it still possesses a hydrogen atom on the -O-O group. Dehydrogenation from the -O-OH group is 0.38 eV higher in energy than the geminal dehydrogenation. However, in order to remove oxygen it is necessary to form structure **24** that has an -O-O group. This chemical step may occur through a hydrogen atom transfer between solvent water molecules or an intramolecular hydrogen atom transfer reaction. This rearrangement is endothermic by 0.34 eV. From structure **24**, oxygen can be evolved with a reaction energy of 0.66 eV to form nonet structure **25**. This complex easily coordinates with a solvent water molecule to fill the vacant site left by the oxygen molecule. The reaction for this coordination is exothermic with an energy of -0.47 eV. If these processes occur in a concerted manner, the overall reaction energy for water addition and oxygen removal is 0.19 eV. The generated structure **26** is an isomer of the resting state of the catalyst. The catalyst can be regenerated via an intramolecular hydrogen atom transfer from an aqua ligand to a hydroxo group on the bottom followed by rotation of several hydroxo and aqua ligands. This regeneration process is also an exothermic process by -0.12 eV. The highest energy step in this reaction pathway is the third dehydrogenation process, which requires 1.66 eV. Note that this step also corresponds to the formation of the oxo group. All the intermediate states except for the second

water addition and the catalyst regeneration steps have endothermic reaction energies. The -O-O bond is formed at a later stage of the reaction pathway on one manganese atom as we have seen in the above reaction pathways. Calculated free energy values are typically lower in magnitude than the respective ΔE values (Table 3.3) except for the $\Delta E_{(22\text{-}21)}$ step where we see 0.04 eV increase.

Table 3.3 Calculated reaction energies and free energies for pathway-3 of Figure 3.8.

Reaction Processes (Pathway-3, Figure 3.8)	**ΔE (eV)**	**ΔG (eV)**
$\mathbf{\Delta E_{(19\text{-}18)}}$	0.84	0.70
$\mathbf{\Delta E_{(20\text{-}19)}}$	0.66	0.57
$\mathbf{\Delta E_{(21\text{-}20)}}$	1.66	1.54
$\mathbf{\Delta E_{(22\text{-}21)}}$	0.80	0.84
$\mathbf{\Delta E_{(22'\text{-}21)}}$	-0.32	-0.24
$\mathbf{\Delta E_{(23\text{-}22)}}$	0.63	0.53
$\mathbf{\Delta E_{(24\text{-}23)}}$	0.34	0.29
$\mathbf{\Delta E_{(25\text{-}24)}}$	0.66	0.59
$\mathbf{\Delta E_{(26\text{-}25)}}$	-0.47	-0.40
$\mathbf{\Delta E_{(18\text{-}26)}}$	-0.12	-0.10

We also investigate a second lowest reaction pathway-4 for the water oxidation process. The second lowest energy pathway starts at structure **18** and proceeds to structures **19**, **20**, and **21** similar to pathway-3. From structure **21**, the next step that could occur is the fourth dehydrogenation process. Although this step is higher in energy than the water addition step from **21** to **22**, it has the advantage that it is an electrochemical step that can be attenuated by application of an external potential. The fourth dehydrogenation takes place at the hydroxo group

adjacent to the Mn-O group. The two oxo groups in structure **27** attack each other to make an O-O group on one manganese atom in structure **28** with a reaction energy of 0.13 eV.

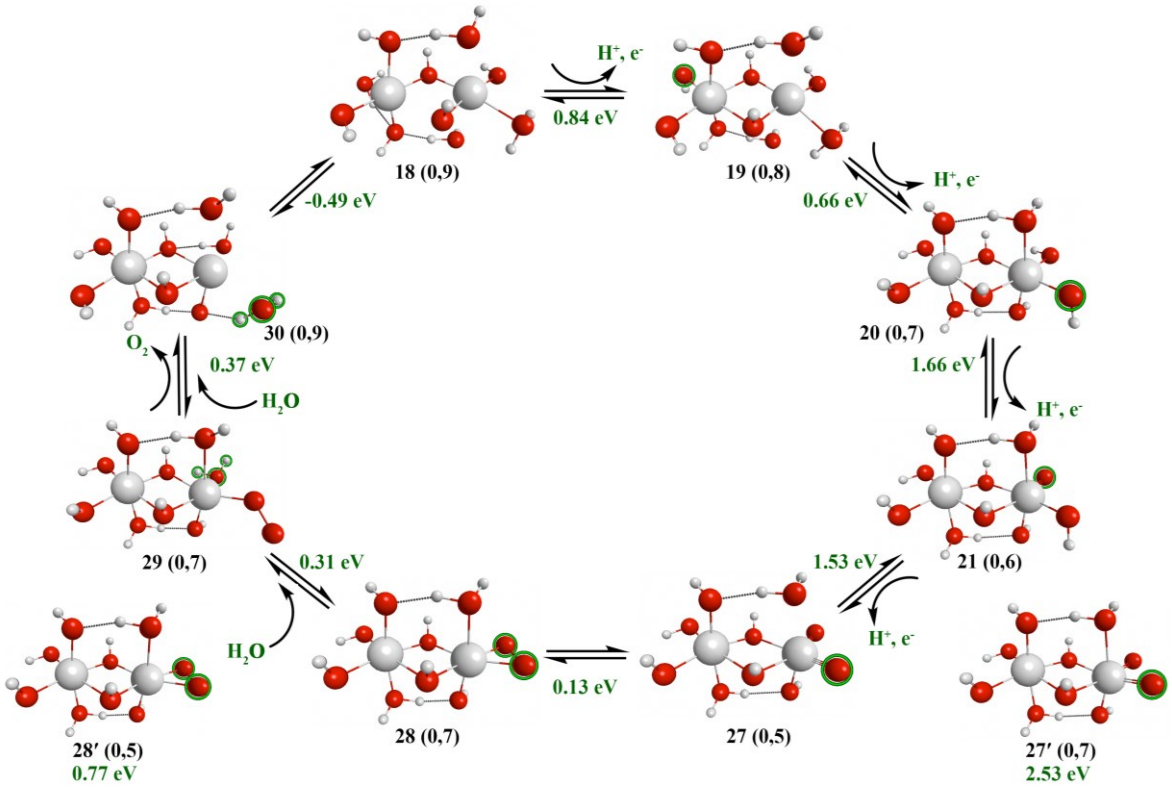

Figure 3.9 The second lowest energy water oxidation pathway-4 on the fully saturated $Mn_2O_3 \bullet 7H_2O$ structure **18**.

The manganese atom with two activated oxo groups in structure **27** has a Mn(VI) formal oxidation state. The lowest energy spin multiplicity changes from quintet in structure **27** to a septet in structure **28**, which would be a spin-forbidden process. The septet state of structure **27 (**structure **27'** in Figure 3.9) is 1.00 eV higher in energy than the quintet state and the quintet state of the structure **28 (**structure **28'** in Figure 3.9) is 0.64 eV higher in energy than the respective septet state.

In the next step, the first water addition results in the breaking of one Mn-O bond. This generates structure **29**, where O-O is bound to one manganese atom with one Mn-O bond. The

vacant site left from this bond breaking is now occupied by the incoming water ligand. The multiplicity does not change in going from structure **28** to **29**. This water addition reaction is endothermic by 0.31 eV. The oxygen molecule is released from structure **29** with the adsorption of the second water molecule, yielding nonet structure **30**. The second water molecule coordinates to the vacant site left by the oxygen. Structure **30** then rearranges back to the resting state of the catalyst with an energy of -0.49 eV. Similar to structure **24** in the lowest energy pathway, structure **30** also requires a hydrogen atom transfer reaction for regeneration of the catalyst that would occur either intramolecularly or via solvent water molecules. All of the intermediate states in the reaction pathway have endothermic reaction energies except for the final catalyst regeneration step. In pathway-4, the highest positive energy step is the third dehydrogenation step (1.66 eV) and the lowest positive energy step is the coupling of the two oxo groups (0.13 eV). The O-O bond is formed after all four dehydrogenation steps have occurred. Similar to previous reaction pathways, the O-O is seen to form on one manganese atom in a μ_2 fashion with two Mn-O bonds. The water oxidation process on the Mn_2O_3•$7H_2O$ complex initiates with a slightly higher dehydrogenation energy of 0.84 eV compared to 0.73 eV on the Mn_2O_3•$6H_2O$ complex. The calculated free energies are given in Table 3.4. In general, the magnitudes of the ΔG values for the reactions are somewhat lower than the ΔE values, with the exception of $\Delta E_{(30\text{-}29)}$.

Table 3.4 Calculated reaction energies and free energies for pathway-4 of Figure 3.9.

Reaction Processes (Pathway-4, Figure 3.9)	ΔE (eV)	ΔG (eV)
$\Delta E_{(19\text{-}18)}$	0.84	0.70
$\Delta E_{(20\text{-}19)}$	0.66	0.57
$\Delta E_{(21\text{-}20)}$	1.66	1.54
$\Delta E_{(27\text{-}21)}$	1.53	1.40
$\Delta E_{(27'\text{-}21)}$	2.53	2.38
$\Delta E_{(28\text{-}27)}$	0.13	0.10
$\Delta E_{(28'\text{-}27)}$	0.77	0.74
$\Delta E_{(29\text{-}28)}$	0.31	0.30
$\Delta E_{(30\text{-}29)}$	0.37	0.42
$\Delta E_{(18\text{-}30)}$	-0.49	-0.47

3.5 General Discussion

In general, Mn_2O_4 and Mn_2O_3 clusters can adsorb up to six or seven water molecules to form $Mn_2(\mu\text{-}OH)(\mu\text{-}O)(H_2O)_3(OH)_5$ and $Mn_2(\mu\text{-}OH)_2(H_2O)_4(OH)_4$ complexes, respectively. The water oxidation process on $Mn_2O_4{\bullet}6H_2O$ proceeds via a nucleophilic attack from a solvent water molecule to the Mn(IV½)O group. The lowest energy pathway on the $Mn_2O_3{\bullet}6H_2O$ complex is embedded in the third lowest energy pathway from the $Mn_2O_4{\bullet}6H_2O$ complex, where it proceeds through an attack of the activated Mn(VI)O geminal oxo group to a surface hydroxo group.

The water oxidation process on the fully saturated $Mn_2O_3{\bullet}7H_2O$ complex initiates with only 0.11 eV higher reaction energy (ΔG = 0.11 eV) compared to that of water oxidation on $Mn_2O_3{\bullet}6H_2O$. This lowest energy pathway involves nucleophilic attack of a solvent water molecule to the Mn(V)O group. The highest positive energy steps with six and seven water

molecules on Mn_2O_3 complexes are 1.77 eV and 1.66 eV, respectively (free energy values are 1.65 eV and 1.54 eV respectively).

There were no similar patterns observed with the reaction initiation processes. In pathway-1 for the water oxidation process with Mn_2O_4•$6H_2O$, the reaction initiates with the dehydrogenation of a geminal hydroxo group followed by a nucleophilic attack of a solvent water molecule to the Mn(IV½)O group, whereas for the Mn_2O_3•$6H_2O$ complex, the water oxidation initiates with dehydrogenation of a geminal aqua and proceeds via an attack of Mn(VI)O group to the surface hydroxo group. In reaction pathway-3 for the Mn_2O_3•$7H_2O$ complex, the reaction initiates with a geminal aqua dehydrogenation followed by two consecutive geminal dehydrogenations of an aqua ligand and a hydroxo group on the other manganese atom. After the third dehydrogenation, the complex undergoes a nucleophilic attack from a solvent water molecule to the Mn(V)O group.

In all the reaction pathways we studied, the O-O bond is formed on one manganese atom with only a single Mn-O bond during nucleophilic attack pathways, whereas a μ_2 bond is formed in other pathways. Formation of the oxo group is an essential step in all reaction pathways where it is activated once reaching at least a formal oxidation state of Mn(IV½). Once they are generated they tend to undergo nucleophilic attack from solvent water molecules or readily couple with nearby hydroxo and oxo groups. We also found that formation of this oxo group is the highest energy step in all the pathways we studied here. This suggests the possible use of this step as a descriptor for selecting a water splitting catalyst with manganese frameworks. However, additional testing with other manganese systems is warranted.

3.6 Conclusions

In this study we revisited the water oxidation process on the fully saturated Mn_2O_4•$6H_2O$ ($Mn_2(\mu\text{-}OH)(\mu\text{-}O)(H_2O)_3(OH)_5$) complex and investigated the saturation and water oxidation processes on Mn_2O_3. Using the six and seven water saturated Mn_2O_3•$6H_2O$ ($Mn_2(\mu\text{-}OH)_2(H_2O)_3(OH)_4$) and Mn_2O_3•$7H_2O$ ($Mn_2(\mu\text{-}OH)_2(H_2O)_4(OH)_4$) complexes, we investigated the thermodynamics of the water oxidation process. The relative energy values and the geometries obtained with BP86/ATZP using the smallest linear dependence cutoff value of $5x10^{-5}$ are generally similar to those calculated with the BP86/TZP level of theory. Because of this good agreement and due to its computational efficiency, we used the BP86/TZP level of theory to investigate the reaction pathways described in this study. The lowest energy pathway on the Mn_2O_4•$6H_2O$ complex occurs through a nucleophilic attack from a solvent water molecule to a Mn(IV½)O group. This reaction initiates with a 1.77 eV (ΔG = 1.65 eV) dehydrogenation. The highest thermodynamic barrier for this pathway is 1.77 eV (ΔG = 1.65 eV), which is the same as that of the Mn_2O_3•$6H_2O$ complex. In comparison, the lowest energy pathway on the Mn_2O_3•$7H_2O$ complex proceeds with a nucleophilic attack of a solvent water molecule to a Mn(V)O group whereas the lowest energy pathway starting on Mn_2O_3•$6H_2O$ occurs via an attack of Mn(VI)O to the surface hydroxo group. The lowest energy water oxidation pathway on the fully saturated Mn_2O_3•$7H_2O$ complex initiates with a dehydrogenation with a 0.84 eV (ΔG = 0.70 eV) reaction energy that is only 0.11 eV (ΔG = 0.11 eV) higher than on Mn_2O_3•$6H_2O$. Based on the reaction pathways studied here, we observed that the first and second lowest energy pathways consist of endothermic chemical steps of up to 0.80 eV in energy which render these catalysts unlikely to act as regenerative catalysts in their simplest form. It is notable that catalytic cycles on the seven and six water saturated complexes exhibit nearly similar thermodynamic

barriers for dehydrogenation (ΔE and ΔG values are 1.66 eV, 1.77 eV and 1.54 eV, 1.65 eV respectively). The formation of an oxo group is an essential step in all these pathways as it corresponds to the highest thermodynamic step; this suggests that the energy of this step can be used as a descriptor for the selection of catalysts and may provide a helpful tool for future catalyst design.

3.7 Acknowledgements

This material is based on work supported by the National Science Foundation under Grant No. CHE-0955515. C.M.A. is grateful to the Camille and Henry Dreyfus Foundation for a Camille Dreyfus Teacher-Scholar Award (2011-2016). The computing for this project was performed on the Beocat Research Cluster at Kansas State University, which is funded in part by NSF grants CNS-1006860, EPS-1006860, and EPS-0919443.

3.8 References

1. Umena, Y.; Kawakami, K.; Shen, J.-R.; Kamiya, N. Crystal Structure of Oxygen-Evolving Photosystem II at a Resolution of 1.9 Å. *Nature* **2011,** *473*, 55-60.

2. Pokhrel, R.; Brudvig, G. W. Oxygen-Evolving Complex of Photosystem II: Correlating Structure with Spectroscopy. *Phys. Chem. Chem. Phys.* **2014,** *16*, 11812-11821.

3. Hirahara, M.; Shoji, A.; Yagi, M. Artificial Manganese Center Models for Photosynthetic Oxygen Evolution in Photosystem II. *Eur. J. Inorg. Chem.* **2014,** *2014*, 595-606.

4. Yamaguchi, K.; Yamanaka, S.; Isobe, H.; Saito, T.; Kanda, K.; Umena, Y.; Kawakami, K.; Shen, J. R.; Kamiya, N.; Okumura, M.; Nakamura, H.; Shoji, M.; Yoshioka, Y. The Nature of Chemical Bonds of the $CaMn_4O_5$ Cluster in Oxygen Evolving Complex of Photosystem II: Jahn-Teller Distortion and its Suppression by Ca Doping in Cubane Structures. *Int. J. Quantum Chem.* **2013,** *113*, 453-473.

5. Yamaguchi, K.; Isobe, H.; Yamanaka, S.; Saito, T.; Kanda, K.; Shoji, M.; Umena, Y.; Kawakami, K.; Shen, J. R.; Kamiya, N.; Okumura, M. Full Geometry Optimizations of the Mixed-Valence $CaMn_4O_4X(H_2O)_4$ (X=OH or O) Cluster in OEC of PS II: Degree of Symmetry Breaking of the Labile Mn-X-Mn Bond Revealed by Several Hybrid DFT Calculations. *Int. J. Quantum Chem.* **2013,** *113*, 525-541.

6. Vinyard, D. J.; Ananyev, G. M.; Charles Dismukes, G. Photosystem II: The Reaction Center of Oxygenic Photosynthesis. *Annu. Rev. Biochem.* **2013,** *82*, 577-606.

7. Pal, R.; Negre, C. F. A.; Vogt, L.; Pokhrel, R.; Ertem, M. Z.; Brudvig, G. W.; Batista, V. S. S_0-State Model of the Oxygen-Evolving Complex of Photosystem II. *Biochemistry* **2013,** *52*, 7703-7706.

8. Kurashige, Y.; Chan, G. K.-L.; Yanai, T. Entangled Quantum Electronic Wavefunctions of the Mn_4CaO_5 Cluster in Photosystem II. *Nat Chem* **2013,** *5*, 660-666.

9. Siegbahn, P. E. M. Mechanisms for Proton Release During Water Oxidation in the S_2 to S_3 and S_3 to S_4 Transitions in Photosystem II. *Phys. Chem. Chem. Phys.* **2012,** *14*, 4849-4856.

10. Siegbahn, P. E. M. Recent Theoretical Studies of Water Oxidation in Photosystem II. *J. Photochem. Photobiol., B* **2011,** *104*, 94-99.

11. Siegbahn, P. E. M. The Effect of Backbone Constraints: The Case of Water Oxidation by the Oxygen-Evolving Complex in PSII. *ChemPhysChem* **2011,** *12*, 3274-3280.

12. Luber, S.; Rivalta, I.; Umena, Y.; Kawakami, K.; Shen, J.-R.; Kamiya, N.; Brudvig, G. W.; Batista, V. S. S_1-State Model of the O_2-Evolving Complex of Photosystem II. *Biochemistry* **2011,** *50*, 6308-6311.

13. Sproviero, E. M.; Gascón, J. A.; McEvoy, J. P.; Brudvig, G. W.; Batista, V. S. Computational Studies of the O_2-Evolving Complex of Photosystem II and Biomimetic Oxomanganese Complexes. *Coord. Chem. Rev.* **2008,** *252*, 395-415.

14. Sproviero, E. M.; Gascón, J. A.; McEvoy, J. P.; Brudvig, G. W.; Batista, V. S. Quantum Mechanics/Molecular Mechanics Study of the Catalytic Cycle of Water Splitting in Photosystem II. *J. Am. Chem. Soc.* **2008,** *130*, 3428-3442.

15. Fernando, A.; Weerawardene, K. L. D. M.; Karimova, N. V.; Aikens, C. M. Quantum Mechanical Studies of Large Metal, Metal Oxide, and Metal Chalcogenide Nanoparticles and Clusters. *Chem. Rev.* **2015,** *115*, 6112-6216.

16. Artero, V.; Fontecave, M. Solar Fuels Generation and Molecular Systems: Is It Homogeneous or Heterogeneous Catalysis? *Chem. Soc. Rev.* **2013,** *42*, 2338-2356.

17. Bediako, D. K.; Lassalle-Kaiser, B.; Surendranath, Y.; Yano, J.; Yachandra, V. K.; Nocera, D. G. Structure–Activity Correlations in a Nickel–Borate Oxygen Evolution Catalyst. *J. Am. Chem. Soc.* **2012,** *134*, 6801-6809.

18. Berardi, S.; La Ganga, G.; Natali, M.; Bazzan, I.; Puntoriero, F.; Sartorel, A.; Scandola, F.; Campagna, S.; Bonchio, M. Photocatalytic Water Oxidation: Tuning Light-Induced Electron Transfer by Molecular Co_4O_4 Cores. *J. Am. Chem. Soc.* **2012,** *134*, 11104-11107.

19. Du, P.; Eisenberg, R. Catalysts Made of Earth-Abundant Elements (Co, Ni, Fe) for Water Splitting: Recent Progress and Future Challenges. *Energy Environ. Sci.* **2012,** *5*, 6012-6021.

20. Evangelisti, F.; Güttinger, R.; Moré, R.; Luber, S.; Patzke, G. R. Closer to Photosystem II: A Co_4O_4 Cubane Catalyst with Flexible Ligand Architecture. *J. Am. Chem. Soc.* **2013,** *135*, 18734-18737.

21. Kanan, M. W.; Nocera, D. G. In Situ Formation of an Oxygen-Evolving Catalyst in Neutral Water Containing Phosphate and Co^{2+}. *Science* **2008,** *321*, 1072-1075.

22. Liu, X.; Wang, F. Transition Metal Complexes that Catalyze Oxygen Formation from Water: 1979–2010. *Coord. Chem. Rev.* **2012,** *256*, 1115-1136.

23. McAlpin, J. G.; Stich, T. A.; Casey, W. H.; Britt, R. D. Comparison of Cobalt and Manganese in the Chemistry of Water Oxidation. *Coord. Chem. Rev.* **2012,** *256*, 2445-2452.

24. McCool, N. S.; Robinson, D. M.; Sheats, J. E.; Dismukes, G. C. A Co_4O_4 "Cubane" Water Oxidation Catalyst Inspired by Photosynthesis. *J. Am. Chem. Soc.* **2011,** *133*, 11446-11449.

25. Sartorel, A.; Bonchio, M.; Campagna, S.; Scandola, F. Tetrametallic Molecular Catalysts for Photochemical Water Oxidation. *Chem. Soc. Rev.* **2013,** *42*, 2262-2280.

26. Dau, H.; Limberg, C.; Reier, T.; Risch, M.; Roggan, S.; Strasser, P. The Mechanism of Water Oxidation: From Electrolysis via Homogeneous to Biological Catalysis. *ChemCatChem* **2010,** *2*, 724-761.

27. Duan, L.; Bozoglian, F.; Mandal, S.; Stewart, B.; Privalov, T.; Llobet, A.; Sun, L. A Molecular Ruthenium Catalyst with Water-Oxidation Activity Comparable to that of Photosystem II. *Nat Chem* **2012,** *4*, 418-423.

28. Tilley, S. D.; Cornuz, M.; Sivula, K.; Grätzel, M. Light-Induced Water Splitting with Hematite: Improved Nanostructure and Iridium Oxide Catalysis. *Angew. Chem. Int. Ed.* **2010,** *49*, 6405-6408.

29. Youngblood, W. J.; Lee, S.-H. A.; Kobayashi, Y.; Hernandez-Pagan, E. A.; Hoertz, P. G.; Moore, T. A.; Moore, A. L.; Gust, D.; Mallouk, T. E. Photoassisted Overall Water Splitting in a Visible Light-Absorbing Dye-Sensitized Photoelectrochemical Cell. *J. Am. Chem. Soc.* **2009,** *131*, 926-927.

30. Cao, C.; Hill, S.; Cheng, H.-P. Strongly Correlated Electrons in the $[Ni(hmp)(ROH)X]_4$ Single Molecule Magnet: A DFT + *U* Study. *Phys. Rev. Lett.* **2008,** *100*, 167206.

31. Zaharieva, I.; Chernev, P.; Risch, M.; Klingan, K.; Kohlhoff, M.; Fischer, A.; Dau, H. Electrosynthesis, Functional, and Structural Characterization of a Water-Oxidizing Manganese Oxide. *Energy Environ. Sci.* **2012,** *5*, 7081-7089.

32. Chen; Tagore, R.; Olack, G.; Vrettos, J. S.; Weng, T.-C.; Penner-Hahn, J.; Crabtree, R. H.; Brudvig, G. W. Speciation of the Catalytic Oxygen Evolution System: $[Mn^{III/IV}_2(\mu\text{-}O)_2(terpy)_2(H_2O)_2](NO_3)_3 + HSO_5^-$. *Inorg. Chem.* **2006,** *46*, 34-43.

33. Ghosh, K.; Eroy-Reveles, A. A.; Olmstead, M. M.; Mascharak, P. K. Reductive Nitrosylation and Proton-Assisted Bridge Splitting of a (μ-Oxo)dimanganese(III) Complex Derived from a Polypyridine Ligand with One Carboxamide Group. *Inorg. Chem.* **2005,** *44*, 8469-8475.

34. Yagi, M.; Narita, K. Catalytic O_2 Evolution from Water Induced by Adsorption of $[(OH_2)(Terpy)Mn(\mu\text{-}O)_2Mn(Terpy)(OH_2)]^{3+}$ Complex onto Clay Compounds. *J. Am. Chem. Soc.* **2004,** *126*, 8084-8085.

35. Limburg, J.; Vrettos, J. S.; Chen, H.; de Paula, J. C.; Crabtree, R. H.; Brudvig, G. W. Characterization of the O_2-Evolving Reaction Catalyzed by $[(terpy)(H_2O)Mn^{III}(O)_2Mn^{IV}(OH_2)(terpy)](NO_3)_3$ (terpy = 2,2':6,2"-Terpyridine). *J. Am. Chem. Soc.* **2000,** *123*, 423-430.

36. Collomb, M.-N.; Deronzier, A.; Richardot, A.; Pecaut, J. Synthesis and Characterization of a New Kind of $Mn_2^{III,IV}$ μ-oxo Complex: $[Mn_2O_2(terpy)_2(H_2O)_2](NO_3)_3.6\ H_2O$, terpy=2,2':6',2"-terpyridine. *New J. Chem.* **1999,** *23*, 351-354.

37. Larson, E. J.; Pecoraro, V. L. The Peroxide-Dependent μ_2-O Bond Formation of Manganese Complex $[Mn^{IV}SALPN(O)]_2$. *J. Am. Chem. Soc.* **1991,** *113*, 3810-3818.

38. Kitajima, N.; Singh, U. P.; Amagai, H.; Osawa, M.; Morooka, Y. Oxidative Conversion of a $Mn(\mu\text{-}OH)_2Mn$ to a $Mn(\mu\text{-}O)_2Mn$ Moiety. Synthesis and Molecular Structures of a (μ-Hydroxo)dimanganese (II,II) and (μ-Oxo)dimanganese(III,III) Complex with a Hindered N_3 Ligand. *J. Am. Chem. Soc.* **1991,** *113*, 7757-7758.

39. Fernando, A.; Aikens, C. M. Ab Initio Electronic Structure Study of a Model Water Splitting Dimer Complex. *Phys. Chem. Chem. Phys.* **2015**, DOI: 10.1039/C1035CP04112K.

40. Sears, J. S.; Sherrill, C. D. The Electronic Structure of Oxo-Mn(salen): Single-Reference and Multireference Approaches. *J. Chem. Phys.* **2006,** *124*, 144314.

41. Blomberg, M. R. A.; Siegbahn, P. E. M.; Styring, S.; Babcock, G. T.; Åkermark, B.; Korall, P. A Quantum Chemical Study of Hydrogen Abstraction from Manganese-Coordinated Water by a Tyrosyl Radical: A Model for Water Oxidation in Photosystem II. *J. Am. Chem. Soc.* **1997,** *119*, 8285-8292.

42. McGrady, J. E.; Stranger, R. Redox-Induced Formation and Cleavage of O−O σ and π Bonds in a Peroxo-Bridged Manganese Dimer: A Density Functional Study. *Inorg. Chem.* **1999,** *38*, 550-558.

43. Lang, S. M.; Fleischer, I.; Bernhardt, T. M.; Barnett, R. N.; Landman, U. Dimensionality Dependent Water Splitting Mechanisms on Free Manganese Oxide Clusters. *Nano Lett.* **2013,** *13*, 5549-5555.

44. Lee, C.; Aikens, C. M. Theoretical Investigation of Water Oxidation Processes on Small $MnxTi_{2-x}O_4$ (x = 0–2) Complexes. *J. Phys. Chem. A* **2014,** *118*, 8204-8221.

45. te Velde, G.; Bickelhaupt, F. M.; Baerends, E. J.; Fonseca Guerra, C.; van Gisbergen, S. J. A.; Snijders, J. G.; Ziegler, T. Chemistry with ADF. *J. Comput. Chem.* **2001,** *22*, 931-967.

46. Becke, A. D. Density-Functional Exchange-Energy Approximation with Correct Asymptotic Behavior. *Phys. Rev. A* **1988,** *38*, 3098-3100.

47. Perdew, J. P. Density-Functional Approximation for the Correlation Energy of the Inhomogeneous Electron Gas. *Phys. Rev. B* **1986,** *33*, 8822-8824.

48. Fernando, A.; Aikens, C. M. Reaction Pathways for Water Oxidation to Molecular Oxygen Mediated by Model Cobalt Oxide Dimer and Cubane Catalysts. *J. Phys. Chem. C* **2015,** *119*, 11072-11085.

Chapter 4 - Theoretical Investigation of Water Oxidation Catalysis by a Model Manganese Cubane Complex

Amendra Fernando and Christine M. Aikens

4.1 Abstract

Manganese is selected by nature for the water oxidation process. In this study, we use an *in silico* approach to study a manganese cubane complex $Mn_4O_4(H_2O)_x(OH)_y$ x = 4-8, y = 8-4 with water-derived ligands. We investigate oxidation state configurations ranging from all Mn(IV) to all Mn(III) states. Understanding these simplest architectures for water splitting is essential for the bottom up design of commercially viable electrocatalysts. Both μ_3-oxo and μ_3-hydroxo versions of the catalysts were examined; μ_3-hydroxo versions are generally higher in energy in all the oxidation state configurations except for the Mn_4(III III III III) state (this rearranges to a Mn_4(II III III IV) state). Out of all the oxidation state configurations we studied, we observed that Mn_4(IV IV IV IV), Mn_4(III IV IV IV), and Mn_4(III III IV V) configurations are thermodynamically viable for water oxidation. All three reaction pathways proceed via nucleophilic attack from a solvent water molecule to the manganese oxo species. The highest thermodynamic energy step corresponds to the formation of the manganese oxo species, which is a significant microscopic property that reoccurred in all these reaction pathways. This can be a significant descriptor in selecting efficient water splitting catalysts.

4.2 Introduction

After millions of years of evolution, nature has selected a manganese-based cubane complex as the active center in the oxygen evolving complex (OEC) of photosystem II (PSII). This active complex catalyzes the water oxidation process, where it converts water into

molecular oxygen, protons and electrons. The catalytic core consists of a $CaMn_4O_4$ structure with a $CaMn_3O_4$ cuboidal core and a dangling Mn atom.[1] Understanding the electronic structure, properties and mechanism of the water oxidation process on this active core is an essential part of designing and developing a commercially viable water splitting catalyst as this artificial water splitting is a clean and sustainable way to produce hydrogen. Consequently, a large number of experimental and theoretical studies have been devoted to achieve this understanding with the OEC and models of the OEC,[1-24] as well as other biomimetic complexes.[25-32] However, the catalysts developed so far other than some of the ruthenium catalysts are a couple of orders of magnitude different from the natural system.[33] Ruthenium is a rare element and use of it on a large scale is not favorable. In contrast, manganese is a common element. The activity of manganese-based cubane complexes and how the OEC achieves such efficiency is still not fully understood. The presence of this remarkable cubane core geometry is found in other water splitting catalysts as well (i.e. Nocera's catalyst,[34] and other cobalt catalysts reported by McAlpin *et al*.,[35] McCool *et al*.,[36] and Evangelisti *et al*.[37]).

Reporting a complete review of the large number of experimental and theoretical studies of the OEC is not possible, so we instead report here a few of the studies that examined a related Mn_4O_4 core (cubane complexes with calcium incorporated in the core are not discussed here), which is the focus of this work. Ruettinger *et al*.[38] reported the synthesis of the first Mn_4O_4 cubane core in 1997. This synthesized $Mn_4O_4(PO_2(Ph)_2)_6$ complex was a fusion of two dimer $Mn_2O_2^{3+}$ units. There have previously been several other manganese complexes synthesized with distorted cubane-like cores[39, 40] or with incomplete core structures[41, 42] or as part of a larger cluster.[43] The core of this $Mn_4O_4(PO_2(Ph)_2)_6$ complex consists of $[Mn_4O_4]^{6+}$ and the highest oxidation state observed in this family of complexes contains a $[Mn_4O_6]^{7+}$ core. There have been

many reports of this $Mn_4O_4(PO_2(Ph)_2)_6$ catalyst and its variants tested as electrocatalysts and photocatalysts in the past few years after the first proposal.

In 2011, Kanady and coworkers[30] reported two cubane clusters where one complex has a Mn_4O_4 cubane core unit and the other has a $CaMn_3O_4$ unit. The Mn_4O_4 complex contains a tri-nucleating 1,3,5-triarylbenzene ligand architecture. This complex was later investigated with Ca and Sc to understand mechanistic studies of reactivity and incorporation of μ_3-oxido moieties.[44] It was found that $Mn^{IV}_3CaO_4$ and $Mn^{IV}_3ScO_4$ were unreactive toward trimethylphosphine (PMe_3) whereas $Mn^{III}_2Mn^{IV}_2O_4$ cubane reacts with PMe_3 readily to generate a new $Mn^{III}_4O_3$ partial cubane plus Me_3PO. These authors also used theoretical calculations to investigate the reaction pathways for oxygen atom transfer to phosphine from cubane cluster. In related work, Lee and Aikens[45] reported a theoretical study of water splitting process on model compounds of these synthetic clusters. The ligands were truncated with simpler ones to reduce the computational time. It was found that the model complex with Mn_4O_4 architecture is thermodynamically more favorable for water splitting than a $Ca_3Mn_4O_4$ complex. Yamaguchi and coworkers[22] reported a computational study of a mixed valance $Mn(III)_{4-x}Mn(IV)_xO_4$ cluster to investigate the Jahn-Teller (JT) effects of Mn(III) ions. The optimized geometries of the cubane demonstrated an acute triangle for $Mn(III)_2Mn(X)$ (X = III, IV) indicating JT effects. It was found that JT effects are not significant for $Mn(IV)_2Mn(III)$ cores showing an obtuse triangle geometry. JT effects are further diminished for the $Mn(IV)_3$ core, which forms an equilateral triangle. It was found that Ca doping suppresses the JT effects even for the $Mn(III)_2Mn(X)$ (X = III, IV) case.

There are only a few studies reported with ligand-free or with water-derived architectures of pure manganese cubane complexes. Recently in 2013, Lang *et al.*[48] demonstrated the water splitting process on singly charged $Mn_2O_2^+$ and $Mn_4O_4^+$ species. These authors used gas phase

ion trap measurements together with Born-Oppenheimer spin density functional molecular dynamic calculations. They found that a two-dimensional ring-like ground state structure of $Mn_4O_4^+$ undergoes a dimensionality change to a three-dimensional cuboidal octahydroxo complex when it was hydrated. These authors further investigated this $Mn_4O_4^+$ system with $D_2{}^{16}O$ and $H_2{}^{18}O$ in gas phase ion trap experiments.[49] Their results indicated exchange of the oxygen atoms of the cluster with water oxygen atoms. Their first principles spin density functional calculations suggested a reaction mechanism that dissociates water via hydroxylation of the oxo bridges. Lang *et al*.[50] also demonstrated interaction of water with the $Mn_4O_4^+$ complex using IR spectroscopy in conjunction with spin density functional calculations. It was found that hydroxylation of μ-oxo bridges is an essential part of the dissociation of the O-H bond water. This hydroxylation continues until all the μ-oxo bridges are hydroxylated. Additional water molecules then bound molecularly with a favored preference for the hydrogen-bridge-bound H_3O_2 units involving hydroxylated bridges. It was found that an open cuboidal structure emerge when $n \geq 3$ for $Mn_4O_4^+(H_2O)_n$, and for $n > 6$ the $Mn_4O_4^+$ cluster transforms into a closed cuboidal structure.

The objective of this study is to investigate manganese cubane complexes ($Mn_4O_4(H_2O)_x(OH)_y$ x = 4-8, y = 8-4) that primarily incorporate water-derived ligands. We investigated these systems with oxidation state configurations ranging from all Mn(IV) to all Mn(III). Herein, we report a comprehensive study of electronic properties, structures, reaction mechanisms for water oxidation on these cubane complexes. We also report microscopic properties that can be used as essential descriptors for designing efficient electrocatalysts. Understanding these characteristic features for water oxidation on these simple model catalyst systems is essential to further develop and enhance water splitting catalysts based on transition

metal oxides. It is also important to note that comprehensive knowledge of the reaction mechanism for water oxidation on these manganese oxide species can help us to find commonalities and differences between these water oxidation catalytic systems, and thus enhance and develop a next generation of future catalysts.

4.3 Computational Methodology

All the structural optimizations are carried out with the Amsterdam Density Functional (ADF) program.[51] We have employed the BP86[52, 53] exchange and correlation functional with a triple-zeta polarized (TZP) basis set for Mn, O, and H atoms. The reaction processes investigated in the water splitting mechanism include four dehydrogenation steps, two water additions, and removal of one oxygen molecule. In this theoretical investigation, our main goal is to study the thermochemistry of the intermediate reactions. Although kinetics also plays an important role, kinetics are not considered in this work because multiple transition states are possible for these dynamic reactions and the transition states are very sensitive to the hydrogen atom orientation. All possible isomers of the intermediate states have been calculated in order to predict the lowest energy step.

For each structure, the charge and the multiplicity are shown in parentheses in the figures. Green circles around atoms are used to highlight areas of the cluster where reactions are occurring between the calculated intermediate states of each structure. All oxidation states discussed in this work are formal oxidation states. We use the terms "surface", "bottom", and "geminal" when discussing the aqua and hydroxo ligands bound to manganese atoms above, below, and to the side of the plane of the $Mn_2(\mu\text{-}OH)_2$ units, respectively; these terms are used to describe the structures with respect to the orientation given in each figure.

The $2H^{\bullet} \rightarrow H_2$ reaction is chosen as the reference system to model the hydrogen extraction process in the catalytic steps. This reference is used instead of the standard hydrogen electrode reaction ($2H^+ + 2e^- \rightarrow H_2$) because the energetics of the latter reaction depends sensitively on the solvation of a proton, which is difficult to calculate accurately with theory. The $2H^{\bullet} \rightarrow H_2$ reference system also removes the strong pH and solvent dependence that exists when protons are present. Nonetheless, choice of the reference system is arbitrary for the electrochemical steps (i.e. dehydrogenation reactions) in the catalytic cycle because the reference choice affects all hydrogen abstractions equally, so the qualitative predictions are not changed. The $2H^{\bullet} \rightarrow H_2$ reference system has previously been used for studying water splitting reactions on manganese dimer complexes as well as cobalt dimer and cubane complexes.[27, 28]

Reaction energies are presented according to $\Delta E = \sum_i^{\text{products}} \nu_i E_i - \sum_i^{\text{reactants}} \nu_i E_i$, where ν_i is the stoichiometric coefficient and E_i is the electronic energy (plus nuclear repulsion energy) calculated for each reactant or product. We have also accounted for the zero-point energy (ZPE), enthalpy and entropy corrections for a temperature of 298.15 K. The nuclear internal energy, which is the sum of ZPE, 3 kT (3/2 kT for rotation and 3/2 kT for translation), and a small correction term due to the vibration partition function, is added with the electronic energy to calculate the total internal energy U of the structure. The enthalpy H is calculated by H=U + pV where pV is obtained from the ideal gas equation, pV/n = RT. The Gibbs free energy is then computed with the standard formula G = H-TS. The energy difference is then calculated according to $\Delta G = \sum_i^{\text{products}} \nu_i G_i - \sum_i^{\text{reactants}} \nu_i G_i$, where ν_i are the stoichiometric coefficients. Unless otherwise noted, the values in the text are the reaction energies; both values are presented in the tables.

The experimental ΔG_{298} value for the overall water splitting reaction ($2H_2O \rightarrow 2H_2 + O_2$) at pH = 0 with reference to the normal hydrogen electrode is given as 4.92 eV. We have calculated ΔG_{298} of 4.56 eV for the overall water splitting reaction for the BP86/TZP level of theory. The required potential for each dehydrogenation reaction would be 4.56 eV/4 = 1.14 eV and the overpotential for each reaction can be calculated by subtracting this value from the electrochemical steps. These overpotential values are not given in this paper.

4.4 Results and Discussion

In this work, we examine the water splitting process on a Mn_4O_4 cubane complex with oxo, hydroxo, and aqua ligands ($Mn_4O_4(H_2O)_x(OH)_y$ x = 4-8, y = 8-4). Formal oxidation states ranging from Mn_4(IV IV IV IV) to Mn_4(III III III III) are considered. The geometry of the resting state of each catalyst possesses an octahedral environment around manganese atoms. Each manganese atom is initially coordinated with three μ_3-oxo groups. We have also investigated protonated versions of the μ_3-oxo groups (in which a μ_3-oxo group is replaced with a μ_3-hydroxo group and a terminal aqua ligand becomes a terminal hydroxo ligand) for each oxidation state configuration; one to four protonated μ_3-oxo groups are considered (new μ_3-hydroxo groups are marked with green circles). In addition to providing an understanding of water splitting on manganese cubane complexes, these systems can also be considered to be small versions of the bulk with increased surface to volume ratio, and thus may elucidate important aspects of catalysis on manganese oxide surfaces. Understanding water splitting on the simplest cubane complex will enable us to determine microscopic patterns that can be used as valuable tools for catalyst design. Each oxidation configuration and its respective lowest μ_3-hydroxo versions are described below.

4.4.1 Mn_4(IV IV IV IV) configuration with μ_3-oxo groups

The lowest energy water oxidation reaction mechanism (pathway-1) on the manganese cubane catalyst with all manganese atoms in the Mn(IV) oxidation state is given in Figure 4.1. The reaction initiates with a dehydrogenation from a surface hydroxo species on structure **1**. This first dehydrogenation requires 1.93 eV of energy (1.83 eV free energy, Table 4.1) and produces structure **2** that contains a Mn(V)O species. Although the Mn(V)O species may also be described as a Mn(IV)-O radical, in this paper we will present the oxidation states without considering the alternative radical form. However, it should be noted that the appropriate description of this group is a topic of research interest.[29, 54-56]

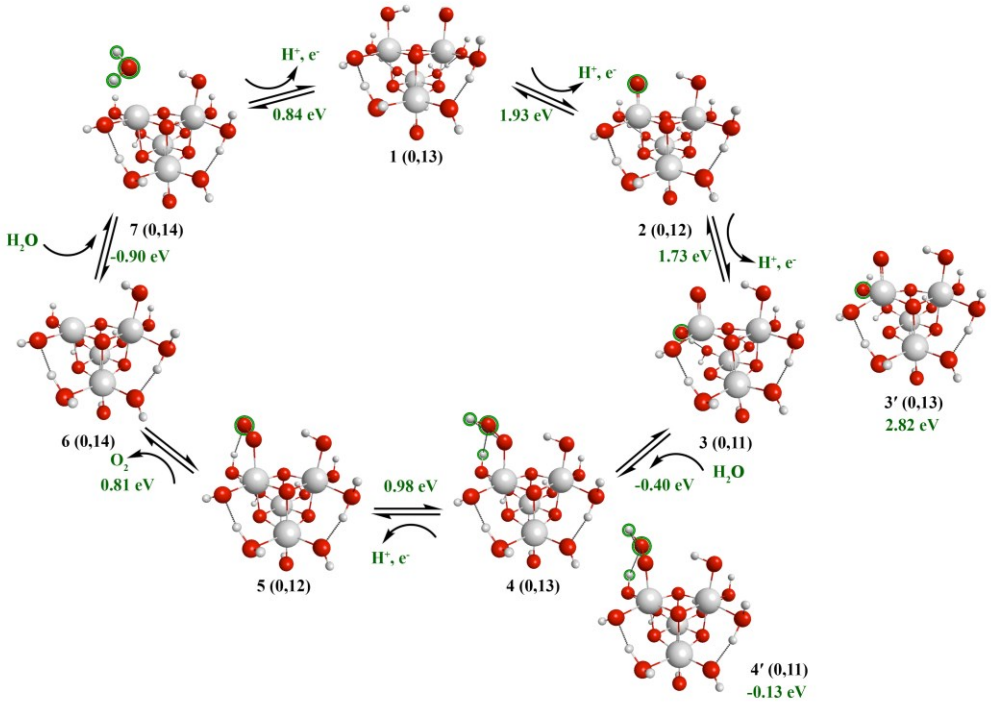

Figure 4.1 Proposed lowest energy reaction pathway-1 from structure **1** with Mn_4(IV IV IV IV) configuration. ΔE values are shown in the figure; ΔG values are presented in Table 4.1.

Notably, the formation of the oxo group is the highest energy intermediate step in this reaction pathway. This is a reoccurring theme in the other reaction pathways examined in our

current work and this property was also recently observed in a study of water splitting on manganese dimers.[27] We have investigated the fate of this oxo species by considering several alternative reaction pathways. For this cluster, nucleophilic attack from a solvent water molecule to the oxo species does not generate a species with a -OOH group. We have observed that water remains in molecular form hydrogen-bound to the cluster. The coupling reaction of the oxo group with a μ_3-oxo species is also not observed. Coupling of the oxo species to a geminal hydroxo group generates structure **S1** (pathway-B1 is shown in Figure B1 in the Appendix B). This coupling is a chemical step and it is a highly endothermic reaction requiring 1.64 eV of energy. Generally, this much energy cannot be attained by a chemical step, and ideally we want an efficient catalyst to have exothermic or at most thermoneutral chemical steps. Since the overall water splitting energy is fixed regardless of catalyst choice, it should also be noted that efficient catalysts should also not have highly exothermic chemical steps, because otherwise the energy will need to be balanced by other steps such as a high-energy electrochemical step in the reaction pathway. In pathway-B1, the first water addition and the oxygen removal processes are endothermic reactions.

The most likely fate of structure **2** is a consecutive second dehydrogenation requiring 1.73 eV of energy. An applied overpotential that is sufficient to overcome the initial dehydrogenation energy of 1.93 eV would also enable this second dehydrogenation. The dehydrogenation takes place on an aqua ligand attached to the manganese atom with the Mn(V) oxidation state and leads to the formation of a Mn(VI)O oxo group on structure **3**. The oxidation state of the other manganese atoms remains Mn(IV) throughout the catalytic cycle. Structure **3** now undergoes an exothermic nucleophilic attack from a solvent water molecule to produce structure **4**; the lowest energy state for structure **4** has multiplicity 13. This attack dissociates one

of the OH bonds of the water molecule and the dissociated hydrogen is abstracted by the geminal hydroxo group, which then becomes an aqua ligand. This step is exothermic by -0.40 eV. The formation of structure **4** with multiplicity 11 (given as **4'**) is calculated to have a reaction energy of -0.13 eV, so it is 0.27 eV higher in energy than formation of the structure with a multiplicity of 13, but it is still exothermic. Due to the potentially spin-forbidden reaction, we also considered the energy of formation of structure **3** with multiplicity 13 (**3'**) from structure **2**. This is calculated to be 1.09 eV higher in energy than the generation of structure **3** with multiplicity 11, which is thus unlikely.

Structure **4** with an -OOH group undergoes a third dehydrogenation reaction requiring 0.98 eV of energy. (Dehydrogenation from structure **4'** also yields structure **5**.) This dehydrogenation occurs at the hydrogen of the -OOH group on structure **4**. Oxygen removal from structure **5** is an endothermic process by 0.81 eV, which is a high-energy chemical step. The resulting structure **6** has a multiplicity of 14. It exothermically coordinates with water to form structure **7** with Mn_4(III IV IV IV) oxidation states. This coordination process yields -0.90 eV in energy. It is reasonable to assume that the oxygen removal process and the water addition reaction occur simultaneously, and the overall reaction would have an exothermic reaction energy of -0.09 eV. This reaction is also exoergic by -0.09 eV.

The catalyst can be regenerated from structure **7** with dehydrogenation of the coordinated second water molecule. The dehydrogenation reactions require less energy as the pathway progresses, and this fourth dehydrogenation requires only 0.84 eV of energy. Notably, structure **7** is the starting structure for the reaction pathway with the Mn_4(III IV IV IV) configuration, so the reaction pathway for the system with these starting Mn oxidation states is embedded in pathway-1, as discussed below. Interestingly, a recent study by Yang *et al.*[57] demonstrated a water

splitting mechanism on calcium birnessite where the manganese atoms surrounding the calcium ion are in the Mn_4(III IV IV IV) oxidation state configuration.

The calculated free energy values for pathway-1 are given in Table 4.1. There were no significant differences in energy with respect to the absolute reaction energy values. However, in general for pathway-1 we noticed a decrease in magnitudes of the ΔG values for the reactions compared to the ΔE values.

Table 4.1 Calculated reaction energies and free energies for pathway-1 of Figure **4.1**.

Reaction Processes (Pathway-1, Figure 4.1)	**ΔE (eV)**	**ΔG (eV)**
$\Delta E_{(2\text{-}1)}$	1.93	1.83
$\Delta E_{(3\text{-}2)}$	1.73	1.57
$\Delta E_{(3'\text{-}2)}$	2.82	2.65
$\Delta E_{(4\text{-}3)}$	-0.40	-0.28
$\Delta E_{(4'\text{-}3)}$	-0.13	-0.05
$\Delta E_{(5\text{-}4)}$	0.98	0.82
$\Delta E_{(6\text{-}5)}$	0.81	0.73
$\Delta E_{(7\text{-}6)}$	-0.90	-0.82
$\Delta E_{(1\text{-}7)}$	0.84	0.72

Overall in pathway-1, the two water addition reactions are exothermic by -0.40 eV and -0.90 eV. The oxygen removal process is endothermic by 0.81 eV. The highest energy step is the first dehydrogenation that resulted in the formation of the oxo species and the highest energy chemical step is the oxygen removal process. After the formation of the -OOH bond in structure **4**, the next thermodynamically favorable step is the dehydrogenation of the hydrogen of -OOH group.

4.4.2 Mn_4(IV IV IV IV) configuration with μ_3-hydroxo groups

The μ_3-hydroxo versions of the Mn_4(IV IV IV IV) oxidation state configuration are found to be higher in energy than the μ_3-oxo structure **1**. Structure **8** with a single μ_3-hydroxo group is the lowest energy isomer in this category and it is found to be 0.41 eV higher in energy than structure **1** with μ_3-oxo groups. This protonation, which replaces a μ_3-oxo group with a μ_3-hydroxo group and replaces a terminal aqua ligand with a hydroxo ligand, changes the formal oxidation states of the Mn atoms to IV⅔ IV⅔ III⅔ III. Each protonation of the μ_3-oxo groups results in higher energy isomers. Isomers with two, three, and four μ_3-hydroxo groups are 0.43 eV, 0.93 eV, and 1.21 eV higher in energy than structure **8**, respectively. The water splitting reaction pathway-2 on structure **8** is given in Figure 4.2.

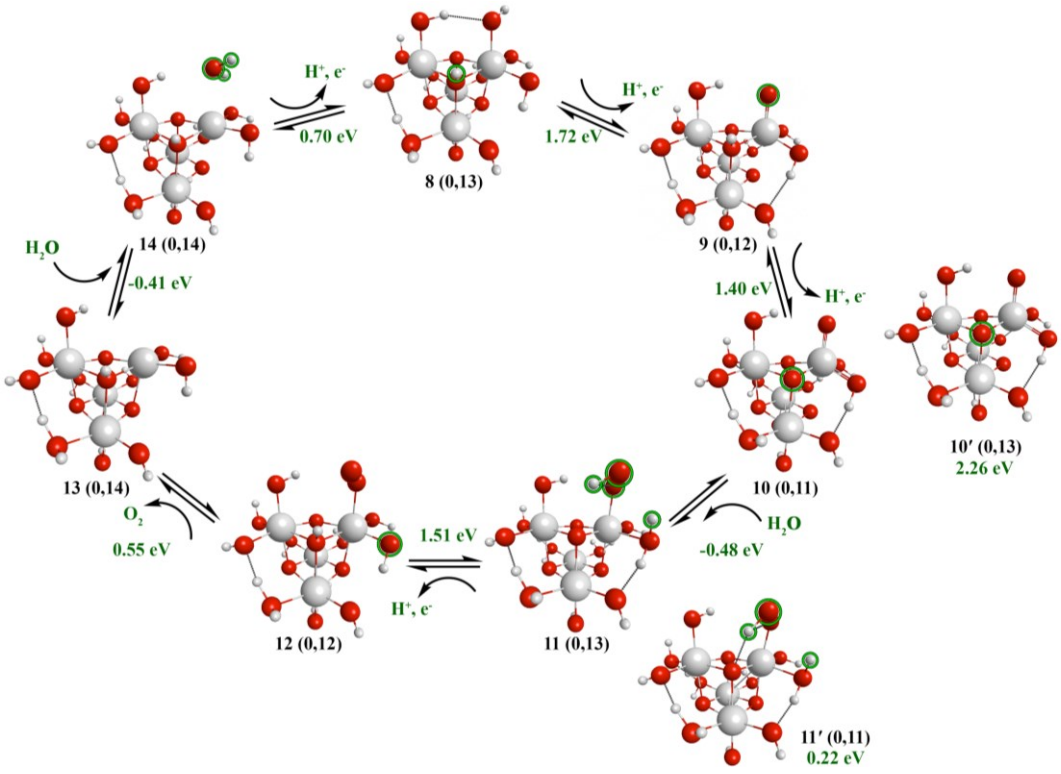

Figure 4.2 Proposed lowest energy reaction pathway-2 from structure **8** with Mn_4(IV⅔ IV⅔ III⅔ III) configuration (**8** is the lowest energy cluster of the structures with μ_3-hydroxo groups that are related to **1**). ΔE values are shown in the figure; ΔG values are presented in Table 4.2.

Similar to pathway-1, the reaction initiates with a dehydrogenation. This step has an endothermic energy of 1.72 eV (and an endoergic free energy of 1.73 eV, Table 4.2) compared to the first dehydrogenation in reaction pathway-1 that requires 1.93 eV. This dehydrogenation also takes place from a surface hydroxo group and results in the generation of a Mn(V⅔)O group on structure **9**. Similar to pathway-1, this manganese oxo formation step is the highest energy step in this reaction pathway. This oxo group can undergo different reaction steps similar to those of structure **2**.

The most probable step after formation of structure **9** is electrochemical dehydrogenation, which will be described in more detail below. Coupling to the geminal hydroxy group, which results in formation of a μ_2-OOH group, is found to require 2.03 eV of energy. We also found a lower energy structure for this oxo-geminal hydroxy coupling reaction where the hydrogen of the μ_2-OOH group is abstracted by the adjacent hydroxo group of the bottom manganese atom. This structure formation is endothermic by 1.18 eV. The coupling reaction of the oxo group with the μ_3-oxo group requires 1.99 eV of energy. The lowest energy step is the nucleophilic attack from a solvent water molecule resulting in generation of structure **S7** shown in Figure B2 in the Appendix B. This chemical step requires 0.64 eV, which is a high value for a chemical step. We investigated this reaction pathway and included it in the Appendix B.

The most likely possible fate of structure **9** is electrochemical dehydrogenation. This consecutive second dehydrogenation occurs at the μ_3-hydroxo group. This step requires 1.40 eV and forms structure **10** with a Mn(VI)O group. In comparison to structure **3**, structure **10** has the same stoichiometry and very similar energy values (structure **3** is 0.09 eV lower in energy than structure **10**). However, structure **3** has Mn_4(VI IV IV IV) oxidation states and structure **10** possesses Mn_4(VI V III IV). We also calculated a higher multiplicity version of structure **10**

(structure **10'**), which requires 2.26 eV to be generated from structure **9**; however, this structure is unlikely to be generated since the reaction energy is so high.

The Mn(VI)O group undergoes a nucleophilic attack from a solvent water molecule to form structure **11** with a -OOH group. Structure **11** also has the same stoichiometry as structure **4** of pathway-1 with different oxidation states for the manganese atoms (structure **4** is 0.004 eV lower in energy than structure **11**). This reaction step has an exothermic energy of -0.48 eV, which is similar to the reaction energy of -0.40 eV for nucleophilic attack leading from structure **3** to **4**. Structure **11** prefers a multiplicity of 13 whereas formation of a structure with multiplicity 11 (structure **11'**) is endothermic by 0.22 eV. This change in multiplicity for the lowest energy states is also seen between structures **3** and **4** in pathway-1. In the next step, hydrogen is removed from the aqua ligand geminal to the -OOH group, which results in an intramolecular hydrogen atom transfer to a μ_3-oxo group. This step requires 1.51 eV in energy; compared to the structure **4** to **5** dehydrogenation, it is 0.53 eV higher in energy.

Oxygen is extracted from structure **12** to produce structure **13**, and in the next step second water molecule is added to complete the coordination of manganese left vacant by the oxygen removal. This water-coordinated structure **14** has a slightly longer bond (2.47 Å, which is 0.30 Å longer compared to typical manganese-aqua bond distances of 2.08 - 2.15 Å) between the manganese atom and the water molecule. The oxygen removal process is endothermic by 0.55 eV and the second water addition is exothermic by -0.41 eV. If we couple these reactions together as described in pathway-1, we have a net energy of 0.14 eV. The fourth hydrogen is removed from the coordinated aqua ligand (requiring 0.70 eV of energy) to regenerate the resting state of the catalyst.

We have calculated the reaction free energies for pathway-2; these values are given in Table 4.2. For most of the reaction steps (except for the first dehydrogenation where the calculated free energy is nearly the same), the magnitudes of the free energy changes are slightly lower than the reaction energies.

Table 4.2 Calculated reaction energies and free energies for pathway-2 of Figure 4.2.

Reaction Processes (Pathway-2, Figure 4.2)	**ΔE (eV)**	**ΔG (eV)**
$\Delta E_{(9\text{-}8)}$	1.72	1.73
$\Delta E_{(10\text{-}9)}$	1.40	1.25
$\Delta E_{(10'\text{-}9)}$	2.26	2.08
$\Delta E_{(11\text{-}10)}$	-0.48	-0.42
$\Delta E_{(11'\text{-}10)}$	0.22	0.26
$\Delta E_{(12\text{-}11)}$	1.51	1.39
$\Delta E_{(13\text{-}12)}$	0.55	0.51
$\Delta E_{(14\text{-}13)}$	-0.41	-0.33
$\Delta E_{(8\text{-}14)}$	0.70	0.42

Overall, in pathway-2, the two water addition reactions are exothermic by -0.48 eV and -0.41 eV, respectively. The oxygen removal process is endothermic by 0.55 eV and this is the highest energy chemical step. The highest energy step overall is the first dehydrogenation to generate the oxo species. In comparison to reaction pathway-1, pathway-2 has a lower overpotential by 0.21 eV. Once the -OOH is formed in structure **11**, the hydrogen of the geminal aqua ligand is dehydrogenated simultaneously as the hydrogen of the -OOH group is transferred to the μ_3-oxo group. The oxygen extraction process (combined oxygen extraction and water coordination) from pathway-1 is exothermic by -0.09 eV and in pathway-2 it is endothermic by 0.14 eV. Both pathway-1 and pathway-2 are thermodynamically favorable reaction pathways for

the water oxidation process. However, both reaction pathways reach a formal oxidation state of Mn(VI) before forming the O-O bond.

4.4.3 Mn_4(III IV IV IV) configuration with μ_3-oxo groups

The lowest energy structure with Mn_4(III IV IV IV) configuration is found to be structure **7** of pathway-1. A related structure **15**, with a Mn_4(III III IV V) configuration, is similar in energy with the latter oxidation state configuration being 0.01 eV lower in energy.

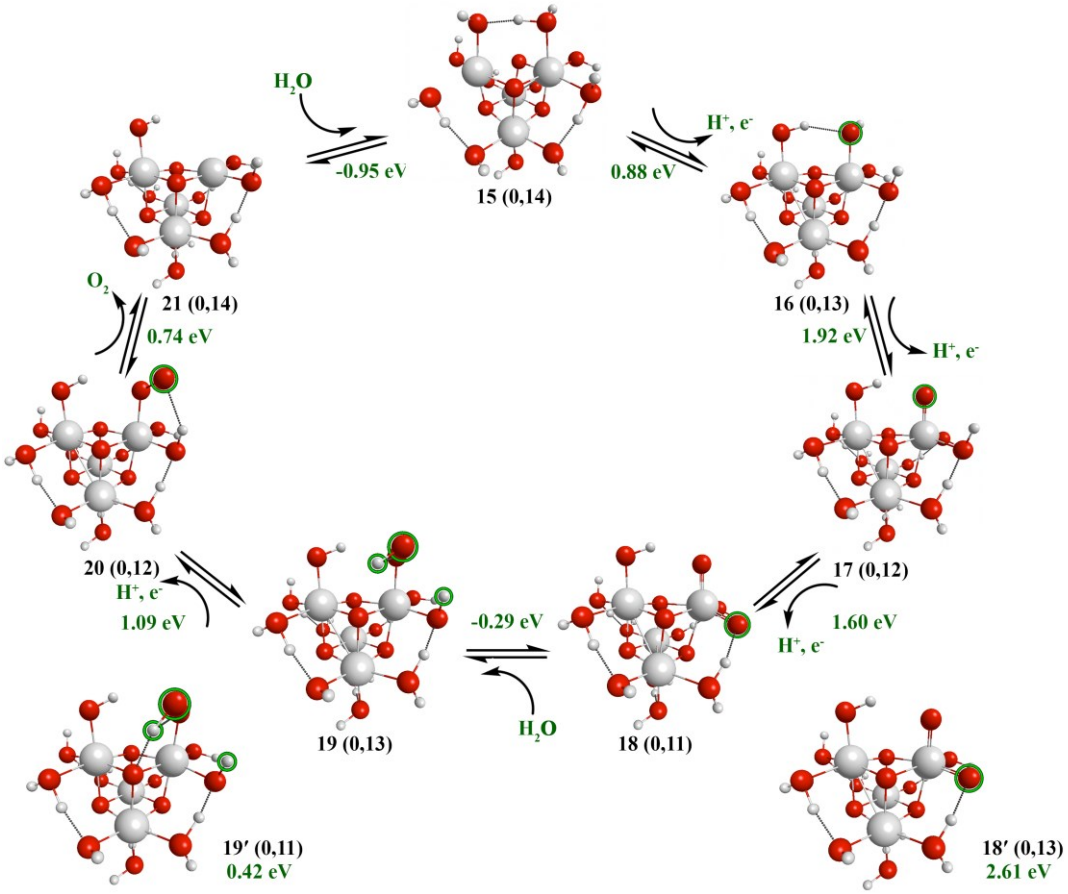

Figure 4.3 Proposed lowest energy reaction pathway-3 from structure **15** with Mn_4(III III IV V) configuration. ΔE values are shown in the figure; ΔG values are presented in Table 4.3.

The lowest energy pathway starting from structure **7** with Mn_4(III IV IV IV) is embedded in pathway-1, so in this section we examine the water splitting mechanism on structure **15** with

Mn_4(III III IV V). The reaction pathway using structure **15** is given in Figure 4.3 (pathway-3). Compared to the first dehydrogenation of pathway-1, the first dehydrogenation reaction in pathway-3 is 1.05 eV lower in energy. This occurs at a surface aqua ligand on a Mn(III) atom which then changes to Mn(V) with an intramolecular hydrogen atom transfer from the bottom Mn(V) atom. The resulting structure **16** is similar in stoichiometry to structure **1** of pathway-1. However, structure **16** has a Mn_4(III IV IV V) configuration and it is 0.03 eV higher in energy than structure **1** with Mn_4(IV IV IV IV). This suggests that structure **16** possibly connects to pathway-1 if it undergoes intramolecular hydrogen atom transfer reactions. We investigated the reaction pathway for the water oxidation process via structure **16** as it is comparable in energy.

Structure 16 undergoes a consecutive second dehydrogenation requiring 1.92 eV energy (1.78 eV free energy, Table 4.4) to produce structure **17** with a Mn_4(III IV IV VI) configuration. This is the thermodynamically highest energy step in reaction pathway-3. Like in the previous pathways, this step corresponds to the generation of the manganese oxo species. In structure **17**, it is for the formation of a Mn(VI)O species. Chemical steps from this oxo group are found to be thermodynamically high in energy: the attack of the oxo group to the geminal hydroxo group is calculated to require 1.71 eV and nucleophilic attack from a solvent water molecule to the oxo species requires 0.61 eV. The reaction pathway that proceeds via a nucleophilic attack is given in Figure B3 of the Appendix B.

Dehydrogenation from structure **17** requires 1.60 eV of energy. This leads to the formation of two oxo species on a single manganese atom with a Mn(VII) formal oxidation state in structure **18**. The geminal coupling reaction of these oxo species is calculated to be endothermic in energy by 0.96 eV. Nucleophilic attack from a solvent water molecule to one of these oxo species is found to be thermodynamically favorable. Once the water attacks the oxo

group, the other geminal oxo group abstracts one of the hydrogen atoms from the water molecule. This reaction step is exothermic by -0.29 eV. The resulting structure **19** has a lowest energy spin state with a multiplicity of 13 and possesses an -OOH group. A similar structure **19'** with a multiplicity of 11 lies 0.71 eV higher in energy; this structure would be spin-allowed from structure **18**. For comparison, we examine an isomer of structure **18** with a multiplicity of 13 (given as **18'**), but it requires 2.61 eV to be generated from structure **17** and is thus unlikely to be formed. The hydrogen removal from the -OOH group to yield structure **20** is the next thermodynamically lowest step, which is 1.09 eV in energy from structure **19**. We have seen this pattern with cobalt species[28] as well, where once the -OOH group is formed the hydrogen may be removed via a dehydrogenation reaction or transferred to another ligand via an intramolecular hydrogen transfer reaction.Molecular oxygen can be extracted from structure **20** to produce structure **21**. Structure **21** readily coordinates with a water molecule to complete the octahedral coordination of manganese and regenerate the resting state of the catalyst. The oxygen removal process from structure **20** is calculated to be endothermic by 0.74 eV and the subsequent water addition is exothermic by -0.95 eV. Overall, this yields an exothermic energy of -0.21 eV for a combined process. This suggests a more favorable oxygen extraction process compared to pathway-1 and pathway-2.

Overall, the favorability of this pathway depends on the highly endothermic second dehydrogenation forming the oxo species, which will be responsible for the overpotential of the reaction pathway. This dehydrogenation of 1.92 eV is similar to the 1.93 eV dehydrogenation energy in pathway-1, and is larger than the dehydrogenation energy of 1.72 eV required in pathway-2. Reaction pathway-3 consisting of structures **15-21** has structures with the same stoichiometries as structures **7** and **1-6** in pathway-1, but with different oxidation state

configurations. The thermodynamic energy values and preferred steps are similar to pathway-1 (i.e. processes like dehydrogenations and water additions occur in the same stage of the catalytic cycles). Calculated free energy values are typically lower in magnitude than the respective ΔE values (Table 4.3) except for the $\Delta E_{(19'-18)}$ step where we see 0.04 eV increase.

Table 4.3 Calculated reaction energies and free energies for pathway-3 of Figure 4.3.

Reaction Processes (Pathway-3, Figure 4.3)	**ΔE (eV)**	**ΔG (eV)**
$\Delta E_{(16-15)}$	0.88	0.76
$\Delta E_{(17-16)}$	1.92	1.78
$\Delta E_{(18-17)}$	1.60	1.48
$\Delta E_{(18'-17)}$	2.61	2.48
$\Delta E_{(19-18)}$	-0.29	-0.22
$\Delta E_{(19'-18)}$	0.42	0.46
$\Delta E_{(20-19)}$	1.09	0.95
$\Delta E_{(21-20)}$	0.74	0.66
$\Delta E_{(15-21)}$	-0.95	-0.85

Both water addition steps in pathway-3 are exothermic (by -0.29 eV and -0.95 eV) respectively. The lowest endothermic chemical step is the oxygen removal process requiring 0.74 eV. In this reaction pathway-3 we see a higher oxidation state buildup of Mn(VII) before the formation of the O-O bond. The highest thermodynamic energy of pathway-3 is similar to the highest energy of pathway-1. However, the net oxygen removal process is more favorable than both pathway-1 and pathway-2.

4.4.4 Mn_4(III IV IV IV) configuration with μ_3-hydroxo groups

The μ_3-hydroxo versions of the Mn_4(III IV IV IV)–based structures are found to be higher in energy, similar to what was observed with the Mn_4(IV IV IV IV) structures. Structure

22 with one μ_3-hydroxo group is found to be the lowest in energy among the μ_3-hydroxo versions. Structure **22** is 0.44 eV higher in energy than the lowest energy structure **15** with μ_3-oxo groups. Structures with two, three, and four μ_3-hydroxo groups are 0.51 eV, 1.06 eV, and 1.13 eV higher in energy than structure **22,** respectively.

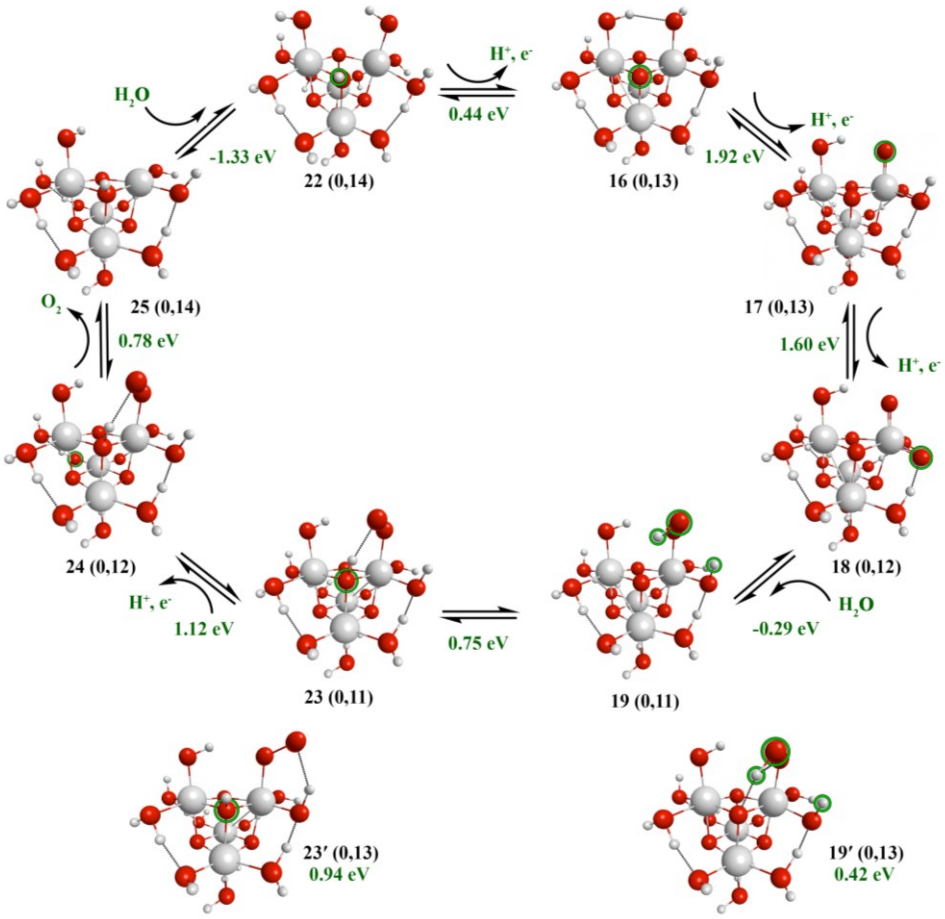

Figure 4.4 Proposed lowest energy reaction pathway-4 from structure **22** with $Mn_4(II^{2}/_{3}\ IV^{2}/_{3}\ III^{2}/_{3}\ IV)$ configuration (**22** is the lowest energy cluster of the structures with μ_3-hydroxo groups that are related to **15**). ΔE values are shown in the figure; ΔG values are presented in Table 4.4.

The structure with a single μ_3-hydroxo group has a $Mn_4(II^{2}/_{3}\ IV^{2}/_{3}\ III^{2}/_{3}\ IV)$ oxidation state configuration. Structure **22** first undergoes dehydrogenation (pathway-4 in Figure 4.4) requiring 0.44 eV of energy; this is half of the first dehydrogenation energy from structure **15** with only μ_3-oxo groups in the system. This dehydrogenation occurs at the μ_3-hydroxo bridge and forms

structure **16** of pathway-3. The catalytic cycle continues through structure **19**, which has an -OOH group formed from a solvent water molecule attack to the oxo group. From structure **19** the hydrogen of the -OOH group can transfer to the μ_3-oxo group endothermically (requiring 0.75 eV) to produce structure **23**. This is a high-energy chemical step and may not be thermodynamically favorable. However, we continued the cycle to understand the behavior of the water splitting process. In the next step the fourth dehydrogenation occurs on an aqua ligand at the bottom manganese atom with 1.12 eV energy. Here, the multiplicity changes from 11 to 12 in structure **24**. Oxygen is extracted from structure **24** with 0.78 eV and in the next step water coordinates with structure **25** exothermically with -1.33 eV of energy to regenerate the catalyst. The net energy of these two steps is exothermic by -0.55 eV. The calculated free energies are given in Table 4.4. In general, the magnitudes of the ΔG values for the reactions are somewhat lower than the ΔE values, with the exceptions of $\Delta E_{(19'\text{-}18)}$ and $\Delta E_{(23'\text{-}19)}$.

The highest energy step in this reaction pathway also corresponds to the formation of the oxo species. Both water addition steps are exothermic energy by -0.29 eV and -1.33 eV respectively. The net reaction energy for the oxygen extraction is -0.55 eV. There are two chemical steps with comparatively similar energy values: the intramolecular hydrogen atom transfer reaction to the μ_3-oxo bridge (0.75 eV) and the oxygen extraction process (0.78 eV). By analyzing the μ_3-oxo and the μ_3-hydroxo versions of this oxidation state combination, we can say that the μ_3-oxo version is thermodynamically favorable. Both pathway-3 and pathway-4 require around 0.20 eV higher of a potential than pathway-2.

Table 4.4 Calculated reaction energies and free energies for pathway-4 of Figure 4.4.

Reaction Processes (Pathway-4, Figure 4.4)	ΔE (eV)	ΔG (eV)
$\Delta E_{(16\text{-}22)}$	0.44	0.31
$\Delta E_{(17\text{-}16)}$	1.92	1.78
$\Delta E_{(18\text{-}17)}$	1.60	1.48
$\Delta E_{(19\text{-}18)}$	-0.29	-0.22
$\Delta E_{(19'\text{-}18)}$	0.42	0.46
$\Delta E_{(23\text{-}19)}$	0.75	0.75
$\Delta E_{(23'\text{-}19)}$	0.94	0.96
$\Delta E_{(24\text{-}23)}$	1.12	0.98
$\Delta E_{(25\text{-}24)}$	0.78	0.74
$\Delta E_{(22\text{-}25)}$	-1.33	-1.26

4.4.5 Mn_4(III III IV IV) configuration with μ_3-oxo groups

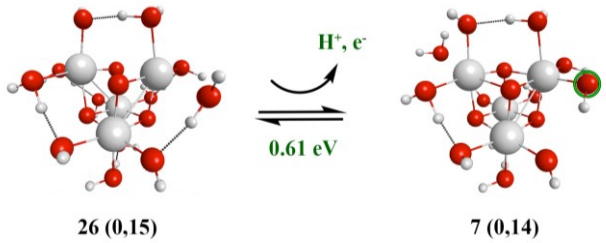

Figure 4.5 First dehydrogenation reaction of pathway-5 from structure **26** with Mn_4(III III IV IV) configuration.

Structure **26** is the lowest energy isomer for the Mn_4(III III IV IV) oxidation state configuration (Figure 4.5). The two manganese atoms with a Mn(III) oxidation state are located on the top of the cubane complex and they show slightly elongated bonds between manganese and one aqua ligand as well as between manganese and one μ_3-oxo group on each side. This may be due to the fact that Mn(III) atoms are known for strong Jahn-Teller effects that lead to

distortions from octahedral geometries.[58] The initial step is the first dehydrogenation that takes place at one of the aqua ligands attached to the manganese atom on top with the Mn(III) oxidation state. This step is endothermic by 0.61 eV (the reaction free energy is similarly endoergic at 0.48 eV) and generates structure **7** of pathway-1. Structure **15** of pathway-3 is similar in energy to structure **7** as discussed above, so pathway-1 and pathway-3 could potentially both be possible after structure **26**. However, both pathway-1 and pathway-3 have four additional dehydrogenations required before molecular oxygen is generated; thus, reactions from structure **26** would involve five dehydrogenations, and the cycle would not be catalytic. Since structure **26** would not need to be regenerated in the cycle, it suggests that it is not the resting state of the catalyst. Throughout this work, this behavior of a non-regenerative reaction is observed when the starting cubane complex includes more than one manganese atom with a Mn(III) oxidation state.

4.4.6 Mn_4(III III IV IV) configuration with μ_3-hydoxo groups

The versions of structures with μ_3-hydroxo groups are found to be higher in energy than structure **26** with μ_3-oxo groups. Versions of structures with one and two μ_3-hydroxo groups are found to be 0.13 eV and 0.53 eV higher in energy than the μ_3-oxo version, respectively. The structure with a single μ_3-hydroxo group is given as structure **27** in Figure 4.6.

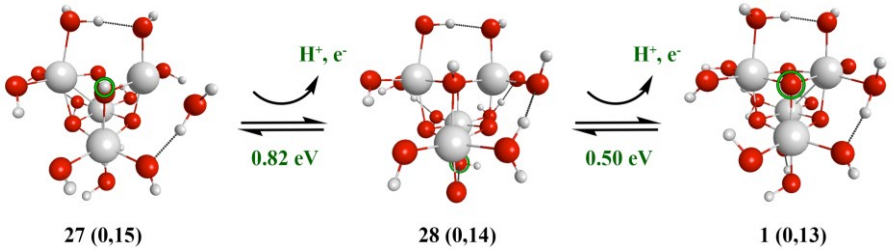

Figure 4.6 First two dehydrogenation reactions of pathway-6 from structure **27** with Mn_4(IV⅔ II⅔ III⅔ III) configuration (lowest energy structure containing μ_3-hydroxo groups related to **26**).

Structure **27** has a Mn_4(IV⅔ II⅔ III⅔ III) formal oxidation state combination. The first step from structure **27** is a dehydrogenation from an aqua ligand at the bottom manganese Mn(III) atom. This step requires 0.82 eV (ΔG = 0.69 eV) in energy and is 0.20 eV higher in energy compared to the first dehydrogenation on **26**. The resulting structure **28** undergoes a consecutive second dehydrogenation requiring 0.50 eV (ΔG = 0.21 eV) of energy to generate structure **1** of pathway-1 (in comparison, as discussed above structure **26** generates structure **7** of pathway-1). This dehydrogenation occurs on a μ_3-hydroxo group. This suggests that μ_3-oxo and μ_3-hydroxo versions act similar and are not capable of regenerating **27** as the resting state of the catalyst.

4.4.7 Mn_4(III III III IV) configuration with μ_3-oxo groups

The Mn_4(III III III IV) oxidation state configuration is found to be 0.48 eV higher in energy than the Mn_4(II III IV IV) oxidation state configuration (structure **29**). Both of these oxidation state combinations have elongated bond lengths (around 0.30 Å longer bond lengths than average manganese aqua ligand bond distances) between the manganese atoms and the aqua ligands. The reaction pathway starts from a dehydrogenation on an aqua ligand attached to Mn(II) atom on the lowest energy structure **29** (pathway-7, Figure 4.7), which then abstracts a hydrogen atom from the adjacent bottom manganese atom.

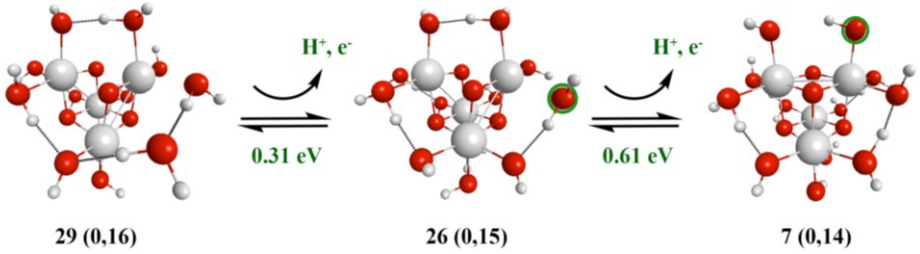

Figure 4.7 First two dehydrogenation reactions of pathway-7 from structure **29** with Mn_4(II IV III IV) configuration.

It should be noted that in all previous structures with μ_3-oxo groups with at least one manganese atom in the Mn(III) oxidation state, the first dehydrogenation occurred from an aqua ligand attached to a Mn(III) atom; however, in this Mn_4(II III IV IV) oxidation state configuration the dehydrogenation proceeds on an aqua ligand attached to the Mn(II) atom, which is the most reduced atom in this system. This first dehydrogenation step is calculated to require 0.31 eV (ΔG = 0.18 eV) in energy, which is the lowest energy dehydrogenation we calculated. The resulting structure rearranges aqua and hydroxy ligands to yield a Mn_4(III III IV IV) configuration, which is similar to structure **26** of pathway-5, indicating that this reaction could eventually proceed through pathway-1 (note: structure **7** and structure **15** are nearly similar in energy so pathway-3 is also a competitive option). This means that **29** would not be regenerated as the resting state of the catalyst in this pathway as well.

4.4.8 Mn_4(III III III IV) configuration with μ_3-hydroxo groups

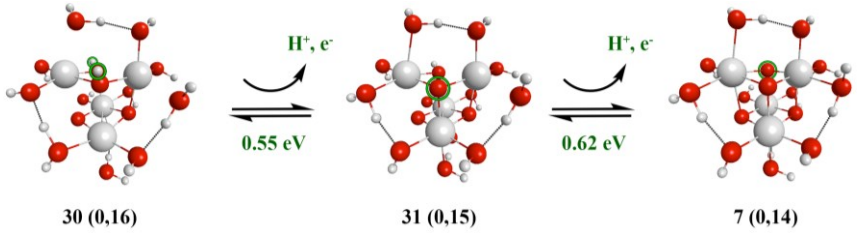

Figure 4.8 First two dehydrogenation reactions of pathway-8 from structure **30** with Mn_4(II⅔ III⅓ III⅓ III⅔) configuration (lowest energy structure containing μ_3-hydroxo groups related to **29**).

The Mn_4(III III III IV) versions with μ_3-hydroxo groups are higher in energy compared to **29** with μ_3-oxo groups. We found that the system with two μ_3-hydroxo groups is the lowest energy version for the Mn_4(III III III IV) combination and this change in ligands changes the formal oxidation states to Mn_4(III⅓ III⅓ III⅔ II⅔). The two μ_3-hydroxo structure **30** (Figure 4.8) is 0.12 eV higher in energy than structure **29**. The first dehydrogenation from structure **30** takes

place at one of the μ_3-oxo groups with 0.55 eV (ΔG = 0.44 eV) of energy to produce structure **31**. This is 0.28 eV higher in energy than the first dehydrogenation of pathway-7 from structure **29**. Consecutively, the second dehydrogenation occurs at the next μ_3-hydroxo group in structure **31** with 0.62 eV (ΔG = 0.48 eV) and generates structure **7** with a Mn_4(III IV IV IV) oxidation state combination. The regeneration of the catalyst with μ_3-hydroxo groups is not favorable.

4.4.9 Mn_4(III III III III) configuration with μ_3-oxo groups

The all Mn_4(III III III III) version with μ_3-oxo groups has elongated bond lengths between the manganese atoms and the aqua ligands suggesting aqua ligands are less favorable to bind with manganese with a Mn(III) oxidation state. The lowest structure we found rearranges to the Mn_4(II III III IV) configuration (structure **32** of pathway-8, Figure 4.9).

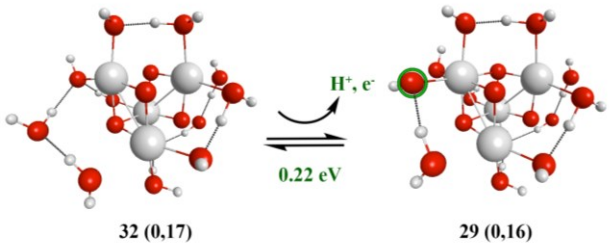

Figure 4.9 First two dehydrogenation reactions of pathway-9 from structure **32** with Mn_4(II III III IV) configuration.

The first dehydrogenation from structure **32** takes place at an aqua ligand attached to the Mn(IV) atom and forms structure **29** of pathway-7. The reaction energy of this step is 0.22 eV (ΔG = 0.06 eV). The manganese atom with Mn(IV) oxidation state has retained its oxidation state by abstracting a hydrogen atom from a bottom manganese atom with Mn(III) oxidation state. The oxidation state of bottom manganese shift from Mn(III) to Mn(IV). Structure **29** eventually continues to pathway-1 or 3 and does not regenerate the catalyst.

4.4.10 Mn_4(III III III III) configuration with μ_3-hydroxo groups

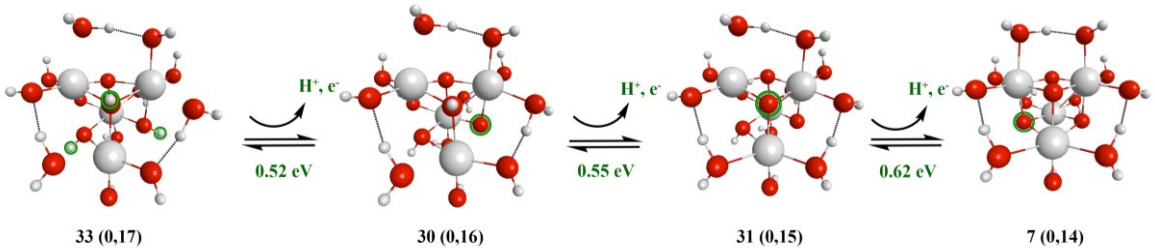

Figure 4.10 First two dehydrogenation reactions of pathway-10 from structure **33** with the Mn_4(II⅓ III⅓ III⅓ V) configuration (lowest energy structure containing μ_3-hydroxo groups related to **32**).

The Mn_4(III III III III) versions with μ_3-hydroxo groups are lower in energy than the corresponding μ_3-oxo version unlike the other μ_3-hydroxo structures we discussed above. We have calculated one, two three and four μ_3-hydroxo versions and they lie -0.42 eV, -0.54 eV, -0.55 eV, and -0.48 eV in energy compared to structure **32**. We used the lowest energy isomer structure **33** (pathway-10 of Figure 4.10) with three μ_3-hydroxo groups and investigated the water splitting process. After three consecutive dehydrogenation reactions, the hydrogen atoms on the three μ_3-hydroxo groups from structure **33** are removed with energies of 0.52 eV, 0.55 eV, and 0.62 eV, respectively (ΔG values are 0.41 eV, 0.44 eV, and 0.48 eV respectively). After the first dehydrogenation reaction, it connects to pathway-8, which connects to structure **7** of pathway-1 with three dehydrogenation reactions. This means that after four dehydrogenations from structure **33**, the system has not produced any active oxo species for the water oxidation process. After the formation of structure **7**, the reaction continues via pathway-1 or 3 but does not regenerate the resting state structure **33**.

4.5 General Discussion

Out of the reaction pathways we investigated for the different formal oxidation state configurations of the manganese cubane complex, we found three reaction pathways that

correspond to resting states with Mn_4(IV IV IV IV), Mn_4(III IV IV IV), and Mn_4(III III IV V) configurations are thermodynamically viable for water oxidation. All these three reaction pathways proceed via nucleophilic attack from a solvent water molecule to the manganese oxo species. The other configurations show a commonality where they connect to one of above configuration reaction pathways. We also note reoccurrence of several other microscopic properties that will be helpful in designing manganese-based water splitting catalysts. Most importantly, we found that the highest energy step in all the reaction pathways we studied here corresponds to the formation of the manganese oxo group. We have likewise demonstrated this property in our theoretical study with manganese dimer complexes.[27] The formation of the oxo group is the most important step as it subsequently leads to O-O bond generation in the reaction. The highest energy step determines the overpotential of a particular catalyst so the feasibility and the efficiency of a catalyst can be determined.

In some cases we noticed rearrangement of investigated oxidation state configurations. For example, Mn_4(III IV IV IV) rearranges to Mn_4(III III IV V) which is nearly similar in energy. The Mn_4(III III III IV) state changes to a Mn_4(II III IV IV) state and the Mn_4(III III III III) rearranges to a Mn_4(II III III IV) oxidation state configuration. The highest formal oxidation states for any manganese atom in the resting state did not surpass the Mn(V) oxidation state. However, we noticed formation of up to Mn(VII) oxidation state during the progress of reaction pathway-3 and pathway-4. We also noticed that similar to our studies with cobalt complexes,[28] after the formation of -OOH species the thermodynamically favorable step is to dehydrogenate the hydrogen on the -OOH group. Sometimes this is seen as an intramolecular hydrogen atom transfer reaction or dehydrogenation of the nearby aqua or hydroxo groups, which eventually results in the hydrogen of the -OOH group transferring to a nearby ligand.

We observed that μ_3-hydroxo versions are generally higher in energy in all the oxidation state configurations except for the Mn_4(III III III III) state (this rearranges to the Mn_4(II III III IV) state). In contrast, in cobalt cubane complexes it has been noticed that μ_3-oxo protonation to form μ_3-hydroxo groups leads to lowering of the energy of the complex.[28, 59] In the lowest energy pathway from Mn_4(IV IV IV IV) and Mn_4(III IV IV IV) (both pathways are embedded in pathway-1), we observed that protonation of the μ_3-oxo group lowers the overpotential of the net reaction. This is mainly because the starting structures of these oxidation state configurations are higher in energy than the other configurations. However, in other configurations this pattern was not a constant property. We also note that compared to the complex with all Mn(IV) oxidation states, the dehydrogenation reactions for systems with Mn(III) oxidation states tend to be lower in energy. When a structure possesses more than one Mn(III) oxidation state in its configuration, we noticed structural distortions to the cubane complex as well as elongated bond lengths between aqua ligands and manganese atoms. This was most significant with all four atoms in the Mn(III) oxidation state.

4.6 Conclusions

In summary, we have employed density functional theory to investigate the water oxidation mechanism on manganese cubane complexes with water-derived ligands. We have investigated oxidation state configurations ranging from Mn_4(IV IV IV IV) to Mn_4(III III III III). Understanding the water oxidation process on these simple forms of manganese cubane complexes is necessary to aid the bottom up design of commercially viable catalysts. We found a reoccurrence of microscopic patterns that may be very helpful in designing water splitting catalysts with a manganese oxide framework. The highest thermodynamic energy for each of the

reaction pathways we studied corresponds to the formation of the Mn-O group and thus this energy can be used as a descriptor to screen efficient water splitting catalysts.

We demonstrated that both μ-oxo and μ-hydroxo versions of Mn_4(IV IV IV IV), Mn_4(III IV IV IV), and Mn_4(III III IV V) configurations are thermodynamically favorable for the water oxidation process. Note that these three reaction pathways show a common mechanistic feature where they undergo nucleophilic attack from a solvent water molecule to the manganese oxo species. In both μ-oxo and μ-hydroxo versions of Mn_4(IV IV IV IV) and Mn_4(III IV IV IV) structures this nucleophilic attack takes place on a Mn(VI)O group whereas in both μ-oxo and μ-hydroxo Mn_4(III III IV V) configurations this occurs on a Mn(VII)O species. The other investigated oxidation state configurations connect to one of these three pathways. They can essentially extract oxygen but cannot regenerate the resting state of the catalysts. In some of the oxidation state configuration we investigated, a rearrangement of oxidation state configurations into other low energy configurations is found. In each oxidation state configuration ranging from all Mn(IV) to all Mn(III), we investigated two types of structures: one with μ_3-oxo groups and one with μ_3-hydroxo groups. The latter μ_3-hydroxo versions of the oxidation state configurations generally tend to be higher in energy than the μ_3-oxo bridged versions except for the Mn_4(III III III III) state. The highest formal oxidation state for any manganese atom in the resting state configurations was Mn(V). During the progress of the catalytic cycle, the Mn(VII) oxidation state was formed in reaction pathway-3 and pathway-4. When a structure has more than one Mn(III) oxidation state, structural distortions to the cubane complex as well as elongated bond lengths between aqua ligands and manganese atoms are evident. We expect this study will be helpful to expand knowledge of the factors affecting the mechanism of water splitting catalysts

and will be essential for the bottom up design and engineering of efficient water splitting catalysts in the future.

4.7 Acknowledgements

This material is based on work supported by the National Science Foundation under Grant No. CHE-0955515. C.M.A. is grateful to the Camille and Henry Dreyfus Foundation for a Camille Dreyfus Teacher-Scholar Award (2011-2016). The computing for this project was performed on the Beocat Research Cluster at Kansas State University, which is funded in part by NSF grants CNS-1006860, EPS-1006860, and EPS-0919443.

4.8 References

1. Umena, Y.; Kawakami, K.; Shen, J.-R.; Kamiya, N. Crystal Structure of Oxygen-Evolving Photosystem II at a Resolution of 1.9 Å. *Nature* **2011,** *473*, 55-60.

2. Fernando, A.; Weerawardene, K. L. D. M.; Karimova, N. V.; Aikens, C. M. Quantum Mechanical Studies of Large Metal, Metal Oxide, and Metal Chalcogenide Nanoparticles and Clusters. *Chem. Rev.* **2015,** *115*, 6112-6216.

3. Siegbahn, P. E. M. O-O Bond Formation in the S_4 State of the Oxygen-Evolving Complex in Photosystem II. *Chem. Eur. J.* **2006,** *12*, 9217-9227.

4. Siegbahn, P. E. M. A Structure-Consistent Mechanism for Dioxygen Formation in Photosystem II. *Chem. Eur. J.* **2008,** *14*, 8290-8302.

5. Siegbahn, P. E. M. Structures and Energetics for O_2 Formation in Photosystem II. *Acc. Chem. Res.* **2009,** *42*, 1871-1880.

6. Siegbahn, P. E. M. An Energetic Comparison of Different Models for the Oxygen Evolving Complex of Photosystem II. *J. Am. Chem. Soc.* **2009,** *131*, 18238-18239.

7. Siegbahn, P. E. M. Water Oxidation in Photosystem II: Oxygen Release, Proton Release and the Effect of Chloride. *Dalton Trans.* **2009**, 10063-10068.

8. Siegbahn, P. E. M. The Effect of Backbone Constraints: The Case of Water Oxidation by the Oxygen-Evolving Complex in PSII. *ChemPhysChem* **2011,** *12*, 3274-3280.

9. Siegbahn, P. E. M. Recent Theoretical Studies of Water Oxidation in Photosystem II. *J. Photochem. Photobiol., B* **2011,** *104*, 94-99.

10. Siegbahn, P. E. M. Mechanisms for Proton Release During Water Oxidation in the S_2 to S_3 and S_3 to S_4 Transitions in Photosystem II. *Phys. Chem. Chem. Phys.* **2012,** *14*, 4849-4856.

11. Siegbahn, P. E. M. Water Oxidation Mechanism in Photosystem II, Including Oxidations, Proton Release Pathways, O—O Bond Formation and O_2 Release. *Biochim. Biophys. Acta, Bioenerg.* **2013,** *1827*, 1003-1019.

12. Siegbahn, P. E. M.; Blomberg, M. R. A. Energy Diagrams for Water Oxidation in Photosystem II Using Different Density Functionals. *J. Chem. Theory Comput.* **2013,** *10*, 268-272.

13. Sproviero, E.; McEvoy, J.; Gascón, J.; Brudvig, G.; Batista, V. Computational Insights into the O_2-Evolving Complex of Photosystem II. *Photosynth. Res.* **2008,** *97*, 91-114.

14. Sproviero, E.; Newcomer, M.; Gascón, J.; Batista, E.; Brudvig, G.; Batista, V. The MoD-QM/MM Methodology for Structural Refinement of PhotosystemII and other Biological Macromolecules. *Photosynth. Res.* **2009,** *102*, 455-470.

15. Sproviero, E. M.; Gascon, J. A.; McEvoy, J. P.; Brudvig, G. W.; Batista, V. S. Characterization of Synthetic Oxomanganese Complexes and the Inorganic Core of the O_2-Evolving Complex in Photosystem II: Evaluation of the DFT/B3LYP Level of Theory. *J. Inorg. Biochem.* **2006,** *100*, 786-800.

16. Sproviero, E. M.; Gascón, J. A.; McEvoy, J. P.; Brudvig, G. W.; Batista, V. S. QM/MM Models of the O_2-Evolving Complex of Photosystem II. *J. Chem. Theory Comput.* **2006,** *2*, 1119-1134.

17. Sproviero, E. M.; Gascón, J. A.; McEvoy, J. P.; Brudvig, G. W.; Batista, V. S. A Model of the Oxygen-Evolving Center of Photosystem II Predicted by Structural Refinement Based on EXAFS Simulations. *J. Am. Chem. Soc.* **2008,** *130*, 6728-6730.

18. Sproviero, E. M.; Gascón, J. A.; McEvoy, J. P.; Brudvig, G. W.; Batista, V. S. Quantum Mechanics/Molecular Mechanics Study of the Catalytic Cycle of Water Splitting in Photosystem II. *J. Am. Chem. Soc.* **2008,** *130*, 3428-3442.

19. Sproviero, E. M.; Gascón, J. A.; McEvoy, J. P.; Brudvig, G. W.; Batista, V. S. Computational Studies of the O_2-Evolving Complex of Photosystem II and Biomimetic Oxomanganese Complexes. *Coord. Chem. Rev.* **2008,** *252*, 395-415.

20. Yachandra, V. K.; Sauer, K.; Klein, M. P. Manganese Cluster in Photosynthesis: Where Plants Oxidize Water to Dioxygen. *Chem. Rev.* **1996,** *96*, 2927-2950.

21. Yamaguchi, K.; Isobe, H.; Yamanaka, S.; Saito, T.; Kanda, K.; Shoji, M.; Umena, Y.; Kawakami, K.; Shen, J. R.; Kamiya, N.; Okumura, M. Full Geometry Optimizations of the Mixed-Valence $CaMn_4O_4X(H_2O)_4$ (X=OH or O) Cluster in OEC of PS II: Degree of Symmetry Breaking of the Labile Mn-X-Mn Bond Revealed by Several Hybrid DFT Calculations. *Int. J. Quantum Chem.* **2013,** *113*, 525-541.

22. Yamaguchi, K.; Yamanaka, S.; Isobe, H.; Saito, T.; Kanda, K.; Umena, Y.; Kawakami, K.; Shen, J. R.; Kamiya, N.; Okumura, M.; Nakamura, H.; Shoji, M.; Yoshioka, Y. The Nature of Chemical Bonds of the $CaMn_4O_5$ Cluster in Oxygen Evolving Complex of Photosystem II: Jahn-Teller Distortion and its Suppression by Ca Doping in Cubane Structures. *Int. J. Quantum Chem.* **2013,** *113*, 453-473.

23. Yamanaka, S.; Isobe, H.; Kanda, K.; Saito, T.; Umena, Y.; Kawakami, K.; Shen, J. R.; Kamiya, N.; Okumura, M.; Nakamura, H.; Yamaguchi, K. Possible Mechanisms for the O–O

Bond Formation in Oxygen Evolution Reaction at the $CaMn_4O_5(H_2O)_4$ Cluster of PSII Refined to 1.9 Å X-ray Resolution. *Chem. Phys. Lett.* **2011,** *511*, 138-145.

24. Yamanaka, S.; Saito, T.; Kanda, K.; Isobe, H.; Umena, Y.; Kawakami, K.; Shen, J. R.; Kamiya, N.; Okumura, M.; Nakamura, H.; Yamaguchi, K. Structure and Reactivity of the Mixed-Valence $CaMn_4O_5(H_2O)_4$ and $CaMn_4O_4(OH)(H_2O)_4$ Clusters at Oxygen Evolution Complex of Photosystem II. Hybrid DFT (UB3LYP and UBHandHLYP) Calculations. *Int. J. Quantum Chem.* **2012,** *112*, 321-343.

25. Brimblecombe, R.; Bond, A. M.; Dismukes, G. C.; Swiegers, G. F.; Spiccia, L. Electrochemical Investigation of Mn_4O_4-Cubane Water-Oxidizing Clusters. *Phys. Chem. Chem. Phys.* **2009,** *11*, 6441-6449.

26. Brimblecombe, R.; Swiegers, G. F.; Dismukes, G. C.; Spiccia, L. Sustained Water Oxidation Photocatalysis by a Bioinspired Manganese Cluster. *Angew. Chem. Int. Ed.* **2008,** *47*, 7335-7338.

27. Fernando, A.; Haddock, T.; Aikens, C. M. Theoretical Investigation of Water Oxidation on Fully Saturated Mn_2O_3 and Mn_2O_4 Complexes. *J. Phys. Chem. A*, Submitted.

28. Fernando, A.; Aikens, C. M. Reaction Pathways for Water Oxidation to Molecular Oxygen Mediated by Model Cobalt Oxide Dimer and Cubane Catalysts. *J. Phys. Chem. C* **2015,** *119*, 11072-11085.

29. Fernando, A.; Aikens, C. M. Ab Initio Electronic Structure Study of a Model Water Splitting Dimer Complex. *Phys. Chem. Chem. Phys.* **2015,** *17*, 32443-32454.

30. Kanady, J. S.; Tsui, E. Y.; Day, M. W.; Agapie, T. A Synthetic Model of the Mn_3Ca Subsite of the Oxygen-Evolving Complex in Photosystem II. *Science* **2011,** *333*, 733-736.

31. Mukherjee, S.; Stull, J. A.; Yano, J.; Stamatatos, T. C.; Pringouri, K.; Stich, T. A.; Abboud, K. A.; Britt, R. D.; Yachandra, V. K.; Christou, G. Synthetic Model of the Asymmetric $[Mn_3CaO_4]$ Cubane Core of the Oxygen-Evolving Complex of Photosystem II. *Proc. Natl. Acad. Sci. U. S. A.* **2012,** *109*, 2257-2262.

32. Sarkar, S.; Kabir, M.; Greenblatt, M.; Saha-Dasgupta, T. The Role of an Oxometallic Complex in OH Dissociation During Water Oxidation: A Microscopic Insight from DFT Study. *J. Mater. Chem. A* **2013,** *1*, 10422-10428.

33. Matheu, R.; Ertem, M. Z.; Benet-Buchholz, J.; Coronado, E.; Batista, V. S.; Sala, X.; Llobet, A. Intramolecular Proton Transfer Boosts Water Oxidation Catalyzed by a Ru Complex. *J. Am. Chem. Soc.* **2015,** *137*, 10786-10795.

34. Kanan, M. W.; Nocera, D. G. In Situ Formation of an Oxygen-Evolving Catalyst in Neutral Water Containing Phosphate and Co^{2+}. *Science* **2008,** *321*, 1072-1075.

35. McAlpin, J. G.; Stich, T. A.; Ohlin, C. A.; Surendranath, Y.; Nocera, D. G.; Casey, W. H.; Britt, R. D. Electronic Structure Description of a $Co(III)_3Co(IV)O_4$ Cluster: A Model for the Paramagnetic Intermediate in Cobalt-Catalyzed Water Oxidation. *J. Am. Chem. Soc.* **2011,** *133*, 15444-15452.

36. McCool, N. S.; Robinson, D. M.; Sheats, J. E.; Dismukes, G. C. A Co_4O_4 "Cubane" Water Oxidation Catalyst Inspired by Photosynthesis. *J. Am. Chem. Soc.* **2011,** *133*, 11446-11449.

37. Evangelisti, F.; Güttinger, R.; Moré, R.; Luber, S.; Patzke, G. R. Closer to Photosystem II: A Co_4O_4 Cubane Catalyst with Flexible Ligand Architecture. *J. Am. Chem. Soc.* **2013,** *135*, 18734-18737.

38. Ruettinger, W. F.; Campana, C.; Dismukes, G. C. Synthesis and Characterization of Mn4O4L6 Complexes with Cubane-like Core Structure: A New Class of Models of the Active Site of the Photosynthetic Water Oxidase. *J. Am. Chem. Soc.* **1997,** *119*, 6670-6671.

39. Pence, L. E.; Caneschi, A.; Lippard, S. J. Synthesis, Structural Studies, and Magnetic Exchange Interactions in Low-Valent Manganese Alkoxide Cubes. *Inorg. Chem.* **1996,** *35*, 3069-3072.

40. Taft, K. L.; Caneschi, A.; Pence, L. E.; Delfs, C. D.; Papaefthymiou, G. C.; Lippard, S. J. Iron and Manganese Alkoxide Cubes. *J. Am. Chem. Soc.* **1993,** *115*, 11753-11766.

41. Wang, S.; Tsai, H.-L.; Hagen, K. S.; Hendrickson, D. N.; Christou, G. New Structural Type in Manganese Carboxylate Chemistry via Coupled Oxidation/Oxide Incorporation: Potential Insights into Photosynthetic Water Oxidation. *J. Am. Chem. Soc.* **1994,** *116*, 8376-8377.

42. Wang, S.; Tsai, H.-L.; Streib, W. E.; Christou, G.; Hendrickson, D. N. Bromide Incorporation into a High-Oxidation-State Manganese Aggregate, and Reversible Redox Processes for the $[Mn_4O_3X(OAc)_3(dbm)_3]$(X = Cl, Br) Complexes. *J. Chem. Soc., Chem. Commun.* **1992**, 1427-1429.

43. Sessoli, R.; Tsai, H. L.; Schake, A. R.; Wang, S.; Vincent, J. B.; Folting, K.; Gatteschi, D.; Christou, G.; Hendrickson, D. N. High-Spin Molecules: $[Mn_{12}O_{12}(O_2CR)_{16}(H_2O)_4]$. *J. Am. Chem. Soc.* **1993,** *115*, 1804-1816.

44. Kanady, J. S.; Mendoza-Cortes, J. L.; Tsui, E. Y.; Nielsen, R. J.; Goddard, W. A.; Agapie, T. Oxygen Atom Transfer and Oxidative Water Incorporation in Cuboidal Mn3MOn Complexes Based on Synthetic, Isotopic Labeling, and Computational Studies. *J. Am. Chem. Soc.* **2013,** *135*, 1073-1082.

45. Lee, C.; Aikens, C. M. Water Splitting Processes on Mn_4O_4 and $CaMn_3O_4$ Model Cubane Systems. *J. Phys. Chem. A* **2015,** *119*, 9325-9337.

46. Li, X.; Siegbahn, P. E. M. Water Oxidation for Simplified Models of the Oxygen-Evolving Complex in Photosystem II. *Chem. Eur. J.* **2015,** *21*, 18821-18827.

47. Krewald, V.; Neese, F.; Pantazis, D. A. On the Magnetic and Spectroscopic Properties of High-Valent Mn_3CaO_4 Cubanes as Structural Units of Natural and Artificial Water-Oxidizing Catalysts. *J. Am. Chem. Soc.* **2013,** *135*, 5726-5739.

48. Lang, S. M.; Fleischer, I.; Bernhardt, T. M.; Barnett, R. N.; Landman, U. Dimensionality Dependent Water Splitting Mechanisms on Free Manganese Oxide Clusters. *Nano Lett.* **2013,** *13*, 5549-5555.

49. Lang, S. M.; Fleischer, I.; Bernhardt, T. M.; Barnett, R. N.; Landman, U. Water Deprotonation via Oxo-Bridge Hydroxylation and ^{18}O-Exchange in Free Tetra-Manganese Oxide Clusters. *J. Phys. Chem. C* **2015,** *119*, 10881-10887.

50. Lang, S. M.; Bernhardt, T. M.; Kiawi, D. M.; Bakker, J. M.; Barnett, R. N.; Landman, U. The Interaction of Water with Free $Mn_4O_4^+$ Clusters: Deprotonation and Adsorption-Induced Structural Transformations. *Angew. Chem. Int. Ed.* **2015,** *54*, 15113-15117.

51. te Velde, G.; Bickelhaupt, F. M.; Baerends, E. J.; Fonseca Guerra, C.; van Gisbergen, S. J. A.; Snijders, J. G.; Ziegler, T. Chemistry with ADF. *J. Comput. Chem.* **2001,** *22*, 931-967.

52. Becke, A. D. Density-Functional Exchange-Energy Approximation with Correct Asymptotic Behavior. *Phys. Rev. A* **1988,** *38*, 3098-3100.

53. Perdew, J. P. Density-Functional Approximation for the Correlation Energy of the Inhomogeneous Electron Gas. *Phys. Rev. B* **1986,** *33*, 8822-8824.

54. Britt, R. D.; Suess, D. L. M.; Stich, T. A. An Mn(V)–Oxo Role in Splitting Water? *Proc. Natl. Acad. Sci. U. S. A.* **2015,** *112*, 5265-5266.

55. Lundberg, M.; Blomberg, M. R. A.; Siegbahn, P. E. M. Oxyl Radical Required for O−O Bond Formation in Synthetic Mn-Catalyst. *Inorg. Chem.* **2003,** *43*, 264-274.

56. Neu, H. M.; Baglia, R. A.; Goldberg, D. P. A Balancing Act: Stability versus Reactivity of Mn(O) Complexes. *Acc. Chem. Res.* **2015,** *48*, 2754-2764.

57. Yang, J.; An, H.; Zhou, X.; Li, C. Water Oxidation Mechanism on Alkaline-Earth-Cation Containing Birnessite-Like Manganese Oxides. *J. Phys. Chem. C* **2015,** *119*, 18487-18494.

58. Aakesson, R.; Pettersson, L. G. M.; Sandstroem, M.; Wahlgren, U. Theoretical Calculations of the Jahn-Teller effect in the Hexahydrated Copper(II), Chromium(II), and Manganese(III) ions, Hexaaquacopper(2+), Hexaaquachromium(2+) and Hexaaquamanganese(3+), and Comparisons with the Hexahydrated Copper(I), Chromium(III), and Manganese(II) clusters. *J. Phys. Chem.* **1992,** *96*, 150-156.

59. Li, X.; Siegbahn, P. E. M. Water Oxidation Mechanism for Synthetic Co–Oxides with Small Nuclearity. *J. Am. Chem. Soc.* **2013,** *135*, 13804-13813.

Chapter 5 - Ab initio electronic structure study of a model water splitting dimer complex

Reproduced by permission of the PCCP Owner Societies:

Fernando, A; Aikens, C. M. *Phys. Chem. Chem. Phys.* **2015**, 17, 32443-32454.

5.1 Abstract

A model manganese dimer electrocatalyst bridged by μ-OH ligands is used to investigate changes in spin states that may occur during water oxidation. We have employed restricted open-shell Hartree-Fock (ROHF), second-order Møller-Plesset perturbation theory (MP2), complete active space self-consistent field (CASSCF), and multireference second-order Møller-Plesset perturbation theory (MRMP2) calculations to investigate this system. Multiconfigurational methods like CASSCF and MRMP2 are appropriate methods to study these systems with antiferromagentically-coupled electrons. Orbital occupations and distributions have been closely analyzed to understand the electronic details and contributions to the water splitting from manganese and oxygen atoms. The presence of Mn(IV)O$^{\bullet}$ radical moieties has been observed in this catalytic pathway. Multiple nearly degenerate excited states were found close to the ground state in all structures. This suggests competing potential energy landscapes near the ground state may influence the reactivity of manganese complexes such as the dimers studied in this work.

5.2 Introduction

Water splitting has been a popular topic over the past few decades as a clean and sustainable way to produce hydrogen. In green plants and in cyanobacteria, the oxygen evolving complex (OEC) of photosystem II (PSII) catalyzes the water oxidation reaction. The active site of the OEC consists of a $CaMn_4O_5$ cuboidal structure and there have been many extensive

theoretical and experimental studies related to determining its electronic structure, properties, oxidative activation and mechanism of water oxidation.[1-12]

Inspired by this cuboidal structure, many synthetic and model catalysts have been proposed that contain high-valent multinuclear manganese μ-oxo bridged complexes.[13-23] The first reports of water oxidation by a dimanganese complex date back to 1985 when Ashmawy and coworkers[13] synthesized a $[\{Mn(salpd)(H_2O)\}_2][ClO_4]_2$ [salpd = propane-l,3-diylbis (salicylideneiminate)] complex that evolves oxygen when irradiated in the presence of a p-benzoquinone. Watkinson and coworkers[14] also reported a dinuclear manganese complex that evolves O_2 in the presence of a p-benzoquinone in 1994. The first functional model of a μ-oxo bridged manganese dimer ($[H_2O(terpy)Mn(O)_2Mn(terpy)OH_2](NO_3)_3$) was reported by Limburg *et al*.[15] This compound is capable of catalyzing the oxygen evolution reaction similarly to the OEC. Collomb and coworkers[16] synthesized this compound independently at the same time as Limburg and coworkers. Formation of a Mn(V)=O species during O-O bridging was first reported by Naruta *et al*.[17] with a porphyrin type Mn(III) dimer. A four electron water oxidation reaction catalyst ($[Mn_2(mcbpen)_2(H_2O)_2](ClO_4)_2$) (mcbpen = *N*-methyl-*N'*-carboxymethyl-*N,N'*-bis(2-pyridylmethyl)ethane-1,2-diamine) synthesized by Poulsen *et al*.[18] has been reported to generate oxygen with the presence of a tert-butylhydrogenperoxide as an oxidant. These μ-oxo bridged manganese complexes for water oxidation have been reviewed thoroughly by Mullins,[19] Liu,[20] Yagi,[21] Mukhopadhyay,[22] and Wu *et al*.[23]

Electronic structure, charge distribution, and spin coupling of manganese μ-oxo compounds surrounded by triazacyclonoane and acetate have been studied in detail by Zhao and coworkers.[24] Their calculated charge distribution showed strong metal-ligand covalency. Blomberg *et al*.[25] reported a theoretical study of a number of model manganese compounds

including μ-oxo bridged manganese complexes. With hybrid density functional theory (DFT) calculations even without using formally correct spin coupling, they were able to reproduce the experimentally known preference for antiferromagnetic coupling between manganese spins. One interesting finding is that because of the small difference in electronic structure between high spin and low spin states, the optimized geometries for these two states were identical.[25] McGrady and coworkers[26] studied the structural and electronic properties of reduction and oxidation of a peroxo-bridged Mn dimer ($Mn_2(\mu\text{-}O)_2(\mu\text{-}O_2)(NH_3)_6^{2+}$). They reported that reductive cleavage of the O-O σ bond is favorable when the manganese centers are antiferromagentically coupled and that ferromagnetic coupling of the manganese centers favors the oxidative formation of the π component of the O-O bond.[26] Lundberg *et al*.[27] have also investigated the μ-oxo bridged manganese dimer ($[H_2O(terpy)Mn(O)_2Mn(terpy)OH_2](NO_3)_3$) to find out the requirements for O-O bond formation in manganese complexes. They determined that the active synthetic catalyst forms a stable Mn(IV) oxyl radical state rather than the Mn(V)-oxo state.[27] A very recent paper by Zhou *et al*.[28] indicates that the aqua ligand environment has an almost symmetric influence on the Mn(III) and Mn(IV) centers even with the hydrogen bonds considered explicitly.

It is known that some 3d transition metals such as Mn show a poor overlap between the 3d and ligand orbitals.[29] This results in orbital near degeneracies and nondynamical correlations.[29] So, the applicability of DFT methods to account for these electron correlations remains questionable. The systems with 3d orbitals also give rise to several low-lying excited states of various multiplicities, which results in surface crossing effects. Such systems with near degenerate electronic states may have antiferromagnetic coupling of Mn atoms.[29] Busch *et al*.[30] have studied a system based on high spin states in a ferromagnetic arrangement that can be treated by standard DFT methods. However, the potential antiferromagnetic coupling in these

systems can be most appropriately described by multi-determinantal wave function representations. Multi-configurational wave function-based methods like complete active space self-consistent field (CASSCF) and multireference 2nd order Møller-Plesset perturbation theory (MRMP2) are methods that can be used in this type of calculation. Choosing the active space for this type of calculation is very important. Electrons and orbitals involved should include those necessary to treat all the important bonding features yet should not be unnecessarily large because they need to remain computationally tractable.

Very few studies have been reported using CASSCF calculations on ligated manganese compounds. Among them, Mn(salen) complex is a popular system that has a high-yield catalytic activity towards enantioselective epoxidation of unfunctionalized olefins. A debatable question with these Mn(salen) complexes is the relative stability of the singlet, triplet and quintet states. Sears *et al*.[29] and Ivanic *et al*.[31] reported a CASSCF study of a model oxoMn(salen) complex to address this issue. Ivanic *et al*.[31] first studied the system with 12 electrons in 11 active space orbitals (CASSCF(12/11)); later, Sears and coworkers[29] used CASSCF(8/7) to study this system. This smaller active space was chosen after examining the unrestricted Hartree-Fock (UHF) natural orbital occupation numbers. Their reports indicated a closed shell singlet as the ground state and that the triplet states are around 3 kcal mol^{-1} higher in energy whereas a quintet state lies at a little more than 40 kcal mol^{-1}. The relative energies calculated using different active spaces differed by 0.5 kcal mol^{-1} for all the states except for the quintet state whose difference was 1.4 kcal mol^{-1}. It is noteworthy that their UHF solutions to the calculations were highly spin-contaminated. In 2014, Wouters and coworkers[32] studied this system with the density matrix renormalization group (DMRG) method with 28 electrons in 22 orbitals. Inclusion of such a large active space is feasible with the DMRG numerical technique. In comparison with previous

results, they found that the triplet is 5 kcal mol^{-1} more stable than the singlet state whereas the quintet lies 12-14 kcal mol^{-1} higher than the singlet state.

With recent advances in the DMRG method, Kurashige and coworkers[33] computed the many-electron wavefunctions of the OEC of PSII with more than 10^{18} quantum degrees of freedom. They confirmed that the S_1 state of the OEC is in the Mn^{III} Mn^{IV} Mn^{IV} Mn^{III} oxidation state that has been established previously; furthermore, they identified multiple low-lying energy states near the S_1 state. The active space they chose for the DMRG-CASSCF calculations is 44 electrons in 35 orbitals.

Other work has also been performed on manganese and manganese-calcium cubane systems related to the OEC of PSII. Numerous recent studies have examined the electronic structure of these systems using high-spin and broken-symmetry DFT calculations. For example, Yamaguchi and coworkers[34] employed UB3LYP and UBHandHLYP calculations to investigate the mixed valance $Ca_4Mn_4O_4X(H_2O)_4$ (X=OH or O) complex. The authors indicated that the degree of symmetry breaking of the Mn-O-Mn bond is not significant with these levels of theory whereas it is predicted to be higher with other hybrid DFT methods. Yamaguchi *et al*.[35] also reported a study of the mixed valance configurations of Mn_5O_5, $CaMn_4O_5$, and $Ca_2Mn_3O_5$ complexes with UB3LYP calculations. The computational results with Mn_5O_5 demonstrated the instability of the uniform-valance structure of $Mn(III)_5O_5$ due to the Jahn-Teller effect of trivalent Mn ion affording a mixed-valance configuration. Krewald *et al*.[36] investigated a high-valent $Mn(IV)_3CaO_4$ complex and demonstrated that the these systems have a ground state with spin 9/2. Recently, Krewald[37] and coworkers have shown that only a high-valent scheme with $Mn(III)_3Mn(IV)$ for the S_0 state up to $Mn(IV)_4$ for the S_3 state can account for the observed spectroscopic data of the semi-stable intermediate states.

These studies with DFT (high spin and broken symmetry approaches) as well as multireference and multiconfiguration methods show the complexity of orbital configuration in manganese and how the surrounding ligand environment plays a major role in describing the chemistry of these systems. These complexes are capable of releasing oxygen electrochemically, photochemically, and in the presence of primary oxidants. In the present study we examine a model catalyst proposed by Busch *et al*.[30] The model catalyst consists of two manganese atoms with a simplified version of the acetylacetonate ligand (in which methyl is replaced by hydrogen) on each atom (structure **1** in Figure 5.1). The purpose of the selection of this model compound is valuable as the two manganese atoms are surrounded by six oxygen atoms, which is similar in that regard to a bulk MnO_2 surface. Capping the manganese atoms with the acetylacetonate ligand ensures that the catalyst is governed towards a direct coupling of two radical moieties. Furthermore, the starting structure with two aqua ligands on top of manganese atoms represents a bulk manganese oxide immersed in a neutral medium with aqua ligands adsorbed to the surface. These factors lead us to conclude that the selected model system is capable of mimicking the actual bulk oxide surface to a satisfactory degree. A synthetic organometallic compound with a similar skeleton to this model catalyst has also been reported as an enhanced magnetic cooler by Manoli and coworkers.[38] The resting state of the catalyst exhibits two water molecules ligated to Mn(III) atoms and these Mn atoms are bridged by hydroxyl groups to balance the neutral charge of the catalyst. The catalytic mechanism proposed[30] is a general direct coupling pathway through Mn-O$^{\bullet}$ radical species that consists of electrochemical steps and chemical steps. It should be noted this radical species is predicted in our current work to be a Mn(IV)-O$^{\bullet}$ group. This will be discussed in detail in the results and discussion. Each electrochemical step experiences a proton coupled electron transfer (PCET) reaction similar to the OEC of PSII. This type of direct

coupling reactions via adjacent oxo radicals has been proposed in ruthenium blue dimer[39, 40] and cobalt oxide catalyst[41] water oxidation systems. A reference system of TyrOH/TyrO$^{\bullet}$ has been used, which has a reduction potential of 0.94 V relative to the normal hydrogen electrode (NHE). The theoretical water oxidation potential value is around 1.23 V with respect to the NHE. This simplified theoretical catalyst system mimics the water oxidation process in a Mn dimer compound.

In this study, we employ both multiconfigurational and mutireference methods to investigate the electronic structure and energetics of this system. These higher levels of theory can account for a detailed description of underlying electronic states that contribute to the catalyst cycle. The primary focus of this study is to observe the orbital configurations that contribute at different stages of this direct-coupling pathway and provide detailed understanding of the electronic states at each stage of the catalytic cycle. We also acknowledge to the readers that these ab initio methods also have their own limitations: in order to accurately address the system of interest we have to carefully select the active space in multiconfigurational calculations. Even with current computational power it is not feasible to include all the valance electrons in this system. Nonetheless, we believe our investigation of electronic excited states and orbitals involved in such reaction pathway may helpful to increase the knowledge base of catalytic water oxidation systems. We find that many nearly degenerate excited states with different spin are present in these systems.

5.3 Computational Methods

All the restricted open-shell Hartree-Fock (ROHF),[42] second-order Møller-Plesset perturbation theory (MP2) using the z-averaged perturbation theory (ZAPT2) approach,[43-45] CASSCF,[46-49] and MRMP2[50-55] calculations in this work employed the code implemented in the

General Atomic and Molecular Electronic Structure System (GAMESS) program.[56, 57] We have selected an active space with 8 electrons distributed among 10 orbitals CASSCF(8/10), which is physically motivated for the first cluster shown in our study. These 10 orbitals for the first structure include the five 3d orbitals from both Mn atoms and can account for the important bonding features happening around the two Mn atoms in the structures. We have examined expanding the active space to 12, 14, and 16 active orbitals by adding the doubly occupied ring π orbitals and corresponding ring π^* orbitals to the active space as described below, but the natural orbital occupation numbers obtained were at least 1.95 for the doubly occupied orbitals. Furthermore, orbitals of the bridging hydroxo groups were also included in the active space to check their contribution to the behavior of this system. We included 16 active orbitals and found that the orbitals have occupations of at least 1.98, so they are well represented when included in the doubly occupied space. The CASSCF(8/10) active space is used throughout the calculations unless otherwise mentioned.

Since accuracy and the convergence of CASSCF calculations depend on the initial input orbitals, choosing a good set of orbitals is always important. In order to improve SCF orbitals as good starting molecular orbitals, several methods available in GAMESS have been used. For example, generating valance virtual orbitals (VVOs), getting a more localized set of occupied orbitals while retaining symmetry using a Boys localization procedure[58] using a symmetry localization approach implemented in GAMESS, or a combination of these methods have been used. The initial set of orbitals was carefully analyzed and reordered as necessary to find the optimal set of orbitals for each structure. All the calculations executed in this study use a triple zeta valance basis set with d and p polarization functions (TZVP).[59, 60] Single point MRMP2 calculations have been performed in order to get better estimates of the relative energies where

necessary. Orbital diagrams reported in all the figures have been calculated with a contour value of 0.03.

5.4 Results and discussion

All the intermediate states in the reaction pathway are initially optimized with ROHF for high-spin states using a TZVP basis set (Figure 5.1). This catalytic cycle was previously reported in Ref. 30 using the B3LYP/6-311++G level of theory. The cycle consists of four electrochemical steps, in which a proton and electron are removed from the Mn complex, and three chemical steps. The two aqua ligands attached to the top of the structure **1** undergo four consecutive dehydrogenations in four electrochemical steps to form structure **5** with two Mn(IV)-O$^{\bullet}$ radical groups. The two radical oxo groups attack each other and generate the O-O bridge on structure **6**. With two consecutive water addition reactions we can break the two Mn-O bonds and extract O_2 from the catalyst. Structures **1-5** have 86 doubly occupied orbitals and structures **6** and **7** possess 85 and 90 doubly occupied orbitals, respectively.

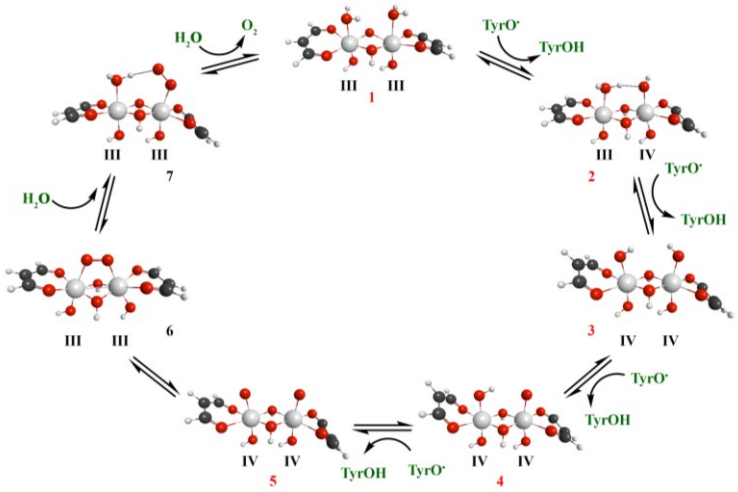

Figure 5.1 ROHF/TZVP optimized structures for the mechanism reported in Ref. 30. Red numbers indicate the electrochemical pathway and the black numbered structures are generated from purely chemical steps. Small white spheres represent hydrogen atoms and large grey spheres represent manganese atoms. Carbon and oxygen atoms are represented by black and red spheres. This color code is used in all figures.

We have employed MP2 level single point energy calculations on the high spin states of ROHF optimized structures of the catalyst. A comparison of these reaction energies is given in Figure 5.2. The reaction energy pattern for the catalytic cycle shows similar behavior with both levels of theory. After the formation of Mn(IV)-O$^{\bullet}$ bonds (structure **5**), the chemical step of forming the O-O bond (structure **6**) is a downhill reaction. The most positive reaction energy difference of the cycle is found between structures **6** and **7**, where attack of a water molecule on the peroxo bridged structure occurs. The reaction energies between structures **4**, **5**, and **6** hints at the flexibility of the direct coupling of the oxo radicals. Except for the catalyst regeneration step (**7** to **1**), ROHF calculations generally overestimate the relative energies of the structures compared to the MP2 single point energies.

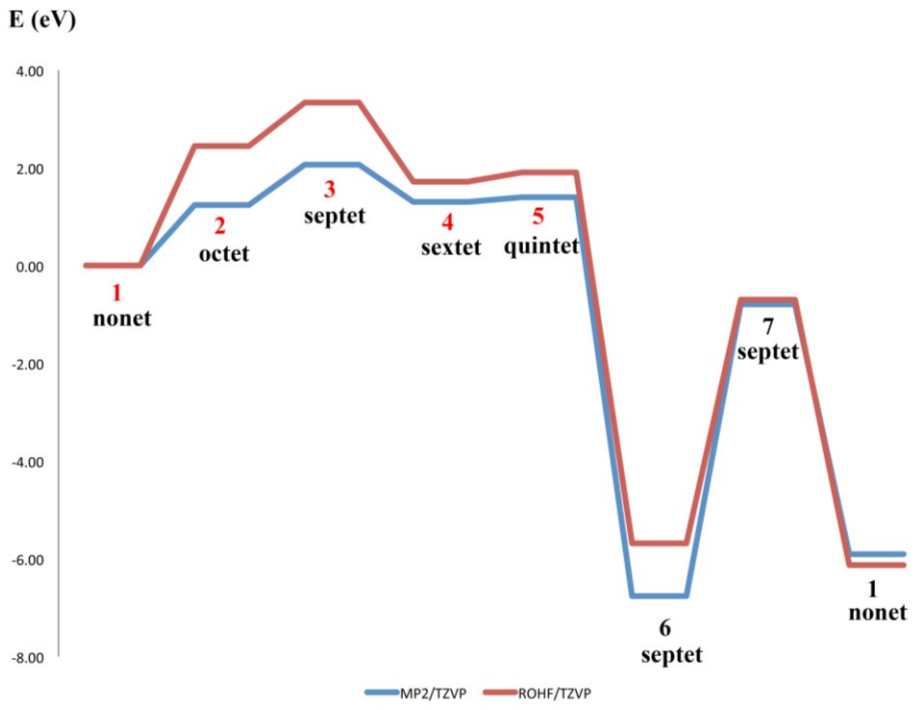

Figure 5.2 Reaction energies (eV) of the high spin states of the catalyst cycle.

All of these structures have C_1 symmetry and possess a pseudo-octahedral geometry around the Mn atoms. The ligands around the manganese atoms show either bent or twisted conformations in structures **1** - **7** and they are not in plane with the μ-hydroxo bonds. With previous B3LYP/6-311++G and BLYP/6-311++G results, the highest thermodynamic energy gap was observed between structures **3** and **4**.[30] In that work, the reaction goes uphill until the formation of structure **5** and then goes downhill to regenerate the catalyst whereas in the current work with ROHF and MP2, the reaction goes uphill to form structure **3** and then proceeds downhill to structure **4**. The next sections provide detailed descriptions of the electronic states and orbitals for each structure together with a comparison of the ROHF, CASSCF, and previous DFT calculations.

5.4.1 Structure 1

In structure **1**, the eight unpaired electrons in the nonet state occupy eight d-based orbitals of the two Mn atoms with two Mn d-based LUMOs. The singly occupied molecular orbitals (SOMOs) are very important as they depict the chemistry occurring around Mn. Orbitals 87 - 94 represent these singly occupied d orbitals optimized with ROHF (Figure 5.3). We also investigated the unrestricted Hartree-Fock (UHF)[61] orbitals for structure **1** (Figures C1 to C4 in Appendix C). In the UHF calculations, singly occupied alpha electrons with a high percentage of manganese d orbitals were seen in the lower energy occupied space (orbitals 50-62). Corresponding beta orbitals were not present, so the overall spin density was found to be four electrons on each Mn atom using both Mulliken and Löwdin partitioning schemes. Overall, differences in orbital occupation were noted for the structures examined in this work. The S^2 value for structure **1** was found to be 20.121 (compared to the idealized value of 20), indicating some spin contamination. Spin contamination was also found to be an issue in previous UHF

calculations on Mn complexes,[29] so the unrestricted calculations will not be further discussed in this work.

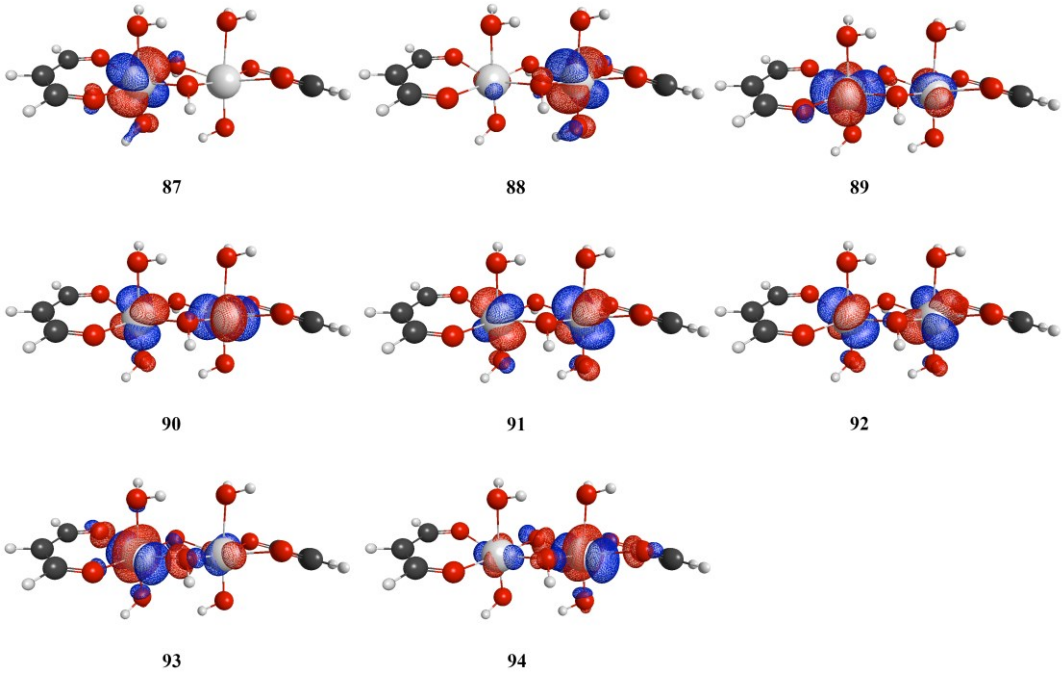

Figure 5.3 ROHF/TZVP SOMOs of structure **1**.

Core orbitals 85 and 86 (Figure 5.4) also have a significant role in the electronic structure. In structure **1** they are doubly occupied orbitals; in structure **2** and onwards we see that these orbitals change their occupancy. These orbitals represent a ring π orbital delocalized over three carbon atoms with contributions from the p orbitals of the two oxygen atoms in the ligand. These orbitals are hereafter labeled as $R\pi_1$ and $R\pi_2$ (ring π orbitals). This type of ring π orbital exhibits a key role in oxo-Mn(salen) complexes[29, 31] where electron transfer occurs in ring π orbitals to non-bonding axial Mn-O π orbitals in excited states.

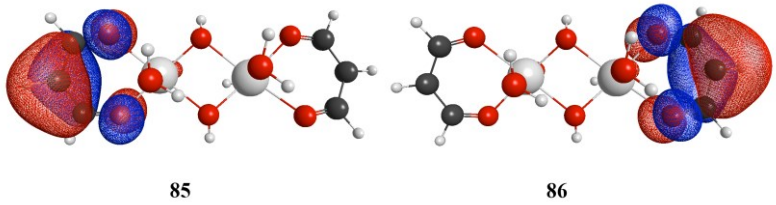

Figure 5.4 ROHF/TZVP doubly occupied Rπ_1 and Rπ_2 orbitals of structure **1**.

Initial orbitals for CASSCF(8,10) calculations were taken from the ROHF orbitals. In this case convergence was obtained without difficulty. A different spatial distribution of orbitals with the CASSCF wave function is observed. These eight singly occupied Mn d natural orbitals are shown in Figure 5.5. The two unoccupied natural orbitals in the active space, 95 and 96, also show d orbital character (Figure 5.5). Doubly occupied orbitals 85 and 86 have Rπ_1 and Rπ_2 character similar to the ROHF orbitals shown in Figure 5.4. The natural orbital occupation numbers (NOONs) are essentially 1 or 0 for singly occupied or unoccupied orbitals, respectively.

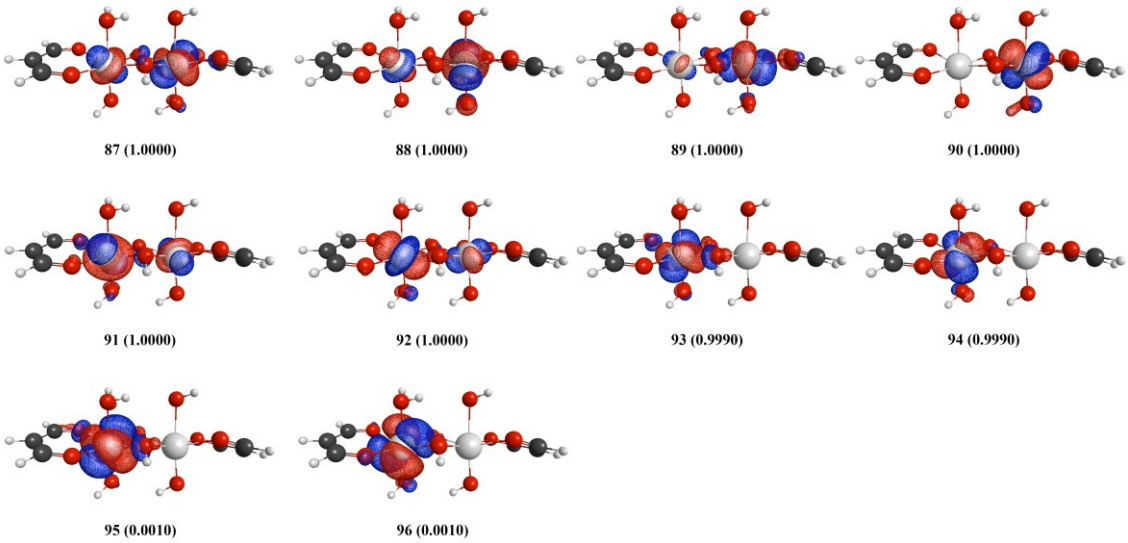

Figure 5.5 CASSCF(8,10)/TZVP active space natural orbitals of structure **1** (natural orbital occupation numbers (NOONs) are given in parentheses).

The structure did not change drastically in going from the ROHF to the CASSCF level of theory. All eight Mn-O bonds around the two Mn centers changed within a 0.001 Å range. Structure **1** was optimized with different multiplicities. The same initial SCF orbitals were used for other multiplicities as the nonet orbitals are similar between ROHF and CASSCF. There were no structural differences observed in these multiplicities within 0.001 Å. Relative energies of these multiplicities are given in Table 5.1.

Table 5.1 Relative CASSCF energies of electronic states for structure **1**.

Multiplicities	**CASSCF**	
	kcal mol^{-1}	cm^{-1}
Triplet	0.035	12.2
Quintet	0.028	9.8
Septet	0.020	7.0
Nonet	0.000	0.0

CASSCF calculations indicate the existence of many low-lying excited states. A CASSCF calculation at the optimized nonet geometry yields the high spin nonet state as the lowest energy state. The previous DFT results also predict the high spin nonet as the lowest energy state.[30] A CASSCF septet calculation at the optimized septet geometry yields an energy of 0.020 kcal mol^{-1} above the nonet state. A CASSCF calculation at the optimized quintet state gives a relative energy of 0.028 kcal mol^{-1}, and a similar CASSCF calculation for the triplet state yields 0.035 kcal mol^{-1}. Even though the high spin electronic state with 8 unpaired electrons is predicted to be the ground state, all of these other states are essentially degenerate. It should also be noted that the orbitals for these 8 unpaired electrons arise mostly from contributions of d orbitals on the two manganese atoms; very small contributions of orbitals from the bridging hydroxo groups are observed in the unpaired electrons of structure **1** and the other structures discussed below. To account for contributions from the hydroxo bridges, we included these

orbitals in the active space; however, all natural orbital occupation numbers were found to be at least 1.98, and thus for the remainder of this work they will be treated in the doubly occupied space.

This degeneracy of the electronic states can be observed in other structures of the reaction mechanism, producing competitive potential energy landscapes. Existence of these multiple nearly-degenerate potential energy landscapes near the ground state for the OEC of PSII have been shown recently with DMRG calculations, thus giving a very reactive environment for the manganese water oxidation systems.[33] For all of the lower spin multiplicities, the NOONs are essentially 1 or 0, indicating that the electrons remain unpaired.

5.4.2 Structure 2

Dehydrogenation leads to a Mn(IV) oxidation state in one of the manganese atoms in structure **2**. CASSCF optimization of structure **2** with different multiplicities reveals a low-lying sextet as the ground state. The octet is calculated to be 0.333 kcal mol^{-1} higher in energy than the sextet state. The natural orbitals used in the active space of the sextet state of structure **2** are provided in Figure 5.6 and those used in the octet state are given in the Appendix C, Figure C5. The doublet and quartet states are 0.414 and 0.056 kcal mol^{-1} higher in energy than the sextet state, respectively (Table 5.2). There are no apparent differences in the structures of these states. As seen for structure **1**, the four spin states are essentially degenerate. To check the effect of the active space on the state ordering, we also performed CASSCF calculations without the three essentially unoccupied orbitals 94-96, leading to a (7,7) active space. Again, the sextet state was found to be the lowest in energy. Even though CASSCF calculations are capable of accurately addressing electronic exchange and nondynamical correlations, they do a poor job of accounting for dynamical electron correlations. To see if the system is drastically affected by these

dynamical correlations, we employed MRMP2(7,10) calculations on structure **2**. In comparison, previous DFT calculations have predicted the octet state as the lowest energy state.[30]

Table 5.2 Relative CASSCF and MRMP2 energies of different states for structure **2**.

Multiplicities	**CASSCF**		**MRMP2**	
	kcal mol^{-1}	cm^{-1}	kcal mol^{-1}	cm^{-1}
Doublet	0.414	144.8	0.017	6.0
Quartet	0.056	19.6	0.002	0.7
Sextet	0.000	0.0	0.000	0.0
Octet	0.333	116.5	0.014	4.9

MRMP2 single point energies (Table 5.2) for the doublet, quartet, sextet, and octet were obtained at the CASSCF optimized geometries for their respective multiplicities. Initial orbitals were taken from the CASSCF wavefunction of structure 2 for each respective multiplicity. We have found that there are no large differences in energy with the MRMP2 level of theory, although the relative energies of the doublet, quartet, and octet states decrease somewhat. MRMP2 reproduced the sextet state as the ground state for structure 2 and the energy ordering of the remaining states is the same as from the CASSCF prediction. It is interesting to note that the CASSCF and MRMP2 calculations do not agree with predictions from a phenomenological Heisenberg-Dirac-Van Vleck (HDVV) Hamiltonian, which would predict either the ferromagnetic (octet) or antiferromagnetic (doublet) states to be lowest in energy depending on the value of the exchange constant J with a spacing of E(S-1)-E(S) = 2JS (where S is the total spin quantum number of the system). It should also be noted that previous B3LYP and BLYP calculations also do not predict state intervals according to HDVV predictions; for structure **1**, the singlet and quintet states were predicted to lie above the nonet state with the triplet highest in

energy, and for structure **2**, although the octet was predicted to lie lowest in energy, the other states were not arranged according to HDVV predictions.[30]

Interesting orbital configurations were observed when hydrogen was abstracted from water ligated on Mn to form an O-H bond in structure **2**. A singly occupied d orbital has now lowered its energy to the doubly occupied core orbital space. (This d orbital 69 is given in the Appendix C (Figure C6) and it has been compared with a range of orbitals in structure **1** to check the existence of this d orbital. We did not observe a similar kind of d orbital in structure **1** and attribute this to a lowering of a singly occupied d orbital into the doubly occupied core orbital space.) In addition, a higher energy ring π ($R\pi_2$) orbital on the side of the molecule that has undergone hydrogen abstraction is now singly occupied. We have also examined active spaces in which both ring π orbitals are active orbitals; however, one always remains doubly occupied (NOON > 1.97) and one stays singly occupied (NOON ~ 1.00). We hypothesize that removal of electron population in this ring π orbital is the cause for out-of-plane bending of the respective ligand that has been observed in this structure. The doubly occupied ring π orbital 86 and the singly occupied ring π orbital along with the remainder of the orbitals are given in Figure 5.6. Singly occupied orbitals 87 and 92 show a very small p orbital contribution from the dehydrogenated aqua ligand. We also observed that there is very little contribution from bridged OH groups. CASSCF calculations were able to find the remaining unoccupied d orbitals in the active space. In comparison to the active space orbital configurations observed with the structure 1, structure 2 possesses a different set of orbitals based on the Mn d orbitals. In this structure, the change in number of unpaired electrons does not solely affect the two manganese atoms; the contribution of the ring π orbital to the active space indicates that ligand framework and its ability to transfer an electron to aid the hydrogen removal process is also an important factor.

Since the character of the orbitals in the active space differs for structures 1 and 2, the CASSCF energies of these systems cannot be directly compared.

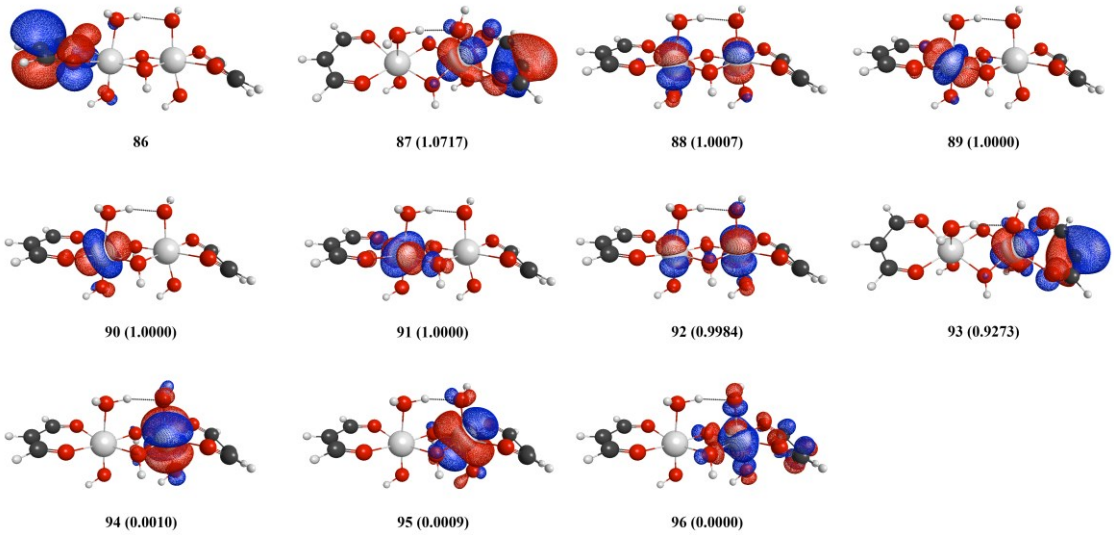

Figure 5.6 CASSCF(7,10)/TZVP natural orbitals 86-96 in the sextet state of structure **2**. Orbital 86 is a doubly occupied core orbital, and the other ten orbitals are included in the active space.

5.4.3 Structure 3

This species has had two hydrogens abstracted from the resting state of the catalyst and two manganese atoms are now in the Mn(IV) oxidation state. As mentioned earlier, when the multiplicities were changed in structures **1** and **2**, there were no geometric differences within 0.001 Å. The CASSCF geometry optimization of the septet state and a single point CASSCF energy calculation at the ROHF geometry for the septet state of structure **3** gave essentially the same energy. Similarly, the geometries for the structures with different multiplicities are not expected to vary greatly. Thus, we used CASSCF single point energies for all the multiplicities of structure **3** at the optimized CASSCF septet geometry to compare in Table 5.3. The previous DFT results predicted the stability order with the BLYP functional as $E_{septet}<E_{singlet}<E_{quintet}<E_{triplet}$ and with the B3LYP functional as $E_{septet}<E_{quintet}<E_{singlet} = E_{triplet}$, where the septet state is

predicted to be the most stable state with both of these functionals.[30] In contrast, the CASSCF calculations suggest the low spin triplet state as the most stable ground state with the septet being 0.28 kcal mol^{-1} higher in energy. These energy values also suggest near degeneracy among these electronic states.

Table 5.3 Relative CASSCF energies of different states of structure **3**.

Multiplicities	**CASSCF**	
	kcal mol^{-1}	cm^{-1}
Singlet	0.012	4.2
Triplet	0.000	0.0
Quintet	0.071	24.8
Septet	0.276	96.5

CASSCF natural orbitals reproduced the orbital configuration from ROHF except for reordering and mixing of the orbitals. Orbitals 87 and 88 both now represent Rπ1 and Rπ2 singly occupied orbitals (NOONs of 1.0000) on each side of the ligands (Figure 5.7). This suggests, consistent with our previous observation, another singly occupied orbital has lowered its energy into the core orbitals leading the doubly occupied Rπ orbital to become a higher energy singly occupied orbital. We extensively investigated this system to find the core d electron in the system but we were unable to positively identify it. The single electron occupations in both of these ring π orbitals in structure 3 cause them to bend out of plane as we hypothesized before for structure 2.

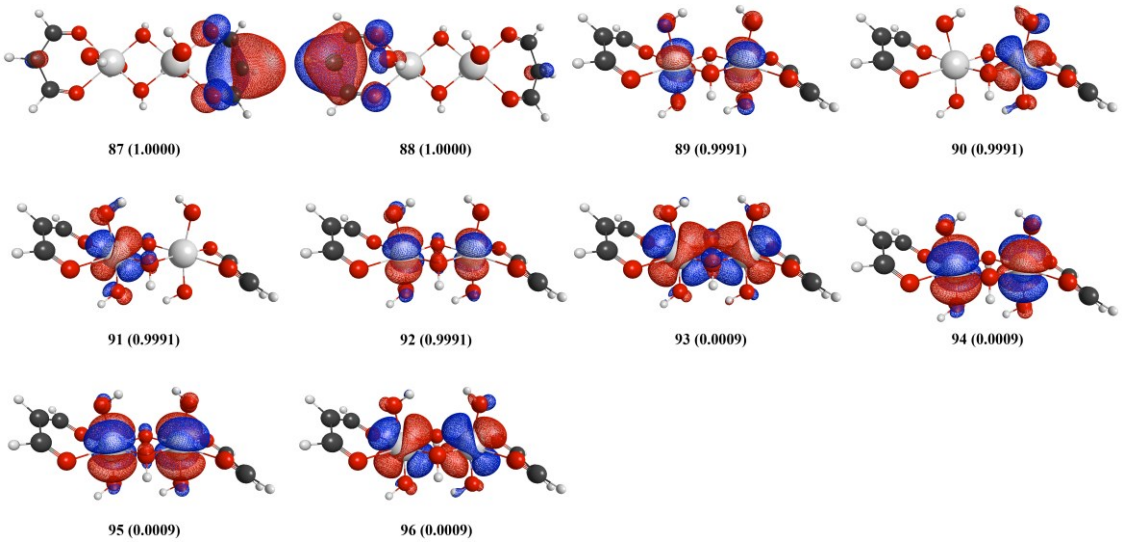

Figure 5.7 CASSCF(6,10)/TZVP active space natural orbitals of structure **3**.

In the singly occupied space starting from orbital 88 to orbital 92 we now see some p orbitals of the two dehydrogenated aqua ligands in the active space contributing to the electronic structure of structure **3**.

5.4.4 Structure 4

An important structure in the catalytic cycle is formed when the third hydrogen is abstracted from the initial structure to form an oxo group directly attached to a Mn atom. Formation of an oxo species plays a crucial role in this direct coupling catalytic pathway as the two oxygen atoms combine to form the bridged peroxo group. The BLYP and B3LYP functionals predicted the sextet/quartet and sextet/octet (both spin states are degenerate: sextet and quartet in BLYP and sextet and octet in B3LYP) as the lowest energy states respectively.[30] CASSCF single point energy calculations on structure **4** revealed that the sextet state is not the ground state. The low spin doublet state is the ground state for structure **4** and the sextet state is 5.805 kcal mol^{-1} higher in energy than the doublet state (Table 5.4). With the formation of this radical Mn(IV)-$O^{\bullet}$ group, low spin states tend to be lower in energy compared to the high spin electronic states.

Table 5.4 Relative CASSCF energies of different states of structure **4**.

Multiplicities	**CASSCF**	
	kcal mol^{-1}	cm^{-1}
Doublet	0.000	0.0
Quartet	0.285	99.7
Sextet	5.805	2030.3

Our study shows that the oxygen in the Mn-O bond has radical character, in line with a prediction of Mn(IV)-O$^{\bullet}$ character rather than Mn(V)=O. This is evident from the oxo p orbital contribution in orbital 89 (Figure 5.8). The singly occupied orbitals 87, 89, 90, and 91 all show contributions from the p orbital of the oxo group. Orbitals 90 and 91 show d orbitals of manganese and π* orbitals between manganese and oxygen. Orbitals 92-96 show LUMOs of structure **4** consisting of manganese d orbitals and π* orbitals between manganese and oxygen atoms.

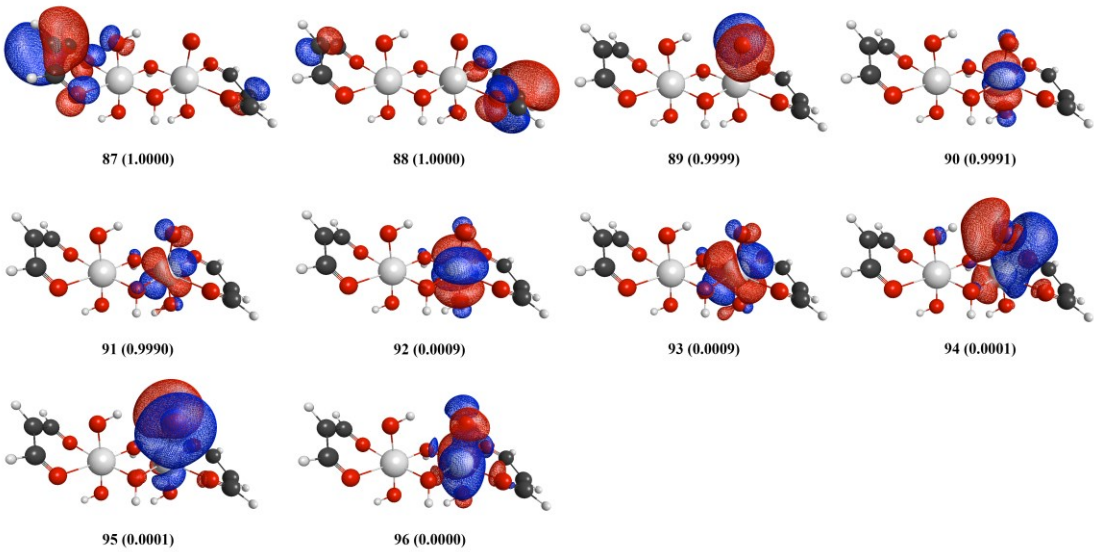

Figure 5.8 CASSCF(5,10)/TZVP active space natural orbitals of structure **4**.

5.4.5 Structure 5

Structure **5** possesses two Mn(IV)-O$^{\bullet}$ species. Orbitals 87 and 89 are singly occupied ring π orbitals similar to those in structures **3** and **4** but with more oxygen p orbitals mixing (Figure 5.9). We were not able to converge structure **5** with an active space of 10 orbitals due to low occupation numbers in the last 4 orbitals. Thus, we selected a smaller active space of 4 electrons in 6 orbitals. We observed a mixing of oxygen p orbitals and ring π orbitals. Generation of another p orbital on the other oxo group can be seen in the active space. Orbitals 88 and 90 both are now singly occupied oxo p orbitals with a slight contribution from ring π orbitals. From structure **5** onwards, singly occupied oxygen p orbitals are also involved in the active space.

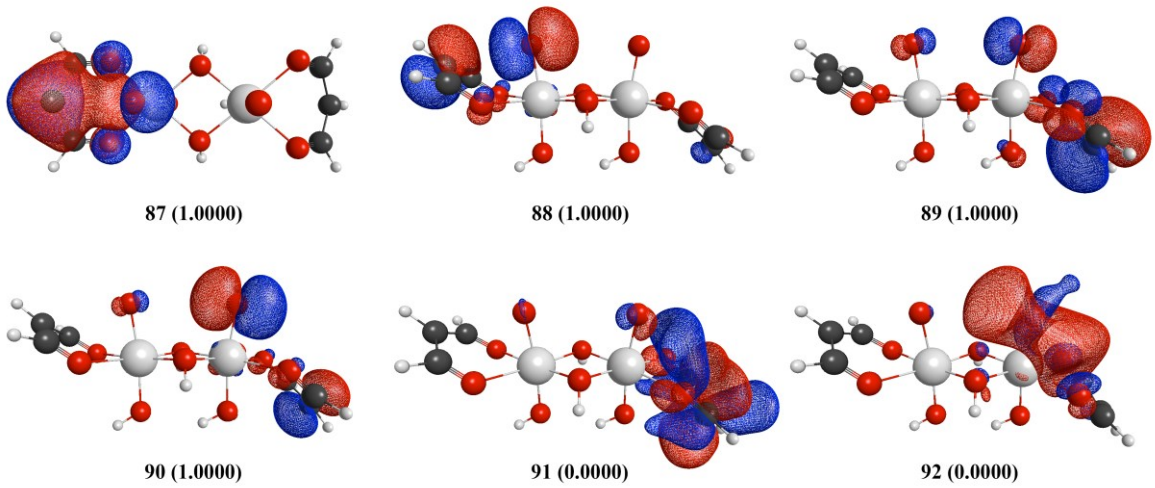

Figure 5.9 CASSCF(4,6)/TZVP active space natural orbitals of structure **5**.

Similar to structure **4**, low spin states tend to be lower in energy with the formation of these higher oxidation states on manganese atoms. Here in structure **5**, the singlet state is the ground state. Single point energy calculations show that the triplet state is 0.002 kcal mol^{-1} higher in energy than the singlet state so these two states are practically degenerate. The quintet state is 0.466 kcal mol^{-1} higher in energy than the ground state. When the structure is optimized

at each respective multiplicity, we found the triplet state to be the ground state and the singlet to be 0.009 kcal mol^{-1} higher in energy. Overall, the singlet state and the triplet state of structure **5** are essentially degenerate. In comparison, the quintet state is predicted as the lowest energy state with the B3LYP functional and BLYP predicts the singlet state as the ground state.[30]

5.4.6 Structure 6

Going from structure **5** to **6** is a purely chemical step, and the reaction energetics suggest that electrons in oxo p orbitals tend to react favorably to generate structure **6**. This represents the formation of the μ-peroxo bridge between the manganese atoms. The number of electrons in the system does not change. However, there are a lot of changes in the electronic structure of the system. The σ bond between the two oxygen atoms is now fully formed, which means that this orbital now lies in the doubly occupied subspace. In structure **6,** we now have 85 doubly occupied orbitals where orbital 85 is a ring π orbital similar to previous doubly occupied ring π orbitals (Figure 5.10). Orbital 86 is a singly occupied ring π orbital. A singly occupied π* orbital between the two bridging oxygen atoms can be seen in orbital 87. Electron filling in these π* orbitals is required for formation of the oxygen molecule. The corresponding π orbital is located in the doubly occupied space. In consequence, the bond order between the two oxygen atoms can be considered to be approximately 1.5. The O-O bond length in structure **6** is around 1.283 Å, which is closer to an oxygen-oxygen double bond than a single bond. A CASSCF relative energy comparison reveals that the triplet state is the ground state for structure **6** (Table 5.5). This is the same as for structure **5**, so no change in the spin state is required for this chemical step (unlike ROHF or DFT calculations examining high-spin states, which suggested a quintet-to-septet conversion). Overall, the multireference calculations examined in this work suggest that spin-

forbidden processes predicted by high-spin calculations may not be truly spin-forbidden, as low-spin states are essentially degenerate to or lower in energy than the high-spin states.

Table 5.5 Relative CASSCF energies of different states of structure **6**.

Multiplicities	**CASSCF**	
	kcal mol^{-1}	cm^{-1}
Singlet	0.793	277.4
Triplet	0.000	0.0
Quintet	0.488	170.7
Septet	3.156	1103.8

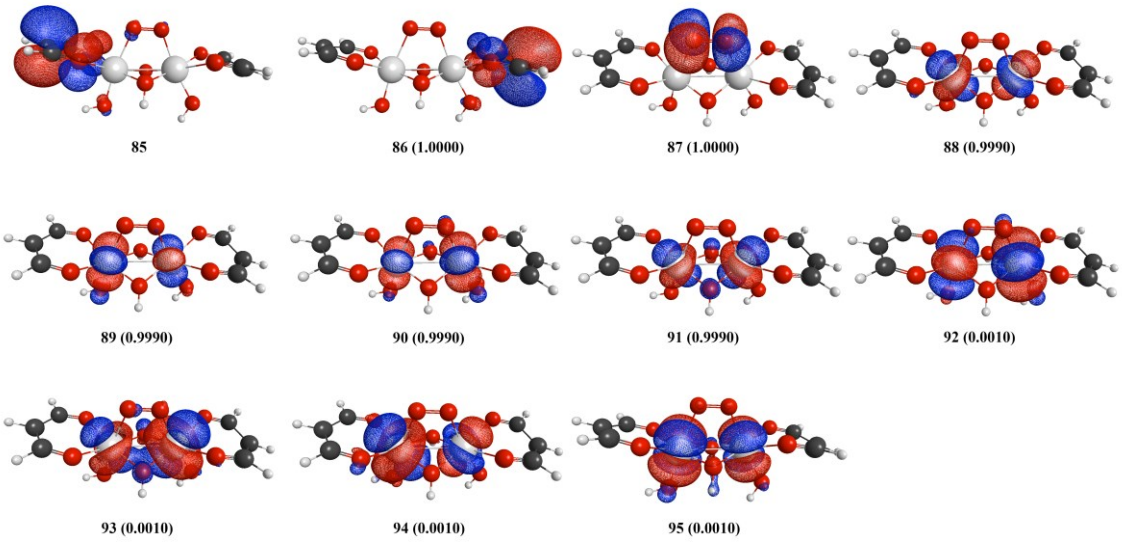

Figure 5.10 CASSCF(6,10)/TZVP natural orbitals 85-95 of structure **6**.

5.4.7 Structure 7

Insertion of a water molecule into structure **6** will break a Mn-O bond but leave O=O still attached to the other manganese atom. The addition of the aqua ligand increases the number of doubly occupied orbitals to 90. Orbital 90 in the septet state of structure **7** is a doubly occupied ring π orbital (Orbital 90 is equal to the ring π orbital 86 in Figure 5.4). The previously observed singly occupied π* orbital on the bridging O=O can now be seen in orbital 91 (Figure 5.11).

Orbital 92 is a singly occupied ring π orbital. The remaining four electrons are present in singly occupied Mn d orbitals and are shown in Figure 5.11 with the LUMOs used in the active space. Relative energies for different spin states are given in Table 5.6, and show that the lowest energy state of **7** is a triplet.

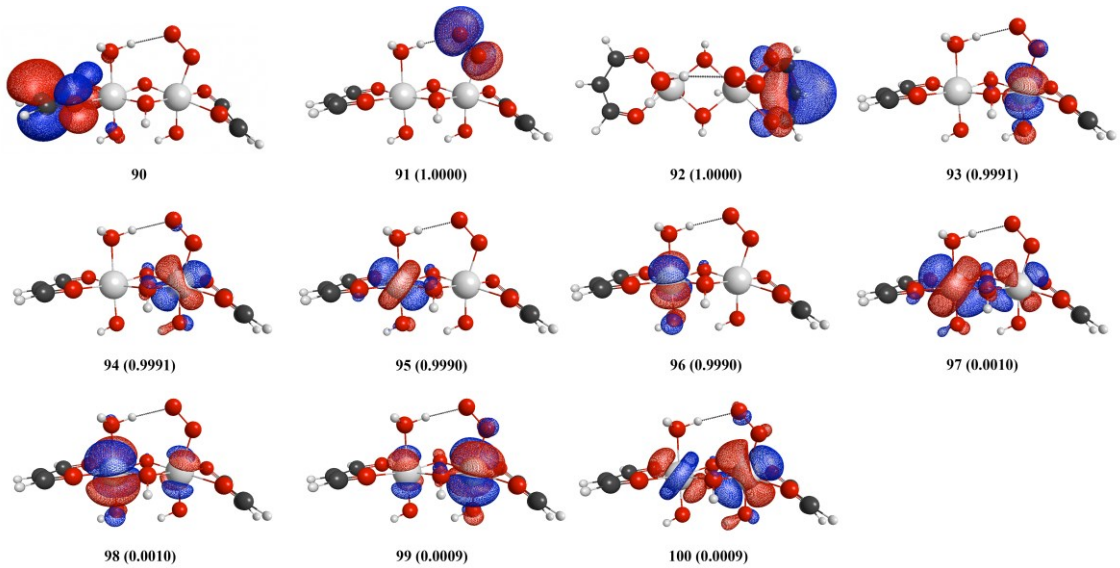

Figure 5.11 Doubly occupied orbital 90 and CASSCF(6,10)/TZVP natural orbitals 91-100 of structure **7**.

Table 5.6 Relative CASSCF energies of different states in structure **7**.

Multiplicities	**CASSCF**	
	kcal mol^{-1}	cm^{-1}
Singlet	0.395	138.2
Triplet	0.000	0.0
Quintet	0.353	123.5
Septet	2.278	796.7

An incoming water molecule can detach the superoxo group in structure **7** leading back to structure **1**, the resting state of the catalyst. This is a downhill reaction indicating the regeneration of the model catalyst. A transition from **7** in its triplet state to **1** in its nonet state

would be spin-forbidden, so it is possible that **7** would actually be present in a higher spin state or that **1** may access a lower spin state. Since the differences in energy between the spin states are small for each structure examined here, the actual spin state accessed may not be important in this case. In comparison, for both structures **6** and **7**, DFT predicted the septet state as the ground state.[30]

Overall, the low-lying electronic states presented in this model system are an important factor to understand the reactivity of manganese. Nearby ligands also play a key role by changing the singly occupied orbitals present in the system. We also observed that the low spin states tend to be more stable when the electrocatalytic oxygen evolution is in progress in the last stages of the reaction. The contributions from orbitals of the bridging oxo groups to the active space were very small. Formation of Mn(IV)-O$^{\bullet}$ groups in structures **4** and **5** resulted in large contributions from the oxo p orbitals to the active space, thus changing the electronic properties of the structure. It should also be noted that the electron occupation in π^* orbitals is required prior to oxygen removal from the catalyst. As described above, we see that the ligands tend to change orientation with the occupation of the ring π orbitals. With two dehydrogenations yielding structure **3** where two manganese atom are in the Mn(IV) oxidation state, the rings were seen to bend out of the manganese dimer plane. This bend was more pronounced at structure **5** with two Mn(IV)-O$^{\bullet}$ groups. When the oxygen-oxygen bridge is formed, the rings bend in the same direction, making a butterfly-like structure in structure **6**. With the detachment of the oxygen bridge from one manganese atom, this symmetric structure distorts somewhat to yield structure **7**.

5.5 Concluding Remarks

In conclusion, we used CASSCF theory to investigate a water splitting reaction mechanism on a model manganese dimer electrocatalyst. Electronic details and contributions to the water splitting from manganese and oxygen atoms involved can be obtained by examining the occupied orbitals. Apart from the resting state of the catalyst, a singly occupied ring π orbital on the ligands can be seen throughout the catalytic cycle. We also hypothesize that this ring π population may be a reason for the out of plane orientation of the respective ligands. In structure **3** with two Mn(IV) atoms, an out of plane bend of both ligands in opposite directions was observed. This became more pronounced upon formation of Mn(IV) oxidation states on two manganese atoms in structure **5**. However, with the formation of the oxygen-oxygen bridge between the Mn(III) atoms on structure **6**, these ligands tend to bend in the same direction forming a butterfly-like structure, which later distorts with the detachment of the oxo bridge from one manganese atom on structure **7**.

Radical properties of a Mn-O moiety have also been observed in this direct coupling pathway. The p orbital contribution to the active space is observed with the formation of the Mn(IV)-O$^{\bullet}$ group and is much more obvious in structure **5** with two Mn(IV)-O$^{\bullet}$. For structure **5** with two Mn(IV) states, we have observed the prominent contribution of p orbitals of both oxo groups to the singly occupied active space. This then yields the oxo bridge in structure **6**. The π* orbitals were seen to be occupied in the oxygen-oxygen bond in structures **6** and **7**.

With the progress of the catalytic cycle, we also note that low spin states have an improved stability in the later stages of the cycle. However, there are multiple nearly degenerate excited states close to the ground state in all the structures studied here. This is an important factor because spin-forbidden processes predicted from high-spin calculations may not truly be

spin-forbidden. In addition, the reaction energies will vary somewhat from those predicted by high-spin calculations. However, since the NOONs of the active orbitals are very close to 2, 1, or 0, and since the energies of the various spin states are typically quite close in energy, this suggests that high-spin calculations may provide a reasonable approximation to reaction pathways. Nonetheless, this should be verified for other systems. Overall, we believe this detailed electronic investigation may helpful in explaining future studies of manganese-based catalysis.

5.6 Acknowledgements

This material is based upon work supported by the National Science Foundation under Grant No. CHE-0955515. C.M.A. also thanks the Alfred P. Sloan Foundation for a Sloan Research Fellowship (2011-2013) and the Camille and Henry Dreyfus Foundation for a Camille Dreyfus Teacher-Scholar Award (2011-2016). The authors thank Dr. Jakub Chalupsky, Prof. Takashi Yanai, Prof. Yuki Kurashige, and Dr. Michael Busch for interesting discussions. The computing for this project was performed on the Beocat Research Cluster at Kansas State University, which is funded in part by NSF grants CNS-1006860, EPS-1006860, and EPS-0919443.

5.7 References

1. Cady, C. W.; Crabtree, R. H.; Brudvig, G. W. Functional Models for the Oxygen-Evolving Complex of Photosystem II. *Coord. Chem. Rev.* **2008,** *252*, 444-455.

2. Dau, H.; Grundmeier, A.; Loja, P.; Haumann, M. On the Structure of the Manganese Complex of Photosystem II: Extended-Range EXAFS Data and Specific Atomic-Resolution Models for Four S-States. *Phil. Trans. R. Soc. B* **2008,** *363*, 1237-1244.

3. Ferreira, K. N.; Iverson, T. M.; Maghlaoui, K.; Barber, J.; Iwata, S. Architecture of the Photosynthetic Oxygen-Evolving Center. *Science* **2004,** *303*, 1831-1838.

4. McEvoy, J. P.; Brudvig, G. W. Water-Splitting Chemistry of Photosystem II. *Chem. Rev.* **2006,** *106*, 4455-4483.

5. Rapatskiy, L.; Cox, N.; Savitsky, A.; Ames, W. M.; Sander, J.; Nowaczyk, M. M.; Rögner, M.; Boussac, A.; Neese, F.; Messinger, J.; Lubitz, W. Detection of the Water-Binding Sites of the Oxygen-Evolving Complex of Photosystem II Using W-Band ^{17}O Electron–Electron Double Resonance-Detected NMR Spectroscopy. *J. Am. Chem. Soc.* **2012,** *134*, 16619-16634.

6. Sauer, K.; Yachandra, V. K. The Water-Oxidation Complex in Photosynthesis. *Biochim. Biophys. Acta, Bioenerg.* **2004,** *1655*, 140-148.

7. Siegbahn, P. E. M. Structures and Energetics for O_2 Formation in Photosystem II. *Acc. Chem. Res.* **2009,** *42*, 1871-1880.

8. Siegbahn, P. E. M. Recent Theoretical Studies of Water Oxidation in Photosystem II. *J. Photochem. Photobiol., B* **2011,** *104*, 94-99.

9. Siegbahn, P. E. M. Mechanisms for Proton Release During Water Oxidation in the S_2 to S_3 and S_3 to S_4 Transitions in Photosystem II. *Phys. Chem. Chem. Phys.* **2012,** *14*, 4849-4856.

10. Siegbahn, P. E. M. Water Oxidation Mechanism in Photosystem II, Including Oxidations, Proton Release Pathways, O—O Bond Formation and O_2 Release. *Biochim. Biophys. Acta, Bioenerg.* **2013,** *1827*, 1003-1019.

11. Siegbahn, P. E. M.; Blomberg, M. R. A. Energy Diagrams for Water Oxidation in Photosystem II Using Different Density Functionals. *J. Chem. Theory Comput.* **2013,** *10*, 268-272.

12. Umena, Y.; Kawakami, K.; Shen, J.-R.; Kamiya, N. Crystal Structure of Oxygen-Evolving Photosystem II at a Resolution of 1.9 Å. *Nature* **2011,** *473*, 55-60.

13. Ashmawy, F. M.; McAuliffe, C. A.; Parish, R. V.; Tames, J. Water Photolysis. Part 1. The Photolysis of Co-ordinated Water in $[\{MnL(H_2O)\}_2][ClO_4]_2$(L = Dianion of Tetradentate O_2N_2-Donor Schiff Bases). A Model for the Manganese Site in Photosystem II of Green Plant Photosynthesis. *J. Chem. Soc., Dalton Trans.* **1985**, 1391-1397.

14. Watkinson, M.; Whiting, A.; McAuliffe, C. A. Synthesis of a Bis-Manganese Water Splitting Complex. *J. Chem. Soc., Chem. Commun.* **1994**, 2141-2142.

15. Limburg, J.; Vrettos, J. S.; Liable-Sands, L. M.; Rheingold, A. L.; Crabtree, R. H.; Brudvig, G. W. A Functional Model for O-O Bond Formation by the O_2-Evolving Complex in Photosystem II. *Science* **1999,** *283*, 1524-1527.

16. Collomb, M.-N.; Deronzier, A.; Richardot, A.; Pecaut, J. Synthesis and Characterization of a New Kind of $Mn_2^{III,IV}$ μ-oxo Complex: $[Mn_2O_2(terpy)_2(H_2O)_2](NO_3)_3.6H_2O$, terpy=2,2':6',2''-terpyridine. *New J. Chem.* **1999,** *23*, 351-354.

17. Naruta, Y.; Sasayama, M.-a.; Sasaki, T. Oxygen Evolution by Oxidation of Water with Manganese Porphyrin Dimers. *Angew. Chem. Int. Ed. Engl.* **1994,** *33*, 1839-1841.

18. Poulsen, A. K.; Rompel, A.; McKenzie, C. J. Water Oxidation Catalyzed by a Dinuclear Mn Complex: A Functional Model for the Oxygen-Evolving Center of Photosystem II. *Angew. Chem. Int. Ed.* **2005,** *44*, 6916-6920.

19. Mullins, C. S.; Pecoraro, V. L. Reflections on Small Molecule Manganese Models that Seek to Mimic Photosynthetic Water Oxidation Chemistry. *Coord. Chem. Rev.* **2008,** *252*, 416-443.

20. Liu, X.; Wang, F. Transition Metal Complexes that Catalyze Oxygen Formation from Water: 1979–2010. *Coord. Chem. Rev.* **2012,** *256*, 1115-1136.

21. Yagi, M.; Syouji, A.; Yamada, S.; Komi, M.; Yamazaki, H.; Tajima, S. Molecular Catalysts for Water Oxidation Toward Artificial Photosynthesis. *Photochem. Photobiol. Sci.* **2009,** *8*, 139-147.

22. Mukhopadhyay, S.; Mandal, S. K.; Bhaduri, S.; Armstrong, W. H. Manganese Clusters with Relevance to Photosystem II. *Chem. Rev.* **2004,** *104*, 3981-4026.

23. Wu, A. J.; Penner-Hahn, J. E.; Pecoraro, V. L. Structural, Spectroscopic, and Reactivity Models for the Manganese Catalases. *Chem. Rev.* **2004,** *104*, 903-938.

24. Zhao, X. G.; Richardson, W. H.; Chen, J. L.; Li, J.; Noodleman, L.; Tsai, H. L.; Hendrickson, D. N. Density Functional Calculations of Electronic Structure, Charge Distribution, and Spin Coupling in Manganese−Oxo Dimer Complexes. *Inorg. Chem.* **1997,** *36*, 1198-1217.

25. Blomberg, M. R. A.; Siegbahn, P. E. M.; Styring, S.; Babcock, G. T.; Åkermark, B.; Korall, P. A Quantum Chemical Study of Hydrogen Abstraction from Manganese-Coordinated Water by a Tyrosyl Radical: A Model for Water Oxidation in Photosystem II. *J. Am. Chem. Soc.* **1997,** *119*, 8285-8292.

26. McGrady, J. E.; Stranger, R. Redox-Induced Formation and Cleavage of O−O σ and π Bonds in a Peroxo-Bridged Manganese Dimer: A Density Functional Study. *Inorg. Chem.* **1999,** *38*, 550-558.

27. Lundberg, M.; Blomberg, M. R. A.; Siegbahn, P. E. M. Oxyl Radical Required for O−O Bond Formation in Synthetic Mn-Catalyst. *Inorg. Chem.* **2003,** *43*, 264-274.

28. Zhou, T.; Lin, X.; Zheng, X. First-Principles Study on Structural and Chemical Asymmetry of a Biomimetic Water-Splitting Dimanganese Complex. *J. Chem. Theory Comput.* **2013,** *9*, 1073-1080.

29. Sears, J. S.; Sherrill, C. D. The Electronic Structure of Oxo-Mn(salen): Single-Reference and Multireference Approaches. *J. Chem. Phys.* **2006,** *124*, 144314.

30. Busch, M.; Ahlberg, E.; Panas, I. Electrocatalytic Oxygen Evolution from Water on a Mn(III-V) Dimer Model Catalyst-A DFT Perspective. *Phys. Chem. Chem. Phys.* **2011,** *13*, 15069-15076.

31. Ivanic, J.; Collins, J. R.; Burt, S. K. Theoretical Study of the Low Lying Electronic States of oxoX(salen) (X = Mn, Mn^-, Fe, and Cr^-) Complexes. *J. Phys. Chem. A* **2004,** *108*, 2314-2323.

32. Wouters, S.; Bogaerts, T.; Van Der Voort, P.; Van Speybroeck, V.; Van Neck, D. Communication: DMRG-SCF Study of the Singlet, Triplet, and Quintet States of Oxo-Mn(Salen). *J. Chem. Phys.* **2014,** *140*, 241103.

33. Kurashige, Y.; Chan, G. K.-L.; Yanai, T. Entangled Quantum Electronic Wavefunctions of the Mn_4CaO_5 Cluster in Photosystem II. *Nat Chem* **2013,** *5*, 660-666.

34. Yamaguchi, K.; Isobe, H.; Yamanaka, S.; Saito, T.; Kanda, K.; Shoji, M.; Umena, Y.; Kawakami, K.; Shen, J. R.; Kamiya, N.; Okumura, M. Full Geometry Optimizations of the Mixed-Valence $CaMn_4O_4X(H_2O)_4$ (X=OH or O) Cluster in OEC of PS II: Degree of Symmetry

Breaking of the Labile Mn-X-Mn Bond Revealed by Several Hybrid DFT Calculations. *Int. J. Quantum Chem.* **2013,** *113*, 525-541.

35. Yamaguchi, K.; Kitagawa, Y.; Isobe, H.; Shoji, M.; Yamanaka, S.; Okumura, M. Theory of Chemical Bonds in Metalloenzymes XVIII. Importance of Mixed-Valence Configurations for Mn_5O_5, $CaMn_4O_5$ and $Ca_2Mn_3O_5$ Clusters Revealed by UB3LYP Computations. A Bio-Inspired Strategy for Artificial Photosynthesis. *Polyhedron* **2013,** *57*, 138-149.

36. Krewald, V.; Neese, F.; Pantazis, D. A. On the Magnetic and Spectroscopic Properties of High-Valent Mn_3CaO_4 Cubanes as Structural Units of Natural and Artificial Water-Oxidizing Catalysts. *J. Am. Chem. Soc.* **2013,** *135*, 5726-5739.

37. Krewald, V.; Retegan, M.; Cox, N.; Messinger, J.; Lubitz, W.; DeBeer, S.; Neese, F.; Pantazis, D. A. Metal Oxidation States in Biological Water Splitting. *Chemical Science* **2015,** *6*, 1676-1695.

38. Manoli, M.; Collins, A.; Parsons, S.; Candini, A.; Evangelisti, M.; Brechin, E. K. Mixed-Valent Mn Supertetrahedra and Planar Discs as Enhanced Magnetic Coolers. *J. Am. Chem. Soc.* **2008,** *130*, 11129-11139.

39. Yang, X.; Baik, M.-H. Electronic Structure of the Water-Oxidation Catalyst $[(bpy)_2(OH_x)RuORu(OH_y)(bpy)_2]^{z+}$: Weak Coupling Between the Metal Centers Is Preferred Over Strong Coupling. *J. Am. Chem. Soc.* **2004,** *126*, 13222-13223.

40. Yang, X.; Baik, M.-H. *cis*,*cis*-$[(bpy)_2Ru^{V}O]_2O^{4+}$ Catalyzes Water Oxidation Formally via in Situ Generation of Radicaloid $Ru^{IV}-O^{\bullet}$. *J. Am. Chem. Soc.* **2006,** *128*, 7476-7485.

41. Wang, L.-P.; Van Voorhis, T. Direct-Coupling O_2 Bond Forming a Pathway in Cobalt Oxide Water Oxidation Catalysts. *J. Phys. Chem. Lett.* **2011,** *2*, 2200-2204.

42. Roothaan, C. C. J. Self-Consistent Field Theory for Open Shells of Electronic Systems. *Reviews of Modern Physics* **1960,** *32*, 179-185.

43. Aikens, C. M.; Fletcher, G. D.; Schmidt, M. W.; Gordon, M. S. Scalable Implementation of Analytic Gradients for Second-Order Z-Averaged Perturbation Theory Using the Distributed Data Interface. *J. Chem. Phys.* **2006,** *124*, 014107.

44. Lee, T. J.; Rendell, A. P.; Dyall, K. G.; Jayatilaka, D. Open- Shell Restricted Hartree–Fock Perturbation Theory: Some Considerations and Comparisons. *J. Chem. Phys.* **1994,** *100*, 7400-7409.

45. Lee, T. J.; Jayatilaka, D. An Open-Shell Restricted Hartree—Fock Perturbation Theory Based on Symmetric Spin Orbitals. *Chem. Phys. Lett.* **1993,** *201*, 1-10.

46. Roos, B. O., The CASSCF Method and its Application in Electronic Structure Calculations. Lawley, K. P., Ed. Wiley Interscience, New York: 1987; Vol. 69, pp 339-445.

47. Ruedenberg, K.; Schmidt, M. W.; Gilbert, M. M. Are Atoms Intrinsic to Molecular Electronic Wavefunctions? II. Analysis of FORS Orbitals. *Chem. Phys.* **1982,** *71*, 51-64.

48. Ruedenberg, K.; Schmidt, M. W.; Gilbert, M. M.; Elbert, S. T. Are Atoms Intrinsic to Molecular Electronic Wavefunctions? III. Analysis of FORS Configurations. *Chem. Phys.* **1982,** *71*, 65-78.

49. Ruedenberg, K.; Schmidt, M. W.; Gilbert, M. M.; Elbert, S. T. Are Atoms Intrinsic to Molecular Electronic Wavefunctions? I. The FORS Model. *Chem. Phys.* **1982,** *71*, 41-49.

50. Hirao, K. Multireference Møller–Plesset Perturbation Treatment of Potential Energy Curve of N_2. *Int. J. Quantum Chem.* **1992,** *44*, 517-526.

51. Hirao, K. Multireference Møller—Plesset Perturbation Theory for High-Spin Open-Shell Systems. *Chem. Phys. Lett.* **1992,** *196*, 397-403.

52. Hirao, K. Multireference Møller—Plesset Method. *Chem. Phys. Lett.* **1992,** *190*, 374-380.

53. Hirao, K. State-specific Multireference Møller—Plesset Perturbation Treatment for Singlet and Triplet Excited States, Ionized States and Electron Attached States of H_2O. *Chem. Phys. Lett.* **1993,** *201*, 59-66.

54. Nakano, H. MCSCF Reference Quasidegenerate Perturbation Theory with Epstein—Nesbet Partitioning. *Chem. Phys. Lett.* **1993,** *207*, 372-378.

55. Nakano, H. Quasidegenerate Perturbation Theory with Multiconfigurational Self-Consistent- Field Reference Functions. *J. Chem. Phys.* **1993,** *99*, 7983-7992.

56. Dykstra, C. E.; Frenking, G.; Kim, K. S.; Scuseria, G. E.; Gordon, M. S.; Schmidt, M. W. Advances in Electronic Structure Theory: GAMESS a Decade Later. In Theory and Applications of Computational Chemistry: The First Forty Years. *Elsevier, Amsterdam* **2005**, 1167-1189.

57. Schmidt, M. W.; Baldridge, K. K.; Boatz, J. A.; Elbert, S. T.; Gordon, M. S.; Jensen, J. H.; Koseki, S.; Matsunaga, N.; Nguyen, K. A.; Su, S.; Windus, T. L.; Dupuis, M.; Montgomery, J. A. General Atomic and Molecular Electronic Structure System. *J. Comput. Chem.* **1993,** *14*, 1347-1363.

58. Boys, S. F., Quantum Theory of Atoms, Molecules, and the Solid State. P. O. Lowdin, Ed. Academic Press, New York: 1966; pp 253-262.

59. Dunning, T. H. Gaussian Basis Functions for Use in Molecular Calculations. III. Contraction of (10s6p) Atomic Basis Sets for the First- Row Atoms. *J. Chem. Phys.* **1971,** *55*, 716-723.

60. Wachters, A. J. H. Gaussian Basis Set for Molecular Wavefunctions Containing Third-Row Atoms. *J. Chem. Phys.* **1970,** *52*, 1033-1036.

61. Pople, J. A.; Nesbet, R. K. Self- Consistent Orbitals for Radicals. *J. Chem. Phys.* **1954,** *22*, 571-572.

Chapter 6 - Reaction pathways for water oxidation to molecular oxygen mediated by model cobalt oxide dimer and cubane catalysts

Reproduced with permission from:

Fernando, A; Aikens, C. M. *J. Phys. Chem. C*, **2015**, *119*, 11072–11085

6.1 Abstract

Hybrid density functional theory calculations have been employed to investigate the water oxidation reaction on model cobalt oxide dimer and cubane complexes. Electronic structure and energetics of these model compounds were thoroughly investigated. The thermodynamically lowest energy pathway on the dimer catalyst proceeds through a nucleophilic attack of a solvent water molecule to Co(V)-O radical moiety. The lowest energy pathway on the cubane catalyst involves a geminal coupling of Co(V)-O radical oxo group with bridging oxo sites. Model systems were found to be very sensitive to the positions of ligands and to the hydrogen-bonding environment leading to different isomer energies.

6.2 Introduction

Hydrogen is a very efficient energy source compared to the present carbon-based fossil fuels and it is environmental friendly as the combustion products are free from carbon monoxide or dioxide. Currently, the most efficient process that harnesses solar energy into chemical energy is water splitting into molecular oxygen, protons, and electrons by the oxygen-evolving complex (OEC) of photosystem II (PSII). The active part of the OEC includes a metal oxide framework that consists of $CaMn_4O_4$ arranged in a cubane fashion. Inspired by this manganese oxide blue print, many synthetic and model compounds have been proposed that have the ability to catalyze the water oxidation process as photocatalysts, electrocatalysts, photo-electrocatalysts, etc.

Currently, industrial water electrolyzers use platinum coated electrodes. Platinum is a very efficient catalyst but it is rare and very expensive so the applicability in large-scale industrial plants is limited. Noble metal oxide catalysts such as ruthenium and iridium oxides have also been reported and are currently used as robust and efficient electrocatalysts.[1-4] However, these noble metal oxide catalysts are also not abundant and therefore are expensive for large-scale deployment. These reasons lead scientists to investigate metal oxide catalysts based on earth abundant elements. Among these less expensive metal oxides, there have been many reports on the catalytic activity of manganese oxides,[5-8] nickel oxides,[9, 10] and cobalt oxides[11-17] for water oxidation.

Cobalt oxides have a long history dating back to the 1960s but their development was slowed when it was found that the catalyst precipitated out from the solution as cobalt oxides or hydroxides.[12] Cobalt oxide gained a wide popularity recently for its remarkable catalytic activity towards water splitting after its reinvention by Nocera and coworkers.[14] This Nocera catalyst is a black thin film deposited on an indium tin oxide surface. It is a heterogeneous catalyst that is very stable, easy to synthesize from readily available precursors, self-healing through a series of linked equilibria, and shows high activity under neutral pH. Diffraction techniques cannot be used to determine the structure of this highly amorphous cobalt oxide catalyst. X-ray absorption spectroscopy (XAS) and extended X-ray absorption spectroscopy (EXAFS) are especially well suited for the local structure analysis of the catalyst. Recent EXAFS studies[18, 19] reported that this catalyst has similar structural features to a manganese cubane complex. They indicated that Co_4O_4 units in the form of $Co(III)O_6$ octahedra are present in the catalyst. Multiple edge sharing and corner sharing structures have also been proposed over the past years based on experimental and theoretical evidence.[18-21] During the last few years, Wang *et al.*,[20] Mattioli *et al.*,[21] Li *et al.*,[22]

and Kwapien *et al*.[23] reported theoretical investigations of the mechanism for oxygen evolution on related cobalt oxide complexes.

Recently, McAlpin *et al*.[24] reported a $[Co_4O_4(C_5H_5N)_4(CH_3CO_2)_4]^+$ complex with a Co_4O_4 unit that has the ability to catalyze the water oxidation reaction. A couple of months later, McCool and coworkers[17] also reported a neutral $[Co_4O_4(C_5H_5N)_4\ (CH_3CO_2)_4]$ molecular cubane complex which catalyzes water oxidation activity efficiently with the presence of standard photochemical or electrochemical oxidation sources. The structure of this molecular catalyst was also found to consist of Co_4O_4 cubane shaped metal oxide units. Recently, Evangelisti and coworkers[13] also reported a Co_4O_4 complex, $[Co^{II}_4(hmp)_4(\mu\text{-}OAc)_2(\mu_2\text{-}OAc)_2(H_2O)_2]$, (OAc = acetate, hmp = 2-(hydroxymethyl)pyridine) as the first Co(II)-based cubane water oxidation catalyst. This catalyst is a distorted cubane catalyst that increases its catalytic activity upon photoirradiation with increasing pH through aqua ligand deprotonation. Rigsby and coworkers[25] reported that cobalt dimer complexes ligated with bispyridylpyrazolate have the ability to serve as molecular electrocatalysts for water oxidation under acidic conditions. In 2014, Smith and coworkers[26] investigated dimer, trimer and tetramer of cobalt oxide catalysts with two sets of ligands for water oxidation activity. These authors reported that dimer and trimer clusters with their synthesized ligand sets are catalytically inactive in contrast to previous report by Rigsby *et al*.[25] This shows that catalytic activity and the mechanism may depend on the ligand environment for cobalt oxide complexes with smaller nuclearity.

The turnover rates of these catalysts are several orders of magnitude slower than the natural OEC of PSII; however, there is potential to improve them enough to be competitive for commercial utilization.[27] Thus, investigation of the electronic structure, electronic properties, and reaction mechanisms of these cobalt oxide catalysts is necessary. We believe such understanding

may be helpful for experimentalists to further enhance and promote the cobalt oxide water oxidation catalyst as a next generation commercially viable electrocatalyst for hydrogen production.

In the present study we used a model cubane complex and a dimer compound, which is a minimal unit of the cubane complex. This cubane-like complex with aqua and hydroxo ligands resembles the primary unit of the catalysts reported by Nocera *et al*., McAlpin *et al*., McCool *et al*., and Evangelisti *et al*. It has been shown experimentally for the Nocera catalyst that the catalytic activity is not affected when the phosphate is replaced with other buffering electrolytes such as methyl phosphonate. So, it can be assumed that phosphate ligands do not play a pivotal role in the oxygen evolution process.[28, 29] There is also evidence from the OEC that substituting ligands of the true catalyst with aqua and hydroxo ligands appears not to have an effect on the qualitative picture of the mechanism proposed.[30]

6.3 Computational methodology

All the reaction pathways promoted by the dimer and cubane catalysts are investigated by the general atomic and molecular electronic structure system (GAMESS)[31, 32] program. We have performed density functional theory (DFT) calculations using the B3LYP exchange correlation functional. The B3LYP functional has been used previously by Wang *et al*.[20] and Li *et al*.[20, 22] to study the cobalt oxide water oxidation catalysts and has shown stable results. Kwapien *et al*.[23] performed coupled cluster (CC) calculations on model cobalt oxide surfaces to benchmark the accuracy of the most popular exchange correlation functionals and found that B3LYP and PBE0 hybrid functionals are in fair agreement with CC results. A polarized Karlsruhe triple zeta (KTZVP) type basis set was used for all atoms. The charge and the multiplicity of the structures are given in parentheses in the figures. Additional broken symmetry calculations were also

performed on some structures to check the antiferromagnetic coupling of the cobalt atoms. Dehydrogenations and other chemically important steps between intermediate states are highlighted in green circles (after reaction steps occurred).

All the reaction energies in the paper are zero-point energy (ZPE), heat capacity, and entropy corrected for a temperature of 298 K and are given as Gibbs free energies. They are calculated according to the standard $E_{(products)}$-$E_{(reactants)}$ concept. For a given reaction, the enthalpy change at 0 K (ΔH_0) can be calculated as $\Delta H_0 = \Delta(E_{(products)} - E_{(reactants)}) + \Delta ZPE$, the enthalpy change at 298 K is computed as $\Delta H_{298} = \Delta H_0 + \Delta(C_{p,298} - C_{p,0})$, and the free energy change at 298 K (ΔG_{298}) is determined from $\Delta G_{298} = \Delta H_{298} - T\Delta S$. The difference in zero point energy (ΔZPE), constant pressure heat capacity (ΔC_p), and entropy change (ΔS) are calculated from DFT vibrational frequencies and correspond to (products) - (reactants). Rather than expressing reaction energies with respect to the standard hydrogen electrode reaction ($2H^+ + 2e^- \rightarrow H_2$), which sensitively depends on the energy of a proton in solution which is challenging to calculate accurately theoretically, the reference system was chosen as $2H^\bullet \rightarrow H_2$. This also has the benefit of removing the strong pH and solvent dependence known for the former reaction. Choice of our $2H^\bullet \rightarrow H_2$ reference system is arbitrary; in theory, any system that allows abstraction of one proton and one electron can be used. Selection of any arbitrary reference system does not affect the qualitative picture of the mechanism proposed as such corrections affect the reactants, products and intermediates equally. With the B3LYP/KTZVP level of theory, the reaction energy for $2H^\bullet \rightarrow H_2$ is calculated to be -4.77 eV.

The experimental ΔG_{298} for the overall water splitting reaction of $2H_2O \rightarrow 2H_2+O_2$ at pH = 0 with reference to the normal hydrogen electrode is given as 4.92 eV. The overall water splitting reaction examined in this work ($2H_2O \rightarrow 2H_2+O_2$) has a ΔG_{298} of 4.31 eV at the B3LYP/KTZVP

level of theory. Thus, the required potential for each dehydrogenation step would be 4.31 eV/4 = 1.08 eV, and overpotentials can be calculated by subtracting this value from the reported highest reaction energies; overpotentials are not reported in this work.

In this paper, we concentrate on the thermochemistry of the intermediate reactions. All possible isomers have been considered for each step of the reactions. The reaction energy values are calculated from the differences of the free energies of the intermediates. Kinetic barriers also play a role but this is not considered in this work primarily because the dynamic nature of these transition states is very sensitive to the hydrogen-bonding environment and there could be multiple transition states for a given reaction. The thermodynamic reaction energies permit the determination of whether or not these electrochemical and chemical reactions are thermodynamically favorable.

6.4 Results and Discussion

6.4.1 Cobalt Dimer Complex

Initial calculations have been performed on the cobalt oxide dimer catalyst. The modeled dimer unit complies with the experimental evidence suggested so far and is constructed to represent the smallest unit cell of edge sharing and corner sharing structure models. The resting state of the catalyst has two aqua ligands and two hydroxyl ligands attached to each cobalt center. Two μ-hydroxo groups link these Co(III)-Co(III) cobalt centers completing the octahedral geometry. It should be noted that many isomers are possible with different positioning of these two aqua and hydroxyl ligands around the cobalt atoms. Structures **D1 - D10** in Figure 6.1 show some of the lowest energy isomers. The hydrogen-bonding environment around these small clusters also has a substantial effect on the stability of the structures. For example, isomers **D10 - D13** in Figure 6.1 represent four isomers of the dimer catalyst where ligands are located in the

same position with different hydrogen orientations altering the hydrogen-bonding environments. The energy difference between the isomers **D10** - **D13** varies up to 0.23 eV, and additional higher energy isomers are possible.

The lowest energy isomer we observed for this ligand architecture with Co(III) species is structure **D1** with one aqua and one hydroxyl group each above (surface), below (bottom), and in the plane (geminal to surface) of the central $Co_2(\mu\text{-}OH)_2$ unit. The **D1** structure is chosen as the resting state of the catalyst to investigate the water oxidation reaction mechanism. We have also investigated water oxidation reaction pathways that could occur from structure **D10**. Structure **D10** (0.89 eV higher in energy than structure **D1**) resembles a minimal unit of a monolayer surface of cobalt oxide where surface and bottom sites are hydroxylated at the resting state of the catalyst. This structure **D10** also represents the top two cobalt atoms in the model cubane structure reported by Wang *et al*.[20]

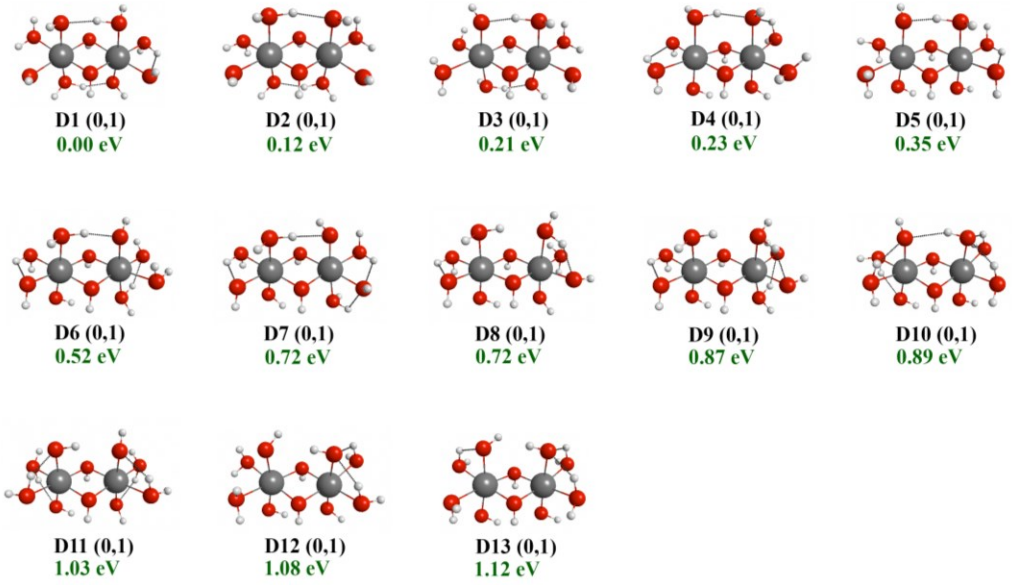

Figure 6.1 Selected isomers for the resting state of the model dimer catalyst. The relative isomer free energies are given in eV with respect to the lowest energy structure **D1**. The charge and multiplicity of the structures are given in parentheses. Small white spheres represent hydrogen atoms, red spheres represent oxygen atoms and gray spheres represent cobalt atoms. This color code is used in all the figures.

6.4.1.1 Pathway 1

The electrochemical oxidation reactions in the pathways are proton-coupled as shown by experimental evidence and thus show a close relationship to proton-coupled electron transfer (PCET) reactions in the OEC of photosystem II.[33, 34] Such proton-coupled oxidation reactions will be hereafter called dehydrogenation reactions. There are fourteen dehydrogenations possible from the lowest energy isomer **D1**. All the possibilities were carefully screened and it was found that removing hydrogen from the aqua ligand geminal to the surface aqua ligand is the most favorable in energy. The reaction energy for this first dehydrogenation step is 1.72 eV (Figure 6.2). The resulting structure **D14** has thirteen possible dehydrogenations. The lowest energy hydrogen removal from **D14** is also from an aqua ligand, which this time is geminal to a surface hydroxo group. This step is 0.19 eV higher in energy than the first dehydrogenation. The structure D15 formed after these first two dehydrogenations has four hydroxo groups in plane with the cobalt atoms. In order to remove oxygen from this dimer complex, a third consecutive dehydrogenation is also considered. Similar to previous structures, **D15** has twelve possibilities for the third dehydrogenation. We found that the third dehydrogenation proceeds through a geminal hydroxo group in the plane with a reaction energy of 1.75 eV. The multiplicity of structure **D1** changes from a singlet to a doublet in **D14** and to a triplet in **D15**. Structure **D16** formed after the third dehydrogenation has doublet and quartet states that are close in energy. The doublet is only 0.04 eV lower in energy than the quartet. The quartet is shown in Figure 6.2 as **D16'**.

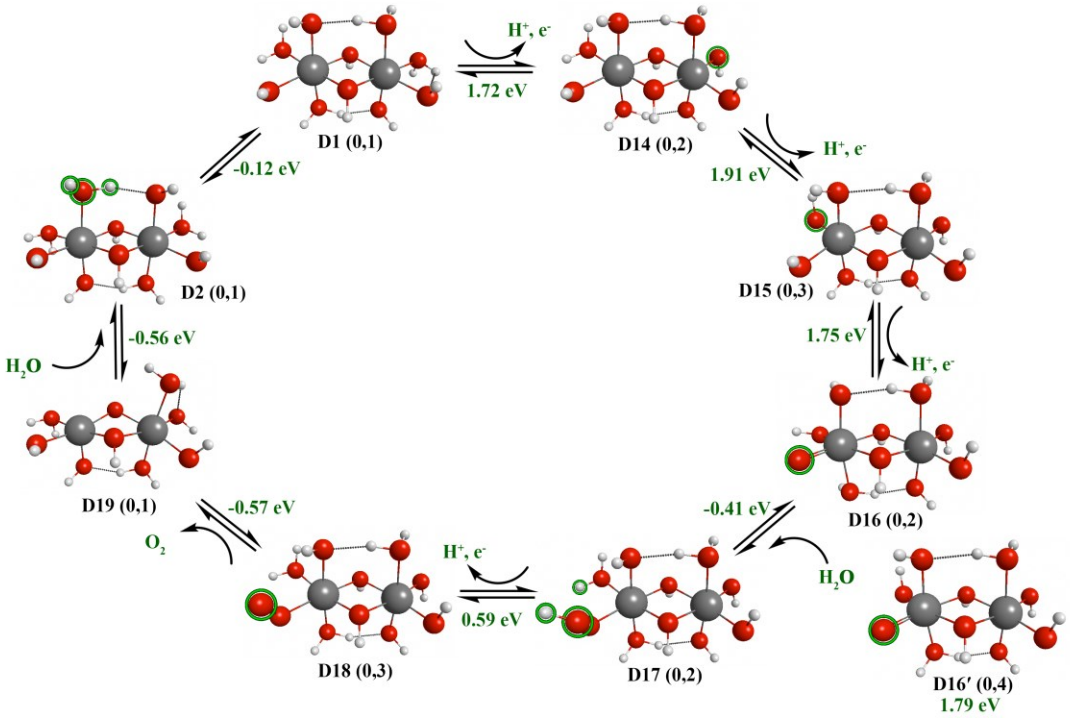

Figure 6.2 Proposed lowest energy reaction pathway 1 for the cobalt dimer catalyst **D1**.

After the first three dehydrogenations, the intermediate structure **D16** has a Co(V)-O radical oxo group. This is a very reactive species that can couple with nearby hydroxo, bridged hydroxo and solvent water molecules. We have investigated these three reaction scenarios (pathways 1 - 3) for the water oxidation process. The lowest energy fourth dehydrogenation from **D16** is found to initiate at the cobalt atom that already has a Co(V) oxidation state. This reaction is endoergic by 2.23 eV. This is thermodynamically not favorable compared to the three reaction pathways reported here, so a geminal oxo radical coupling pathway is not considered.

The lowest energy reaction pathway from the cobalt dimer catalyst **D1** proceeds with a nucleophilic attack of a solvent water molecule to the Co(V)-O radical oxo species. The radical oxo coupling reactions with bridged hydroxo and surface/geminal hydroxo groups are given below in reaction pathways 2 and 3, respectively. The reaction energy for **D16** to **D17** is exoergic

by -0.41 eV. Structure **D17** favors a doublet state; this corresponds well with the slight preference of a doublet state for **D16**. The oxygen of the water molecule binds with the radical oxo species and one hydrogen atom of the water molecule transfers to the geminal hydroxo group to form a geminal aqua ligand. In order to accommodate the attack of the solvent water molecule, this hydrogen abstraction is a necessary step.

Structure **D17** then undergoes the final dehydrogenation step of the reaction pathway. The thermodynamically most favorable dehydrogenation is hydrogen removal from the -O-OH group. This dehydrogenation step is endoergic by 0.59 eV. The dehydrogenated intermediate **D18** is a triplet state with an O-O group. Oxygen can be removed from this complex spontaneously with a ΔG_{298} of -0.57 eV. During this process, an intramolecular hydrogen atom transfer is observed from the bottom aqua ligand to the bottom hydroxo group. This hydrogen transfer reaction leads to a return of the oxidation states of the two cobalt atoms to (III).

In comparison to the other intermediate states seen in this pathway, **D19** has a distorted geometry. The two cobalt atoms are not in plane with bridging hydroxo groups. This type of distortion pattern is observed in other structures with vacant coordination sites in the present study. The surface hydroxo group fills the vacant site left by oxygen removal, leaving behind a vacant site on the surface of singlet **D19**. A second solvent water molecule spontaneously coordinates to this vacant site with a ΔG_{298} of -0.56 eV. The other surface aqua ligand transfers one hydrogen atom to the geminal hydroxo group, which lowers the energy for coordination of the incoming water molecule. The resulting structure **D2** is an isomer of **D1**. The surface and bottom intramolecular hydrogen transfer reactions from the aqua ligand to the hydroxo group with subsequent ligand rotation regenerates the resting state of the dimer catalyst **D1**. This rearrangement step is a spontaneous process with a reaction energy of -0.12 eV.

The highest positive energy step in reaction pathway 1 is the second dehydrogenation reaction (1.91 eV) and the lowest positive reaction energy is the fourth dehydrogenation (0.59 eV). The nucleophilic attack of the water molecule, second water addition reaction, and the oxygen removal reaction are exoergic reactions. The water addition reactions in this study are usually observed to be exoergic reactions.

Although most calculations presented in this work are performed in the gas phase, we used the polarizable continuum model (PCM) to investigate the solvent effect on a subset of the reaction energies. The PCM single point energy calculations on the optimized structures show very little variation to the calculated reaction energies. These energy values for pathway 1 are given in the Appendix D (Table D1) together with the reaction energies calculated using absolute potential energy values neglecting the entropy, zero point energy and enthalpy correction at 298 K. The solvent effect is found to be small, so it is not further considered in this work.

6.4.1.2 Pathway 2

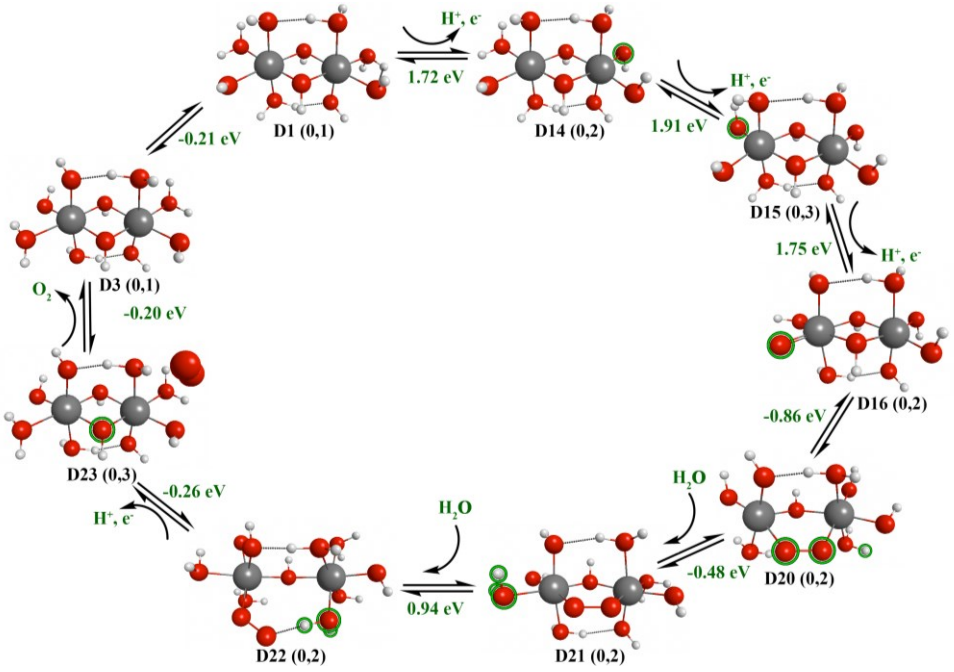

Figure 6.3 Proposed second lowest energy reaction pathway 2 from the cobalt dimer catalyst **D1**.

The second lowest energy reaction (pathway 2, Figure 6.3) begins from isomer **D1** and continues through isomer **D16**, as described in pathway 1. After **D16**, this pathway continues via attack of the Co(V)-O radical oxo group to the bridging hydroxo group. The hydrogen on the bridging hydroxo group transfers to the bottom hydroxo ligand with the attack of the oxo radical. This step leads to **D20**, which is a doublet structure, with a reaction energy of -0.86 eV. Compared to the nucleophilic attack, this process is 0.17 eV higher in energy. The -O-O- group is not in the plane of the two cobalt atoms and the μ–OH group of **D20**; one cobalt atom has a vacant site. A solvent water molecule spontaneously adds to this vacant site to form doublet **D21** with a reaction energy of -0.48 eV. This coordination returns the cobalt atoms and -O-O- bridge to a planar geometry. An intramolecular hydrogen atom transfer is observed from the bottom aqua ligand to a geminal hydroxo group.

In order to remove the oxygen from this complex, a second water molecule must coordinate with one of the cobalt atoms. This coordination is endoergic by 0.94 eV and leads to an open form of the cobalt dimer without two bridging units. Structure **D22** is held together by the hydrogen bonding between surface aqua and hydroxo ligands, the -O-O- group, and the coordinated aqua ligand, together with the bridging hydroxo group. In solution, this complex may break apart into cobalt monomers. As an example, Smith *et al*.[26] experimentally demonstrated that a dimer $[(Co_2(OH)_2(OAc)_3(py)_4]^+$ and a trimer $[Co_3O(OH)_2(OAc)_3(py)_5]^{2+}$ of a cobalt complex undergo decomposition during the O_2 evolution process. However, since this may or may not occur in our system we completed the reaction pathway.

The fourth dehydrogenation proceeds at the coordinated aqua ligand in the previous step. This is exoergic by -0.26 eV. The hydrogen removal process leads to reformation of the second hydroxo bridge in the complex, thus detaching the oxygen molecule from the complex. This

detachment may largely contribute to the total exoergic energy of -0.26 eV. The resulting structure **D23** is a triplet. The direct oxygen removal from **D22** leads to large structural distortions, and the dehydrogenation and the detachment of oxygen is found to be preferable. Oxygen removal from **D23** is an exoergic reaction. The reaction energy of this step is -0.20 eV and the generated structure **D3** is an isomer of **D1**. An intramolecular hydrogen atom transfer from the geminal aqua ligand to the geminal hydroxo group regenerates the resting state of the catalyst.

In this reaction pathway 2, the highest positive energy step is the second dehydrogenation (1.91 eV) and the lowest positive energy step is the second water addition (0.94 eV). The first water addition and the oxygen removal are observed to be exoergic reactions while the second water addition is endoergic.

6.4.1.3 Pathway 3

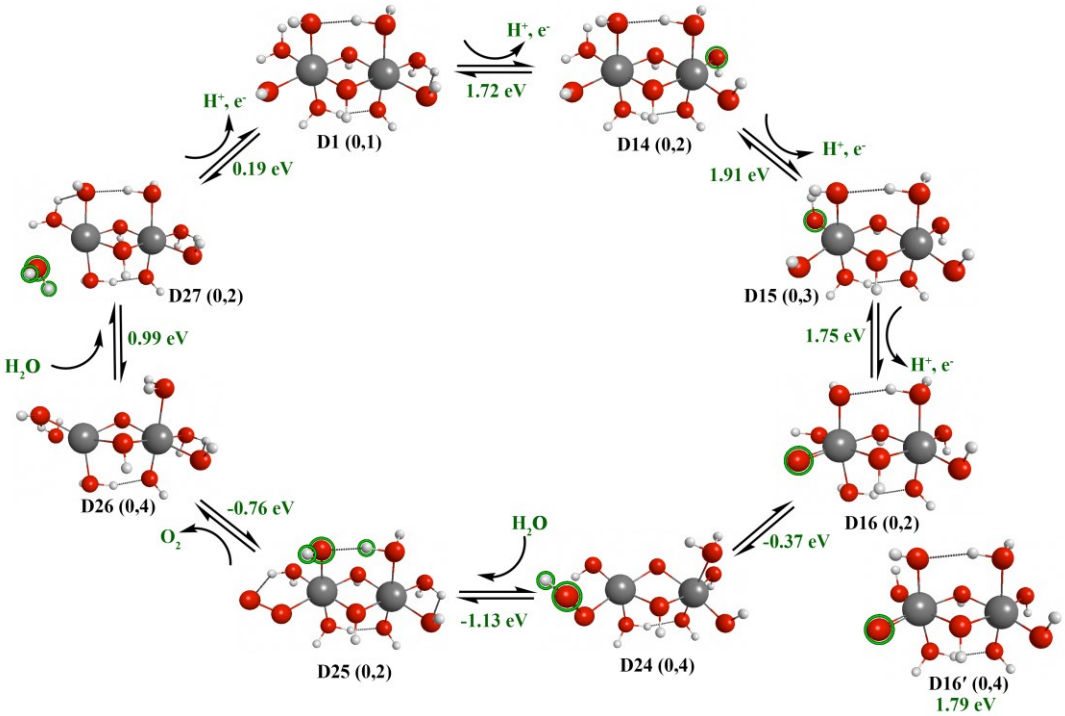

Figure 6.4 Proposed third lowest energy reaction pathway 3 from the cobalt dimer catalyst **D1**.

The reaction pathway 3 (Figure 6.4) proceeds with an attack of Co(V)-O oxo radical in **D16** to the surface hydroxo group. This leads to a quartet **D24.** The doublet state of **D24** is 0.40 eV higher in energy compared to the quartet state. The transformation from quartet **D16'** to quartet **D24** may be preferable in this step. It should also be noted that oxo radical attack to the geminal hydroxo ligand also generates the **D24** intermediate structure. The **D24** structure with one vacant site has a distorted geometry as seen in previous reaction pathways where the structure is slightly bent at the hydroxo bridge groups. This surface or geminal hydroxo coupling is exoergic by -0.37 eV and it is 0.49 eV higher in energy than the hydroxo bridge coupling.

The vacant site left by the hydroxo group after formation of -O-OH in **D24** can easily coordinate with a solvent water molecule. The reaction energy for this coordination is exoergic by -1.13 eV. Subsequently, the hydrogen on the -O-OH group transfers to the geminal hydroxo group, leaving an -O-O bond in **D25**. In the next step, oxygen is removed spontaneously with a ΔG_{298} of -0.76 eV. We also calculated the dehydrogenation from the adjacent aqua ligand in plane with the -O-O group and it is found to be endoergic by 0.80 eV; thus, this step is less likely to occur than oxygen removal. The spin multiplicity changes from a doublet in **D25** to a quartet in **D26**. The generation of the doublet state of **D26** is 0.66 eV higher in energy than the quartet state. It is interesting to note that in both pathways 1 and 3, once the -O-O- bond is formed it is spontaneously removed from the complex, whereas in reaction pathway 2 we have seen that dehydrogenation of the coordinated solvent water molecule lead to reformation of the hydroxo bridge and then detachment of the oxygen molecule from the complex.

The water molecule coordination to the vacant site in **D26** is endoergic by 0.99 eV. In previous reaction pathways, coordination of a water molecule to vacant sites is typically a spontaneous process. **D27** formed after the coordination of second water molecule possesses an

extra hydrogen compared to the resting state of the catalyst. In the next step, this hydrogen is removed to generate the **D1** structure. This dehydrogenation is endoergic by 0.19 eV; it is the lowest dehydrogenation and the lowest positive thermodynamic step in reaction pathway 3. The highest positive energy step is the second dehydrogenation as seen in pathways 1 and 2. The first water addition and the oxygen removal steps in this pathway are exoergic reactions whereas the second water addition to a high spin quartet state is calculated to be endoergic.

6.4.1.4 Comparison of Pathways 1-3

The three reaction pathways (pathways 1, 2, and 3) discussed in this work with the **D1** structure suggest three possibilities of oxygen generation via the formation of Co(V)-O radical oxo species. The **D1** catalyst preferentially removes the first two hydrogen atoms from aqua ligands coordinated in the $Co_2(\mu\text{-}OH)_2$ plane. The third hydrogen atom is removed from a hydroxo ligand in plane. We found that the water addition reactions are usually but not always exoergic. The oxygen extraction is always a spontaneous process. This extraction is favored when the cobalt atoms can return to the Co(III) oxidation state. It is also noteworthy that once the -O-OH bridge is formed, its hydrogen tends to be removed via a dehydrogenation reaction or an intramolecular hydrogen atom transfer to a nearby hydroxo group. If this step competes with coordination of an aqua ligand to a vacant site, the latter is seen to be preferred. The highest positive free energy step is the removal of the second hydrogen in all three reaction pathways.

6.4.1.5 Pathways from Structure D10

We now investigate the water oxidation reaction from isomer **D10**. As discussed above, structure **D10** resembles a minimal unit of a monolayer surface of cobalt oxide where surface and bottom sites are hydroxylated in the resting state of the catalyst. **D10** also represents the top two cobalt atoms in the model cubane structure reported by Wang *et al*.[20] This isomer has two

hydroxo groups on top and bottom with two aqua ligands coordinated to each of the cobalt atoms. After an intricate investigation of 8 reaction pathways from **D10**, we found that the lowest energy pathway (Figure D1 in Appendix D) from structure **D10** proceeds through coupling of a bridging oxo group with a surface hydroxo group. This is also a complicated reaction pathway similar to pathway 2, where at one step the dimer opens up to accommodate the incoming solvent water molecule. After oxygen is removed from this reaction pathway, it forms a structure (**D5)** that is lower in energy than the starting structure **D10**. In consequence, if a system contains species similar to **D10** with two hydroxyl groups on top, oxygen evolution may actually occur via another reaction mechanism starting from **D5** (or similar species) as the catalyst. This may also suggest that **D10** is not a good model on which to investigate the water oxidation reaction mechanism from the dimer catalyst. It also implies that care should be taken in order to obtain the lowest energy isomer of the model compound to be used in the investigation of reaction pathways.

We also included a direct oxo coupling pathway D2 (highest energy out of 8 pathways we studied) in the Appendix D. The direct removal of bridging -O-O-, which is formed after coupling of two oxo radicals between two cobalt atoms, was found to be thermodynamically unfavorable. The oxygen molecule removal from **D36** has a reaction energy of 1.66 eV or a reaction energy of 0.04 eV from **D37**. It is also necessary to point out that oxygen removal from **D40** leads to structural distortions. From **D41,** O_2 removal requires -0.19 eV, which is similar to and potentially competes with the second water addition that is also exoergic by -0.19 eV. Step-by-step water addition and oxygen removal is considered in pathway D2. All the pathways studied with **D10** are found to lead to a lower energy intermediate state than the starting structure, which suggests that the dimer catalyst is unlikely to have a form with two hydroxyl

ligands on top for its resting state. Structures with one hydroxyl and one aqua ligand are preferred.

6.4.1.6 Comparison between pathways from D1 and D10

There are some similarities and many differences for the lowest energy reaction pathways from **D1** and **D10**. Overall, reaction pathway 1 from **D1** proceeds with a nucleophilic attack of solvent water molecule to the radical moiety, whereas in pathway D1 with **D10**, it proceeds via a coupling reaction of a bridging oxo group with a surface hydroxo group. In reaction pathway 1, dehydrogenation is preferred via a H_2O>OH>μ-OH pattern, whereas in pathway D1 the pattern is μ-OH>OH>H_2O. The first three dehydrogenation steps are lower in energy in the lowest energy pathway D1 from **D10** than the lowest energy pathway 1 from **D1**. The highest positive energy step from **D1** in pathway 1 is the second dehydrogenation requiring 1.91 eV, whereas for **D10** in pathway D1 it is the first dehydrogenation that has a free energy change of 1.68 eV. The lowest positive energy in pathway 1 is the fourth dehydrogenation requiring 0.59 eV, and in pathway D1 it is the rearrangement of **D5** to **D10** which requires 0.54 eV. The water addition reactions and oxygen removal reactions are exoergic in both of the lowest energy reaction pathways. The **D1** structure forms a Co(V)-O radical oxo species in the lowest energy pathway 1, whereas in pathway D1 the Co(V) oxidation state was not observed. The O-O bond is formed after three dehydrogenations followed by a nucleophilic attack of a water molecule in pathway 1 of **D1**, while in the **D10** of pathway D1, the O-O bond is formed after two dehydrogenations. The generation of two oxo radical groups on one or two cobalt atoms for a direct oxo coupling type reaction mechanism is found to be thermodynamically unfavorable for both **D1** and **D10**. The oxygen molecule is removed from the cluster once the oxidation of the -O-O attached cobalt atom reaches the Co(III) oxidation state in **D1** (pathways 1, 2 and 3), and in **D10** (pathway D1).

6.4.2 Cobalt Cubane Complex

Following the investigation of the cobalt dimer complex, we explored possible mechanisms for water oxidation on a model cubane complex. The resting state of our model cubane catalyst complex consists of four Co(III) centers, each coordinated with three μ_3-O (bridged oxo) sites, two aqua ligands, and a hydroxyl group. Each cobalt atom in the cubane complex is coordinated with six oxygen atoms in an octahedral fashion. Similar to the dimer complex, the cubane complex also possesses many isomers that are sensitive to both positions of the aqua and hydroxo ligands and the hydrogen-bonding environment. We have chosen the lowest energy isomer **C1** together with isomer **C7** that has two hydroxo groups on top (with respect to the orientation given in Figure 6.5) similar to the dimer complex (**D10**) to investigate the water oxidation mechanism. The μ_3-O sites are not protonated in our model compound and the number of hydrogen atoms are similar to the model cubane complex proposed by Wang *et al*.[20] Our model compound **C1** is 0.98 eV lower in energy than isomer **C7**, which is the lowest energy version of the structure used in the Wang *et al*.[20] model.

The lowest energy structure **C1** prefers a ligand architecture where two aqua ligands are coordinated at the surface and bottom of the cubane core (with respect to the orientation given in Figure 6.5) and the other aqua and hydroxo groups are positioned perpendicular to aqua ligands on top and bottom. In contrast to the lowest energy cubane complex **C1**, we have seen that the lowest energy dimer **D1** structure has one aqua and one OH group on top and bottom. It is noteworthy that **C1** does not bear any adjacent hydroxo groups on any cobalt atom sites, whereas in **C7** there are two sites with adjacent hydroxo groups: one between two surface cobalt atoms and the other on bottom two cobalt atoms. There are two adjacent hydroxo group sites seen on both **D1** and **D10** dimer complexes; on **D1** these hydroxo groups are geminal to each other on

one cobalt atom, whereas on **D10** the hydroxo groups are on the top and bottom of the two cobalt atoms. We also calculated a structure similar to the model compound proposed by Li et al.[22] with two protonated μ_3-O sites. This structure is -0.69 eV lower in energy than the model we used. However, protonation of the μ_3-oxo sites in the cubane complex changes the formal oxidation state of the bottom cobalt layer. Our model contains a cubane core with all cobalt atoms in the Co(III) formal oxidation state.

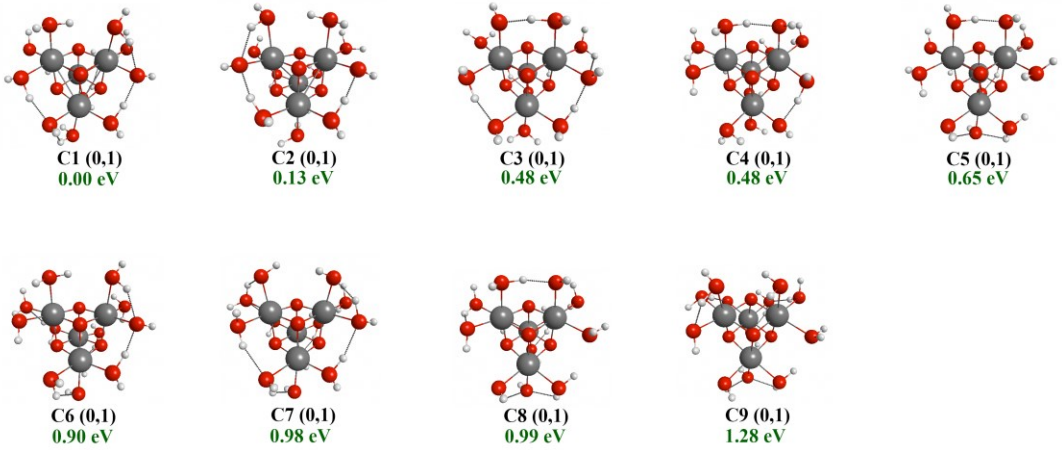

Figure 6.5 Selected low energy isomers of the model cobalt cubane complex.

6.4.2.1 Pathway 4

Starting from the lowest energy isomer **C1** we investigated all the possible dehydrogenation reactions. The **C1** cubane complex prefers a dehydrogenation from a geminal aqua ligand. This is a similar characteristic to what we have seen with the lowest energy dimer **D1**. The initial dehydrogenation from **C1** is endoergic by 1.62 eV, which is 0.1 eV lower in energy compared to the dimer **D1**. The resulting doublet structure **C10** now has two geminal hydroxo groups on one cobalt atom. The thermodynamically lowest second dehydrogenation (1.34 eV) occurs from the hydroxo group that already lost one hydrogen atom in the first

dehydrogenation step when it was coordinated as a geminal aqua ligand. In the case of dimer **D1**, the second dehydrogenation is seen to favorably occur from an aqua ligand.

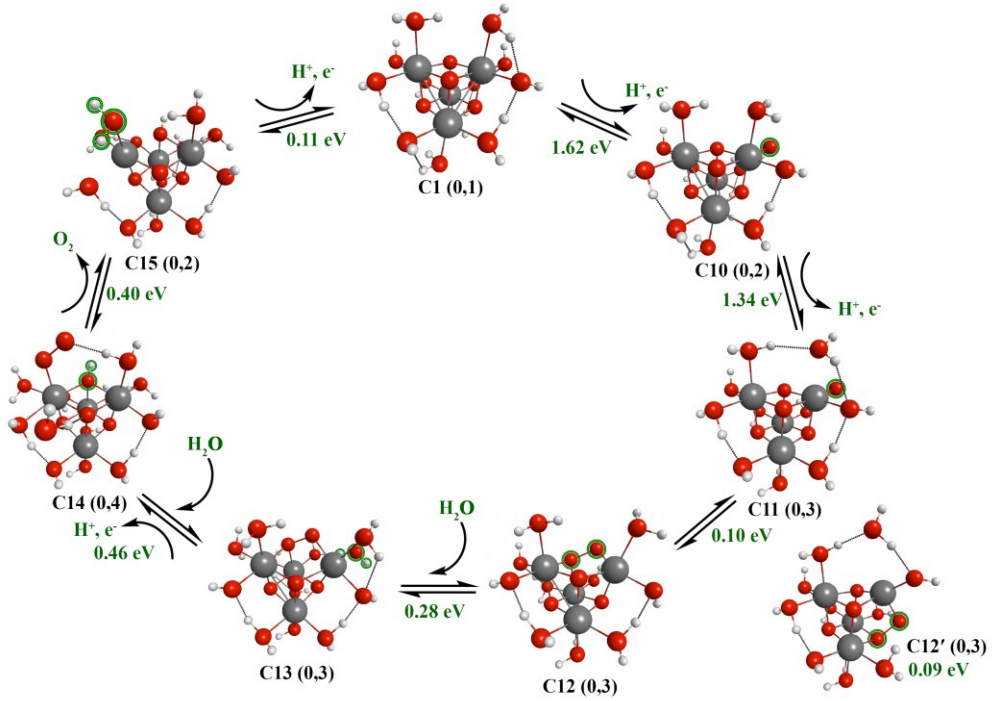

Figure 6.6 Proposed lowest energy reaction pathway 4 from the cobalt cubane complex **C1**.

After the first two consecutive dehydrogenation steps, the cubane complex **C11** possesses an active Co(V)-O oxo radical. In contrast in the dimer complex, formation of the Co(V)-O radical requires removal of three hydrogen atoms. The multiplicity changes from a doublet in **C10** to a triplet in **C11**. The lowest energy intermediate state with the Co(V)-O radical species in the dimer complex is a doublet whereas in the cubane it is a triplet state. The generation of this radical moiety results in an elongated bond length between the surface water molecule and the cobalt atom in **C11**. The radical oxo group can potentially couple with nearby bridging oxo species, geminal hydroxo species, and solvent water molecules. We have investigated the fate of this oxo radical in all three possible scenarios. The reaction energies for these steps are endoergic by 0.10 eV, 0.47 eV, and 0.52 eV, respectively. These energy values are competitive and lie in a

thermodynamically reasonable range so a detailed description is necessary to fully understand the system.

It should be noted that a Co(V)-O radical moiety has not been experimentally observed. Wang and Van Voorhis[20] suggested that the lowest energy pathway for water oxidation from the cobalt cubane complex is a direct oxo coupling (between two cobalt atoms) pathway that proceeds through Co(IV)-O moieties. They ruled out a nucleophilic attack from the solvent water molecule because of lack of experimental evidence. It is possible that intermediate structure **C11** with the Co(V)-O group may be so reactive that the existence of it may be rather difficult to ascertain. In 2013, Li and Siegbahn[22] in their model complexes suggested an attack of a water molecule to oxygen radical coupled with Co(IV) state; however, they proposed that a state with Co(V) formal oxidation state is needed for reactivity. Mattioli and coworkers[21] studied two different models of cobalt catalyst with ab initio molecular dynamic simulations starting from a system which four electrons had been removed. Similar to Wang[20] *et al*., they found that a Co(IV)-O species is the driving species of the reaction. They suggested that removal of two electrons from a terminal Co-OH is sufficient to promote the formation of Co=O moieties. Such initial electron removals were not considered in our work; all the mechanistic pathways treated in this study follow through neutral reaction intermediates via proton coupled electron transfer reactions.

Our results indicate that the thermodynamically most favorable pathway follows through coupling of the oxo radical with μ_3-O groups (pathway 4 in Figure 6.6). There are two μ_3-O positions on top and bottom competing for this radical moiety where both of these coupling reactions are endoergic by 0.10 eV and 0.09 eV, and the resulting species are given in Figure 6.6 as **C12** and **C12'**, respectively. We looked at the coupling reaction with the top μ_3-O site leading

to **C12**. Even though the **C12'** structure is 0.01 eV lower in energy than **C12**, it has an aqua ligand with a longer bond length (almost detached as the unpaired electrons on water molecule are pointing away from the cobalt atom). The **C12** intermediate state now has a vacant site left by the oxo group. A solvent water molecule coordinates with this vacant site endoergically by 0.28 eV to generate **C13**. This water is relatively weakly bound, as shown by the elongated bond length between this water molecule and the cobalt atom. To extrude the trapped oxygen molecule in the core, a second water molecule coordinates with one of the surface cobalt atoms bound to the -O-O- group and a hydrogen atom is removed with an overall endoergic reaction energy of 0.46 eV, leaving a μ_3-OH group in the complex (similar to the dimer **D21** to **D22** and **D22** to **D23** steps). The resulting structure **C14** has a high spin quartet state. With the coordination and dehydrogenation of an aqua ligand, the -O-O- group leaves the cubane core and occupies a surface site on a single Co atom. Oxygen ejection from the **C14** cluster is found to be the most thermodynamically preferred option for the next step with a reaction energy of 0.40 eV.

From **C14** to **C15**, intramolecular hydrogen atom transfer reactions may serve to increase the oxidation state of the -O-O bound cobalt atom. Given that hydrogen atoms of both aqua ligands in **C14** are transferred to bottom cobalt atoms, the highest formal oxidation state the cobalt atom with the -O-O bond can achieve is Co(IV 2/3). The generated cluster **C15** is a doublet state. The fourth hydrogen can be easily removed from the μ_3-OH group forming the starting structure **C1**. This dehydrogenation is exoergic by 0.11 eV. The formal oxidation states of the bottom two cobalt atoms change to Co(II) Co(III) in **C12**, Co(II) Co(IV) in **C13**, and Co(III) Co(IV) in **C14** and **C15**. The highest positive energy step in pathway 4 is the first dehydrogenation (1.62 eV) and the lowest positive energy step is the radical oxo coupling with

μ_3-O groups (0.10 eV). The two water addition and the oxygen removal reactions are calculated to be endoergic.

Our lowest energy **D1** dimer and the **C1** cubane complexes thermodynamically favor the formation of the Co(V)-O radical. The lowest energy reaction mechanism for the dimer proceeds through nucleophilic attack of a solvent water molecule to the radical moiety, whereas in the cubane complex, the radical is seen to prefer coupling with the nearby μ_3-O groups. The O-O bond formation with the dimer **D1** is observed after three consecutive dehydrogenation steps followed by a water addition. In the cubane complex, the O-O bond is formed after two consecutive hydrogen removals. Removal of the first and second hydrogen atoms from aqua ligands are preferred in the lowest energy dimer complex, whereas in the cubane complex the first hydrogen is removed from an aqua ligand and the second is removed from a hydroxo group. The oxygen removal and water addition reaction are all exoergic in reaction pathway 1 whereas in pathway 4 they are all endoergic reactions.

6.4.2.2 Pathway 5

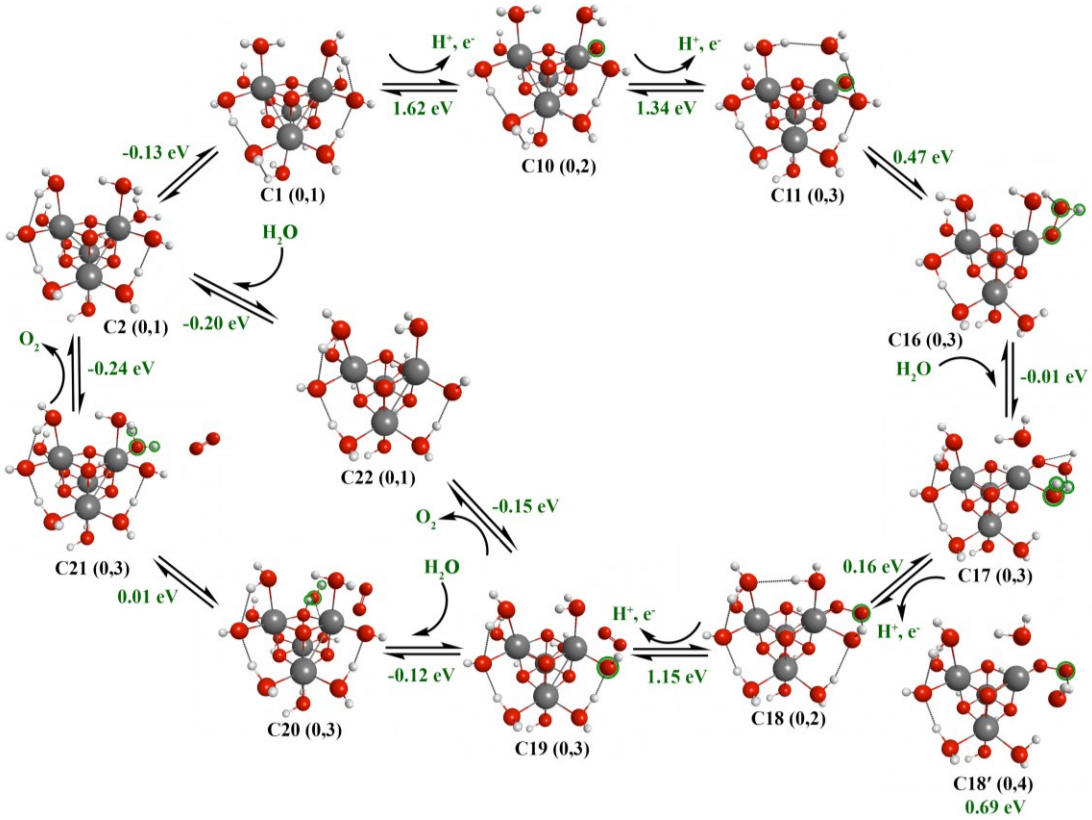

Figure 6.7 Proposed second lowest energy reaction pathway 5 from the cobalt cubane complex **C1**.

The second lowest reaction pathway (pathway 5 in Figure 6.7) from the **C11** structure involves a coupling reaction of a Co(V)-O oxo radical with the geminal hydroxo ligand. The generated structure **C16** has an -O-OH bond and this step is endoergic by 0.47 eV. Coordination of a water molecule to the vacant site left by the geminal hydroxo group is an exoergic process by -0.01 eV. With this coordination, an elongation of the bond between surface aqua and cobalt ligand is observed in **C17**. The oxidation states of the bottom two Co atoms are observed to become Co(II) Co(III), and this remains unchanged throughout the cycle after **C17**. The thermodynamically lowest next step is dehydrogenation from the -O-OH group. This is endoergic by 0.16 eV. We have observed this phenomenon (dehydrogenation from the -O-OH

group) throughout all the reaction pathways in the dimer as well as in the cubane complex. The spin multiplicity of the resulting structure **C18** is a doublet state. The formation of the quartet state is 0.53 eV higher in energy than the **C18** and it is given as **C18'** in Figure 6.7. We also looked at the direct oxygen removal from the **C18** structure. This step is calculated to require 1.27 eV, which is 0.12 eV higher in energy than the fourth dehydrogenation step to yield **C17**. The cobalt atom has to acquire a Co(IV) oxidation state in order to remove its oxygen molecule. This higher oxidation state can also be achieved via intramolecular hydrogen atom transfer reactions. However, the oxygen coordinated cobalt atom in **C18** has a saturated ligand environment blocking these transfer reactions. The fourth dehydrogenation with 1.15 eV free energy change is seen at the aqua ligand adjacent to the -O-O group. This final hydrogen atom removal resulted in an elongated bond between cobalt atom and the -O-O group in the triplet structure **C19**.

The oxygen removal from the **C19** intermediate state and the second water addition reactions are both exoergic competitive reactions. The oxygen removal is found to be 0.03 eV more favorable than the second water addition reaction. In order to understand the impact of nearby solvent water molecules to the thermodynamics of oxygen removal, we considered step-by-step water addition and oxygen removal process through **C20**, **C21**, and **C2**. A direct oxygen removal process also connects **C19** to **C2** via **C22**. All these steps are found to be thermodynamically very favorable. The second water molecule approaches at the side of μ_3-O and coordinates to the core through hydrogen bonding exoergically by -0.12 eV to generate **C20**. The second water coordination to **C22** is 0.08 eV more favorable than the water addition to **C19** and 0.09 eV more favorable than the combined steps of water addition and coordination to **C19** (**C19** to **C20** and **C20** to **C21**). The -O-O group is replaced with the solvent water molecule in

the step leading from **C20** to **C21**. This process is endoergic by 0.01 eV. The oxygen removal from the triplet **C21** is exoergic by -0.24 eV and gives rise to the singlet **C2**. Intermediate **C2** is an isomer of **C1** and spontaneously rearranges back to the starting structure with intramolecular hydrogen atom transfer reactions. This regeneration has a reaction energy of -0.13 eV.

Overall, the highest positive energy in pathway 5 is the first dehydrogenation reaction, which is 1.62 eV, and the lowest positive energy step is the coordination of the second water molecule to the detached -O-O site. The addition of two water molecules and the oxygen removal steps are found to be exoergic reactions.

6.4.2.3 Pathway 6

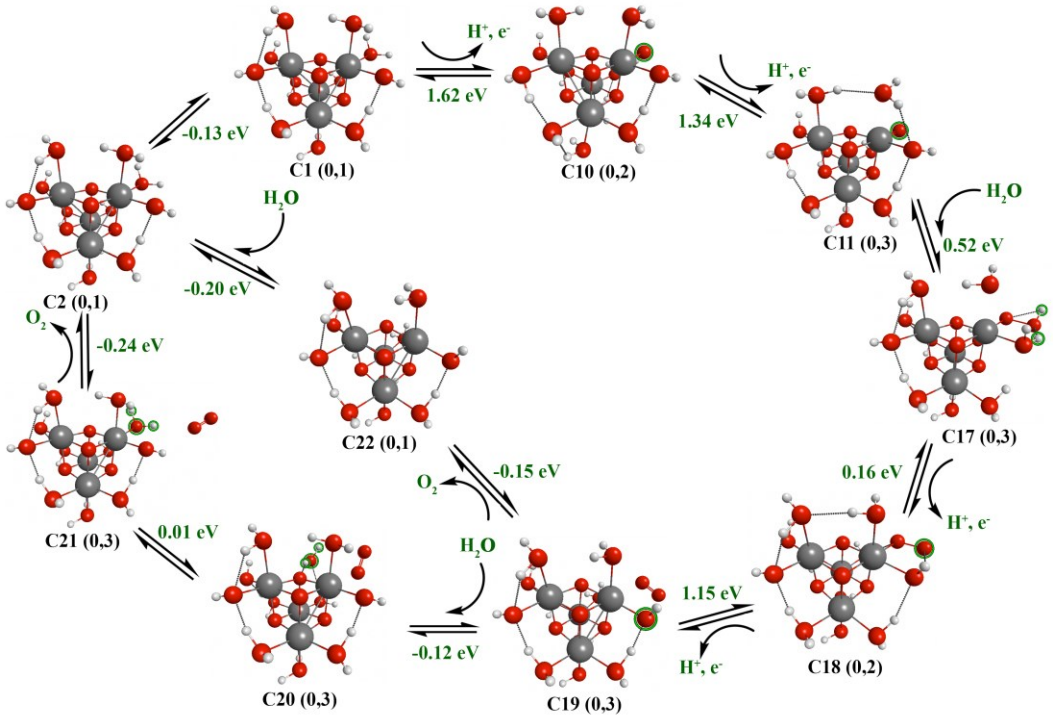

Figure 6.8 Proposed third lowest energy pathway 6 from the cobalt cubane catalyst **C1**.

A nucleophilic attack from a solvent water molecule to the Co(V)-O radical in **C11** with 0.52 eV energy is the third lowest energy pathway (pathway 6 in Figure 6.8) for the oxygen evolution from the cubane complex. The oxygen from the solvent water molecule couples with

the radical oxo species and simultaneously a hydrogen of the water molecule is transferred to the geminal hydroxo group, forming structure **C17** in pathway 5. This nucleophilic attack reaction is an endoergic reaction, whereas for the **D1** structure the nucleophilic attack is calculated to be a spontaneous exoergic process. The second water addition and the oxygen removal are exoergic reactions. The catalytic cycle then follows through pathway 5. The highest and lowest positive energy steps are similar to pathway 5.

6.4.2.4 Discussion of pathways 1-6

Overall, the oxygen removal process from the cobalt cubane core is a complicated process. The thermodynamically lowest process involves the coupling of an oxo radical with μ_3-O sites. The nucleophilic attack of a solvent water molecule and the geminal hydroxo coupling reactions have nearly similar free energy changes (with a difference of 0.05 eV). Due to the highly amorphous nature of the Nocera catalyst, several catalytic pathways may occur experimentally from the coupling of these Co(V)-O and μ_3-O sites. The corners and edges of this amorphous catalyst may favor geminal hydroxo coupling and nucleophilic attack reactions. However, as seen with the dimer complex, it is also possible that all these reaction pathways are collectively contributing to the oxygen evolution process. The isotopic labeling investigations for the Nocera catalyst suggest initial oxygen evolution via unlabeled oxygen from the solvent water. This can be explained from geminal hydroxo coupling and solvent water attack mechanisms. The oxygen removal process from **D1** (after -O-O bond is formed) is seen once the cobalt atom achieves the Co(III) oxidation state in pathways 1, 2 and 3, whereas in pathway 5 and 6 for the lowest energy cubane **C1**, it requires a Co(IV) oxidation state. In the lowest energy pathway 4, the cobalt atom may acquire oxidation states of either Co(IV 2/3) or Co(III 2/3) before oxygen removal. The water addition reactions are generally exoergic reactions, but are

occasionally endoergic. The highest positive energy step in pathways 4-6 from **C1** is the first dehydrogenation reaction (1.62 eV), which is much smaller in comparison to the dimer, where the second dehydrogenation is the highest energy step at 1.91 eV. Both the lowest energy dimer **D1** and the lowest energy cubane **C1** form the Co(V)-O radical oxo species. Once the radical moiety is formed, it couples with nearby hydroxo or bridging oxo groups and also undergoes nucleophilic attack from a solvent water molecule. All six pathways from the lowest **D1** dimer and from the **C1** cubane complex follow through this fundamental behavior. To understand more about these competitive reactions, kinetic properties are also required. Given the dynamic nature of these reactions with solvent water molecules as reactants, barrier heights obtained from DFT calculations cannot be solely used to predict the final outcome.

6.4.2.5 Pathway 7 from C7 isomer

In addition, we have examined reaction pathways for the **C7** structure (0.98 eV higher in energy than **C1**, which is 0.09 higher than the difference between **D1** and **D10**) as the resting state of the cubane catalyst. The lowest energy reaction pathway 7 from **C7** is given in Figure 6.9 and it is carefully screened from multiple reaction pathways. We also included a reaction pathway that demonstrates a direct coupling of two surface oxo radicals (pathway 8 in Figure 6.10). These two reactions have the same property of finding a lower energy intermediate state than the starting structure **C7**, as observed with the **D10** dimer. However, since the **C7** model has been used in previous studies and the reaction pathways from the cobalt cubane complex are currently under debate, we included a description of these two reaction pathways.

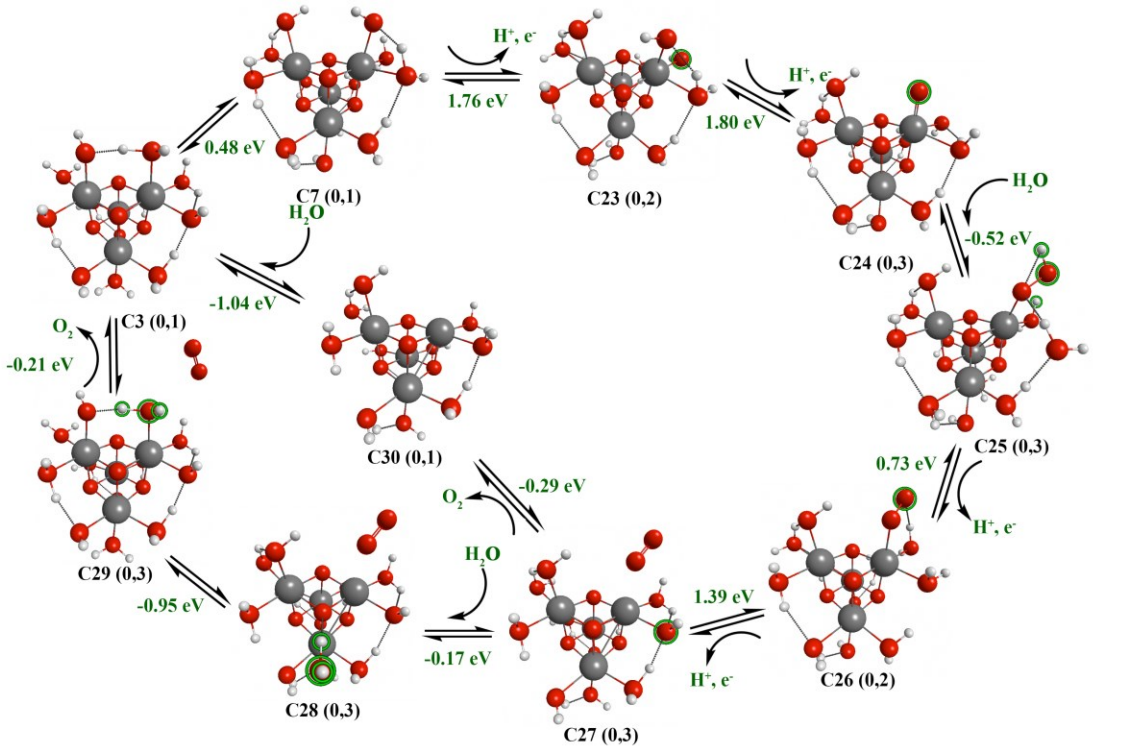

Figure 6.9 The lowest energy reaction pathway 7 from structure **C7**.

The first step in pathway 7 is a geminal aqua dehydrogenation reaction similar to that of pathway 4 (the lowest energy pathway from **C1**) and the reaction energy is 0.14 eV higher than that from pathway 3. The second consecutive dehydrogenation from structure **C23** requires 1.80 eV, which is 0.04 eV higher in energy than the first dehydrogenation; this step is found to be the highest energy step for pathway 7. The **C7** structure can be rotated in a fashion that the two aqua ligands are located on top similar to that of **C1**. Both **C1** and **C7** prefer to remove first two hydrogen atoms from sites with aqua and hydroxo groups. The first dehydrogenation from an aqua ligand forms a structure with two hydroxo groups on one cobalt atom for both **C1** and **C7**. Subsequently, the second dehydrogenation is initiated from one of these hydroxo groups. These two dehydrogenation reactions from the **C7** isomer are higher in energy than the first two dehydrogenations from **C1**. The resulting doubly dehydrogenated structure **C24** carries a Co(V)-

O radical center. This radical moiety is generated after the first two consecutive dehydrogenations similar to that of **C1**.

Pathway 7 proceeds through a nucleophilic attack of a solvent water molecule to yield **C25**. This nucleophilic attack is exoergic by -0.52 eV and the multiplicity remains unchanged in the triplet state. The three possible reaction steps from the **C11** radical oxo species generated from **C1** were all calculated to be endoergic, whereas nucleophilic addition in pathway 7 from **C7** is an exoergic reaction. Similar to pathway 5, the oxygen atom from the solvent water molecule couples with the radical oxo species, and one hydrogen of the water molecule is transferred to the nearby hydroxo group forming a -O-OH group on the surface of structure **C25**.

In the next step, the hydrogen on the O-OH group is dehydrogenated, requiring a reaction energy of 0.73 eV. In order to remove the O-O group from the surface cobalt atom of **C26**, one aqua ligand coordinated to this cobalt atom has to be dehydrogenated. The direct oxygen removal from **C26** is expected to be higher in energy as the ligand environment around -O-O is similar to that of the **C18** structure. This dehydrogenation is the fourth dehydrogenatrion of the catalytic cycle and it changes the spin multiplicity from a doublet to a triplet in structure **C27**. The reaction energy for this is 1.39 eV, and it is higher in energy than the third dehydrogenation. The oxygen molecule is now at most physisorbed to the catalyst in structure **C27**.

The direct oxygen removal from **C27** is calculated to be -0.29 eV, which is a more favorable reaction compared to the second water addition to form **C28** which is exoergic by -0.17 eV. This is also observed in the **C19** structure of pathway 5 where both have similar ligand environments. We looked at both second water addition and direct oxygen removal steps to the structure **C27** in order to compare with pathway 5. All the reaction steps in these two branches are found to be exoergic. From **C27** to **C28** the second water molecule approaches sideways to a

μ_3-O group; it then coordinates with the sixth vacant position left by the detaching oxygen molecule. This coordination is also an exoergic reaction by -0.95 eV and generates structure **C29** with a triplet spin state. From structure **C29**, oxygen is released exoergically with -0.21 eV to produce a singlet state structure **C3**. Coordination of the second water molecule to the vacant site of **C30** is 0.87 eV more favorable than second water addition (**C27** to **C28**). This also produces singlet **C3**. This structure **C3** is a lower energy isomer than structure **C7** and requires 0.48 eV of energy to regenerate **C7**. Even though water oxidation can occur from the **C7** structure to evolve oxygen, it does not regenerate the resting state. The highest positive energy in pathway 7 is the second dehydrogenation that is 1.80 eV, and the lowest positive energy step is the **C5** regeneration step with 0.48 eV free energy change.

There are multiple similarities observed in the lowest energy reaction pathways from **C1** and **C7**. The dehydrogenation preference is similar where the first hydrogen removal from both **C1** and **C7** occurs from a geminal aqua ligand and then the second hydrogen is removed from one of the two hydroxo ligands on the same cobalt atom. The oxygen molecule is removed from the cobalt atom in **C1** and **C7** once it reaches the Co(IV) oxidation state except for pathway 4. Aside from these similarities there are also several differences. The overall lowest energy reaction pathway from **C7** involves a nucleophilic attack to a Co(V)-O radical whereas in **C1** it proceeds via a geminal coupling of a radical oxo group with bridging oxo groups. The nucleophilic attack of solvent water, second water addition, and oxygen removal steps are found to be exoergic in pathway 7 from **C7**, whereas in **C1** we found that all these steps are endoergic. The highest positive energy step for pathway 4 from **C1** is the first dehydrogenation (1.62 eV), whereas in the pathway 7 from **C7** it is the second dehydrogenation (1.80 eV). This is reversed for dimers **D1** and **D10**.

6.4.2.6 Pathway 8 from C7 isomer

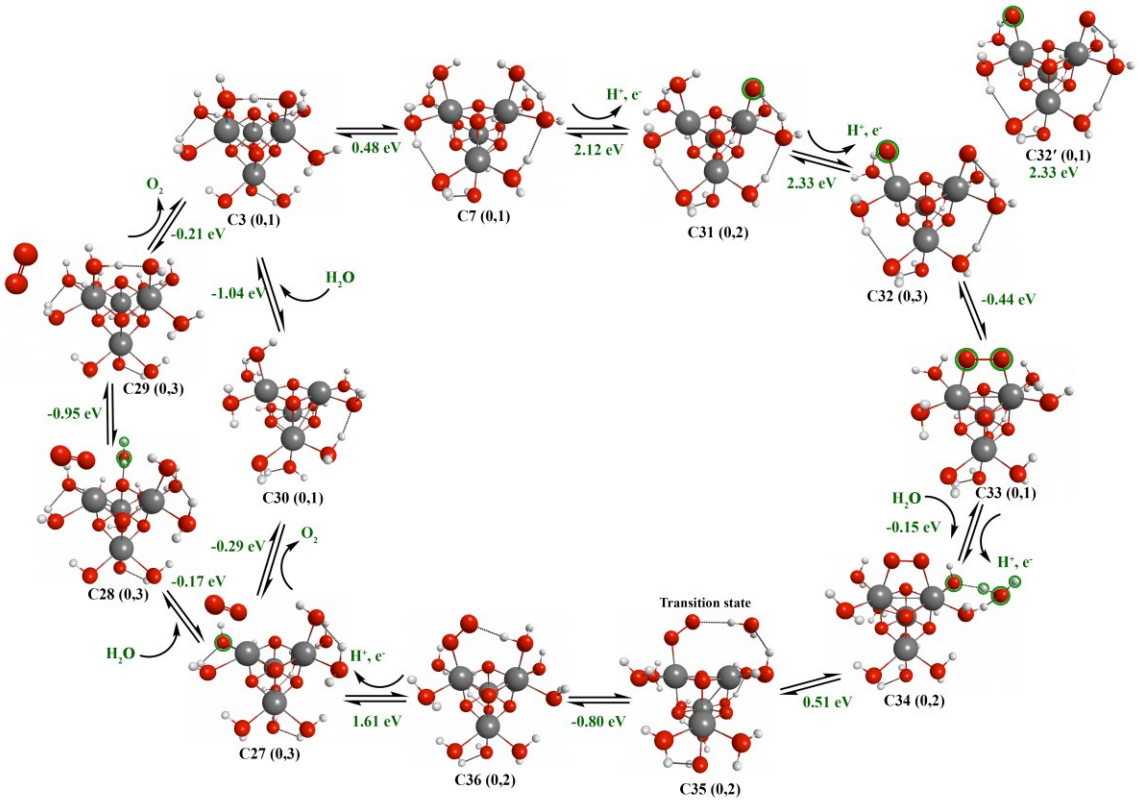

Figure 6.10 Direct coupling pathway 8 from structure **C7**.

The direct oxo coupling pathway 8 from **C7** is given in Figure 6.10. This pathway has some similar properties to the direct coupling pathway proposed by Wang *et al*. for the cubane complex. This type of direct coupling pathway has been proposed earlier for other water oxidation catalysts as well (e.g. ruthenium blue dimer[35, 36]). We found that this pathway is thermodynamically the highest energy pathway from **C7**. The first two dehydrogenation reactions, **C7** to **C31** and **C31** to **C32**, have higher endoergic reaction energies of 2.12 eV and 2.33 eV, respectively, than any other reactions. In reaction pathway 8 for structure **C32**, broken symmetry singlet calculations show that the cobalt atoms are antiferromagentically coupled; the triplet spin state for this structure is nearly degenerate with the singlet state. The singlet state is 0.0015 eV higher in energy than the triplet state and it is given in Figure 6.10 as **C32'**. Two

surface Co(IV)-O radical groups in structure **C32** directly couple with each other to generate an O-O bridge in structure **C33** that has a singlet spin state. This coupling reaction is exoergic by -0.44 eV.

The direct oxygen extraction from **C33** is endoergic by 0.62 eV. This is a thermodynamically higher energy process as seen with the **D10** dimer as well. In the next step, a geminal aqua ligand in structure **C33** is dehydrogenated to facilitate the incoming water molecule in structure **C34**. The reaction energy for these processes is -0.15 eV and the spin state changes from singlet to doublet in structure **C34**. With the incoming aqua ligand, the O-O bridge disconnects and attaches to one cobalt atom via the transition state **C35** (163.79*i* cm^{-1}). This reaction has a barrier height of 0.51 eV. The aqua ligand fully coordinates to the vacant site of the cobalt atom in structure **C36** with an energy of -0.80 eV compared to the transition state, and a -0.29 eV overall reaction energy from **C34**. The cobalt atom with the coordinated -O-O group has a Co(III) oxidation state in **C34** indicating less preference for oxygen removal according to the previous pattern. However, we were not able to get a converged structure after oxygen removal from **C36**.

The fourth dehydrogenation occurs from a geminal aqua ligand attached to the O-O group with 1.61 eV. At the same time, the hydrogen atom is transferred from the coordinated surface aqua ligand to the geminal hydroxo group in **C27**. With the formation of **C27**, the cycle reconnects back to pathway 7 through two branches and eventually forms **C3**, which again is a lower energy intermediate state than the resting state **C7**. The second dehydrogenation step is the highest positive energy step with a reaction energy of 2.33 eV and the lowest positive energy step is the catalyst regeneration that requires 0.48 eV. The oxidation states of the bottom two cobalt atoms in all structures arising from **C7** pathways 7 and 8 remain Co(III) Co(III), whereas

in the pathways from **C1** these oxidation states changed for different intermediates in the reaction pathways.

6.4.2.7 Cubane Pathways Discussion

Reaction pathways 7 and 8 suggest many interesting characteristics even though **C1** and **C7** differ by almost 1 eV in free energy. As discussed above, there are some similarities such as the origin of first two dehydrogenations and formation of Co(V)-O radical species, etc. If small cubane complexes with four cobalt atoms are components of the Nocera catalyst, there could be multiple instances of these clusters. These clusters are very sensitive to the ligand orientations, and there could be many competing orientations and rotations of hydroxo and aqua ligands present due to the dynamic nature of the system. Energetically, instances with two hydroxo groups on top for a cubane complex (similar to **C7**) as a component of the catalyst are likely to be a higher in energy. However if this occurs, nucleophilic attack of a solvent water molecule is favored. Water oxidation on these structures may lead to other lower energy structures, yielding oxygen evolution from different pathways. The lowest energy **C1** complex shows an instance where two aqua ligands are on top (with reference to the orientation given in Figure 6.5). This architecture may be the most probable scenario in the neutral pH condition as it is the thermodynamically lowest isomer for the cubane systems examined in this work. In such cases, the water oxidation pathway may proceed through geminal coupling to bridging oxo groups. If the catalyst occurs primarily on an extended surface, it is possible that the only option is to follows through a direct coupling mechanism between two oxo radicals since geminal dehydrogenation would not be possible. The edges and corners of the catalyst may enhance the oxygen evolution because of their susceptibility to lower energy dehydrogenations as seen by the preference of geminal dehydrogenations for both the dimer and cubane complexes. Overall,

oxygen evolution from the cobalt cubane catalyst is a very complex reaction and we can hypothesize that multiple reaction pathways from different instances contribute to the collective oxygen evolution.

6.5 Conclusions

Ab initio density functional theory was used to investigate water oxidation processes promoted by model cobalt oxide dimer and cubane catalysts. These models were designed based on experimental evidence and are related to cubane complexes with water-derived (aqua and hydroxyl) ligands that have been examined before. Several reaction pathways from two model dimer and cubane catalysts were investigated to propose the thermodynamically lowest energy pathways. The best thermodynamically favored mechanism found for both the lowest energy dimer and cubane catalyst is initiated with the formation of Co(V)-O radical species. In the dimer complex this is followed by a nucleophilic attack of a solvent water molecule to the radical moiety, whereas for the cubane complex the lowest energy pathway involves a geminal coupling with the μ_3-O. There is a higher probability that these are activated at the edges or defects of cobalt oxide catalytic surfaces ligated with aqua ligands**,** suggesting that the amorphous nature of the Nocera catalyst may enhance its water oxidation ability. The first dehydrogenations from the lowest energy dimer (1.72 eV) and cubane complexes (1.62 eV) are nearly similar in energy. The O-O bond coupling on the dimer starts after three dehydrogenation reactions, whereas in the cubane the O-O bond is formed after first two dehydrogenations. We also found that if an -O-OH group is formed in a reaction pathway, the next thermodynamically lowest energy step is dehydrogenation of its hydrogen atom; if this step is competing for completion of the octahedral geometry then the latter is seen to be preferred with both dimer and cubane catalysts. The cobalt atom returns back to Co(III) in pathways 1, 2 and 3 for the lowest energy cobalt dimer **D1** before

oxygen is removed, whereas in pathway 5 and 6 of the lowest energy cubane **C1**, oxygen removal occurs from Co(IV). In the lowest energy pathway 4, the cobalt atom may acquire oxidation states of Co(IV 2/3) or Co(III 2/3) before oxygen removal. Based on the competitive thermodynamic reaction pathways demonstrated by dimer and cubane complexes, we can hypothesize that various condensed clusters in cobalt oxide catalytic systems may follow through different pathways, collectively enhancing the oxygen evolution reaction.

6.6 Acknowledgements

This material is based on work supported by the National Science Foundation under Grant No. CHE-0955515. C.M.A. is grateful to the Camille and Henry Dreyfus Foundation for a Camille Dreyfus Teacher-Scholar Award (2011-2016).

6.7 References

1. Trasatti, S. Electrocatalysis in the Anodic Evolution of Oxygen and Chlorine. *Electrochim. Acta* **1984,** *29*, 1503-1512.

2. Trasatti, S. Physical Electrochemistry of Ceramic Oxides. *Electrochim. Acta* **1991,** *36*, 225-241.

3. Marshall, A.; Børresen, B.; Hagen, G.; Tsypkin, M.; Tunold, R. Preparation and Characterisation of Nanocrystalline $Ir_xSn_{1-x}O_2$ Electrocatalytic Powders. *Mater. Chem. Phys.* **2005,** *94*, 226-232.

4. Carmo, M.; Fritz, D. L.; Mergel, J.; Stolten, D. A Comprehensive Review on PEM Water Electrolysis. *Int. J. Hydrogen Energy* **2013,** *38*, 4901-4934.

5. Gorlin, Y.; Jaramillo, T. F. A Bifunctional Nonprecious Metal Catalyst for Oxygen Reduction and Water Oxidation. *J. Am. Chem. Soc.* **2010,** *132*, 13612-13614.

6. Jiao, F.; Frei, H. Nanostructured Manganese Oxide Clusters Supported on Mesoporous Silica as Efficient Oxygen-evolving Catalysts. *Chem. Commun.* **2010,** *46*, 2920-2922.

7. Najafpour, M. M.; Ehrenberg, T.; Wiechen, M.; Kurz, P. Calcium Manganese(III) Oxides ($CaMn_2O_4 \cdot xH_2O$) as Biomimetic Oxygen-Evolving Catalysts. *Angew. Chem. Int. Ed.* **2010,** *49*, 2233-2237.

8. Najafpour, M. M.; Nayeri, S.; Pashaei, B. Nano-size Amorphous Calcium-manganese Oxide as an Efficient and Biomimetic Water Oxidizing Catalyst for Artificial Photosynthesis: Back to Manganese. *Dalton Trans.* **2011,** *40*, 9374-9378.

9. Risch, M.; Klingan, K.; Heidkamp, J.; Ehrenberg, D.; Chernev, P.; Zaharieva, I.; Dau, H. Nickel-oxido Structure of a Water-oxidizing Catalyst Film. *Chem. Commun.* **2011,** *47*, 11912-11914.

10. Singh, A.; Chang, S. L. Y.; Hocking, R. K.; Bach, U.; Spiccia, L. Highly Active Nickel Oxide Water Oxidation Catalysts Deposited from Molecular Complexes. *Energ. Environ. Sci.* **2013,** *6*, 579-586.

11. Berardi, S.; La Ganga, G.; Natali, M.; Bazzan, I.; Puntoriero, F.; Sartorel, A.; Scandola, F.; Campagna, S.; Bonchio, M. Photocatalytic Water Oxidation: Tuning Light-Induced Electron Transfer by Molecular Co_4O_4 Cores. *J. Am. Chem. Soc.* **2012,** *134*, 11104-11107.

12. Du, P.; Eisenberg, R. Catalysts Made of Earth-Abundant Elements (Co, Ni, Fe) for Water Splitting: Recent Progress and Future Challenges. *Energ. Environ. Sci.* **2012,** *5*, 6012-6021.

13. Evangelisti, F.; Güttinger, R.; Moré, R.; Luber, S.; Patzke, G. R. Closer to Photosystem II: A Co_4O_4 Cubane Catalyst with Flexible Ligand Architecture. *J. Am. Chem. Soc.* **2013,** *135*, 18734-18737.

14. Kanan, M. W.; Nocera, D. G. In Situ Formation of an Oxygen-Evolving Catalyst in Neutral Water Containing Phosphate and Co^{2+}. *Science* **2008,** *321*, 1072-1075.

15. Liu, X.; Wang, F. Transition Metal Complexes that Catalyze Oxygen Formation from Water: 1979–2010. *Coord. Chem. Rev.* **2012,** *256*, 1115-1136.

16. McAlpin, J. G.; Stich, T. A.; Casey, W. H.; Britt, R. D. Comparison of Cobalt and Manganese in the Chemistry of Water Oxidation. *Coord. Chem. Rev.* **2012,** *256*, 2445-2452.

17. McCool, N. S.; Robinson, D. M.; Sheats, J. E.; Dismukes, G. C. A Co_4O_4 "Cubane" Water Oxidation Catalyst Inspired by Photosynthesis. *J. Am. Chem. Soc.* **2011,** *133*, 11446-11449.

18. Kanan, M. W.; Yano, J.; Surendranath, Y.; Dincă, M.; Yachandra, V. K.; Nocera, D. G. Structure and Valency of a Cobalt−Phosphate Water Oxidation Catalyst Determined by in Situ X-ray Spectroscopy. *J. Am. Chem. Soc.* **2010,** *132*, 13692-13701.

19. Risch, M.; Khare, V.; Zaharieva, I.; Gerencser, L.; Chernev, P.; Dau, H. Cobalt−Oxo Core of a Water-Oxidizing Catalyst Film. *J. Am. Chem. Soc.* **2009,** *131*, 6936-6937.

20. Wang, L.-P.; Van Voorhis, T. Direct-Coupling O_2 Bond Forming a Pathway in Cobalt Oxide Water Oxidation Catalysts. *J. Phys. Chem. Lett.* **2011,** *2*, 2200-2204.

21. Mattioli, G.; Giannozzi, P.; Amore Bonapasta, A.; Guidoni, L. Reaction Pathways for Oxygen Evolution Promoted by Cobalt Catalyst. *J. Am. Chem. Soc.* **2013,** *135*, 15353-15363.

22. Li, X.; Siegbahn, P. E. M. Water Oxidation Mechanism for Synthetic Co–Oxides with Small Nuclearity. *J. Am. Chem. Soc.* **2013,** *135*, 13804-13813.

23. Kwapien, K.; Piccinin, S.; Fabris, S. Energetics of Water Oxidation Catalyzed by Cobalt Oxide Nanoparticles: Assessing the Accuracy of DFT and DFT+U Approaches against Coupled Cluster Methods. *J. Phys. Chem. Lett.* **2013,** *4*, 4223-4230.

24. McAlpin, J. G.; Stich, T. A.; Ohlin, C. A.; Surendranath, Y.; Nocera, D. G.; Casey, W. H.; Britt, R. D. Electronic Structure Description of a $Co(III)_3Co(IV)O_4$ Cluster: A Model for the

Paramagnetic Intermediate in Cobalt-Catalyzed Water Oxidation. *J. Am. Chem. Soc.* **2011,** *133*, 15444-15452.

25. Rigsby, M. L.; Mandal, S.; Nam, W.; Spencer, L. C.; Llobet, A.; Stahl, S. S. Cobalt Analogs of Ru-Based Water Oxidation Catalysts: Overcoming Thermodynamic Instability and Kinetic Lability to Achieve Electrocatalytic O_2 Evolution. *Chem. Sci.* **2012,** *3*, 3058-3062.

26. Smith, P. F.; Kaplan, C.; Sheats, J. E.; Robinson, D. M.; McCool, N. S.; Mezle, N.; Dismukes, G. C. What Determines Catalyst Functionality in Molecular Water Oxidation? Dependence on Ligands and Metal Nuclearity in Cobalt Clusters. *Inorg. Chem.* **2014,** *53*, 2113-2121.

27. Jiao, F.; Frei, H. Nanostructured Cobalt Oxide Clusters in Mesoporous Silica as Efficient Oxygen-Evolving Catalysts. *Angew. Chem. Int. Ed.* **2009,** *48*, 1841-1844.

28. Dincă, M.; Surendranath, Y.; Nocera, D. G. Nickel-Borate Oxygen-Evolving Catalyst that Functions Under Benign Conditions. *Proc. Natl. Acad. Sci. U. S. A.* **2010,** *107*, 10337-10341.

29. Surendranath, Y.; Dincă, M.; Nocera, D. G. Electrolyte-Dependent Electrosynthesis and Activity of Cobalt-Based Water Oxidation Catalysts. *J. Am. Chem. Soc.* **2009,** *131*, 2615-2620.

30. Siegbahn, P. E. M. O-O Bond Formation in the S_4 State of the Oxygen-Evolving Complex in Photosystem II. *Chem. Eur. J.* **2006,** *12*, 9217-9227.

31. Dykstra, C. E.; Frenking, G.; Kim, K. S.; Scuseria, G. E.; Gordon, M. S.; Schmidt, M. W. Advances in Electronic Structure Theory: GAMESS a Decade Later. In Theory and Applications of Computational Chemistry: The First Forty Years. *Elsevier, Amsterdam* **2005**, 1167-1189.

32. Schmidt, M. W.; Baldridge, K. K.; Boatz, J. A.; Elbert, S. T.; Gordon, M. S.; Jensen, J. H.; Koseki, S.; Matsunaga, N.; Nguyen, K. A.; Su, S.; Windus, T. L.; Dupuis, M.; Montgomery, J. A. General Atomic and Molecular Electronic Structure System. *J. Comput. Chem.* **1993,** *14*, 1347-1363.

33. Barber, J. Photosynthetic Energy Conversion: Natural and Artificial. *Chem. Soc. Rev.* **2009,** *38*, 185-196.

34. Dau, H.; Limberg, C.; Reier, T.; Risch, M.; Roggan, S.; Strasser, P. The Mechanism of Water Oxidation: From Electrolysis via Homogeneous to Biological Catalysis. *ChemCatChem* **2010,** *2*, 724-761.

35. Yang, X.; Baik, M.-H. Electronic Structure of the Water-Oxidation Catalyst $[(bpy)_2(OH_x)RuORu(OH_y)(bpy)_2]^{z+}$: Weak Coupling Between the Metal Centers Is Preferred Over Strong Coupling. *J. Am. Chem. Soc.* **2004,** *126*, 13222-13223.

36. Yang, X.; Baik, M.-H. *cis*,*cis*-$[(bpy)_2Ru^{V}O]_2O^{4+}$ Catalyzes Water Oxidation Formally via in Situ Generation of Radicaloid $Ru^{IV}-O^{\bullet}$. *J. Am. Chem. Soc.* **2006,** *128*, 7476-7485.

Chapter 7 - Conclusions

Designing and developing a commercial water oxidation catalyst that can split water into its constituent molecular hydrogen and oxygen is a very essential cornerstone of renewable energy research. We learned the concept of artificial water splitting from nature. Natural water splitting occurs during the process of photosynthesis in the oxygen-evolving complex of photosystem II. The active core of this complex consists of a $CaMn_4O_4$ core with a cubane structure and a dangling manganese atom. From this blueprint many biomimetic catalysts have been proposed over the last few decades that are built on transition metal oxides. In the present day, this is still a hot topic and new structures and complex families are proposed daily that can act as possible water splitting catalysts. The main goal is to design catalysts from earth abundant materials that are cheap, efficient and can be utilized commercially. However, to date there are no definitive catalysts that can match the efficiency of the natural water splitting active core. This is likely because researchers still do not understand the fundamental properties, electronic structure, mechanisms and reactivity of these catalysts. To approach this, we started looking at two transition metal oxide species: manganese oxides, which have been selected by nature, and cobalt oxides, which are a very recent emerging interest in transition metal oxide catalytic complexes. Most of these water splitting complexes including the aforementioned $CaMn_4O_4$ active complex show a common cubane shape geometry. Thus, we used design principles to model the simplest architecture of these complexes with two manganese and cobalt atoms in a dimer fashion, as well as a dimer of a dimer in a cubane fashion. We designed these model systems to bear the essential features seen in actual catalysts, i.e. with μ-oxo and μ-hydroxo groups. These model complexes are then coordinated with water-derived ligands. In this manner, we can gain a vast knowledge of the fundamental properties of these complexes, understand the

mechanism and identify commonalities and discrepancies and therefore ultimately design catalysts from a bottom-up approach.

In our manganese dimer studies with $Mn_2(\mu\text{-}OH)_2(H_2O)_4(OH)_4$ and $Mn_2(\mu\text{-}OH)(\mu\text{-}O)(H_2O)_3(OH)_5$ complexes, we observed that the thermodynamically favorable water oxidation pathways proceed through nucleophilic attack from solvent water molecules to Mn(IV½)O and Mn(V)O groups, respectively. With the manganese cubane complexes we investigated oxidation state configurations ranging from all Mn(IV) to all Mn(III) with both μ-oxo and μ-hydroxo versions of these configurations. We noticed three reaction pathways that are thermodynamically favorable for the water oxidation process. The μ-oxo Mn_4(IV IV IV IV) and Mn_4(III IV IV IV) configuration states have the same reaction pathway for the water oxidation process and this is competing with the reaction pathway from the Mn_4(III III IV V) configuration state. All these reaction pathways follow through a nucleophilic attack from solvent water molecule to manganese oxo species. In both μ-oxo and μ-hydroxo versions of Mn_4(IV IV IV IV) and Mn_4(III IV IV IV) configurations, a Mn(VI)O group attacks a solvent water molecule. For both μ-oxo and μ-hydroxo versions of Mn_4(III III IV V) configuration this nucleophilic attack is seen on a Mn(VII)O species. We note that the thermodynamically highest energy step in both these manganese dimer and cubane complexes corresponds to the formation of their respective manganese oxo species. Thus, this can be used as a descriptor to screen out water oxidation catalysts based on the overpotential to form oxo species.

Our next step was to use higher level of theories to further investigate a manganese dimer catalyst and extract electronic structure and properties relevant to the water oxidation process. In this study, we used a $Mn_2(\mu\text{-}OH)_2(H_2O)_2(OH)_2(O(CH)_3O)_2$ model complex with CASSCF and MRMP2 level of theories. The reaction mechanism investigated follows through a direct

coupling of adjacent oxo groups. The presence of a Mn(IV)O• radical moiety has been observed. The intermediate states in this catalytic pathway have multiple nearly degenerate excited states that lie close to the ground state. This allows multiple oxidation state channels during the water oxidation process. We also observed the contribution of certain orbitals to the structure of intermediate states, i.e. structural distortions caused by a singly occupied ring π orbital.

Thermodynamically favorable water oxidation pathways from both cobalt dimer and cubane complexes involve formation of a Co(V)O moiety. The pathway on the cobalt dimer complex proceeds through a nucleophilic attack from solvent water molecule to this oxo species whereas the pathway in the cobalt cubane complex involves a geminal coupling of a Co(V)O group with a bridging oxo group. However, we also demonstrated other competitive reaction pathways for water oxidation on both dimer and cubane complexes. For both cobalt and manganese complexes we found that once the -OOH is formed in the progress of the catalytic cycle, the thermodynamically lowest energy step is to remove the hydrogen of the -OOH group. This is sometimes seen as a dehydrogenation reaction or as an intramolecular hydrogen atom transfer reaction. We believe these microscopic properties will be helpful for the development of a next generation of electrocatalysts.

In the future, we are planning to investigate the water oxidation process on a model manganese trimer complex and understand its electronic structure and properties. Furthermore, the manganese cubane complex study can be extended to investigate the effects of incorporating a calcium and/or scandium atom in the cubane core. In this way, we can investigate the effects on the water oxidation process from these atoms.

Appendix A - Supporting information for "Theoretical Investigation of Water Oxidation on Fully Saturated Mn_2O_3 and Mn_2O_4 Complexes"

Table A1 The lowest energy water oxidation reaction pathways for the fully saturated Mn_2O_4 and Mn_2O_3 complexes calculated with PBE/TZP level of theory.

Reaction Processes (Pathway-A1, Figure A1)	**Reaction energies in eV (PBE/TZP)**	**Reaction Processes (Pathway-4, Figure 3.9)**	**Reaction energies in eV (PBE/TZP)**
$\mathbf{\Delta E_{(2-1)}}$	1.81	$\Delta E_{(19-18)}$	0.87
$\mathbf{\Delta E_{(8-2)}}$	1.37	$\Delta E_{(20-19)}$	0.70
$\mathbf{\Delta E_{(31-8)}}$	0.57	$\Delta E_{(21-20)}$	1.69
$\mathbf{\Delta E_{(32-31)}}$	-0.25	$\Delta E_{(27-21)}$	1.54
$\mathbf{\Delta E_{(33-32)}}$	-0.29	$\Delta E_{(28-27)}$	0.14
$\mathbf{\Delta E_{(17-33)}}$	0.89	$\Delta E_{(29-28)}$	0.25
$\mathbf{\Delta E_{(34-17)}}$	0.76	$\Delta E_{(30-29)}$	0.39
$\mathbf{\Delta E_{(35-34)}}$	0.86	$\Delta E_{(18-30)}$	-0.50
$\mathbf{\Delta E_{(1-35)}}$	-0.64		

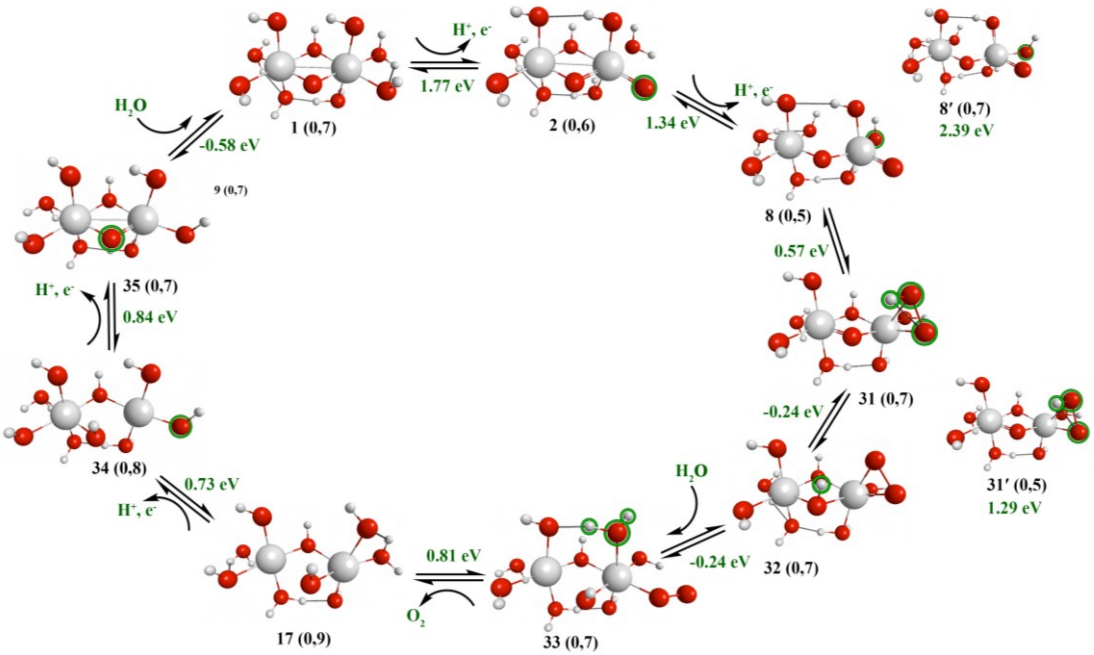

Figure A1 The third lowest energy reaction pathway-A1 on the fully saturated Mn_2O_4•$6H_2O$ structure **1** and lowest energy pathway from Mn_2O_3•$6H_2O$ starting with structure **17** calculated using the BP86/TZP level of theory.

Table A2 Calculated reaction energies and free energies for pathway-A1 of Figure A1.

Reaction Processes (Pathway-A1, Figure A1)	**ΔE (eV)**	**ΔG (eV)**
$\Delta E_{(2-1)}$	1.77	1.65
$\Delta E_{(8-2)}$	1.34	1.20
$\Delta E_{(8'-2)}$	2.39	2.23
$\Delta E_{(31-8)}$	0.57	0.57
$\Delta E_{(31'-8)}$	1.29	1.30
$\Delta E_{(32-31)}$	-0.24	-0.27
$\Delta E_{(33-32)}$	-0.24	-0.18
$\Delta E_{(17-33)}$	0.81	0.74
$\Delta E_{(34-17)}$	0.73	0.59
$\Delta E_{(35-34)}$	0.84	0.75
$\Delta E_{(1-35)}$	-0.58	-0.50

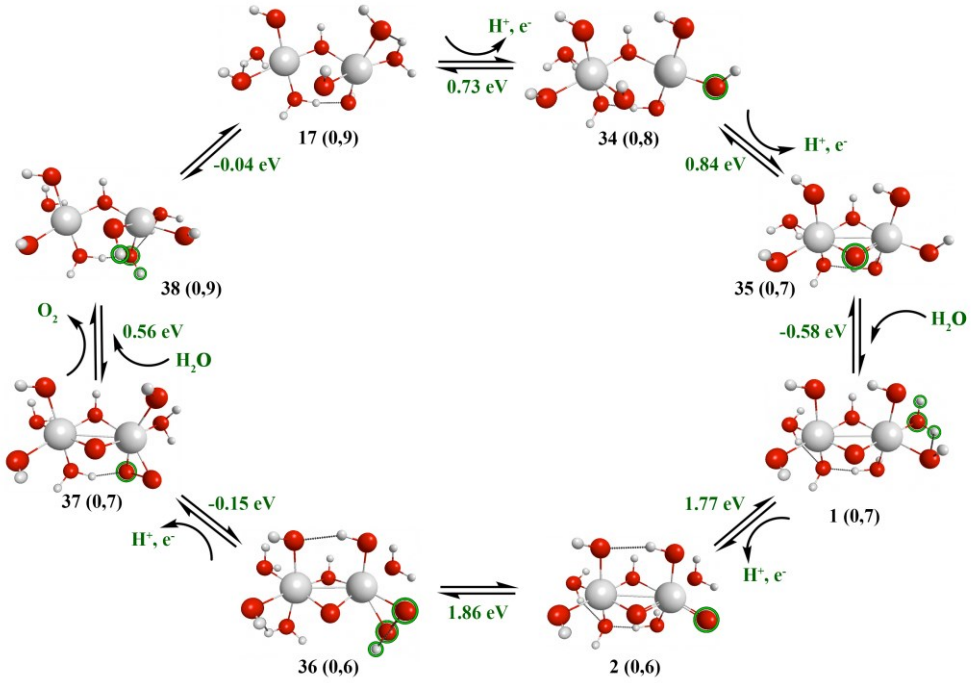

Figure A2 The second lowest reaction pathway-A2 from Mn_2O_3•$6H_2O$ structure **17**.

Table A3 Calculated reaction energies and free energies for pathway-A2 of Figure A2.

Reaction Processes (Pathway-A2, Figure A2)	**ΔE (eV)**	**ΔG (eV)**
$\Delta E_{(34-17)}$	0.73	0.59
$\Delta E_{(35-34)}$	0.84	0.75
$\Delta E_{(1-35)}$	-0.58	-0.50
$\Delta E_{(2-1)}$	1.77	1.65
$\Delta E_{(36-2)}$	1.86	1.89
$\Delta E_{(37-36)}$	-0.15	-0.30
$\Delta E_{(38-37)}$	0.56	0.48
$\Delta E_{(17-38)}$	-0.04	-0.01

Appendix B - Supporting information for "Theoretical Investigation of Water Oxidation Catalysis by a Model Manganese Cubane Complex"

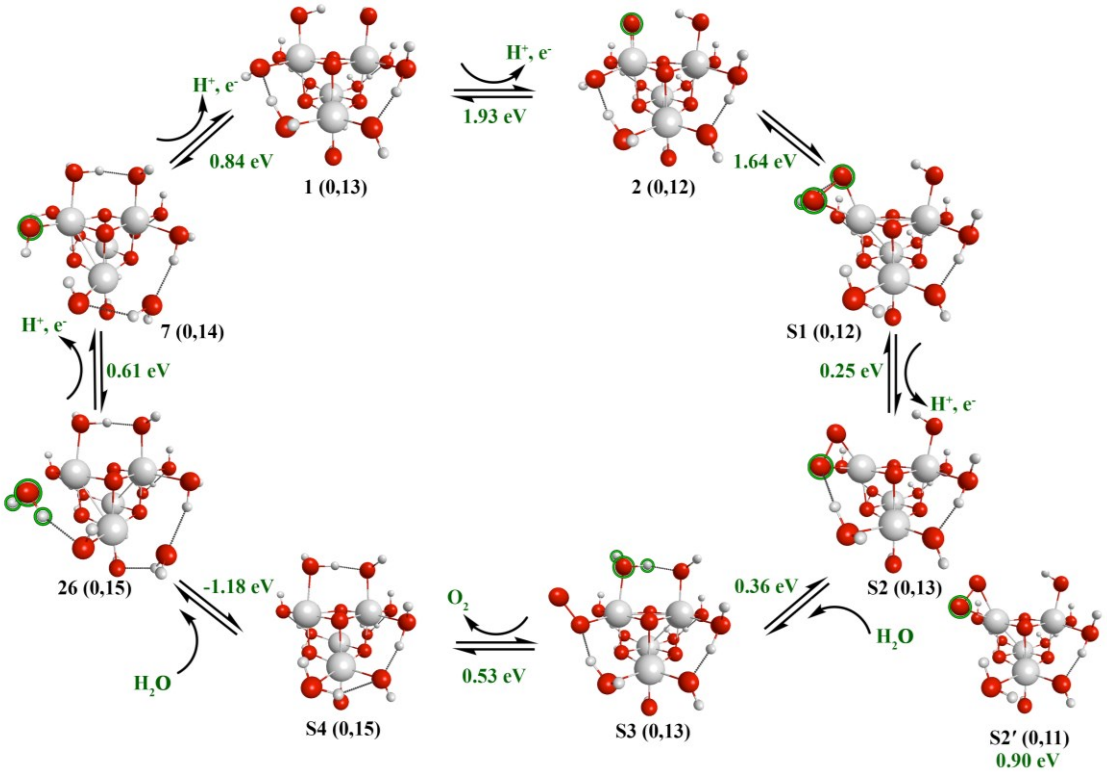

Figure B1 Proposed second lowest energy reaction pathway-B1 from structure **1** with Mn_4(IV IV IV IV) configuration.

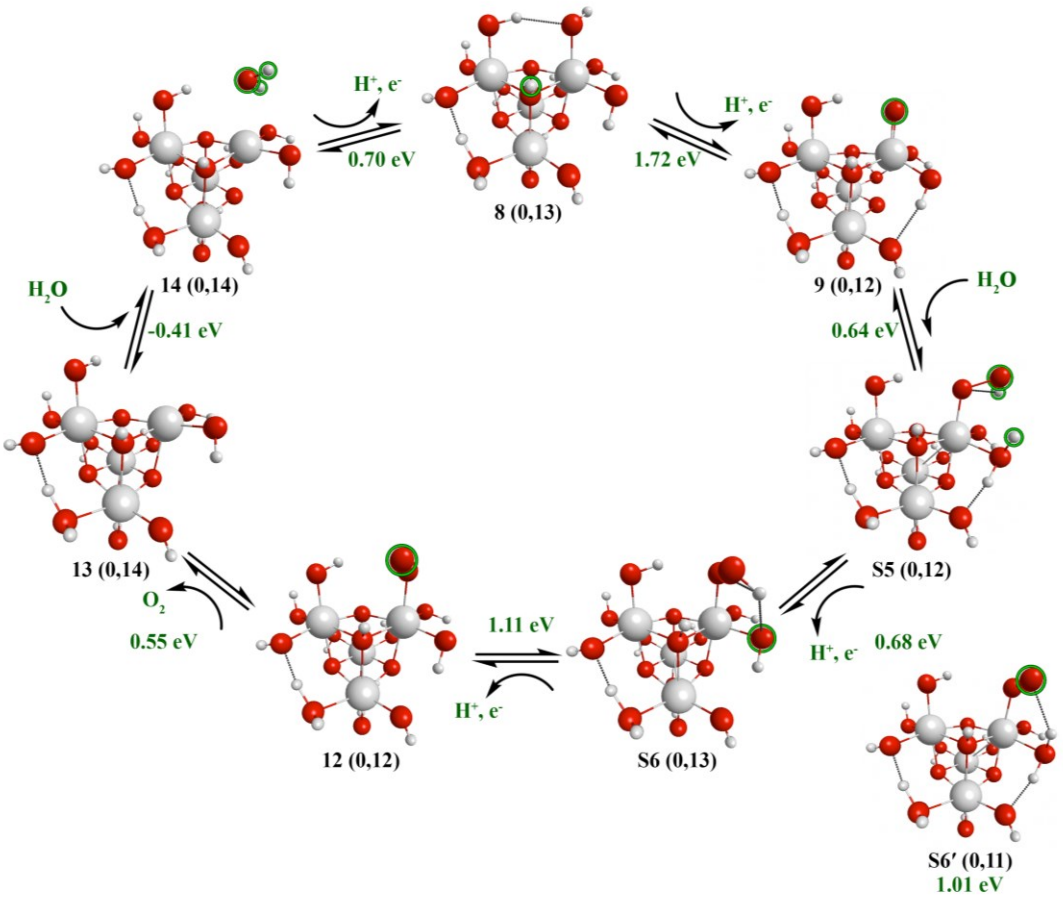

Figure B2 Proposed second lowest energy reaction pathway-B2 from structure **8** with Mn_4(IV⅔ IV⅔ III⅔ III) configuration (lowest energy structure of the structures with μ_3-hydroxo groups that are related to **1**).

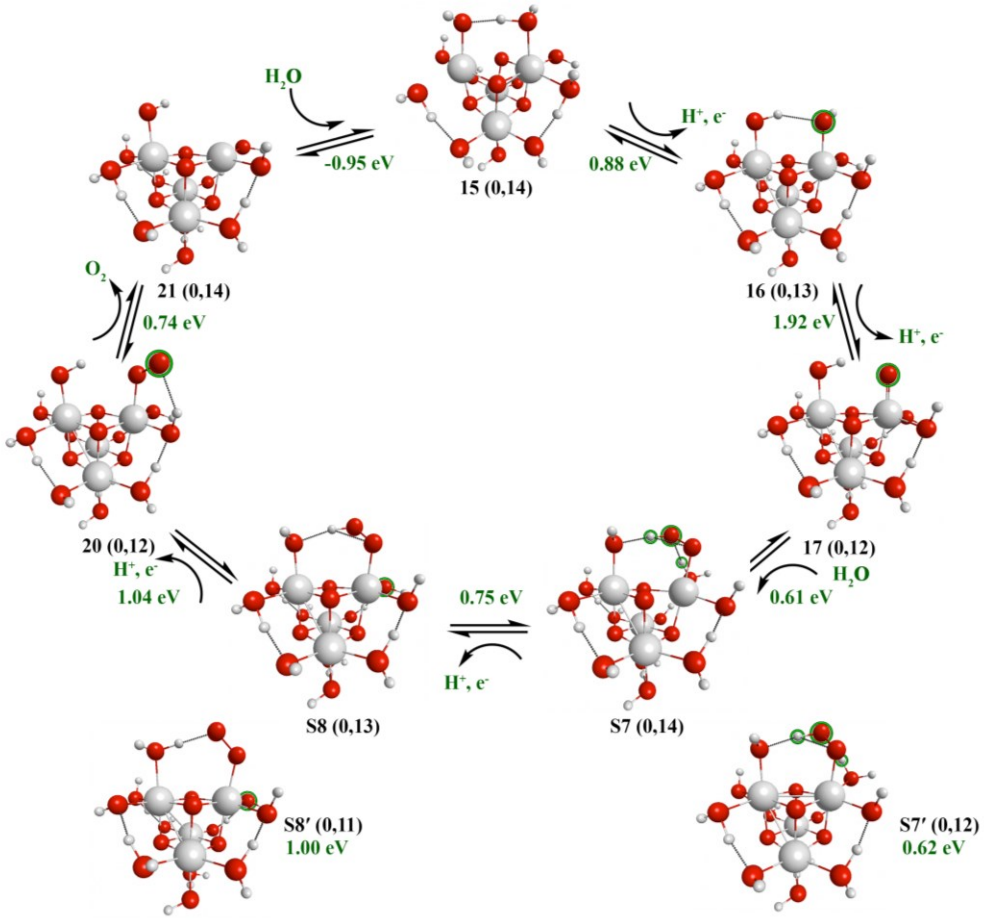

Figure B3 Proposed second lowest energy reaction pathway-B3 from structure **15** with Mn_4(III III IV V) configuration

Appendix C - Supporting Information for "Ab initio electronic structure study of a model water splitting dimer complex"

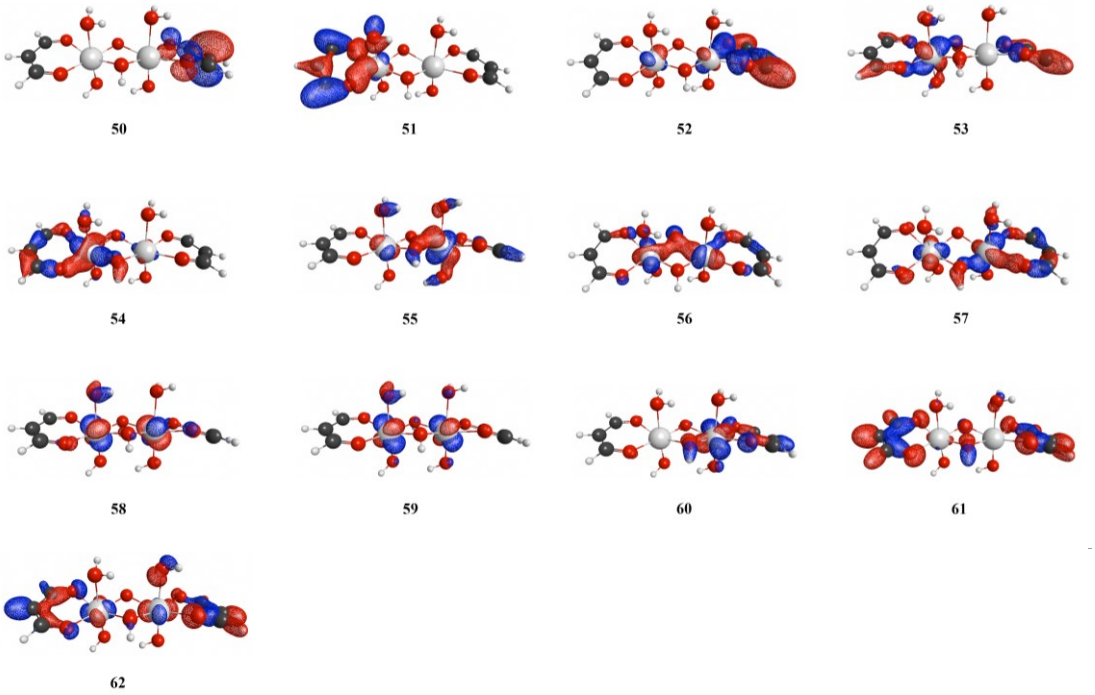

Figure C1 Occupied UHF/TZVP alpha orbitals 50-62 in the nonet state of structure **1** (Contour value = 0.05)

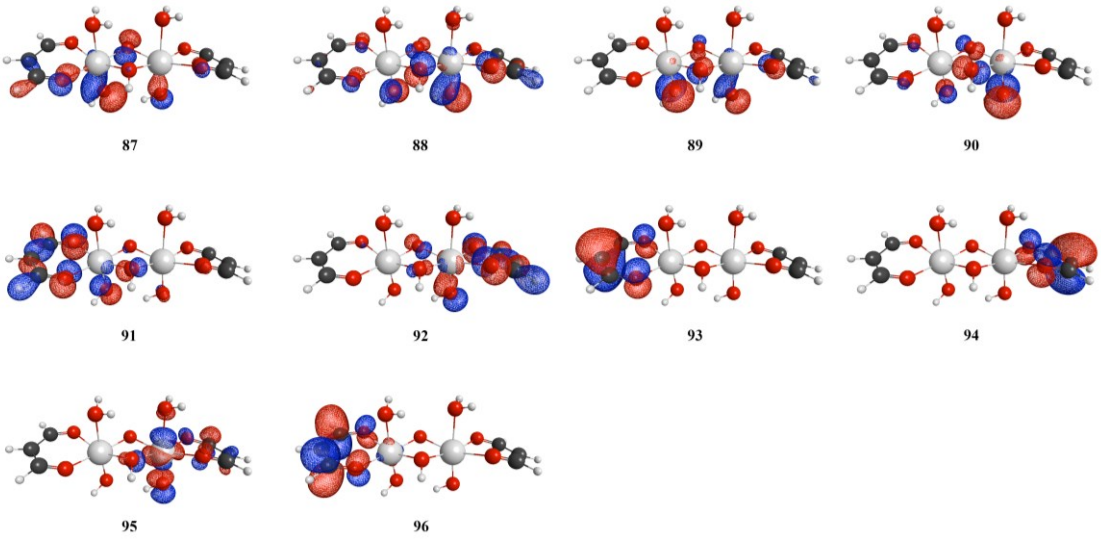

Figure C2 UHF/TZVP alpha orbitals 87-96 in the nonet state of structure **1** (Contour value = 0.05). Orbitals 87-94 are occupied and 95-96 are unoccupied.

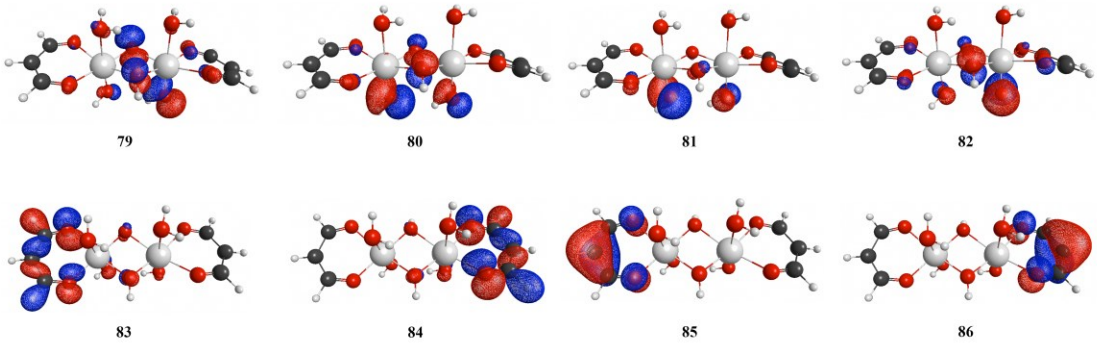

Figure C3 Occupied UHF/TZVP beta orbitals 79-86 in the nonet state of structure **1** (Contour value = 0.05).

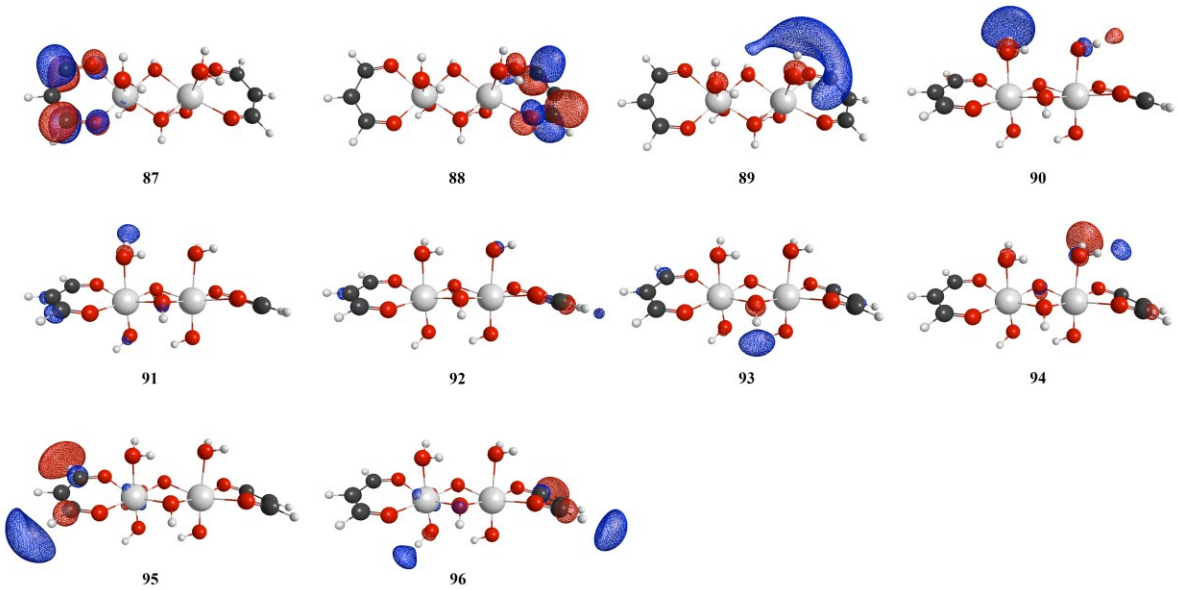

Figure C4 Unoccupied UHF/TZVP beta orbitals 87-96 in the nonet state of structure **1** (Contour value = 0.05).

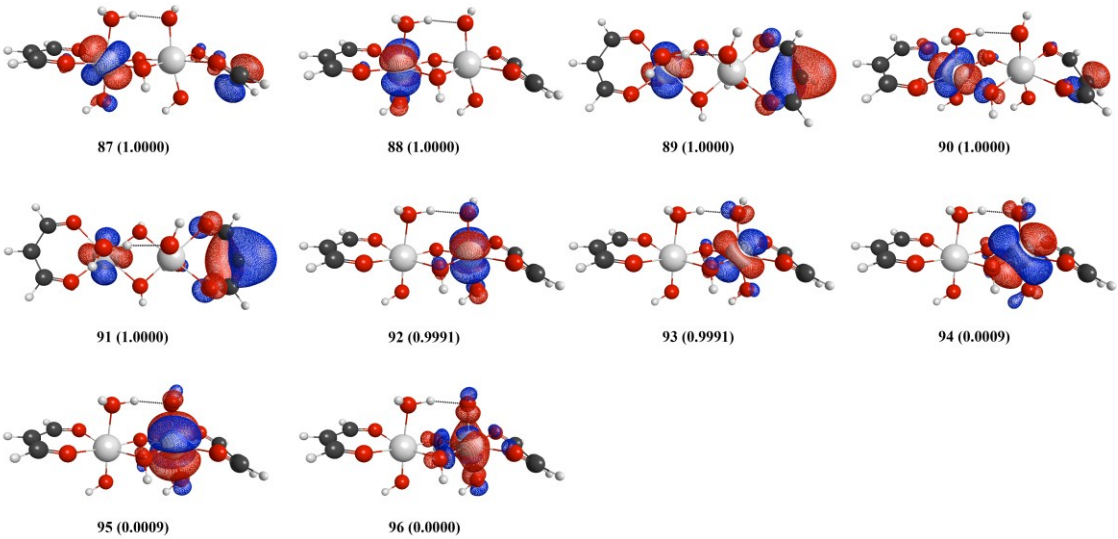

Figure C5 CASSCF(7,10)/TZVP active space natural orbitals in the octet state of structure **2**.

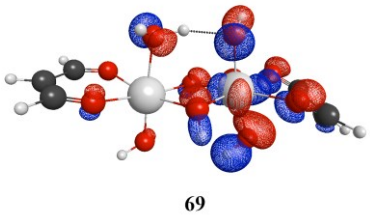

Figure C6 CASSCF(7,10)/TZVP natural core orbital 69 in the octet state of structure **2** (Contour value = 0.05).

Appendix D - Supporting Information for "Reaction pathways for water oxidation to molecular oxygen mediated by model cobalt oxide dimer and cubane catalysts"

Table D1 Comparison of reaction energies with entropy and enthalpy correction at 298 K and with solvent effect

Reaction Steps	Reaction energies calculated from absolute energy (ΔE_0) (eV)	Reaction energies calculated from Gibbs free energy (ΔG_{298}) (eV)	Reaction energies (ΔE_0) with PCM (eV)
Structure D1 to D14	2.05	1.72	2.07
Structure D14 to D15	2.24	1.91	2.19
Structure D15 to D16	2.14	1.75	2.59
Structure D16 to D17	-1.06	-1.03	-1.55
Structure D17 to D18	0.95	0.59	0.97
Structure D18 to D19	0.02	-0.57	0.02
Structure D19 to D2	-1.26	-0.56	-1.31
Structure D2 to D1	-0.09	-0.12	0.005

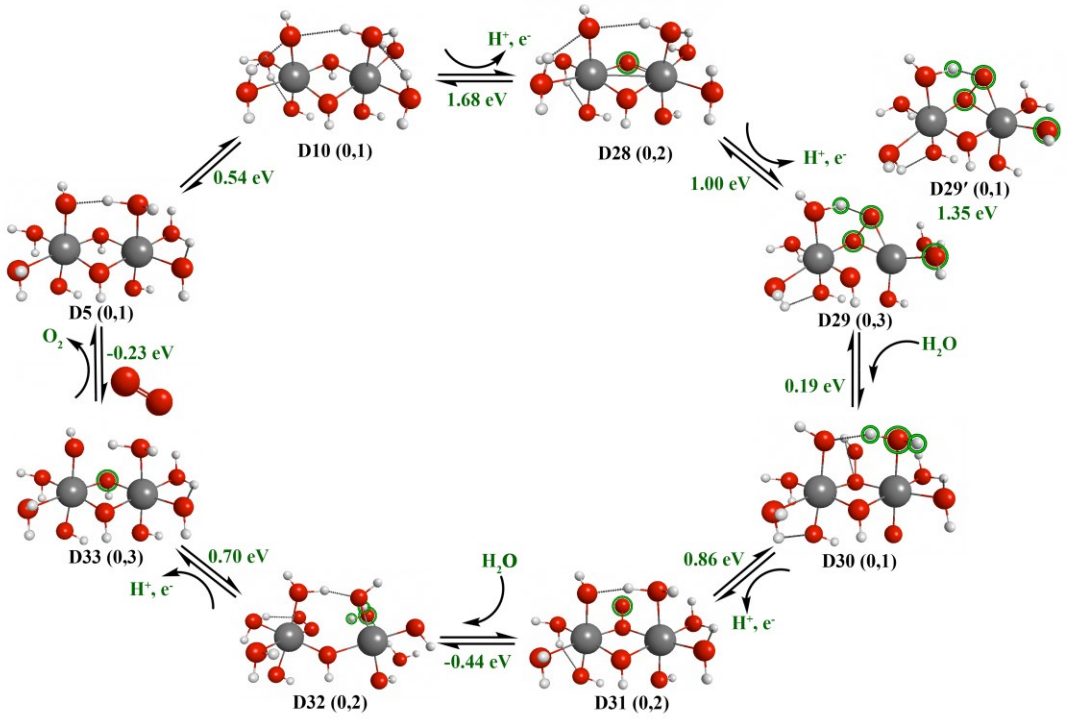

Figure D1 Proposed lowest energy reaction pathway-D1 from the cobalt dimer catalyst **D10**.

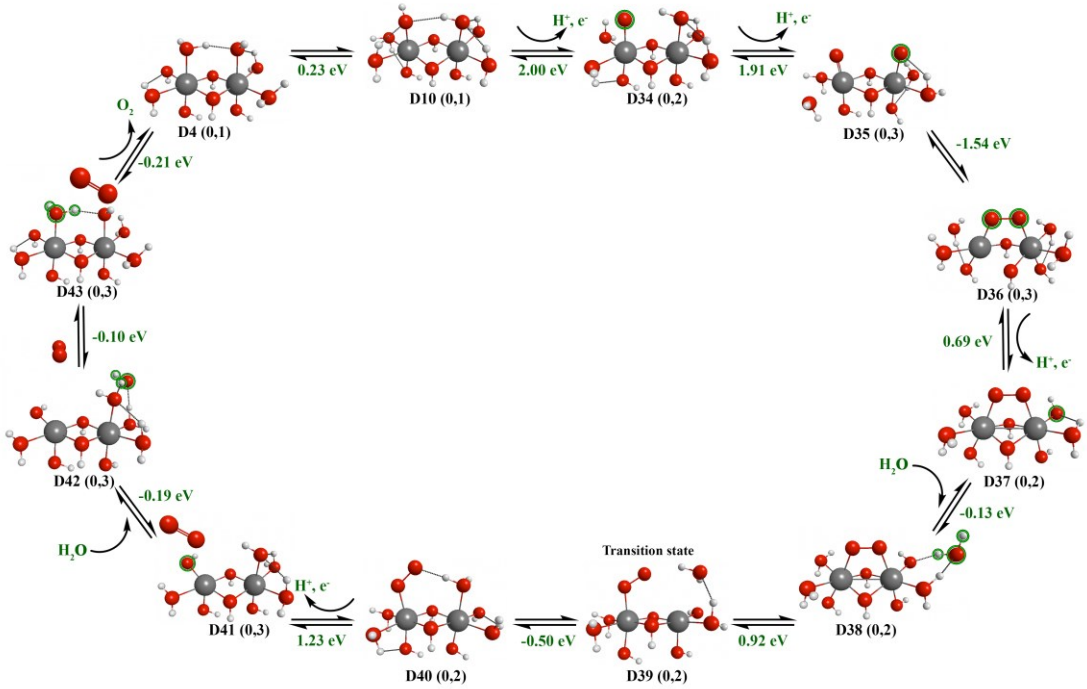

Figure D2 Direct radical oxo coupling pathway-D2 from the cobalt dimer catalyst **D10**.